

Advanced Low Temperature Metal Hydride

Materials for Low Temperature

Proton Exchange Membrane Fuel Cell

Application

By

Bulelwa Ntsendwana

UNIVERSITY of the
WESTERN CAPE

A thesis submitted in fulfilment of the requirements for the degree of
Masters in the Department of Chemistry, University of the Western Cape

Supervisor: Dr. M. Lototskyy

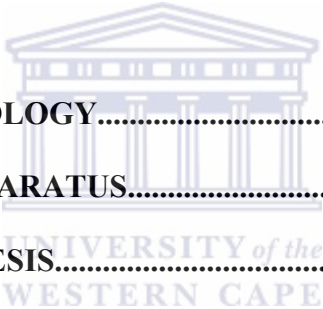
Co-supervisor Dr. M. Williams

November 2010

TABLE OF CONTENTS

Declaration.....	<i>i</i>
Acknowledgements.....	<i>ii</i>
Abstract.....	<i>iv</i>
Keywords.....	<i>viii</i>
List of figures.....	<i>ix</i>
List of Tables.....	<i>xiv</i>
List of Abbreviations.....	<i>xv</i>
List of Symbols.....	<i>xvi</i>
CHAPTER 1: INTRODUCTION.....	1
1.1 BACKGROUND ON LOW-TEMPERATURE POLYMER EXCHANGE MEMBRANE FUEL CELL APPLICATIONS.....	1
1.1.1 MOTIVATION AND STATE OF THE ART.....	1
1.1.2 TECHNICAL REQUIREMENTS FOR HYDROGEN FUEL CELL SYSTEMS.....	2
1.2 HYDROGEN STORAGE METHODS.....	4
1.2.1 HIGH PRESSURE GAS CYLINDERS.....	5
1.2.2 CRYOGENIC LIQUID.....	6
1.2.3 SOLID STATE STORAGE METHOD.....	7
1.2.3.1 <i>Binary Hydrides</i>	9
1.2.3.2 <i>Intermetallic hydrides</i>	10
1.2.3.3 <i>Complex Hydrides</i>	11
1.3 PROBLEM STATEMENT.....	13

1.4	RESEARCH AREA AND HYPOTHESIS.....	14
1.5	EXPERIMENTAL TASK.....	15
1.6	THESIS OUTLINE.....	16
CHAPTER 2: LITERATURE REVIEW.....		18
2.1	THE METAL - HYDROGEN REACTION.....	18
2.1.1	MECHANISM AND KINETICS.....	19
2.1.2	THERMODYNAMICS.....	23
2.1.3	COMMERCIALLY AVAILABLE KINDS OF HYDRIDE-FORMING ALLOYS.....	25
2.1.3.1	<i>AB intermetallic compounds</i>	26
2.1.3.2	<i>AB₂ laves phase intermetallic compounds</i>	29
2.1.3.3	<i>AB₅ intermetallic compounds</i>	30
2.2	ADVANTAGES AND LIMITATIONS OF THE AB ₅ -TYPE METAL HYDRIDE FORMING ALLOYS.....	36
2.3	MODIFICATION / IMPROVEMENT OF PERFORMANCES OF AB ₅ -TYPE MATERIALS.....	37
2.3.1	ELEMENTAL SUBSTITUTION.....	37
2.3.2	SURFACE MODIFICATION.....	39
2.4	STATE -OF -ART OF HEAT AND MASS TRANSFER IN METAL HYDRIDE STORAGE UNIT.....	42
2.4.1	FEATURES AND CHALLENGES.....	42
2.4.2	IMPROVEMENT OF HEAT TRANSFER.....	43
2.4.2.1	<i>Insertion of solid matrices</i>	43
2.4.2.2	<i>Metal hydride compacts</i>	43

2.4.2.3	<i>Internal heat exchangers.....</i>	44
2.4.3	REDUCTION OF HEAT LOSSES.....	45
2.4.4	ENHANCEMENT OF MASS TRANSFER.....	45
2.4.4.1	<i>Reduction of Hydraulic loss.....</i>	45
2.4.4.2	<i>Reduction of particle entrainment.....</i>	46
2.5	METAL HYDRIDE REACTOR DESIGNS.....	46
2.5.1	TUBULAR REACTOR.....	47
2.5.2	DISC REACTOR.....	47
2.5.3	TANK OR CHAMBER REACTOR.....	48
2.6	CONCLUSION OF LITERATURE REVIEW.....	48
		
CHAPTER 3:	METHODOLOGY.....	51
3.1	CHEMICALS AND APPARATUS.....	51
3.2	METHODS OF SYNTHESIS.....	51
3.2.1	PREPARATION OF AB ₅ -TYPE ALLOY BY ARC MELTING.....	51
3.2.2	SURFACE MODIFICATION METHOD.....	52
3.2.2.1	<i>Functionalisation of AB₅-type powders prior metal layer encapsulation.....</i>	52
3.2.2.2	<i>Sensitization and activation of AB₅-type metal powders.....</i>	53
3.2.2.3	<i>Electroless deposition of palladium on the activated AB₅ metal surface.....</i>	54
3.3	MATERIALS AND SYSTEMS CHARACTERISATION.....	54
3.3.1	X-RAY DIFFRACTOMETRY.....	55

3.3.2	SCANNING ELECTRON MICROSCOPY (SEM) AND ENERGY DISPERSIVE SPECTROSCOPY (EDS).....	64
3.3.3	ATOMIC ABSORPTION SPECTROSCOPY (AAS).....	67
3.3.4	BRUNAUER-EMMETT-TELLER TECHNIQUE.....	69
3.3.5	VOLUMETRIC MEASUREMENTS OF HYDROGEN SORPTION PERFORMANCES.....	70
3.3.5.1	<i>Kinetic studies</i>	70
3.3.5.2	<i>Thermal cycling in hydrogen</i>	72
3.3.5.3	<i>Measuring of Pressure – Composition –Temperature (PCT) equilibrium characteristics</i>	73
3.3.6	MODELLING OF PHASE EQUILIBRIA IN THE SYSTEM OF AB ₅ HYDRIDE-FORMING ALLOY WITH GASEOUS HYDROGEN.....	76
3.3.6.1	<i>Approach</i>	76
3.3.6.2	<i>Algorithm</i>	81
3.3.7	TESTING OF METAL HYDRIDE UNITS.....	87
3.3.7.1	<i>General layout of the unit</i>	87
3.3.7.2	<i>Charge – discharge testing procedure</i>	89
3.4	CONCLUSION OF METHODOLOGY.....	90
CHAPTER 4: RESULTS AND DISCUSSION.....		91
4.1	SELECTION OF APPROPRIATE METAL HYDRIDE FORMING ALLOY.....	91
4.1.1	COMPARISON OF PERFORMANCES OF TYPICAL AB ₂ AND AB ₅ TYPE ALLOYS.....	91
4.1.1.1	<i>Phase-structural characteristics</i>	92

4.1.1.2	<i>Morphology and elemental composition.....</i>	94
4.1.1.3	<i>Pressure-Composition Temperature characteristics.....</i>	97
4.1.1.4	<i>Hydrogen absorption kinetics.....</i>	99
4.1.2	JUSTIFICATION OF SELECTION OF THE AB ₅ -TYPE ALLOY FOR THE APPLICATION.....	101
4.2	PREPARATION AND ADVANCED CHARACTERISATION OF AB₅ TYPE MATERIAL FOR THE APPLICATION.....	101
4.2.1	INTERRELATION BETWEEN COMPOSITION, STRUCTURE AND THERMODYNAMIC CHARACTERISTICS OF HYDROGENATION FOR La _{1-x} Ce _x Ni ₅ INTERMETALLICS.....	101
4.2.2	PHASE COMPOSITION AND LATTICE PERIODS OF THE CONSTITUENT PHASES FOR La _{0.85} Ce _{0.15} Ni ₅ ALLOY AND ITS HYDRIDE.....	108
4.2.3	MORPHOLOGIES AND SPECIFIC SURFACE AREAS FOR STUDIES OF La _{1-x} Ce _x Ni ₅ ALLOY AND ITS HYDRIDE.....	110
4.2.4	HYDROGEN SORPTION CHARACTERISTICS OF La _{0.85} Ce _{0.15} Ni ₅ ALLOY.....	113
4.2.4.1	<i>Activation and hydrogen absorption kinetics.....</i>	113
4.2.4.2	<i>Thermal cycling in hydrogen.....</i>	120
4.2.4.3	<i>Measurement and modelling of pressure-composition isotherms.....</i>	121
4.3	INTERGRATION OF THE SELECTED AB₅-TYPE MATERIAL INTO HYDROGEN STORAGE UNIT FOR LT-PEMFC APPLICATIONS.....	127
4.3.1	EXPERIMENTAL STUDY OF UPSCALE EFFECTS.....	127

4.3.1.1	<i>Experimental study of charge/discharge performances and temperature distributions within 150 cm³ size MH reactor.....</i>	127
4.3.1.2	<i>Charge-discharge performances of the prototype air heated / cooled 2.5L-size MH hydrogen storage unit.....</i>	138
4.3.2	DESIGN AND CHARGE/DISCHARGE PERFORMANCES OF PROTOTYPE 1 GALLON SIZE WATER HEATED/COOLED HYDROGEN STORAGE UNIT.....	143
CHAPTER 5:	CONCLUSION AND RECOMMENDATIONS.....	149
5.1	CONCLUSION.....	149
5.2	RECOMMENDATIONS AND FUTURE WORK.....	154
CHAPTER 6:	BIBLIOGRAPHY.....	155



DECLARATION

I declare that “*Advanced metal hydride materials for low temperature Polymer Exchange Membrane Fuel Cell*” is my own work and that it has not been submitted for any degree or examination in any other university, and that all the sources that I have used or quoted have been indicated and acknowledged by complete references.

Bulelwa Ntsendwana



November, 2010

Signed.....

ACKNOWLEDGEMENTS

- This journey would not have been as interesting without the fascinating people I met along the way. I would first and foremost like to thank my supervisor, **Dr. Mykhaylo Lototskyy** for the opportunity to carry out this research project. The trust and support that he has provided throughout the project is very much appreciated. It is often said that in life, you will come across very few people that will take a chance on you and give you an opportunity to change your direction in life. **Dr. Lototskyy** has taken such a chance, and I thank him for that.
- The subsequent intimidating experience of presenting for a large audience was somewhat lessened knowing that I have strong supporting system that is always there to back me up if the audience decided to use me as ‘target practice’. Thus, I see fitting to express my sincere gratitude to **Dr. O. Ulleberg, Dr. E. Klochko, Dr. J. Ren, Dr. M. Williams, Mr M.W. Davids, Mr. M.J Sibanyoni** and **Mr. M.K. Modibane**.
- I would also like to thank **Mr. Adrian Josephs** (Department of Physics, UWC) and **Ms. M Waldron** (Department of Physics, UCT) for their assistance in electron microscopy.
- Thank you to **Dr. B. Remy** (Materials Research Group, iThemba Labs) for his assistance for X-ray diffraction measurement and **Mr. L. Cyster** (Department of Biodiversity and Conservation Biology, UWC) for his help in Atomic Absorption Spectroscopy.
- Heartfelt gratitude goes to my fellow colleagues who created a friendly working environment. Their enthusiasm and determination have allowed my own passion for research to flourish, and enabled me to accomplish things I would have previously thought to be inaccessible

- A warm thanks to **Hydrogen South Africa** in connection with **Department of Science and Technology** for the financial support.
- The work was also supported by the South African – Norwegian Program of Research Cooperation (2007-2010), Project #180344.
- I am indebted to thank my family for tolerating my eccentric ways the past 2 years and for standing by me through thick and thin. I thank them for all the sacrifices they have made to help me achieve my goals. They were never more than a phone call away, and their support was invaluable.
- Finally, I would like to express my appreciation to my **Grand Creator, Jehovah** for imparting me with power that is beyond normal. Even at times when I feared that darkness might enfold me, your spirit God had found me even there.



ABSTRACT

A future *hydrogen based society* in which hydrogen is the primary energy carrier, is viewed a solution to many of the energy related problems of the world such as depletion of fossil fuels. Although, for the hydrogen based society to become realizable, several technical difficulties must be dealt with, this includes cheap, safe and reliable way of storing hydrogen with high storage capacity, fast kinetics and favourable thermodynamics.

The hydrogen storage solution showing the greatest potential in fulfilling the hydrogen storage criteria with respect to fast kinetics at moderate conditions is solid state storage in intermetallic compounds such as AB, AB₂ and AB₅ type alloys particularly for stationary/low temperature Proton Exchange Membrane fuel cell application. For successful utilization, these compounds must exhibit dynamic charge/discharge performances, enhanced heat and mass transfer and improved tolerance towards gaseous impurities.

AB₅ type alloy was identified as an appropriate material due to its easiness of activation resulted from catalytic activity of metallic Ni observed as a minority phase by XRD which facilitates H₂ dissociation process. On the analysis of thermodynamic characteristics, AB₅ shows better behaviour at reasonable pressure – temperature conditions.

AB₅-type alloys exhibiting the composition La_{1-x} Ce_xNi₅ (x = 0- 0.2) were prepared by arc melting method and characterized using XRD technique. All the alloys consisted of (La, Ce) Ni₅ phase (major phase) with a CaCu₅-type hexagonal structure. Metallic Ni was identified as a minority phase at high Ce concentrations.

Thermodynamic characteristics of the partially substituted alloys showed that $|\Delta H|$ decreases with the increase in Ce concentration leading to a decrease in thermal stability of the corresponding hydride. It was also deduced that the composition $\text{La}_{0.85}\text{Ce}_{0.15}\text{Ni}_5$ can give an equilibrium pressure at room temperature of about 5 bar, which satisfies the pressure requirements of the given application.

In depth XRD studies of the $\text{La}_{0.85}\text{Ce}_{0.15}\text{Ni}_5$ alloy and its hydride were carried out. The volume expansion upon hydrogenation ($\Delta V/V_0$) was found to be 24.2 %, which is volume that should be reserved for expansion to prevent strain stress on the storage container. The effect on the surface morphology of $\text{La}_{0.85}\text{Ce}_{0.15}\text{Ni}_5$ alloy after exposure to 4 charge/discharge cycles was studied using SEM. The alloy disintegrated into small particles of grain size in the range of 10-50 μm with increased BET surface area of 0.3800 m^2/g .

Improvement of activation and hydrogen sorption kinetics by development of surface engineering solutions based on electroless deposition of Pd (0.5 g/l) on the metal surface of AB_5 type alloy was carried out. Influence of functionalisation with γ -APTES on the metal surface properties prior electroless deposition was investigated. The non-functionalised AB_5 type alloy (without γ -APTES) exhibited high Pd loading of 13.60 wt. % and 0.66 wt.% as determined by EDS and AAS analysis respectively.

The kinetics of the Pd-modified alloy was greatly increased for the first cycle in comparison to unmodified alloy whereas for the second, third and fourth cycles, the kinetics were the same. This was evident to the removal of the oxide films after the first cycle leading to a clean fresh metal surface enabling fast H_2 dissociation processes. The unmodified and surface modified alloys exhibited identical behaviour during thermal cycling.

Phase equilibria of the $\text{La}_{0.85}\text{Ce}_{0.15}\text{Ni}_5$ alloy were experimentally studied using volumetric (Sievert) techniques including thermal cycling at constant H_2 pressure and measurements of pressure-composition isotherms. The obtained data was processed using the model of phase equilibria in metal-hydrogen systems.

The PCT model assumed hydrogen occupies the metal matrix as a Van der Waals lattice gas, where parameters of α - β phase transformation below critical temperature have a random nature. The thermodynamic parameters were evaluated by fitting the detailed PCT data in the range required for the operation of the hydrogen storage unit ($T = 0\text{-}70^\circ\text{C}$, $P_{\text{H}_2} = 0.01\text{-}50$ bar).

The heat and mass transfer studies on the experimental MH-reactor containing 600 g of $\text{La}_{0.85}\text{Ce}_{0.15}\text{Ni}_5$ alloy made of stainless steel fitted with thermocouples for measuring temperature distribution within MH bed were carried out using in house testing station unit.

It was observed that heating/cooling of the MH-reactor during desorption and absorption which is limited by poor thermal conductivity in the MH-powder, significantly affects the hydrogen desorption/absorption flow rates. Initially, (first 2-3 minutes) the flow rates rapidly slow down from ~ 10 L H_2 (STP)/min to ~ 1 L/min during desorption, and 2.5 L/min during absorption.

An air cooled/heated prototype MH storage unit of 2.5 L size which comprises 8.77 kg of $\text{La}_{0.85}\text{Ce}_{0.15}\text{Ni}_5$ alloy developed by HySA Systems Competence Centre in collaboration with Resource Driven Technology Concept Centre (RETEZCA) at Tshwane University of Technology, within the special DST project A HI FAMBENI, has been tested.

The rates of the unit quickly dropped to 0.4-1 L/ min during charge continued for a very long time not completing in 20 hrs; and to 0.6-1 L/ min during discharge remaining nearly constant for more than 10 hours. The rates followed gradual heating/cooling the unit due to heat exchange with the environment. It was suggested that the problems of the charge / discharge dynamics that originate in a poor heat exchange between hydrogen storage tank and the environment can be addressed by the intensification of heat removal from the MH during charging the tank

A water cooled/heated prototype MH storage unit based on a standard 1 gallon Swagelok sample cylinder with incorporated internal exchanger was developed and tested. The unit comprises 13 kg of $\text{La}_{0.85}\text{Ce}_{0.15}\text{Ni}_5$ alloy.

The unit exhibited faster reaction rates which are attributed to insertion of internal heat exchangers capable to considerably increase temperature response during heating/cooling mainly due to intensification of heat transfer processes.

The measured hydrogen storage capacity during charging ($P= 15$ bar, $T= 10$ °C) and discharging ($P= 1$ bar, $T= 40$ °C) of the unit was 2000 L H_2 (STP) and 1900 L H_2 (STP) respectively. The achieved hydrogen storage capacity shows that the MH unit can provide more than 2 hours of full-load operation of a 1 kW LT PEMFC-stack.

KEYWORDS

Hydrogen energy

Polymer Exchange Membrane Fuel Cell

Solid state hydrogen storage

Metal hydrides

AB₅ hydride-forming alloy

Ce-substituted LaNi₅

Surface modification

Kinetics

Thermodynamics

Pressure-Composition Isotherm

Thermal conductivity

Heat and Mass transfer



LIST OF FIGURES

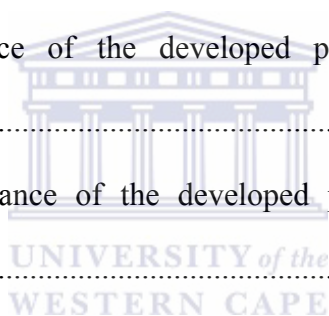
Figure 1.1:	Diagram of hydrogen PEMFC systems for Telecommunication application.....	3
Figure 1.2:	Primitive phase diagram for H ₂	5
Figure 1.3:	Tank systems for storing cryogenic liquid H ₂ at -253°C.....	7
Figure 1.4:	Classification of metal hydride materials.....	9
Figure 1.5:	Periodic table indicating possible hydride-forming elements.....	10
Figure 2.1:	Lennard-Jones potential of hydrogen approaching the metallic surface.....	18
Figure 2.2:	Schematic illustration of the different mechanisms involved in MH formation and decomposition.....	20
Figure 2.3:	The two major classes of hydrogenation/dehydrogenation curves.....	22
Figure 2.4:	Pressure-Composition-Isotherms for a hypothetical metal hydride.....	24
Figure 2.5:	Contour maps of electronic densities on the atomic plane of Ti ₂₀ Fe ₂₀ H ₄₃ cluster.....	27
Figure 2.6:	Schematic illustration of the hydride of the compounds with CsCl-type structure.....	28
Figure 2.7:	Schematic drawing of Laves phase structures with cubic (C15) and hexagonal (C14 and C36).....	30
Figure 2.8:	Schematic Flow Diagram of AB ₅ Intermetallic Compound Development.....	32
Figure 2.9:	Crystal structure of (a) AB ₅ type alloy and (b) typical AB ₅ hydride	33
Figure 2.10:	Hydride formation enthalpies for the ternary intermetallides (a) La(Ni,Al) ₅ , (b) La(Ni,Mn) ₅ , (c) La(Ni,Co) ₅ and (d); (La,Ce)Ni ₅	38
Figure 3.1:	Constructive interference of X-rays.....	56
Figure 3.2:	The definition of relations between angles and axes in unit cells.....	57
Figure 3.3:	Schematic representation of the unit cells for the seven crystal systems.....	59

Figure 3.4:	The 14 Bravais lattices.....	60
Figure 3.5:	Low index lattice planes of fcc solid.....	61
Figure 3.6:	Schematic representation of double beam flame spectrophotometers.....	67
Figure 3.7:	Schematics of the experimental setup (IFE) for studies of hydrogen absorption by the unmodified and surface modified AB ₅ -type alloy.....	73
Figure 3.8:	Schematics of experimental setup for PCT studies (A) and PCT picture (B).....	75
Figure 3.9:	Schematic representation of the algorithm of calculation of the concentration according to Equation 3.29 . The scalar starting data and calculation results are outlined by thin-line rounded boxes, and their flows are shown by line arrows. The data arrays are outlined by thick line rounded boxes, and their flows are shown by block arrows. Cyclic calculations are shown as multi-boxes.....	83
Figure 3.10:	Schematic representation of the algorithm of calculation of the filling fraction, θ , for the i -th plateau segment. The indexes (i) for the elements of arrays containing parameters of the plateau segment are omitted.....	85
Figure 3.11:	Schematic representation of the calculation $\theta(X)$ at $Z=T_C/T \leq 1$ (a) and $Z=T_C/T > 1$ (b).....	86
Figure 3.12:	Schematics of the reactor for studying activation and heat and mass transfer performances of MH beds.....	88
Figure 3.13:	Schematic diagram of the set up for testing of hydrogen storage unit.....	89
Figure 4.1:	Indexed XRD pattern of the AB ₂ -type alloy.....	93
Figure 4.2:	Indexed XRD pattern of the AB ₂ -type alloy.....	94
Figure 4.3	SEM images of AB ₂ alloys (a) x 100 and (b) x 1100 magnification.....	95
Figure 4.4:	SEM images of AB ₅ alloy (a) x100 (b) x1100 magnification.....	95

Figure 4.5: Calculated hydrogen absorption isotherms ($T=300\text{ K}$) for AB_2 and AB_5 -type alloys.....	98
Figure 4.6: Dynamics of hydrogen absorption ($T = 20\text{ }^\circ\text{C}$, $P_{H_2} = 50\text{bar}$) for AB_2 -type alloy.....	99
Figure 4.7: Dynamics of hydrogen absorption ($T = 20\text{ }^\circ\text{C}$, $P_{H_2} = 50\text{bar}$) of AB_5 -type alloy.....	100
Figure 4.8: XRD pattern of $La_{1-x}Ce_xNi_5$ when (a) $x=0$, (b) $x=0.1$, (c) $x=0.15$ and (d) $x=0.2$	102
Figure 4.9: Calculated lattice parameters with x value in $La_{1-x}Ce_xNi_5$ alloy.....	103
Figure 4.10: Dependence of c/a ratio on x value in $La_{1-x}Ce_xNi_5$ alloys.....	104
Figure 4.11: Relation of cell volume with x value in $La_{1-x}Ce_xNi_5$ alloy.....	105
Figure 4.12: Estimated enthalpies of hydride formation for cerium-substituted intermetallide $LaNi_5$ (a) and corresponding values of equilibrium hydrogen pressure at room temperature (b) calculated assuming the entropy of the hydride formation equal to $-110\text{ J}/(\text{mole } H_2.K)$	106
Figure 4.13: XRD pattern of AB_5H_x	108
Figure 4.14: SEM images of AB_5 alloy (a) before hydrogenation and (b) after hydrogenation.....	110
Figure 4.15: Particle size distribution of AB_5 type alloy before hydrogenation.....	111
Figure 4.16: Particle size distribution of AB_5 alloy after exposure to charge/discharge cycles.....	112
Figure 4.17: SEM images of (a) unmodified AB_5 , (b) AB_5 -Pd (c) AB_5 (γ -APTES) Pd.....	114
Figure 4.18: EDX spectrum of (a) AB_5 (γ -APTES) Pd. (b) AB_5 -Pd.....	115
Figure 4.19: Dynamics of hydrogen absorption by the unmodified and surface modified AB_5 type alloy.....	117

Figure 4.20: Index of power, n , depending on the rate-limiting step.....	119
Figure 4.21: Behaviour of unmodified AB ₅ hydrogen storage alloy during cooling (C) and heating (H) at various pressures.....	120
Figure 4.22: Thermal behaviour of Pd-surface modified AB ₅ alloy during cooling (C) and heating (H) at various pressures.....	121
Figure 4.23: Hydrogen absorption / desorption isotherms for the La _{1-x} Ce _x Ni ₅ alloy.....	122
Figure 4.24: 3D plots of absorption (A) and desorption (B) equilibria for H – La _{0.85} Ce _{0.15} Ni ₅ system.....	123
Figure 4.25: General view of the MH reactor before installation of the internal thermocouples (Top); and its schematic cross-section indicating location of the thermocouple joints (Bottom).....	128
Figure 4.26: Performances of the MH reactor during first (a) and second (b) charge (P=50 bar, T=30°C).....	130
Figure 4.27: Influence of pressure on charge performance of MH unit at P = 10 (a), 15 bar (b), 25 bar (c) and 50 bar (d).....	131
Figure 4.28: Pressure dependence of the reciprocal time necessary for charging MH reactor at T ₀ =30 °C to the capacity of 40 (1) and 80 (2) L H ₂ corresponding to H/AB ₅ value of 2.57 and 5.15, respectively.....	133
Figure 4.29: Influence of temperature variation at T = 25 °C (a), T = 35 °C (b) on the charge performance of the MH reactor.....	134
Figure 4.30: Temperature dependence of the reciprocal time necessary for charging MH reactor at P=20 bar to the capacity of 40 (1) and 80 (2) L H ₂ corresponding to H/AB ₅ value of 2.57 and 5.15 respectively.....	135
Figure 4.31: Discharge performance of MH unit at P = 1.5 bar, T = 30 °C (a); P = 2 bar, T = 30 °C (b); P = 3 bar, T = 30 °C (c); and P = 3 bar, T = 40 °C (d).....	136

Figure 4.32: Layout of the air heated / cooled MH hydrogen storage unit.....	138
Figure 4.33: General view of the assembled hydrogen storage unit.....	139
Figure 4.34: Charge performances of the prototype H ₂ storage unit at charge pressure of 10 bar and ambient temperature of 12 °C.....	141
Figure 4.35: Discharge performances of the prototype H ₂ storage unit at discharge pressure of 1 bar and ambient temperature of 17 °C.....	142
Figure 4.36: Schematic drawing (top) and photo (bottom) of the MH hydrogen storage unit.....	143
Figure 4.37: Collapsible copper fin element (a) and procedure of its insertion into MH container (b).....	144
Figure 4.38: Charge performance of the developed prototype MH hydrogen storage unit.....	146
Figure 4.39: Discharge performance of the developed prototype MH hydrogen storage unit.....	147



LIST OF TABLES

Table 2.1:	Typical representatives of AB ₅ metal hydride.....	34
Table 2.2:	Thermodynamic characteristics of the LaNi _{4.75} Al _{0.25} -H ₂ and LaNi _{4.8} Sn _{0.2} -H ₂ systems.....	35
Table 3.1:	Materials used in the surface modification of AB ₅ -type alloy.....	51
Table 3.2:	Relations between the length of unit cell axes and the angles between them.....	58
Table 4.1:	Elemental composition data of AB ₂ -type alloy.....	96
Table 4.2:	Elemental composition data of AB ₅ hydride-forming alloys.....	97
Table 4.3:	Lattice parameters of La _{1-x} Ce _x Ni ₅ alloy.....	103
Table 4.4:	Enthalpy and unit cell volume of x in La _{1-x} Ce _x Ni ₅ alloy.....	107
Table 4.5:	The unit cell constants and cell volumes of AB ₅ alloy and hydride.....	109
Table 4.6:	Quantitative elemental composition data for AB ₅ -Pd and AB ₅ (γ-APTES) Pd.....	116
Table 4.7:	Fitting parameters obtained from the JMA equation.....	118
Table 4.8:	Fitting parameter from Lototsky model.....	124
Table 4.9:	Summary of the calculated PCT properties for the AB ₅ hydride-forming alloy.....	125

LIST OF ABBREVIATIONS

AAS	Atomic absorption spectroscopy
ABS/DES	Absorption/desorption
APU	Auxiliary power unit
BET	Brunauer-Emmett-Teller
EDS	Energy dispersive spectroscopy
FC	Fuel cell
HCL	Hollow cathode lamp
IFC	International fuel cell
IMC	Intermetallic compound
JMA	Johnson-Mehl-Avrami
LH₂	Liquid hydrogen
LT-PEMFC	Low temperature proton exchange membrane fuel cell
MH	Metal hydride
NMR	Nuclear magnetic resonance
PCI	Pressure composition isotherm
PCT	Pressure composition temperature
PGM	platinum group metals
PMT	Photo multiplier tube
RE	Rare earth
SEM	Scanning electron microscopy
UPS	Uninterrupted power supply
XRD	X-ray diffractometry

LIST OF SYMBOLS

α	Reacted fraction
$E_{\text{HH}}(\theta)$	Energy of indirect H-H interaction (J)
ΔG°_f	Standard Gibbs free energy (kJ mol^{-1})
ΔH	Enthalpy (kJ/mol H_2)
ΔH^0	Apparent standard enthalpy (kJ/mol H_2)
H_0 and h	Constants (Lacher model)
K	Permeability (H/m)
n	Avrami exponent
ρ_{SH}	Pearson correlation coefficient
μ	Viscosity (Pa.s)
σ_h	Standard deviation of the enthalpy (kJ/mol)
σ_s	Standard deviation of the entropy (J/mol/K)
θ	Filling fraction of the metal matrix with hydrogen
ΔS	Standard entropy of formation (J/mol K H_2)
ΔS^0	Apparent standard entropy (J/mol K H_2)
φ	Distribution function (u)

CHAPTER 1: INTRODUCTION

1.1. BACKGROUND ON LOW-TEMPERATURE POLYMER EXCHANGE MEMBRANE FUEL CELL APPLICATIONS

1.1.1 MOTIVATION AND STATE OF THE ART.

Energy is one of the basic needs of human beings and is extremely crucial for continued development of human life. Our work, leisure and our economic, social and physical welfare all depend on the sufficient, uninterrupted supply of energy. Therefore, it is essential to provide adequate and affordable energy for improving human welfare and raising living standards. Global concern over environmental climate change linked to fossil fuel consumption has increased pressure to generate power from renewable sources [1].

Although substantial advances in renewable energy technologies have been made, significant challenges remain in developing integrated renewable energy systems due primarily to mismatch between load demand and source capabilities [2]. The output from renewable energy sources such as photo-voltaic, wind, tidal, and micro-hydro fluctuate on an hourly, daily, and seasonal basis. As a result, these devices are not well suited for directly powering loads that require a uniform and uninterrupted supply of input energy.

To overcome the problem related to the intermittent nature of power production of these sources, a storage medium or energy carrier is needed. One of the most promising alternatives is the use of hydrogen based fuel cell (FC) power systems where hydrogen takes up the role of the energy carrier or means of storage.

Hydrogen FC systems represent an economical and technical feasible option for reliable power supply and reduce world's dependence on imported oil reserve [3]. They also hold a great promise in meeting in a unique way the Kyoto obligation [4,5] to reduce green house gas emissions since these systems give off water as the harmless by-product [6,7]. They require less maintenance, offer higher power densities during extended run times, and have less expensive full life cycle costs without safety and disposal issues. The load demand can be achieved by addition of FC power module in parallel.

1.1.2 TECHNICAL REQUIREMENTS FOR HYDROGEN FUEL CELL SYSTEMS.

Natural disasters, unprecedented acts of terrorism and power outages from failure of aging power grid have reinforced the need for reliable back up power supply. Prolonged outages have emphasized the need for extended run times especially for critical application such as telecommunication industry. Backup power technologies currently available such as conventional batteries and generators operating on diesel can provide a continued electrical service until the power from the grid is restored [8]. Most backup power communication and data control systems use a combination of generators and batteries to provide redundancy to avoid service disruptions. Although these systems are reliable and well established, however issues associated with overcharging in batteries which eventually lead to degradation in energy output and excessive periodic maintenance, loud noise, or noxious emission in generators encourage users to seek out alternatives that provide high reliability and durability at a reasonable cost [9].

Fuel cells, particularly low temperature proton exchange membrane fuel cells (LT-PEMFCs), appear as strong contenders to replace conventional batteries and generators in the emergency back-up or uninterrupted power systems (UPS) market (**Figure 1.1**) due to their ability to start rapidly and very high power density [10]. They are more attractive in grid-connected applications where good quality, reliable power supply is required and where interruptions could last several hours since they successfully meet the requirements chosen for such applications.

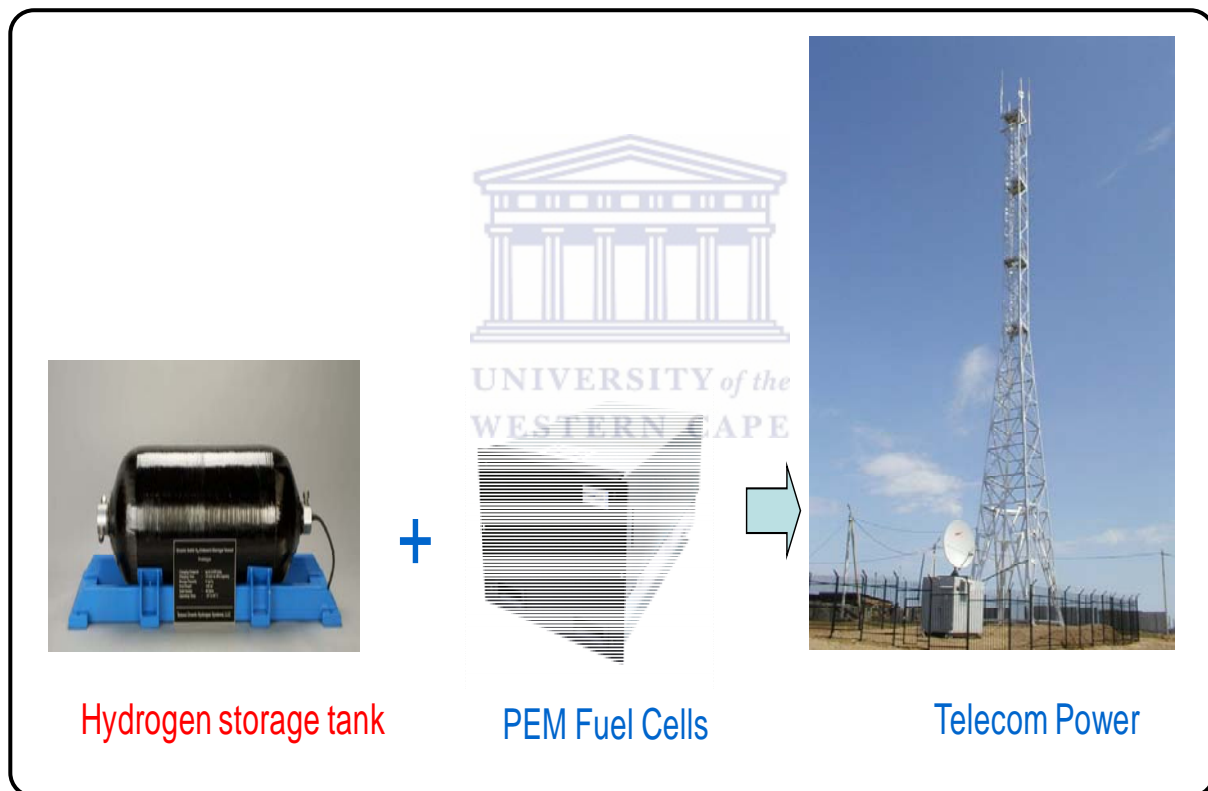


Figure 1.1: Diagram of hydrogen PEMFC systems for Telecommunication application

The typical requirements for hydrogen FC systems are the following:

- Power range: 1 to 10 kW but can rise up to 50 kW for multipurpose sites with many suppliers [11, 12].

- Autonomy: 1-2 hours according to Teledyne report [12] or 24 hours according to IFC [13].
- Duration of operation: < 300 hours per year [11].

However, a challenging problem in hydrogen PEMFC systems is in the hydrogen storage, which is a key enabling technology for the advancement of fuel cell systems.

1.2 HYDROGEN STORAGE METHODS.

Hydrogen is the most abundant element in the universe and can be produced by a variety of processes such as electrolysis and chemical extraction. As the smallest element, H₂ has the highest energy density which is 120 MJ/kg. This energy density is approximately three times the energy density of gasoline (44.5 MJ/kg) and diesel (42.5 MJ/kg) [14, 15].

Molecular hydrogen can be found in various forms depending on the temperature and pressure as shown in the phase diagram (**Figure 1.2**). There are basically three main methods that can be used to reversibly store H₂ with a high volumetric and gravimetric density and they are:

- High pressure gas cylinders
- Liquid in cryogenic tanks
- Solid state in hydride forming materials

Which choice is best, depends on several factors: the application, the energy density needed, the amount to be stored and the storage time, the forms of energy available, maintenance requirements, capital and operating cost.

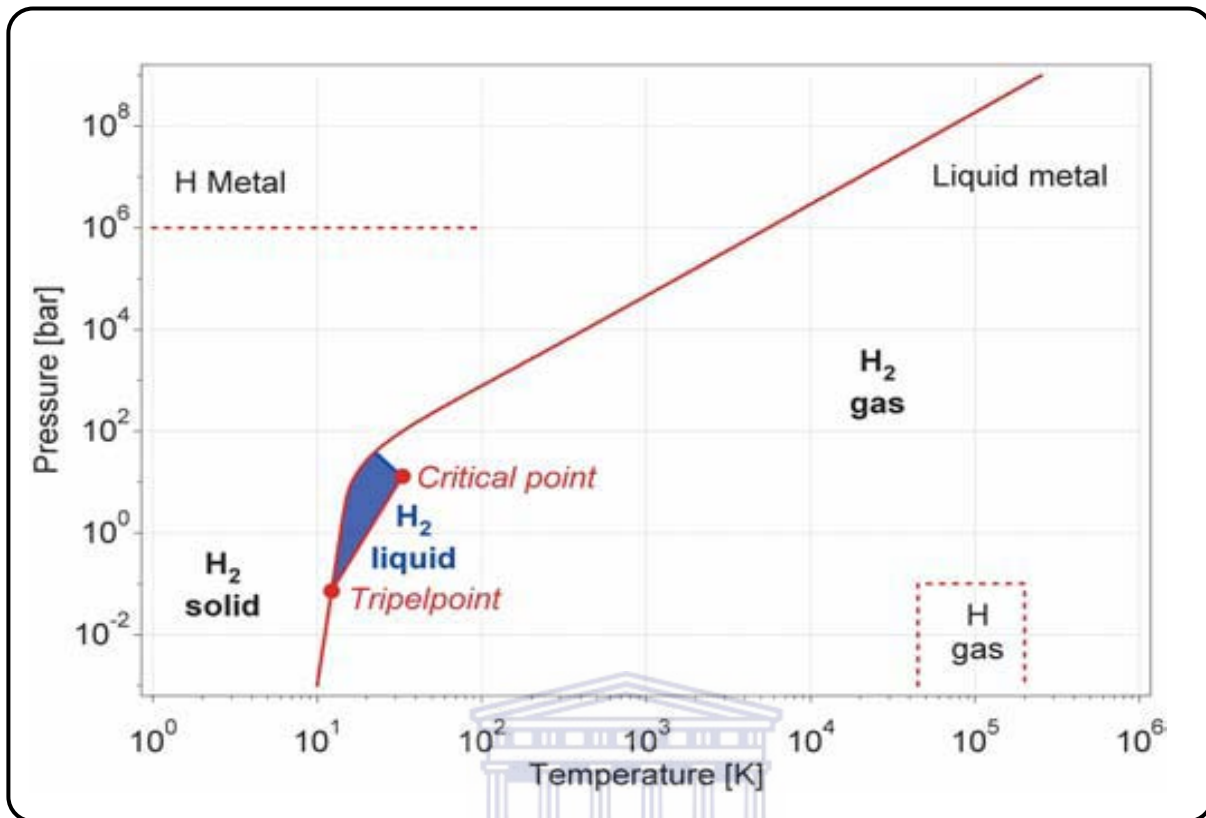


Figure 1.2: Primitive phase diagram for H₂ [16].

UNIVERSITY of the
WESTERN CAPE

1.2.1 HIGH PRESSURE GAS CYLINDERS

Gaseous hydrogen is stored predominantly in steel cylinders at a pressure of 150-200 bars and at ambient temperature of approximately 298 K. However steel cylinders suffer from low weight hydrogen capacity (standard steel cylinder weighing 60 kg has a storage capacity of 1.4 wt. %) and possibility of H₂ embrittlement [17, 18]. Certain chromium-rich steels and Cr-Mo alloys have been found suitable in resisting H₂ embrittlement. Light weight composite materials are preferred since they can reduce the overall weight of the storage [19].

Compressed hydrogen gas technologies suffer from low volumetric densities not exceeding – 40 Kg H/m³. Even at pressures as high as 70-80 MPa, the energy content of compressed hydrogen (4.4 MJ/L) is significantly less than that for the same volume of gasoline (31.6

MJ/L). Even though considered to be quite simple and inexpensive, the high pressure of 80 MPa involved in hydrogen gas cylinders raises safety concerns [20].

1.2.2 CRYOGENIC LIQUID.

Liquid hydrogen (LH₂) tanks can store more hydrogen in a given volume than compressed gas tanks. The volumetric capacity of liquid hydrogen is 0.070 kg/L, which is nearly twice that of compressed hydrogen at 70MPa. A major concern in LH₂ storage is minimizing hydrogen losses from liquid boil-off that results from evaporation of H₂ due to heat transfer and thus leading to a net loss in system efficiency. This necessitates the use of insulated cryogenic containers (**Figure 1.3**) or Dewar which consists of double wall construction and the space between these walls is filled with multi-layer insulation having several layers of aluminium foil in order to prevent radiant heat transfer [21].

LH₂ storage method consumes nearly 30 % of the total energy contained in the hydrogen and requires expensive equipment and energy to retain hydrogen in the liquid state. This relatively large amount of energy necessary for liquefaction and the continuous boil-off of liquid limit this storage system to utilizations where the cost of hydrogen is not an important issue and the hydrogen is used in a rather short time, e. g air and space applications.

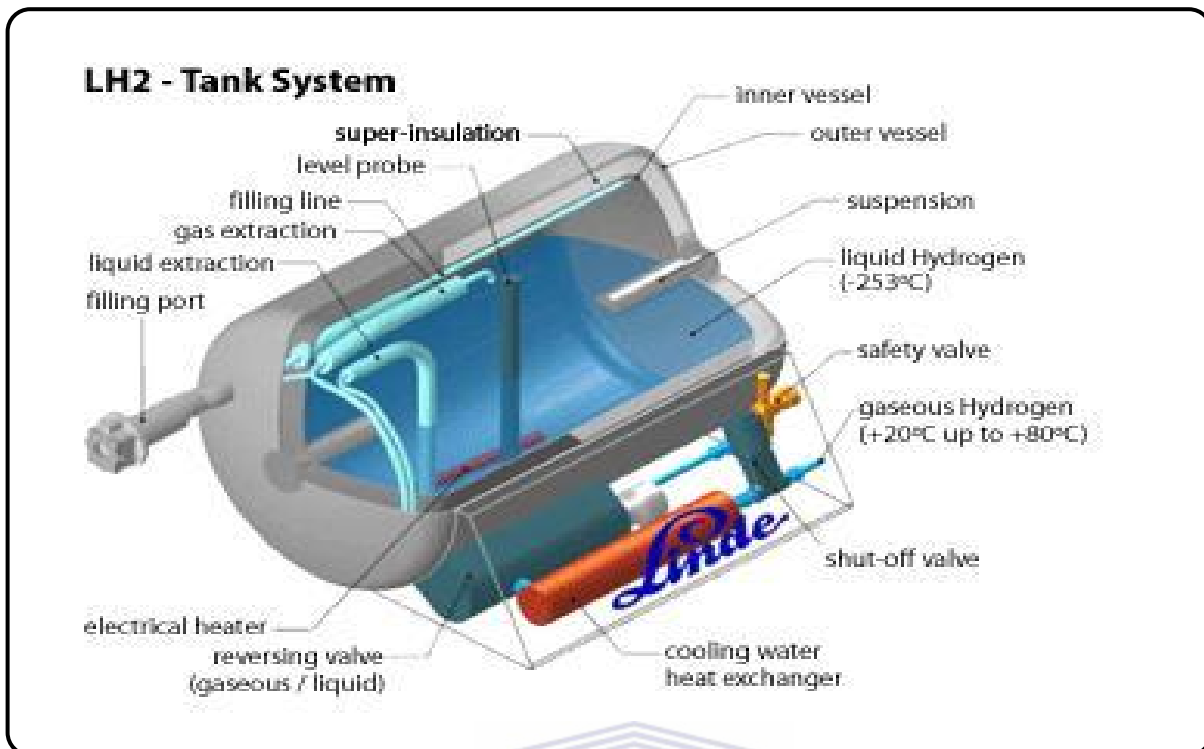


Figure 1.3: Tank systems for storing cryogenic liquid H₂ at -253°C [22]

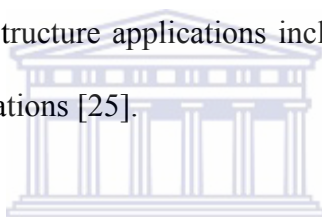
1.2.3 SOLID STATE STORAGE METHOD.

Storing hydrogen in the solid-state hydride form holds a volumetric advantage over compressed and liquid hydrogen states [23]. Solid hydrogen storage systems also have features of low-pressure operation, compactness, safety, tailorable delivery pressure, excellent absorption /desorption kinetics, modular design for easy scalability. Typical examples of commercially available solid hydrogen storage systems includes portable canisters, lightweight fibre wrapped vessels (both developed by Texaco Ovonic Hydrogen Systems LLC), metal hydride canisters developed by Heliocentric [24, 25], etc.

MH hydrogen storage units for portable power systems: The hydrogen storage units (manufactured by Texaco Ovonic Hydrogen Systems LLC) consist of four canisters each storing approximately 80g of reversible hydrogen which is capable of running a 1 kW

PEMFC for more than 247 minutes at full power. Canisters show no degradation after more than 500 charge/discharge cycles. The canisters are in the early commercialization stage for uninterrupted power supply (UPS) and auxiliary power unit (APU) application [24, 25].

Lightweight fibre-wrapped vessel: A lightweight fibre-wrapped vessel engineered with metal hydride and internal heat exchanger is being developed for mobile applications. At the system level, the vessel has a volumetric energy density of 50g H₂/L and a gravimetric density of 1.6 wt. %. The vessel can store 3 kg of H₂ with a fast refuelling capability. About 90% of the storable H₂ can be refuelled in 10 minutes at 1500 psig. The vessel can easily release the hydrogen at a rate of 350 slpm at 70 °C. Aluminium tubular vessels are being designed and tested for bulk storage and infrastructure applications including stationary power, hydrogen shipment and hydrogen service stations [25].



Metal Hydride Storage Canister: Metal hydride storage canisters can be used in compact portable or mobile systems with limited storage space or in efficient stationary systems for low-pressure hydrogen storage. The individual canisters are available in three sizes and can be cascaded depending on the storage requirements. These materials have a storage capacity of about 760 SL with volumetric energy density of 7 kg of hydrogen. This stored hydrogen can be released at a rate of 7S L/min at 20 °C and controlled pressure around 17 bar for an hour [25].

1.2.3.1 Binary Hydrides.

There are different types of hydrides as possible H₂ storage candidates, and they can be classified in terms of composition and bond nature as illustrated in the **Figure 1.4**.

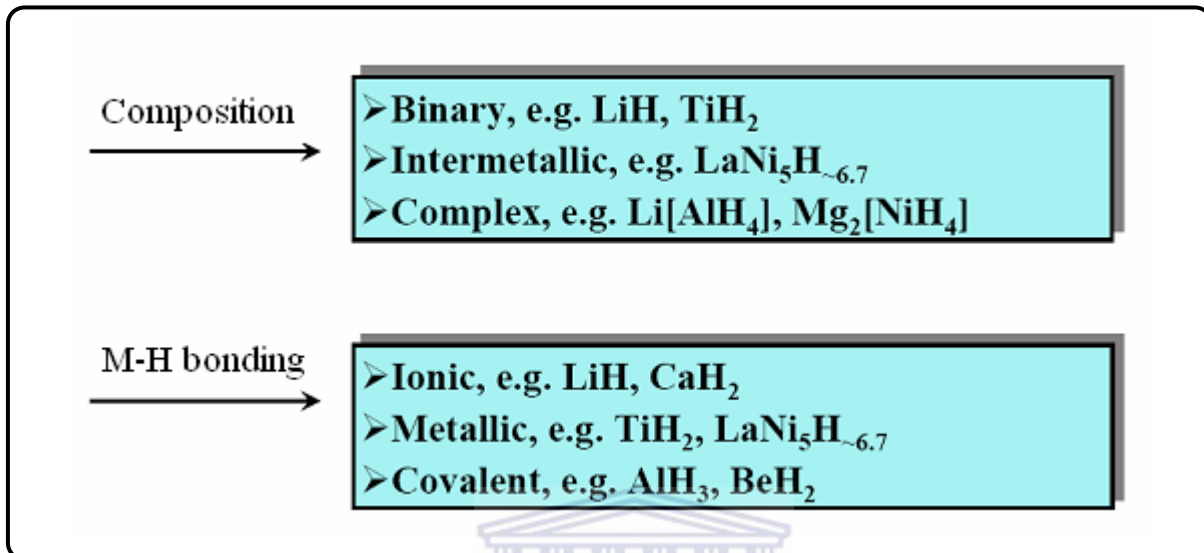


Figure 1.4: Classification of metal hydride materials.

Hydrogen directly reacts with the majority of metals (through ionic, metallic, or covalent bond), forming binary hydrides MH_x. At present binary hydrides are synthesized from all metals of the Periodic System (**Figure 1.5**) except for some Group VI, VIII transition metals [26-28]

The formation of binary hydrides requires a high metal-hydrogen chemical affinity, which means a strong metal-hydrogen bond must be formed. For these hydrides, the reaction between metal and H₂ gas is reversible only at high temperatures/pressures and exhibit too slow kinetics [28]. Another extreme case is the formation of unstable binary hydrides of transition metals (e.g., Ni) having weak M — H bond. For these metals, hydride formation takes place by hydrogen sorption from a gas phase only under high, about several kilo bars,

hydrogen pressures. Thus their utilization in most application is limited. In terms of the type of the hydrogen metal bond, metal hydrides are subdivided into three classes with essentially different physical and chemical properties.

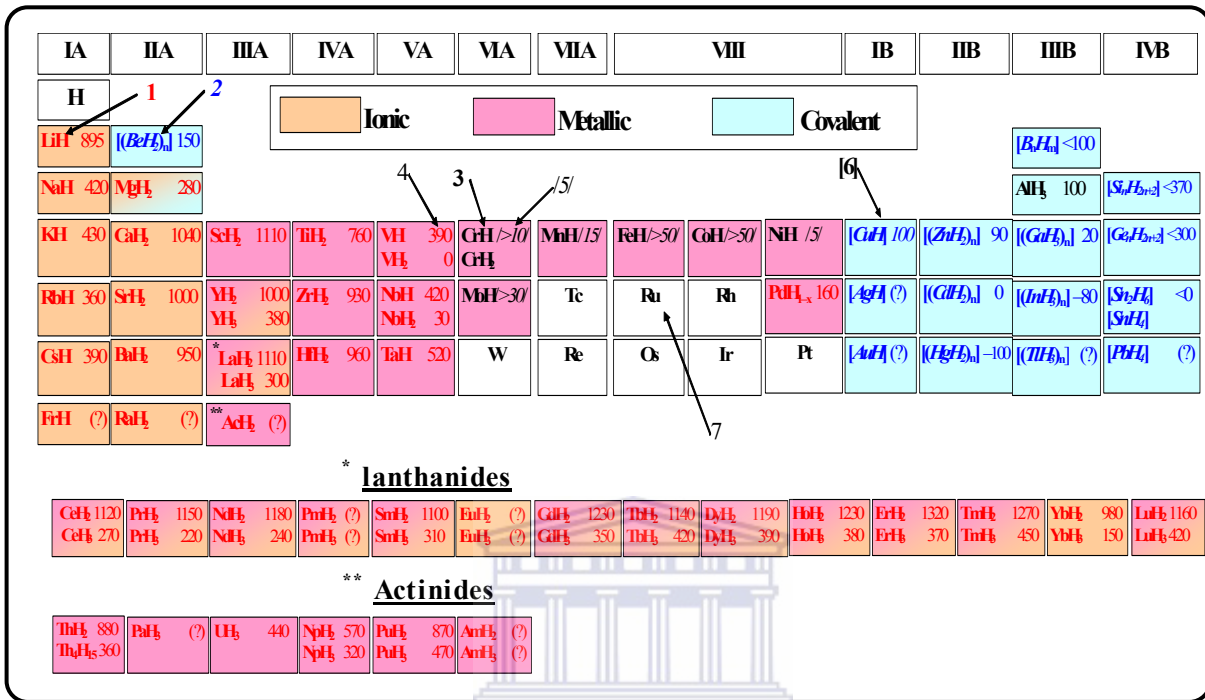


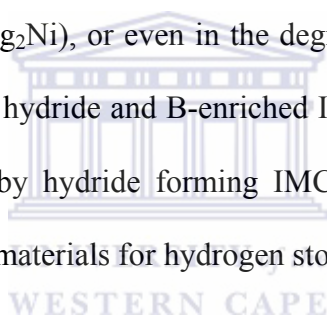
Figure 1.5: Periodic table indicating possible hydride-forming elements [26-28]. 1 – exothermic hydrides ($\Delta H_f < 0$); 2 – endothermic hydrides ($\Delta H_f > 0$); 3 – hydrides for which $\Delta H_f \sim 0$; 4 – decomposition temperature at $P_{H_2} = 1$ bar; 5 – dissociation pressure (kbar) at RT; 6 – the hydride can be synthesized only by chemical routes; 7 – binary hydrides are unknown.

1.2.3.2 Intermetallic hydrides.

The intermetallic compounds (IMCs) are the compounds of two or more metals, at least one of which (A) has a strong affinity to hydrogen, e.g. forms a stable binary hydride. The component B does not interact with hydrogen at usual conditions. Hydride-forming intermetallides are commonly classified on the basis of their component ratio m/n . Of a great

number of families of hydride-forming IMCs, the most practically valuable are AB_5 (structural type $CaCu_5$), AB_2 (Laves phases), and AB (structural type $CsCl$). In AB_5 compounds, Rare earth metal and/or calcium are used as component A, in AB_2 and AB , titanium subgroup elements [28]. The most common components B in all the families are transition metals (Fe, Co, Ni, V, Mn, Cr, etc.) [29].

The formation of IMC hydrides is accompanied by insertion of hydrogen atoms in interstitials of the metal matrix and significant expansion of the crystal lattice. However, when the contents of the A-component increases, hydrogenation of the intermetallide results in more significant changes of the arrangement of metallic atoms that results either in the essential changing the symmetry ($TiFe$, Mg_2Ni), or even in the degradation with the formation of the mixture of stable A-based binary hydride and B-enriched IMC (Mg_2Cu). The fast kinetics of hydrogen absorption/desorption by hydride forming IMC at mild conditions makes these compounds the most appropriate materials for hydrogen storage systems [30, 31].

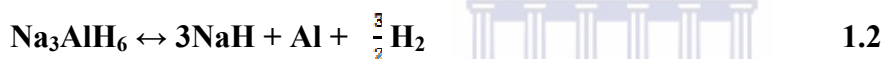
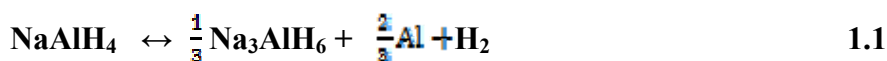


The main drawback of IMC is their low gravimetric densities of at most 1.5 wt. % [28]. However, the weight of these materials is of trivial issue for stationary application. Therefore, it is beyond dispute that, at least for LT-PEMFC application, IMC can be considered interesting as near- and medium-term solutions to the hydrogen storage problem, especially for their intrinsic safety features.

1.2.3.3 Complex Hydrides.

One more class of MH are coordination compounds where hydrogen presents as a ligand. These compounds (complex hydrides), as a rule, can be synthesized only by methods of preparative chemistry and cannot be a medium for reversible hydrogen storage. Well known

examples of chemical hydrides feature anions of hydrogenated group III elements, in particular boron and aluminium. Compounds such as LiBH_4 (lithium borohydride), and NaAlH_4 (sodium alanate) are among the most widely studied chemical hydrides [32-34]. LiBH_4 can carry a capacity of 18 wt % H_2 . However, this capacity cannot be reached practically due to high temperatures required to release H_2 [35]. Also, boron hydrides form volatile products which can damage the FC systems [36]. In addition, NaAlH_4 has theoretically reversible H_2 storage capacity of 5.6 wt% releases H_2 through a series of decomposition reactions as shown in the following equations.

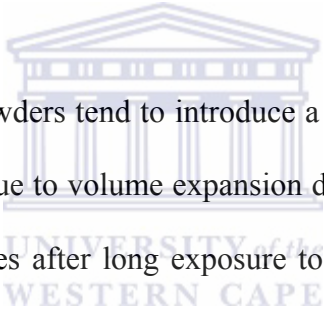


Stoichiometrically, the first step consists of 3.7 wt% H_2 release and the second step 1.9 wt%, for a theoretical net reaction of 5.6 wt% reversible gravimetric H_2 storage capacity [37, 38]. The process is characterized by slow kinetics and reversibility only under severe conditions which limits their industrial application as hydrogen storage materials.

Developments in improving the hydrogen absorption/desorption behaviour with the aid of catalysts (transition metals and their compounds) on the basis of NaAlH_4 have been achieved [39].

1.3 PROBLEM STATEMENT.

The basic construction element in most MH applications is cylindrical reaction beds or reactors, containing the MH. The dynamic behaviour of the reaction beds is of great interest i.e. fast absorption /desorption of hydrogen is required. MH can be used for a variety of applications due to their ability absorb H_2 reversible at low temperature and pressures. However, this property can be lost when these materials are suddenly exposed to air due to the formation of oxide film which prevents dissociation and diffusion of H_2 into the interstitial site of the alloy leading to a reduced reversible H_2 capacity. Activation of the alloy to remove the oxide layer prior to hydrogenation requires several activation cycles which include heating under vacuum followed by absorption of hydrogen at higher pressures.



Another challenge is that MH powders tend to introduce a significant level of strain changes on hydrogen storage tank used (due to volume expansion during absorption) and finally self-pulverized into fine small particles after long exposure to hydrogen absorption –desorption cycles. The decrepitated particles may entrain in the gas stream and pack in the container and also may damage the important parts of the tank such as valves. This can lead to contamination of pipelines, gas impedance, poor heat transfer and stressing of the container walls. For example, reaction beds are usually filled with hydride powder of a given grain size (50-100 μ m). After some 10-100 absorption/desorption cycles, the powder decomposes to an equilibrium grain size of about 1 μ m with poor thermal conductivity on the order of 1 W/m K. Such a powder or grain bed usually has insufficient heat transfer due to low thermal conductivity of the metal hydride powder and the high thermal contact resistance to the wall and also the imperfect permeability of the gas. The poor heat and mass transfer can therefore limit the absorption /desorption reaction rate [40].

1.4 RESEARCH AREA AND HYPOTHESIS.

The objectives of this study involve optimisation of the composition of the AB₅ type alloy to be used for hydrogen storage in LT PEMFC systems, their characterisation and incorporation into an experimental MH storage unit followed by study of its charge/discharge performance.

The proposed hypothesis is formulated as follows:

Advanced metal hydride forming alloy based on rare earth metal alloys with variation of composition can be prepared via arc melting. The AB₅ type alloy (La_xCe_{1-x}Ni₅, where x=0-2) whose properties will maximally correspond to operation conditions chosen for LT-PEMFC application will be selected after evaluation of their structural and thermodynamic performances. The in-depth PCT, kinetic and heat and mass transfer studies of the alloy having an optimal composition will be a basis of the integration of the material in hydrogen storage systems for the target application. Moreover, hydrogen sorption kinetics can be enhanced by surface modification of the metal alloy with palladium using electroless deposition technique. The fabricated material should exhibit fast sorption kinetics and superior dynamics of activation in non-inert environment. The developed material can be reliably characterised by standard analytical techniques.

In addressing the formulated hypothesis the sub-objective will be satisfied:

- ❖ Selection of appropriated metal hydride-forming alloy within the class of intermetallic compounds viz AB₂ and AB₅ type alloy.
- ❖ Preparation and advanced characterisation of the selected AB₅ hydrogen absorbing material based on its chemical composition, structural features and thermodynamic characteristics.

- ❖ Improvement of hydrogen absorption kinetics of AB₅-type alloy by surface modification with palladium using electro-less deposition technique.
- ❖ Evaluation of pressure composition temperature (PCT) experimental data using phase equilibria model in the systems of hydrogen gas with AB₅ hydride forming alloy.
- ❖ Experimental studies of heat-and-mass transfer performances of MH bed on the basis of the studied AB₅-type material.
- ❖ Incorporation of the studied AB₅-type material into a prototype hydrogen storage unit for LT- PEMFC applications and testing the unit as regards to its charge/discharge performance.

1.5 EXPERIMENTAL TASK.

The hydrogen storage material on the basis of AB₅ metal hydride- forming alloys characterized by easy activation, tuneable thermodynamic performances and fast hydrogen absorption / desorption kinetics at moderate temperatures (10–100 °C) will be selected.

The hydrogen sorption properties of the selected AB₅ type alloy will be studied. In so doing, the PCT relationships in MH – hydrogen systems will be measured followed by their fitting using the model of phase equilibria in metal-hydrogen systems. As a result, a set of thermodynamic parameters characterising each MH material will be obtained. The advanced surface-modified metal hydride-forming materials with palladium characterised by rapid H₂ charge/discharge cycle times using electro-less plating will be developed.

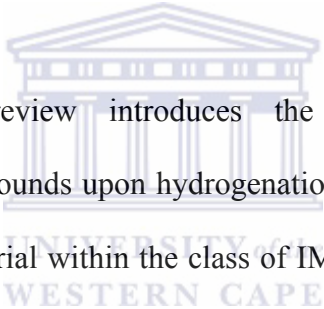
The special reactor design allowing monitoring of temperature distributions in the MH bed will be developed in order to eliminate uncertainties due to scale effects. The experimental

hydrogen storage unit ($\sim 2 \text{ m}^3 \text{ H}_2 \text{ STP}$) will be finally developed and tested as regards to its charge / discharge dynamic performances.

AB₅-type alloys will be modified using metal layer encapsulation technique. The fabricated materials will be characterised using a range of analytical techniques such as XRD, SEM/EDS, BET and AAS. The volumetric measurements for studying hydrogen properties and kinetics of the AB₅-type alloy will be carried out using Sievert type apparatus. Finally, dynamic performance of the experimentally developed MH unit will be tested using in house MH testing unit.

1.6 THESIS OUTLINE.

Chapter 2: *Literature review*



This literature review introduces the thermodynamic behaviour of intermetallic compounds upon hydrogenation and also focuses on selection of H₂ absorbing material within the class of IMCs such as AB, AB₂ and AB₅ on the basis of their structural and H₂ sorption properties. The role of surface treatment is discussed and a set of properties influencing the behaviour of the selected material is identified. In addition, the behaviour of MH storage unit as regards to its charge and discharge performance is discussed in detail as to introduce the problem areas of the study. Techniques to improve poor thermal conductivity of MH unit are also reviewed.

Chapter 3: *Methodology*

This chapter fundamentally serves as a continuation of the literature review, but with more emphasis placed on the characterization techniques employed in the study. It also gives an outline of the different materials that were used in the study.

Chapter 4: *Results and discussions*

This chapter begins by focusing on selection of the suitable metal hydride material within the class of intermetallic compound and characterisation of the selected AB₅-type alloy through chemical composition, phase-structural and thermodynamic characteristics. Phase composition and lattice periods of the constituent phases on the parent alloy and its hydride followed by investigation of influence of hydrogenation on the morphologies and specific surface areas of the parent alloy and corresponding hydride are evaluated. This is then followed by study of influence of Pd deposition on the activation and hydrogen absorption kinetics of the fabricated AB₅-type alloy and its performance during thermal cycling. The main properties of the AB₅-type alloy that characterise its suitability as a appropriate materials for optimisation of MH units are investigated through experimental measurements and modelling of the pressure composition isotherm of the parent alloy. The chapter concluded by studying the performance of the developed experimental MH storage unit and effect of internal heat exchangers on the heat and mass transfer performance of developed prototype MH unit.

Chapter 5: *Conclusion and Recommendations*

The study is concluded with a concise discussion of the objectives achieved pertaining to the study of kinetic properties of fabricated AB₅ type alloy and heat and mass transfer performance of developed MH storage unit. Recommendations are made, anomalies noted, and the greater relevance and implications of the study are discussed.

CHAPTER 2: LITERATURE REVIEW

2.1 THE METAL-HYDROGEN REACTION.

The reaction between hydrogen and a metal can be expressed by the following reaction [28].



Where Me , is a metal, solid solution or intermetallic compound. MeH_x is the metal hydride and x is the ratio of hydrogen to metal denoted as H/Me . Q is released heat during the reaction. This reaction is schematically illustrated in **Figure 2.1**. Far from the metal surface the potential of a H_2 molecule and of two H atoms are separated by the dissociation energy 436 kJ/mol [41].

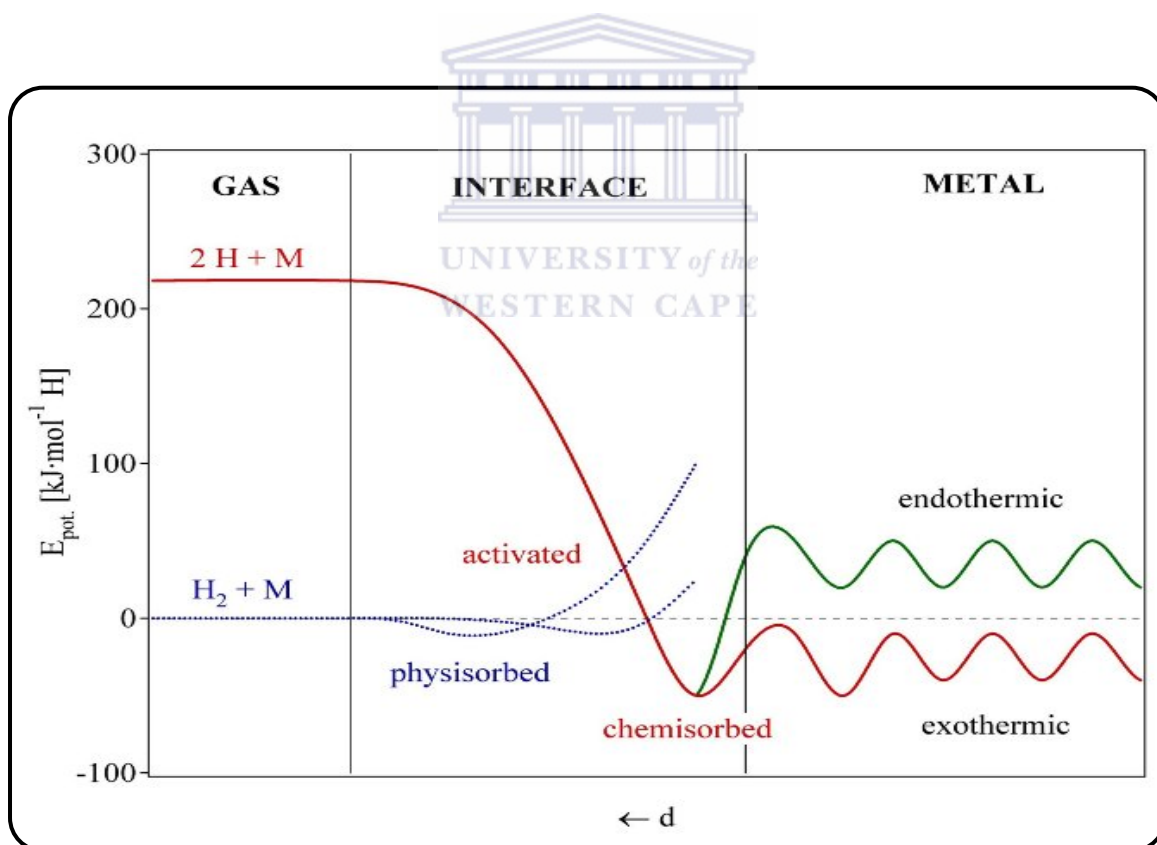


Figure 2.1: Lennard-Jones potential of hydrogen approaching the metallic surface [41, 42].

Figure 2.1, the first attractive interaction of the hydrogen molecule is the Van der Waals force in the range of 0-10 kJ corresponding to molecular physisorption [42]. If the molecule is moved closer to the metal surface the potential energy will increase due to repulsion. When a H_2 molecule crosses this activation barrier, dissociation will occur and H-atoms will be bonded to the metal surface. If intersection is at a potential energy larger than zero relative to gas H_2 , dissociation is said to be non-activated and the height determines the activation barrier. If the intersection is located at approximately zero potential energy, dissociation is said to be activated. In the former case only the fraction of H_2 molecules with energy larger than the activation barrier will be able to dissociate.

After dissociation the H-atoms find a potential energy minimum which corresponds to the H-atoms being bonded to the metal surface (chemisorption). Beyond the point of chemisorption, the H-atoms can penetrate the first metal atomic layer into the subsurface through an activated process from which it can diffuse into the bulk (as a solid solution) of the metal. If the potential energy of bulk H-atoms is below zero relative to gas phase H_2 , hydrogen solid solution is said to be exothermic and if the potential energy of bulk H-atoms is above zero, hydrogen solid solution is said to be endothermic.

2.1.1 MECHANISM AND KINETICS.

Absorption and desorption of H_2 occurs in individual reaction steps including bulk processes and can be divided into several independent steps [43-46] as shown in **Figure 2.2** and the absorption steps are listed below.

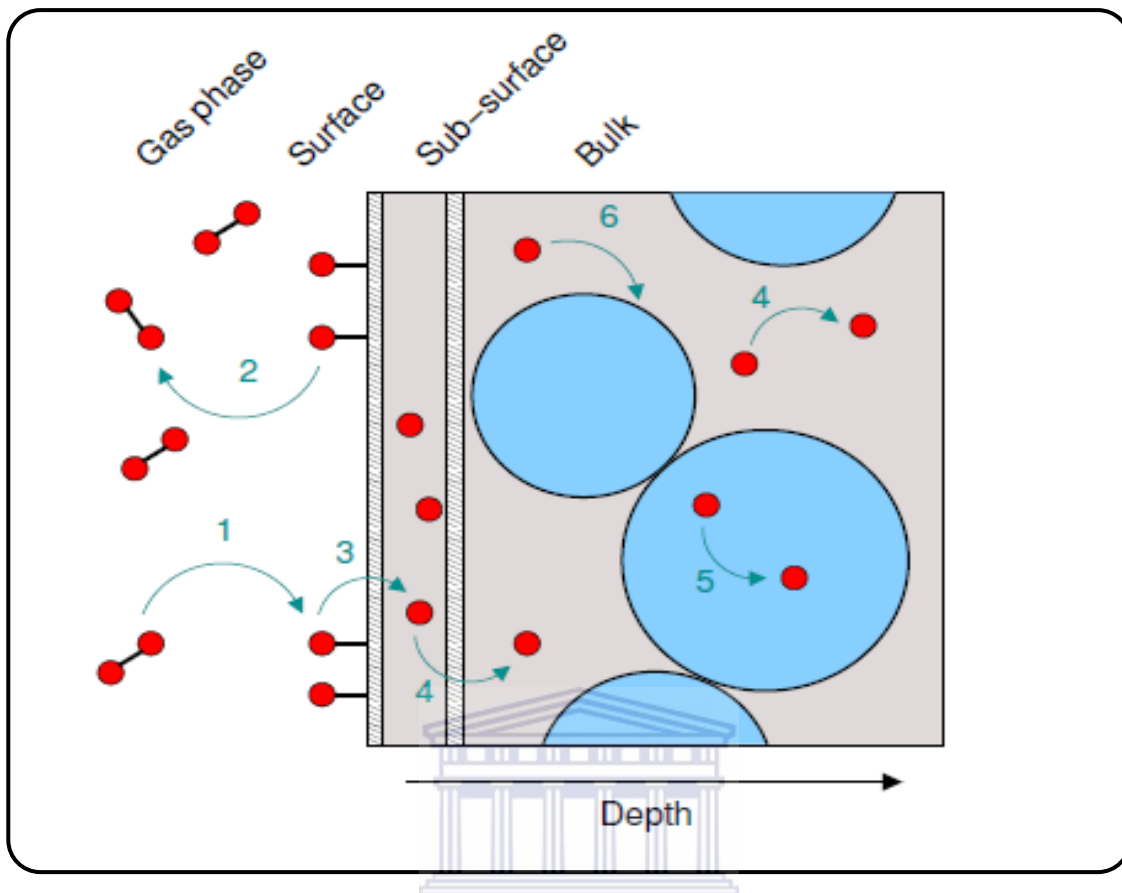


Figure 2.2: Schematic illustration of the different mechanisms involved in MH formation and decomposition. H-atoms are shown in red, the metal host lattice is shown in grey, and the MH is shown in blue [47].

Dissociation/adsorption: The first step is the dissociative adsorption of H_2 on the metal/hydride surface (Path 1 in **Figure 2.2**).

Surface penetration: From the surface, the H- atoms can penetrate into the sub-surface (Path 3).

Bulk diffusion: From the sub-surface, the H-atoms can diffuse into the bulk or from the bulk and further in (Path 4).

Hydride formation: H-atoms in the bulk (corresponding to a solid solution) can create hydride nuclei which can grow to larger hydride grains by trapping of additional hydrogen atoms (Path 6). H₂ diffusion can also take place through the hydride (Path 5).

For dehydrogenation the process is the reverse i.e. the hydride phase decomposes and hydrogen atoms diffuses to the sub-surface and subsequently to the surface, where the H-atoms recombine and desorbs as H₂ (Path 2).

A reaction mechanism can be proposed on the basis of the above reversible reactions.

Hydrogenation/dehydrogenation curves obtained by plotting macroscopic H₂ uptake/release as a function of time can roughly be divided into two major classes; one with a monotonically decreasing uptake rate and one with a sigmoidal shape [48]. The former corresponds to curve A and the latter corresponds to B as illustrated in **Figure 2.3**.

Curve A is usually rationalized in terms of either a surface process such as dissociation or bulk diffusion is rate limiting the overall kinetics whereas for curve B nucleation and growth mechanism are usually rate limiting the overall kinetics. Furthermore, rate limiting steps can be also identified by fitting the experimental data with a kinetic mode or rate equation [48]. Nucleation and growth kinetics is usually explained by a Johnson-Mehl-Avrami (JMA) rate equation [49, 50] in the following form.

$$\alpha = 1 - \exp(-(kt)^n) \quad 2.2$$

Where α is a fraction reacted at time, t , and k the rate constant. The exponent, n , referred as the Avrami exponent an integer or non integer, the value of which is governed by the geometries associated with the rate-controlling process.

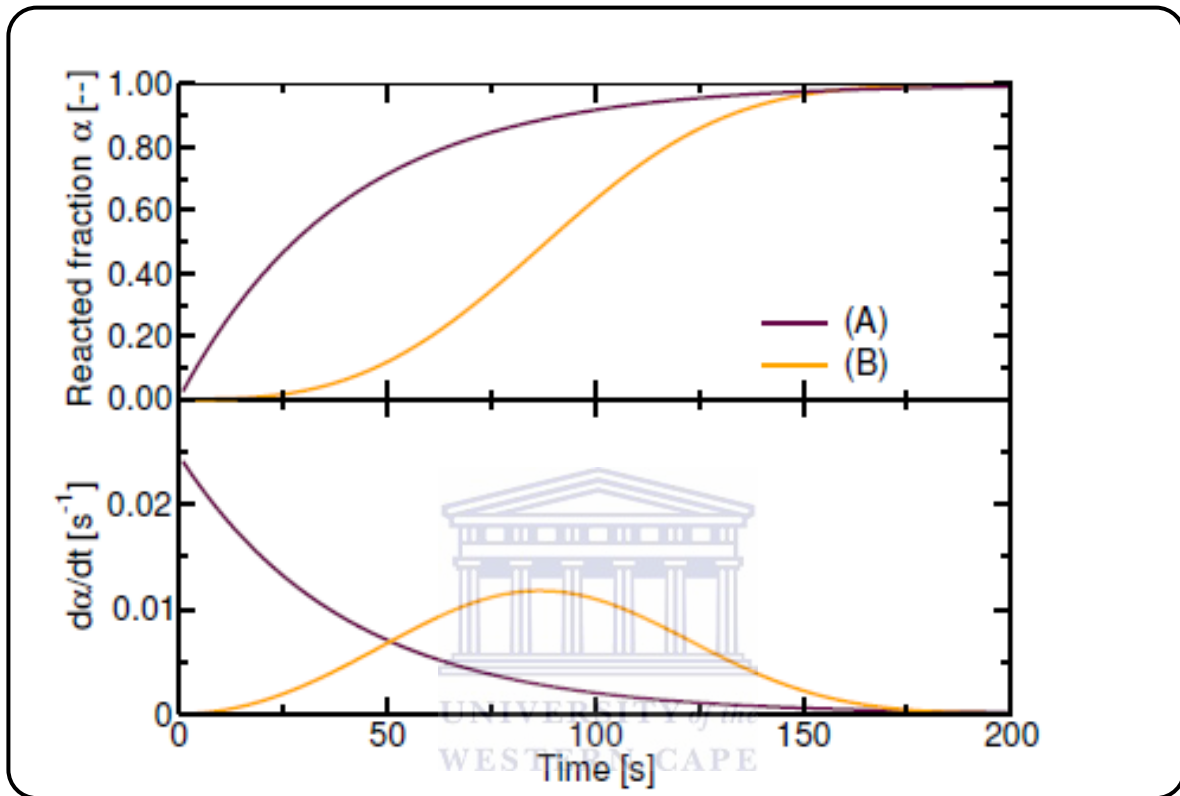


Figure 2.3: The two major classes of hydrogenation/dehydrogenation curves [43]. The H_2 uptake is shown in the upper part; the hydrogenation rate is shown in the lower part.

The temperature dependency of the rate constant k is usually described by an Arrhenius relation [51].

$$k = A \exp\left(-\frac{Ea}{RT}\right) \quad 2.3$$

Where A is a pre-exponential factor, E_a is the apparent activation energy and R is the gas constant.

JMA equation can be used to explain also curves of type A shown in **Figure 2.3**, i.e. situations where diffusion may be rate limiting, when n is allowed to have values of 1 or less. Moreover, sigmoidal uptake curve can be a result of a hydride with a protective surface oxide layer [52-54].

2.1.2 THERMODYNAMICS.

The equilibrium behaviour of MH systems is best represented by pressure –composition- isotherms (PCI) whose complete set represents pressure – composition - temperature (PCT) diagram. A generic PCI is depicted in **Figure 2.4**. At isothermal conditions initially the adsorbed amount of H_2 will increase slightly with increasing pressure leading to a formation of α -phase (solid solution of H in the host metal). When the maximum solubility of hydrogen in the α -phase is reached, the β -phase (hydride) begins to precipitate [42]. Increasing the H_2 pressure further results in complete formation of the β -phase. The pressure at which this phase transformation occurs is referred as the plateau pressure. The plateau region is the most segment of PCI, and in this region the α -phase and β -phase coexist. The plateau width gives valuable information on reversible storage capacity while the plateau pressure at a given temperature is related to the stability of the hydride [55].

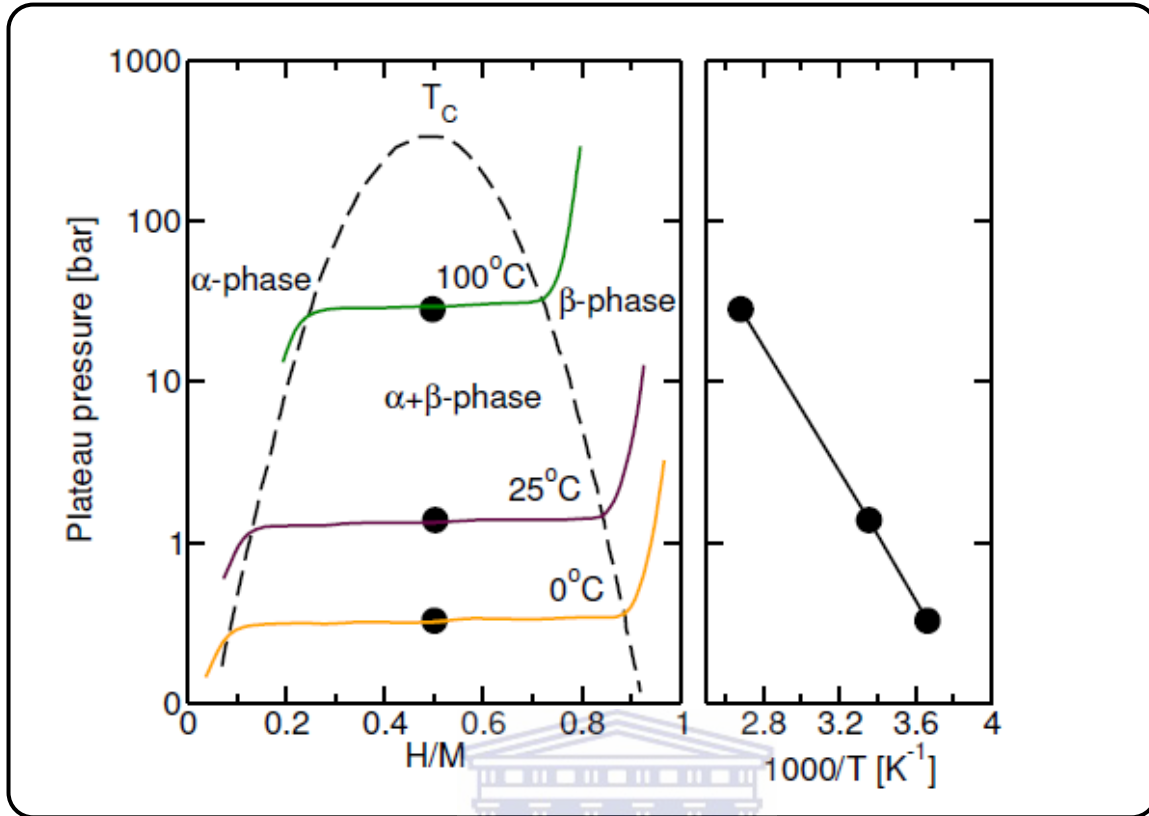


Figure 2.4: Pressure-Composition-Isotherms for a hypothetical metal hydride [56]. Right: Van't Hof plot for a hypothetical MH derived from the measured pressures at plateau midpoints from the PCI's.

Thermodynamic parameters, standard enthalpy of formation ΔH°_f , the standard Gibbs free energy ΔG°_f and standard entropy of formation ΔS°_f for MH can be calculated from the PCT data, using the following Gibbs equation:

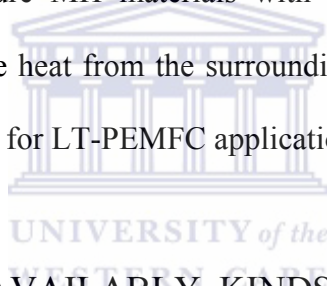
$$\Delta G^{\circ}_f = -RT \ln K_p = \frac{x}{2} RT \ln P_{H_2} \quad 2.4$$

$$\Delta G^{\circ}_f = \Delta H^{\circ}_f - T\Delta S^{\circ}_f \quad 2.5$$

$$\ln P_{H_2} = \frac{2}{x} \frac{\Delta H^{\circ}_f}{RT} - \frac{2}{x} \frac{\Delta S^{\circ}_f}{R} \quad 2.6$$

$$\ln P_{H_2} = -\frac{\Delta S^0}{R} + \frac{\Delta H^0}{RT} \quad 2.7$$

Equations 2.6 and 2.7 are known as the Van't Hoff equation. ΔH^0_f can be evaluated from the slope of the straight line as shown in **Figure 2.4**. Hence, from a number of measurements of plateau pressures at different temperatures the Van't Hoff equation can be applied to determine enthalpy and entropy of formation of metal hydride. Züttel *et al.* [57] reported that for a MH to be able to utilise heat from the surrounding when releasing H_2 , the enthalpy of formation should be about -30 kJ/mol that is typical for intermetallic hydrides (incl. AB_5 -type ones) to be low temperature MH materials with low enthalpy of formation [57]. Therefore, they are able to utilize heat from the surroundings or take heat directly from the fuel cell and thus are better suited for LT-PEMFC application.



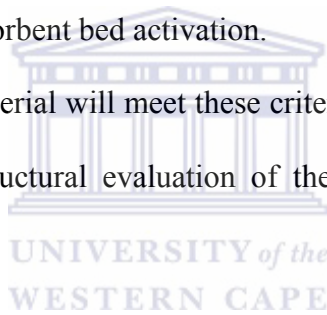
2.1.3 COMMERCIALY AVAILABLY KINDS OF HYDRIDE-FORMING ALLOYS.

The intermetallics are the compounds of two or more metals, at least one (metal A) of which has strong affinity towards H_2 . The other component is non hydride forming metal B. Based on the ratio of A to B, IMCs are classified as several families in which many of them of practical importance, namely AB_5 ($CaCu_5$ structure type), AB_2 (Laves phases) and AB (CsCl-related structure type). In AB_5 type, rare earth elements or Ca are the A-component; in AB_2 and AB, A is the element of Ti group elements. Of all the class of compounds, B component is mainly formed by transition metals (Fe, Co, Ni, Mn, Cr etc). Nowadays, these IMCs have received attention in practical applications like solid state hydrogen storage tanks [58] for PEMFC power system. However, the selection of material as a storage medium will depend

on the ability of the metal alloy to satisfy a number of criteria for successful utilization with PEMFC power systems. These may include:

- H-storage capacity >1 wt. % (nominal—depends on the specific application).
- Low cost (both materials and processing).
- Desorption pressure (P_{des}) 1–10 bar.
- Use waste heat for desorption (i.e., <90 °C for PEMFC).
- Fast kinetics (especially, H₂ absorption during refuelling process).
- Durability during absorption/desorption and temperature cycling.
- Safety and low toxicity.
- Resistance to contamination and common impurities.
- Minimal demands for hydride sorbent bed activation.

In order to know whether the material will meet these criteria, a study of thermodynamic and kinetic behaviour as well as structural evaluation of the materials under investigation is necessary.



2.1.3.1 AB Intermetallic compounds.

History: AB compound, ZrNi, was the first demonstration of reversible intermetallic hydrides [59]. Unfortunately, practical application of ZrNiH₃ was limited due to high desorption temperature of about 300 °C. Around 1970 Reilly and Wiswall demonstrated TiFe as the first practical AB hydride [60], since then TiFe and its substitution modifications remain the best of the AB today.

Crystal structure: TiFe-based AB alloys are based on an ordered body-centred cubic structure (prototype CsCl, strukturbericht B2, Pearson cP2, space group $Pm-3m$). In the CsCl-type structure, hydrogen atom occupies a central site of the octahedron which is constructed with

four Ti and two Fe atoms (hereafter referred to as the $\text{Ti}_4\text{Fe}_2\text{H}$ octahedron). The H_2 absorption capacity in TiFe is known to be smaller ($\text{H}/\text{M}=1.0$) than the value ($\text{H}/\text{M}=1.5$) which would be expected from their crystal geometry [61, 62]. This is due to a formation of another octahedron which is constructed with two Ti and four Fe atoms ($\text{Ti}_2\text{Fe}_4\text{H}$ octahedron) as shown (Figure 2.5).

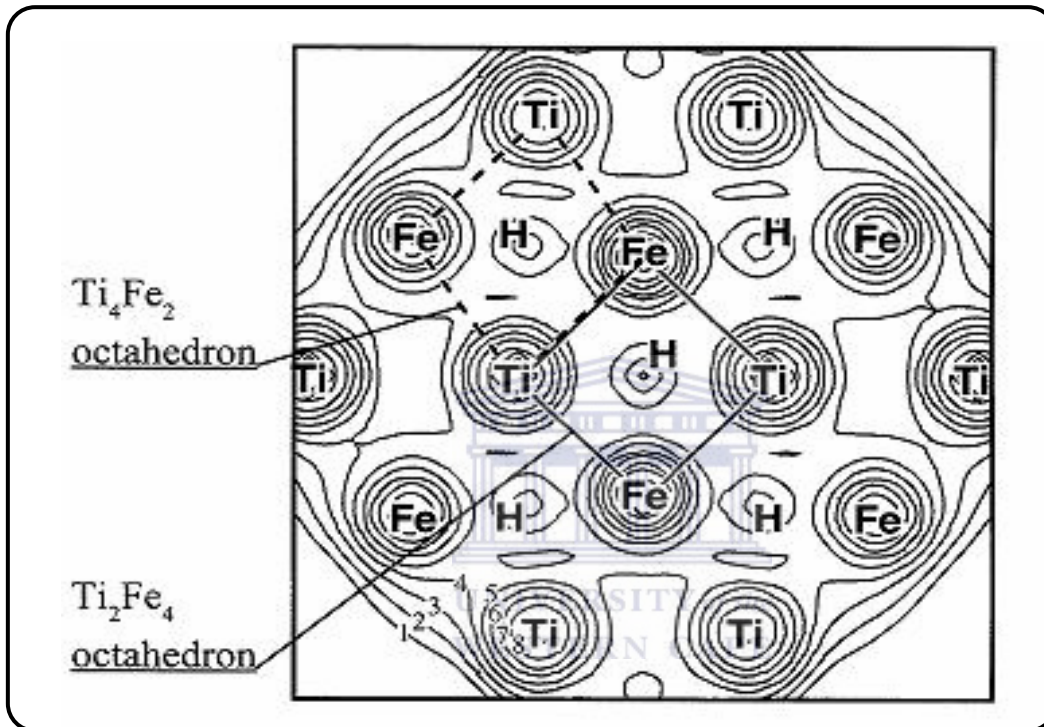


Figure 2.5: Contour maps of electronic densities on the atomic plane of $\text{Ti}_{20}\text{Fe}_{20}\text{H}_{43}$ cluster [62].

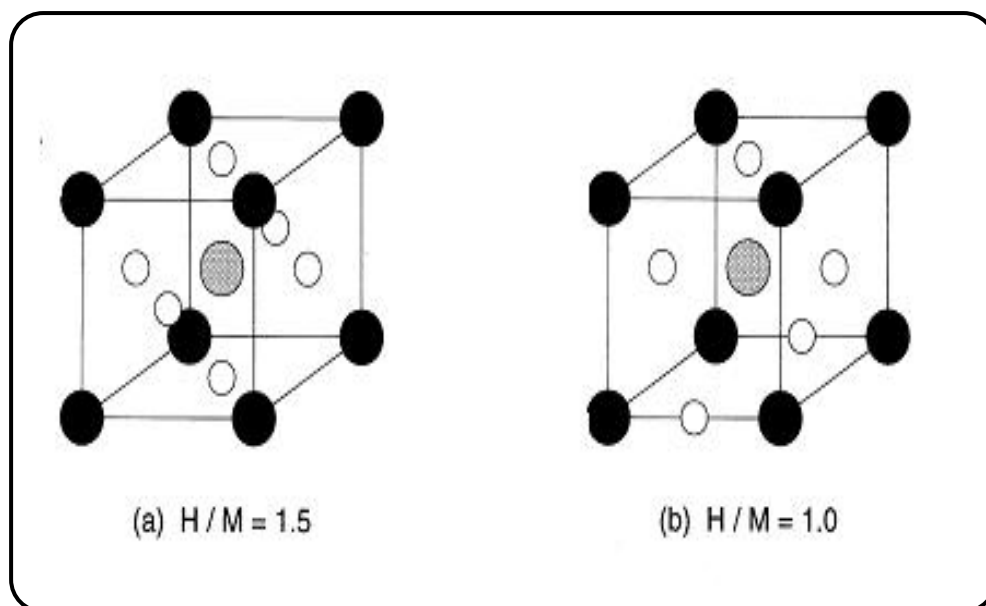


Figure 2.6: Schematic illustration of the hydride of the compounds with CsCl-type structure; (a) simple hydride, (b) TiFe hydride [62]

Once the Ti_2Fe_4 sites are occupied by H atoms as shown in **Figure 2.6** (b), the nearest Ti_4Fe_2 octahedral sites cannot be occupied anymore by H atoms. Therefore, the H-capacity expected for Ti compound with CsCl structure as illustrated in **Figure 2.6** (a) is reduced from 1.5 to 1.0 due to lesser number of Ti atoms which serves as H_2 absorbing atoms in comparison to Ti_4Fe_2 octahedral sites.

PCT and other properties: TiFe compounds tend to have two plateaus, both with reasonable pressures at ambient temperature and the hysteresis is quite large. Activation is relatively slow and difficult for the TiFe compounds due to formation of passive oxide films on the metal surface which prevent hydrogen diffusion leading to a decreased reversible H_2 capacity and slow reaction kinetics [63]. PCT properties can be modified by partial substitution of Fe by Mn or Ni [28]. The problems associated with gaseous impurities, slow kinetics and upper plateau instabilities have prevented large scale commercial use of the AB alloys.

2.1.3.2 *AB₂ Laves phase intermetallic compounds.*

History: Laves phases form the largest group of IMCs. More than 1400 binary and ternary Laves phases are reported in Pearson's Handbook of Crystallographic Data for Intermetallic Phases [64]. The discussion on the special properties of the crystal structure of Laves phases started in the 1920s and 1930s [65, 66]. The work of Laves gave the first valuable insight into the characteristics and properties of this class of intermetallics. This led Schulze to introduce the term 'Laves phase compounds which are commonly expressed as AB₂ [66].

Crystal structure: AB₂ alloys crystallize in Lave phase structures which can be hexagonal (C14 MgZn₂ or C36 MgNi₂) or cubic (C15 MgCu₂) as shown in **Figure 2.7** [67, 68]. The structural stability of the Laves phases depends on the geometric factor, that is, ratio of the atomic radii of the two elements (optimum $r_A/r_B=1.225$) and the electronic factor related to the electro negativity and the valence of the elements [69, 70].

Van Midden *et al.* [71] reported that hexagonal C14 ZrCr₂ Laves phases can be easily stabilized in comparison with cubic C15 and Hong *et al.* [72] observed that full H₂ occupancy is not a real option in Laves phase structures due to limitation related to the Switendick criterion which states that two hydrogen atoms occupying interstitial sites should be at least 0.21nm apart [73].

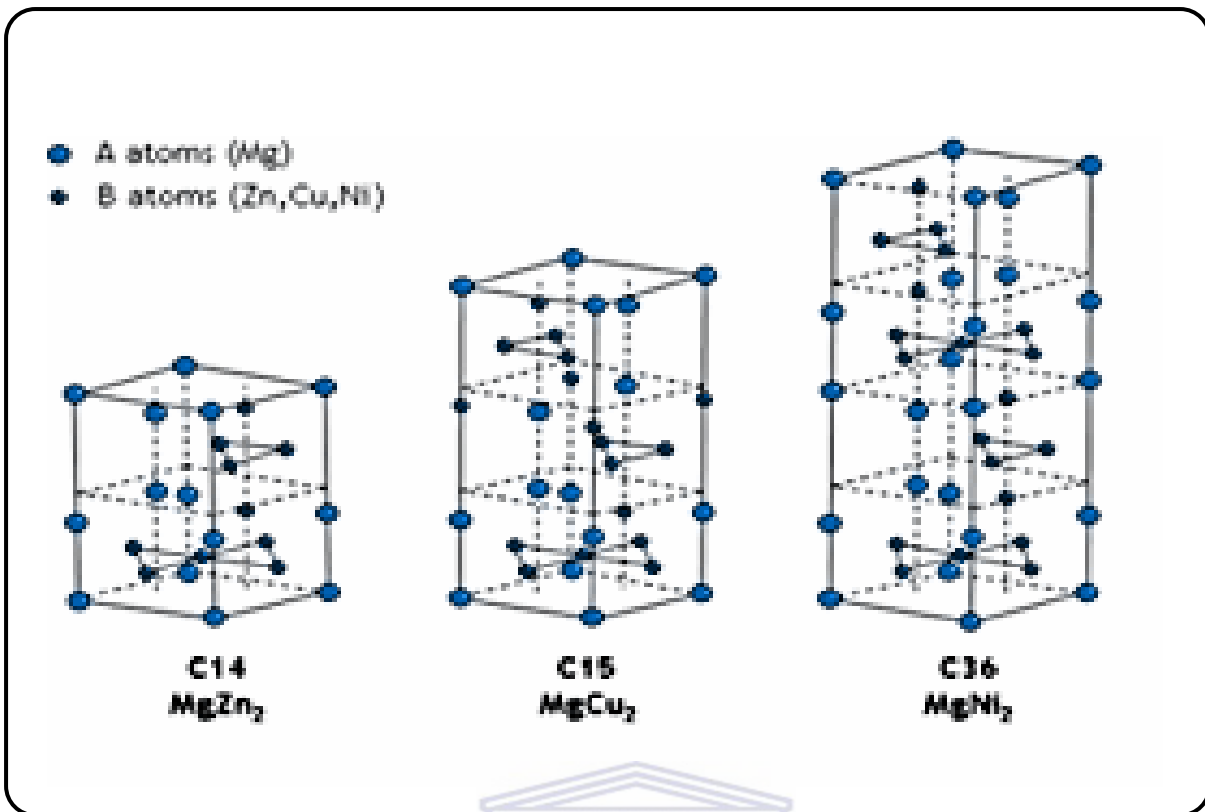


Figure 2.7: Schematic drawing of Laves phase structures with cubic (C15) and hexagonal (C14 and C36) [68, 69, 74].

PCT and other properties: The AB_2 compounds have H_2 storage capacity of nearly 2 wt. %, and exhibit low hysteresis. Laves phases show relatively faster kinetics, longer life (when operating with pure H_2) and a relatively low cost in comparison to the LaNi_5 -related systems [28]. The main drawback of these types of compounds is the surface passivation by zirconium oxide which reduces the kinetics and increases the activation period.

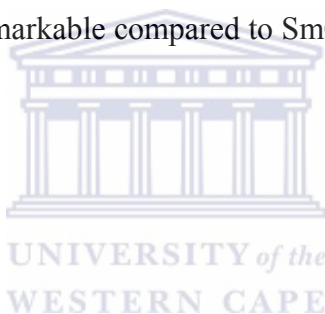
2.1.3.3 AB_5 intermetallic compounds.

Evolution of AB_5 hydrides: The hydrides based on AB_5 alloys represent the most versatile and commercially important family of reversible hydriding alloys. AB_5 s are essentially line compounds, meaning they are closely restricted to the atomic A: B ratio of 1:5.

The impressive hydriding properties of AB₅ intermetallics were accidentally discovered at the Philips Eindhoven laboratory about 1969 while studying the AB₅ permanent magnet alloy SmCo₅ [75]. It was noticed that direct reaction of SmCo₅ with H₂ gas at RT resulted in a new reversible hydriding reaction (**Equation 2.8**) but H-capacity was not remarkable [76].



The researchers wanted to study the positions of the H-atoms in SmCo₅ hydride by Nuclear Magnetic Resonance (NMR) [76], but that required a sample that is not ferromagnetic. For the NMR study, isostructural AB₅ compound LaNi₅ was selected. The reaction of LaNi₅ with H₂ (**Equation 2.9**) was indeed remarkable compared to SmCo₅ with hydrogen capacity higher than 1 wt. % [77].



The discovery of LaNi₅ intrigued researchers to improve properties of LaNi₅ by complete or partial substitution of either La or Ni site [78]. These substitutions led to a formation of compounds known as multi-component alloys (**Figure 2.8**) which are the mainstay of today's commercially available H- storage alloys.

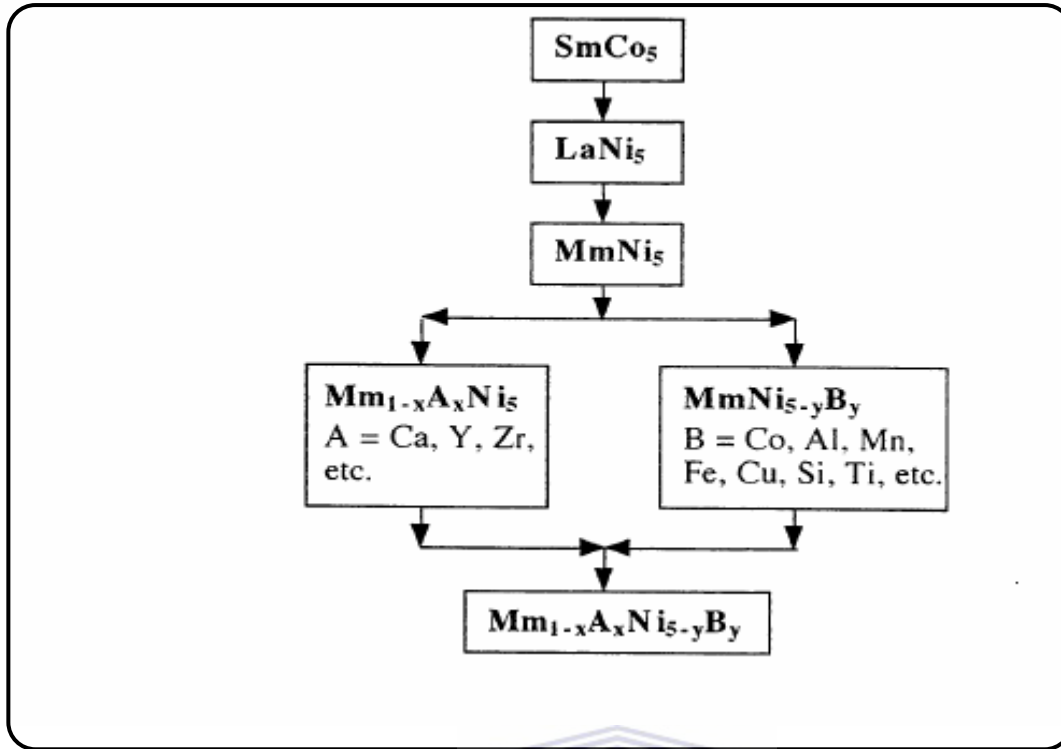


Figure 2.8: Schematic Flow Diagram of AB₅ Intermetallic Compound Development [78].

Crystal structure: Almost all the AB₅ intermetallic compounds crystallise with the same structure as the LaNi₅ intermetallic compound [79]. Hence, the crystal structure of AB₅ alloys usually belongs to space group *P6/mmm*. This is a CuCa₅-type hexagonal structure with A-type atoms in the 1a positions (000), and B-type atoms in both the 2c (1/3,2/3,0) and the 3g (1/2,0,1/2) positions, as shown in **Figure 2.9 (a)**. The possible overstoichiometry of the LaNi₅ intermetallic compound (LaNi₅ up to LaNi_{5.5}) has been explained by the replacement of some lanthanum atoms (1a) by dumbbells of nickel atoms in the 2e positions and oriented along the c axis.[80,81]

The A-type atoms are restricted to the 1a positions in the crystal structure, but the substitution of the B-type atoms may occur on both the 2c and the 3g sites [82-85]. Large atoms preferentially occupy the 3g sites, which provide more space to fit them, whereas substitution

atoms with a size similar to nickel have an almost random distribution on the two types of sites.

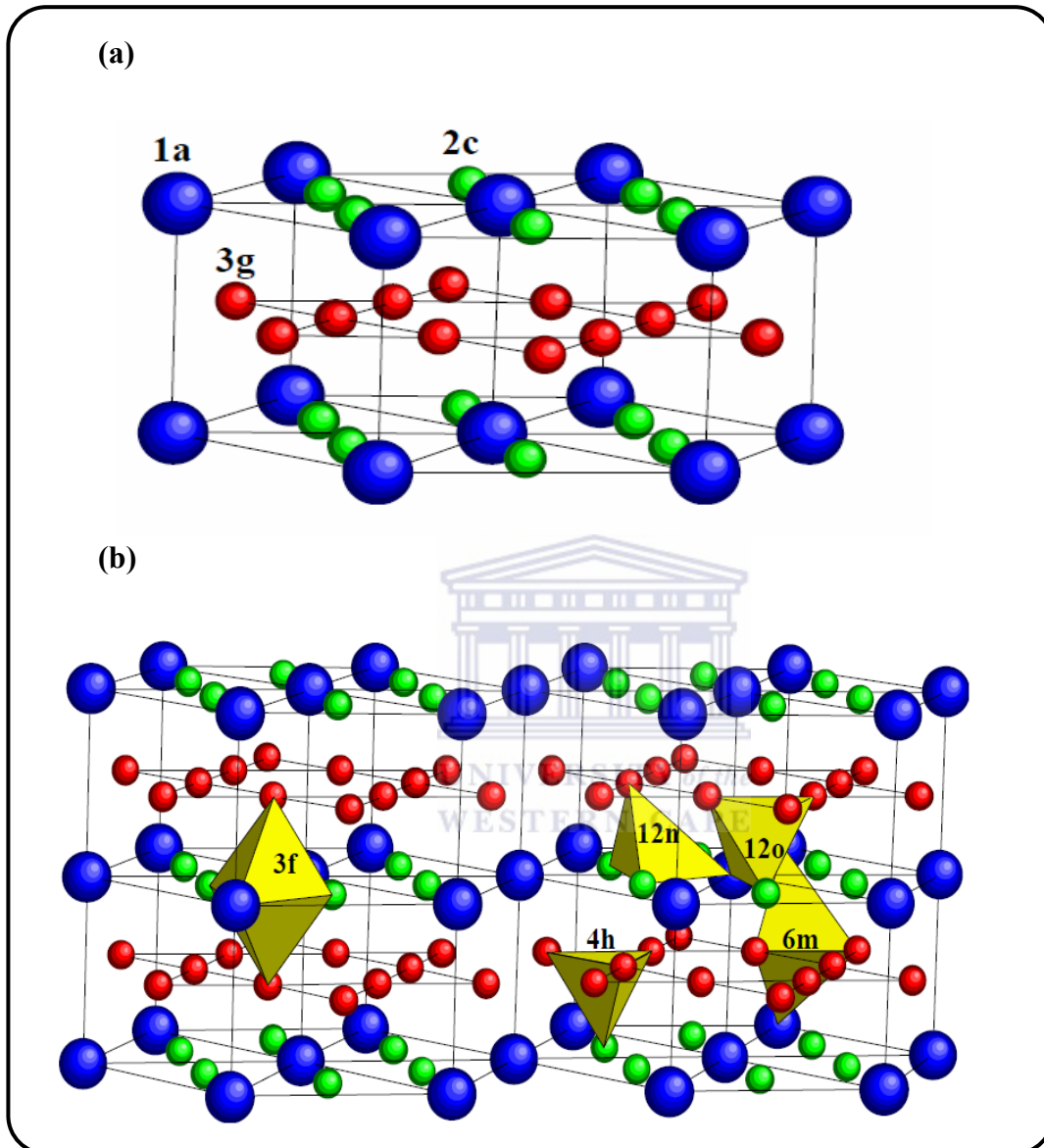


Figure 2.9: Crystal structure of (a) AB₅ type alloy and (b) typical AB₅ hydride [40, 88]. The large blue atoms are A-type atoms and smaller red and green atoms are B-type atoms. 12o, 12n, 6m and 4h are interstitial sites containing accommodated H atoms.

The AB₅ hydrides do generally have the same crystal structure as the corresponding intermetallic compounds. However, the hydride formation involves a pronounced increase of the unit cell volume (**Table 2.1**). As a consequence of this swelling the AB₅ materials are readily pulverised during hydrogen absorption/desorption cycling.

Table 2.1: Typical representatives of AB₅ metal hydride [28, 40, 42, 56, 86].

Parent Compound			Hydride		
Formula	Structure	Lattice periods	Formula	Structure	Lattice periods
CaNi ₅	Hexagonal (CaCu ₅)	a=4.950 c=3.936	CaNi ₅ H _{4.5}	Hexagonal (CaCu ₅)	a=5.305 c=4.009
LaNi ₅		a=5.015 c=3.987	LaNi ₄ H ₆		a=5.426 c=4.269
LaNi ₄ Al		a=5.319 c=4.235	LaNi ₄ AlH _{4.3}		a= 5.319 c=4.235

UNIVERSITY of the
WESTERN CAPE

The AB₅ structure contains a variety of tetrahedral and octahedral interstices and the H-atom occupancy depends on the composition of the AB₅ alloy. There are basically four different tetrahedral sites and these are referred to as 4h, 6m, 12n and 12o, where the surrounding atoms are B₄, A₂B₂, AB₃ and A₃B, respectively (**Figure 2.9 b**) [87]. Hydrogen atoms can also occupy an octahedral site in the structure referred to as 3f with A₂B₄ surrounding atoms [87]. These interstices are surrounded by both A and B atoms, such leading in interstitial environments that are averages of the very strongly H bonding A-atoms and the very weakly H bonding B-atoms, thus resulting in an intermediate strength H–M bond that is important to practical, ambient temperature reversible hydrides.

PCT and other Properties: The most important example of AB₅ class is LaNi₅. The family has an extra-ordinary versatility because many different elemental species can be substituted into A and B lattice sites. Usual examples of the substitutes for A are Mm (a natural mix of rare earth metals such as Ce, La, Nd, Pr, Sm, etc), Ca, Y, Zr and for B are Al, Mn, Si, Zn, Cr, Fe and Cu. Hydrides are formed with plateau pressures of a few atmospheres at temperatures up to 373K with enthalpy change; ΔH in the order of -30.1 kJ/mol H₂ [28]. However, the absolute values of the enthalpies can vary due to the influence of substitution (**Table 2.2**).

Table 2.2: Thermodynamic characteristics of the LaNi_{4.75}Al_{0.25}-H₂ and LaNi_{4.8}Sn_{0.2}-H₂ systems [89].

T/K	LaNi _{4.75} Al _{0.25} -H ₂		LaNi _{4.8} Sn _{0.2} -H ₂	
	ΔH_{dif} (kJ/mol H ₂)	ΔS_{dif} (J/mol K H ₂)	ΔH_{dif} (kJ/mol H ₂)	ΔS_{dif} (J/mol K H ₂)
308	-33.7 ± 2.6	-110.9 ± 5.5	-33.5 ± 2.4	-111.7 ± 5.7
328	-35.9 ± 2.2	-115.2 ± 5.7	-33.4 ± 2.5	-110 ± 5.5
353	-36.5 ± 1.9	-116.6 ± 5.4	-33.5 ± 2.4	-111.8 ± 5.9
	(-31.4 ± 2.6)	(-102.9 ± 4.8)	(-35.2 ± 2.4)	(-115.4 ± 5.4)

With AB₅s, the hysteresis is usually quite low except for MmNi₅ [28]. LaNi₅ shows good kinetics with Ni serving as a catalyst in the hydriding reaction. The AB₅ alloys are easy to activate, seldom requiring any heating. They decrepitate on the first sorption cycle to fine powder which is mildly pyrophoric if suddenly exposed to air, a well-known factor that must be included in safety considerations. Easy activation means that the AB₅ alloys do not form protective oxide layers.

This property is a distinct advantage that gives AB₅'s unusually good tolerance to small amounts of O₂ and H₂O in the H₂. These impurities do not poison the AB₅ but act as reactants that only slowly reduce capacity. The hydrogen capacity of AB₅ alloys is unfortunately low. A maximum capacity of 1.90 wt. % can be achieved with LaCo₅ and Ca_{0.7}Mm_{0.3}Ni₅ with a nominal amount of about 1 wt. % [28].

Cost: The AB₅ alloys are more expensive as compared to AB₂ and AB type alloys. The lower cost AB₅ alloy can be made by substituting the unrefined rare earth mixture mischmetal (Ce, Pr, Sm and Nd) denoted as MmNi₅ for the more expensive material refined lanthanum. One of the problems with MmNi₅ is that its equilibrium dissociation pressure (about 13 atm at 20°C) is higher than that of LaNi₅ hydride (about 2 atm at 20°C) [28].

Resistance of AB₅ alloys towards small amount of gaseous impurities and fast kinetics [28], makes them suitable materials for development of MH storage unit for LT-PEMFC power systems since fast absorption/desorption rates are of basic interest for these units.

2.2 ADVANTAGES AND LIMITATIONS OF THE AB₅-TYPE METAL HYDRIDE FORMING ALLOYS.

Generally, MH storage units require fast response during heating and cooling of the unit. This means that the rate at which heat is supplied (discharging) and removed (charging) from unit is the limiting step for fast dynamic behaviour of these units [90, 91]. AB₅ type alloys have been used in many application including for MH storage units, due to their ability to absorb and release H₂ reversible comparatively large amount of H₂ at reasonable temperatures (T= 0-100 °C) and low pressures (0.1-10 bar). In addition, AB₅ alloys tend to pulverise in the first

ABS/DES cycle into fine powders of low thermal conductivity resulting to poor heat transfer and mass transfer which eventually reduces H₂ absorption/desorption rate.

The hydrogen sorption properties of AB₅ materials can be lost when these materials are suddenly exposed to air due to the formation of oxide film which prevents dissociation and diffusion of H₂ into the interstitial site of the alloy leading to a reduced reversible H₂ capacity [28]. The oxide layer can be removed or disintegrated by activation, but the activation requires subjecting the alloy at high H₂ pressure and/or temperatures and longer incubation time to fully activate the materials. Furthermore, AB₅ alloys are easy to activate [28] and then the performance of these materials can be improved by elemental substitution and surface modification.



2.3 MODIFICATION/IMPROVEMENT OF PERFORMANCES OF THE AB₅-TYPE MATERIALS.

For AB₅ alloys to be considered as potential candidates for MH storage units for LT-PEMFC power systems application long-term hydrogen sorption stabilities, improve heat transfer rate and resistance or tolerance towards impurities are required. Hence, *(i)* modification by partial substitution of either A or B of AB₅ type alloy to match into specified pressure – temperature conditions; and *(ii)* surface treatment techniques for improving tolerance of the alloy against impurities are worth investigating.

2.3.1 ELEMENTAL SUBSTITUTION.

One of the promising methods for improving the overall performances of LaNi₅ is the partial substitution of elements either on the La or Ni site [92-94]. It was reported that high contents of Co, Mn and Al substituting Ni is known to significantly increase the stabilities of the

intermetallic hydrides as shown in **Figure 2.10 a-c** [86]. However, partial substitution on the B-site with Ce results to reduction of thermal stability of the alloy with increasing content of Ce as seen in **Figure 2.10 d** [86]. This is attributed to the low metal hydrogen binding energy of Ce and thus makes it easier in expelling hydrogen from the material. Therefore AB₅ alloy with maximum Ce content can be recommended for the usage in metal hydride hydrogen storage unit, to lower power inputs necessary for hydrogen desorption there from.

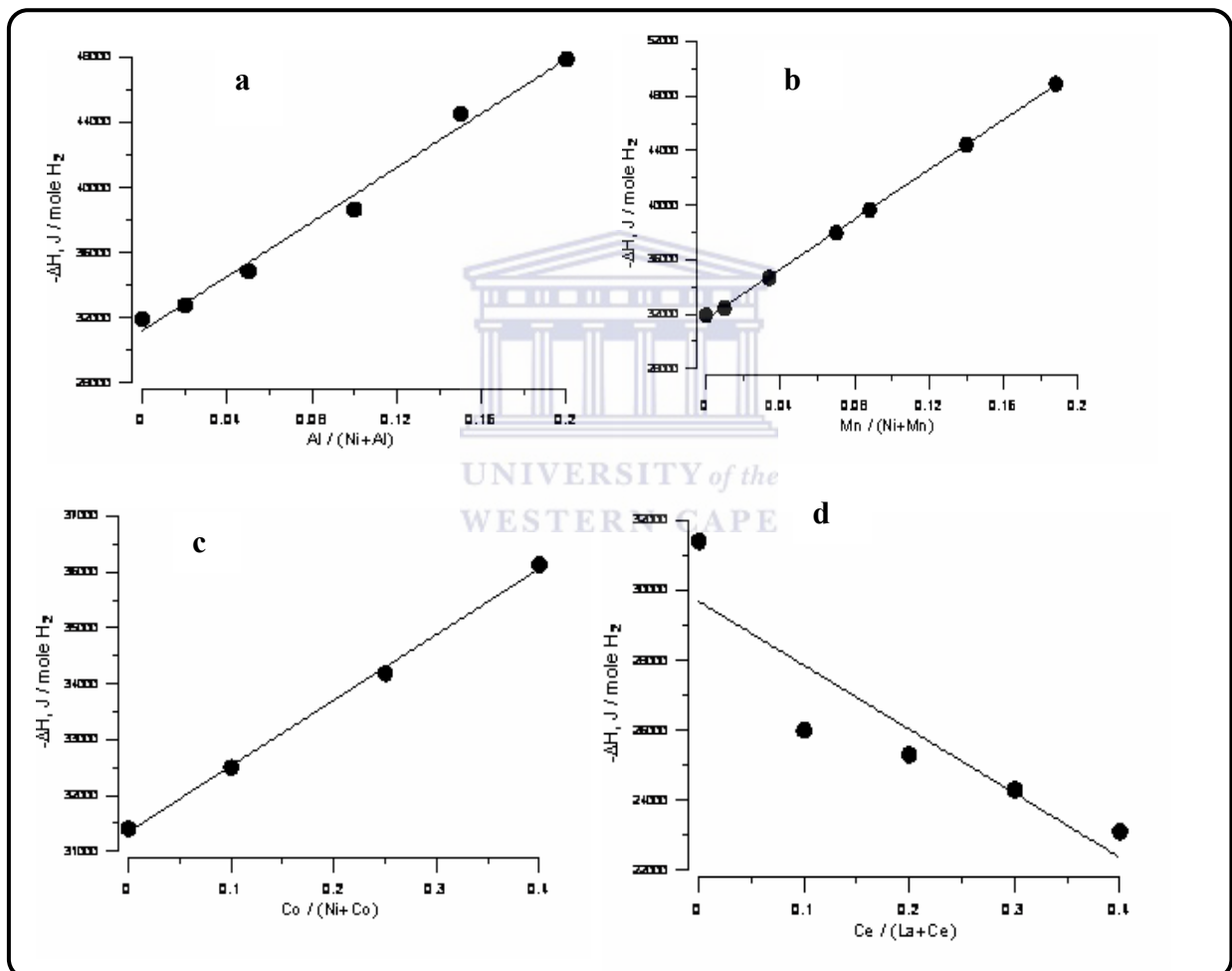


Figure 2.10: Hydride formation enthalpies for the ternary intermetallics (a) La(Ni,Al)₅, (b) La(Ni,Mn)₅, (c) La(Ni,Co)₅ and (d); (La,Ce)Ni₅ [86].

Furthermore, Ce substitution has a beneficial effect on the H₂ sorption properties of AB₅ due to variation of Ce valence from intermediate toward trivalent state upon H₂ absorption [95, 96]. This leads also to a variation of Ce volume (atomic size) which can reduce the stresses due to H₂ absorption and therefore the sample decrepitation [96].

2.3.2 SURFACE MODIFICATION.

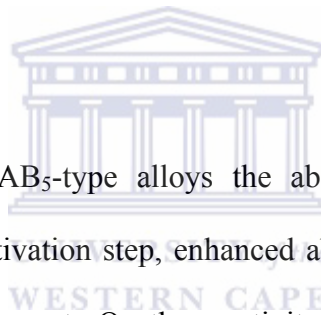
H₂ gas often used in industrial application consists of gaseous impurities such as SO₂, H₂S, CO, O₂ and CO₂ (in decreasing order of severity) [97]. The vulnerability of the AB₅-type alloys to surface contamination by these aggressive gases leads to a formation of stable surface films (such as oxides, sulphides and carbonyls). These impurities can be dramatic in damaging the AB₅ metal surfaces, resulting in a surface barrier that reduces their usually good kinetics, lowers capacity or sometimes even eliminates all H₂ reactivity [28]. Therefore, some surface treatment or modification procedures are needed to enhance hydrogen dissociation surface processes and increase the tolerance of the AB₅-type alloys towards gaseous impurities.

Promising surface modifications involves introduction of protective layers onto the alloy surface. The formed layer exhibits high permeability of hydrogen but resistant towards impurities. These methods range from fluorine treatment [98-104], hot alkaline solution [105-111] and acid treatment [112, 113], treatment with a variety of metal oxides [114] and encapsulation using metal layers [115-117].

Encapsulation with metal layers appears to be the suitable surface modification technique since it provides enhancement of hydrogenation performance; increased surface poisoning resistance; improved thermal and electrical conduction; improvement of H₂ dissociation rate,

discharge rate and cycle lifetime [115-117]. Platinum group metals (PGMs) are also used in surface modification of the alloy [116, 117]. The PGMs are known to be good catalysts for various chemical and electrochemical reactions, resulting in the production of catalytic surfaces with a range of particle sizes.

The presence of the PGMs enables hydrogen to pass rapidly through the surface of the alloy to the bulk, while maintaining the hydrogenation activity even after extensive exposure to an oxidising environment [118, 119]. Pd and Ru are the most attractive catalysts in the PGM group for surface reactions involving hydrogen exchange processes [111]. However, Pd exhibits higher permeability towards hydrogen at lower temperatures compared to the other PGMs [120].



Palladium deposition provides AB₅-type alloys the ability to absorb hydrogen at low temperature without a special activation step, enhanced absorption properties and enhanced activation rates [121]. After exposure to O₂, the reactivity of Pd can be recovered due to the easy decomposition of the palladium oxide and this increases the resistance of Pd towards gaseous impurities [122]. Resistance of Pd towards impurities may lead to the protection of Ni clusters in AB₅-type alloys resulting in fast H₂ dissociation rate. Zaluski *et al.* [123] reported that the presence of Pd as a catalyst in nanocrystalline Mg₂Ni, LaNi₅ and FeTi systems, enhance the absorption rates even at lower temperatures and maintain less sensitivity to air exposures. Even small addition of Pd (0.25 wt. %) can greatly improve the activation behaviour of MH storage alloys [124]. Pd deposition can be carried out using various methods which include chemical vapour deposition [125,126], sputtering deposition [127-130], mechano-chemical deposition [124,131,132], electrolytic [133] and electro-less plating [128].

Electroless deposition provides better grain sizes of deposited Pd layers and thus better suited for coating AB₅ metal surfaces. This technique is carried out using plating bath compositions. Generally, the bath contains the following component: metal salt precursor; reducing agent; complexing agent; and bath stabilizer [116]. Electro-less plating involves two processes, namely surface sensitization and activation; and film growth by decomposition of the reducing agent [116].

Sensitization of the surface substrate is commonly used to increase the surface roughness and is achieved by using aqueous SnCl₂ solution while activation is achieved by immersing the substrate in an aqueous PdCl₂ solution in order to reduce the activation energy of the reaction needed to initiate and catalyse the oxidative decomposition of the reducing agent. Activation and sensitization can be also carried out in one step process where the substrate is immersed in a mixed acidic PdCl₂-SnCl₂ colloidal solution consisting of colloidal particles with a core made of Pd and Sn, and surrounded by a Sn-rich layer [134,135]. Film growth in electroless plating is driven by the oxidation of the reducing agent such as sodium hypophosphite which reduces the metal ions with the associated deposition of phosphorus within the film, by donating electrons [136].

Geng *et al.* [137] observed significant enhancements in the hydriding/dehydriding ability of AB₅-type alloys after electroless plating of about 1wt. % Pd on the surface. However, Xu *et al.* [138] argued that Pd particles have poor adhesion to the AB₅ substrate material due to the absence of chemical conjunction. Thus, during plating, the Pd nuclei can leach out of the solution resulting to reduced Pd loading on the AB₅ metal surface. Williams *et al.* [116] reported that pre-treatment of AB₅ metal surface with amino- propyltriethoxysilane (γ -APTES) facilitates deposition of higher Pd loading on the surface of AB₅. The pre-treatment

resulted to uniform Pd deposition on the metal surface and thus enhanced hydrogenation kinetics was observed.

2.4 STATE –OF -ART OF HEAT AND MASS TRANSFER.

2.4.1 FEATURES AND CHALLENGES.

It is well known that the overall metal hydride reaction is nearly reversible at moderate temperatures and pressures with a substantial amount of enthalpy change (-30 kJ/mol H_2) leading to a change in the MH bed temperature during the reaction [57]. The temperature affects the reaction rate greatly through both driving force and chemical activation [139].

Furthermore, metal hydride materials tend to introduce a significant level of strain changes (due to volume expansion during absorption and volume contraction during desorption) and finally self-pulverized into fine small particles after long exposure to hydrogen absorption – desorption cycles [140-142]. Such a powder bed exhibits poor thermal conductivity on the order of 0.1 W/m K [143]. The decrepitated particles may also entrain in the gas stream and pack in the container and also may damage the important parts of the tank such as valves.

This can lead to gas impedance, poor heat and mass transfer and stressing of the container walls. The poor heat and mass transfer can therefore limit the absorption /desorption reaction rate and this can affect the overall performance of MH systems. Therefore, to obtain better performance in MH systems, methods to improve heat and mass transfer rate should be developed.

2.4.2 IMPROVEMENT OF HEAT TRANSFER.

Following the thermal circuit analysis, heat transfer resistance from MH to heat source/sink is composed of three parts in series [144]. Generally the thermal resistance of wall separating MH from heat transfer fluid is small and negligible, and the rest two parts represent internal and external heat transfer processes, respectively [144]. In comparison to the internal heat transfer (i.e. inside MH bed) the external heat process through fluid proceeds more quickly and thus is paid less attention, especially when the fluid is liquid in the state of turbulent flow. Therefore internal heat transfer processes dominates poor performances of MH bed. Methods to increase the effective thermal conductivity of the MH bed had been investigated which include insertion of solid matrices, MH compacts, and internal heat exchangers.

2.4.2.1 *Insertion of solid matrices.*

A simple choice is circular or longitudinal fins, and more complicated structures such as wire matrix, multiple-waved sheet and corrugated helical band, while the most popular candidate ever developed is Al foam [145-158]. Suda *et al.* [153] investigated the performance of metal hydride bed packed with Al foam to enhance the poor thermal conductivity of the bed. The heat transfer of this type of hydride bed was found to be 5-7 W/m k, which is 10 times higher than that of general hydride beds [153]. It was also shown that this type of matrix could prevent powder's flow and stack in the bed. However, the cost and poor commercial availability of Al foam has limited its industrialization.

2.4.2.2 *Metal hydride compacts.*

This method was firstly proposed by Ron *et al.* [154, 155], later Kim *et al.* [143,156-158] and Klein *et al.* [145, 159] carried out more relevant studies to further develop the technique. The preparation of compacts involves mixing the MH powders with some binder materials such

as Al powder, Cu powder Chen *et al.* [160] or expanded natural graphite, and then a cold pressing process is needed to make the composite materials into compacts. However, addition of Al and Cu powder requires complex chemical processing of the powders and also increases the parasitic thermal mass of the reactor bed substantially and therefore, introduces a significant thermodynamic penalty on performance. Kim *et al.* [143] reported that MH compacts made from expanded graphite showed improved thermal conductivity without large parasitic thermal penalty. Furthermore, by using expanded graphite the cost for the heat transfer enhancement can be significantly reduced [145].

2.4.2.3 Internal heat exchangers.

Heat transfer can be also improved by introduction of heat exchangers in the reactor. Melloili *et al.* [161] investigated the heat transfer characteristics of MH reactor based on the spiral-type heat exchanger. The inserted heat exchanger provided significant insight into the problem of minimizing the total storage time by manipulating the spiral coolant flow rate and temperature. The experimental results showed that the charge/discharge times of the reactor were considerably reduced.

In addition, the use of fins as heat exchangers also improves reaction process of MH storage tanks. McDonald *et al.* [144] reported that MH reactors with fins exhibit favourable characteristics to fulfil a periodic hydrogen demand, such as fast response and high supply pressure. Mellouli *et al.* [162] reported that heat exchange parameters such as length thickness and arrangement of fins have a profound effect on the performance of the charging process of MH storage tank. The results revealed that absorption rate was improved by increasing the length of fins as well as by alteration of fin arrangement from oppose to

shifted fin arrangement [162]. This was attributed to formation of thinner beds by shifted fins resulting in relatively short conduction path leading in a rapid charging duration.

2.4.3 REDUCTION OF HEAT LOSS.

The performance of MH reactors is also affected by sensible heat loss that accompanies the temperature change of the MH reactor. For example, when the MH hydrogen storage container is discharged, it should be heated from a low temperature T_L (normally ambient temperature) to a high temperature T_H . While the heating of MH materials is necessary to reach a higher equilibrium pressure for discharge, extra thermal energy is consumed by parasitic mass such as vessels, pipelines and fluid. The sensible heat loss results in the decrease of system energy efficiency [163-165]. Reduction of parasitic mass can be achieved by using MH reactors made from light materials and have compact configuration [166,167].

2.4.4 ENHANCEMENT OF MASS TRANSFER.

MH systems cannot work without efficient supply or withdrawal of hydrogen gas. While the design of external pipelines is well defined, difficulty mainly lies in the management of hydrogen flow in the reactor bed. Hydraulic loss and particle entrainment caused by H_2 flow are the main issues that contribute to poor mass transfer from and to the bed.

2.4.4.1 *Reduction of Hydraulic loss.*

The flow of hydrogen through the MH bed can be described by Darcy's law:

$$\vec{U} = \frac{K}{\mu} \nabla P \quad 2.10$$

Similar to the heat conduction process, the mass flow rate of hydrogen is determined by the

driving force, mass transfer distance and related physical properties (permeability K and viscosity μ).

The driving force is the pressure drop, namely the hydraulic loss which should be minimized. Therefore decrease in the mass transfer distance or changes of physical properties are realistic choices. Hydraulic loss can be reduced by introducing gas arteries or filter tube (for powder beds) [168,169-171], which distributes radial flow uniformly over the longitudinal direction. In addition hydraulic loss can be minimized by variation of the packing state of MH particles [172].

2.4.4.2 *Reduction of particle entrainment*

The fine MH particles tend to move with hydrogen by drag forces, and may be brought out of the bed during hydride decomposition, resulting in immigration or entrainment of fine powder [28]. These particles will cause blockage of valves and manifolds leading to poor hydrogen gas permeability which eventually result to reduced absorption/desorption reaction rate. Particle entrainment can be avoided by using filter or screen with fine pores ($\sim\mu\text{m}$), also the filter tube used as gas artery can play a similar role [173,174].

2.5 METAL HYDRIDE REACTOR DESIGNS.

Any successful application of metal hydrides is closely related to the better design of reactors. Optimum hydride reactors should have the maximum possible volume for containing hydrides and the largest heat transfer area. Many MH reactors have been developed so far [161,162, 168, 175-183], and the basic configuration for these MH reactors roughly falls into three categories in terms of the geometry of the reaction bed.

2.5.1 TUBULAR REACTOR.

In this type of reactor, a central artery is usually provided for hydrogen flow. MH materials are packed in the annular space between the artery and the wall, while the heat exchange of the reaction bed with heat source/sink can be conducted through the external surface of the tube wall. The outer diameter is generally no more than 30 mm for a single tube unit in order to allow sufficient heat transfer in the radial direction [168,175-183]. Correspondingly, the length of the tube must be increased to hold a certain amount of MH. The aspect ratio, defined as the ratio of cylinder height to the diameter, is generally larger than 10 for the tube unit. Tubes of circular cross section are most often used, but elliptical tubes may be superior in the aspect of compact structure and small hydraulic loss according to Veerajou *et al.* [178].

The reactor is quite simple to manufacture and maintain due to easiness in standardized tubing. It also features good sealing and high bearing pressure. Moreover, the tube units are modular and can work independently, thus the reactor is relatively easy to scale up by increasing the number of units.

2.5.2 DISC REACTOR.

The reaction bed of disc reactor is flat in shape and the aspect ratio is much smaller than 1 [179,180,183]. H₂ flows into or out of the reactor axially through the screen covering the MH layer, meanwhile heat exchange is carried out on the other side. This type of reactor has a large heat transfer area and shows fast reaction kinetics. However, a single disc can only hold a small amount of MH. Furthermore, the bearing pressure, sealing and cumbersome heat transfer pipelines are all practical problems against its development and industrial application.

2.5.3 TANK OR CHAMBER REACTOR.

In a tank or chamber MH reactor, a cylinder or cube chamber of a considerable size is used as the reaction bed, allowing more MH materials. Through either surrounding outer filter or inserted arteries, H_2 can enter or leave the reactor freely. The performance of the MH reactor can be effectively improved by selecting a proper geometry [181,182,183]. Large capacity is the most important characteristic of the tank reactor. Therefore it is recommended to be used for some application where more MH materials are needed for the required output.

2.6 CONCLUSION OF LITERATURE REVIEW.

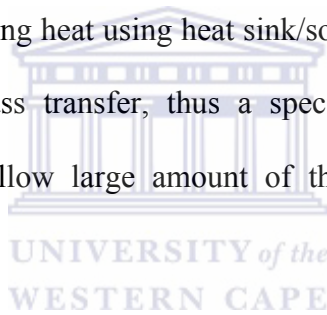
From the family of intermetallic compounds under consideration, AB_5 compounds were identified as the one of the most attractive groups of MH alloys for development of MH storage units for stationary application due to fast H_2 absorption rates; reasonable absorption kinetics; applicability in over a wide temperature and pressure range (0-200°C; 1-200 bar) and extraordinary versatility that makes it possible to tune their properties according to the specified application.

The partial substituted AB_5 with Ce was identified as a suitable hydride-forming alloy for metal hydride units due to its low metal hydrogen binding energy resulting in reduction of thermal stability and thus improve discharge performance at near-ambient conditions.

The slow H_2 absorption rates due to oxide formation; longer incubation periods and high activation pressures normally observed in AB_5 type alloy can be addressed by surface modification. Encapsulation of metal layers using electro-less deposition technique was identified as the attractive method for surface modification of the AB_5 -type alloys due to enhancement of hydrogenation performance; increased surface poisoning resistance;

improved thermal and electrical conduction; improvement of H₂ dissociation rate and discharge rate. Pd catalysis potentially enhances hydrogen sorption rates and offer protection towards the surface of metal hydride-forming alloys. For this reason Pd encapsulation was investigated as a suitable surface modification technology.

The purpose of this research is to improve heat and mass transfer of the MH powder bed which result from disintegration of metal powders into fine particles of low thermal conductivity. Incorporation of internal heat exchangers was selected as the effective method for enhancing heat and mass transfer of MH storage unit. The advantage of using heat exchangers is that it allows the unit to use heat from the surroundings for hydrogen uptake/release rather than supplying heat using heat sink/source. Also the tank design plays a role in improving heat and mass transfer, thus a special tank reactor was selected as appropriate design since they allow large amount of the material without affecting the performance of the MH unit.



Based on the review of the literature the following experimental tasks were undertaken in this study:

1. Preparation of the La_{1-x}Ce_xNi₅ type alloys by arc melting method and their characterisation thereof.
2. Preparation and characterisation of surface modified AB₅ hydride-forming alloys via electroless deposition technique and evaluation of their hydrogen sorption properties under moderate conditions.
3. Measurement and modelling of PCT isotherms of the parent AB₅-type alloy.

4. Study of heat and mass transfer performance of experimental MH storage unit (150 cm³) during charge/discharge cycles.
5. Evaluation of charge/discharge performance of air heated/cooled prototype MH storage unit (2.5L)
6. Study effect of incorporated internal heat exchangers on heat and mass transfer behaviour of developed water heated/cooled prototype MH storage unit (1 GAL).

The research design and methodologies which address the minimum set of sample characteristics of the AB₅-type metal hydride-forming alloys including the developed MH storage units, and the experimental tasks used in their investigation, are described in details in *chapter 3* including analytical tools used in the characterization study.



CHAPTER 3: METHODOLOGY

3.1 CHEMICALS AND APPARATUS.

The materials used for the surface modification procedure in this study and their suppliers are listed in **Table 3.1**.

Table 3.1: Materials used in the surface modification of AB₅-type alloy.

MATERIALS	SUPPLIERS
Palladium Chloride (99%)	Industrial Analytical,
Ammonium hydroxide (28 %)	Sigma-Aldrich
HCl (32 %)	Kimix
Ammonium Chloride	Kimix
Sodium hypophosphite	Kimix
Tin Chloride	Industrial Analytical
Sodium Ethyl diamine tetra acetate	Kimix
Aminopropyl triethoxy silane	Industrial Analytical
Pd standard solution (1000ppm)	B & M Scientific

3.2 METHODS OF SYNTHESIS.

3.2.1 PREPARATION OF AB₅-TYPE ALLOY BY ARC MELTING.

The laboratory samples of La_{1-x}Ce_xNi₅ alloys (x=0–0.2) were prepared by arc-melting (Institute for Energy Technology) of the high-purity metals (>99.99%) taken in the amounts corresponding to the target formula (total mass ~5.0 g) on a water-cooled copper crucible in protective argon atmosphere.

The kg amounts of the $\text{La}_{0.85}\text{Ce}_{0.15}\text{Ni}_5$ alloy powders were prepared from a high purity metals by a modified arc melting technique under an inert gas atmosphere and reduced pressure, in collaboration with the Guangzhou Research Institute of Non-Ferrous Metals (China). The metals were cast into sheets using a special high-pressure roller system fitted within a furnace. The rolling speed was varied between 5-15 $\text{m}\cdot\text{s}^{-1}$. The resulting alloy sheet was annealed at 1295 °C for 2 hours under an inert atmosphere to ensure homogeneity. The sheet was then mechanically pulverised by ball-milling in a sodium hypophosphite solution and sieved. There was no special storage conditions for the prepared alloys, thus oxide films formed on the surface of the powders due to exposure to non-inert atmospheres.

3.2.2 SURFACE MODIFICATION METHOD.

3.2.2.1 *Functionalisation of AB₅-type powders prior metal layer encapsulation.*

Pd is an especially good catalyst for hydrogen dissociation reaction. However, the oxide layer on the surface of the core material inhibits interactions with PGM precursor ions in the solution and the Pd colloidal particles have poor adhesion to the metal substrate due to the absence of chemical conjunction. Thus the PGM nuclei tend to leach out into the solution resulting to low Pd loading. Improvement of adhesion can be achieved by pre-treating the material with an organic compound prior to deposition of Pd resulting to a chemical bond formation which will facilitate high Pd loading. Prior to encapsulation of Pd layers, the AB₅ alloy powders were functionalised by addition aqueous solution 1% v/v of γ -APTES (pH-neutralised using 10% HCl) solution at 90 °C for 1h with constant stirring (300 rpm). The functionalised powders were then filtered and dried at 80°C.

3.2.2.2 *Sensitization and activation of AB₅-type metal powders.*

The deposition of Pd layers onto the metal surface of both functionalized and non-functionalized samples requires a sensitization / activation step.

Approximately 5.0 g of the AB₅-type powders were treated in 50 mL of Pd-Sn colloidal solution for 20 minutes at room temperature. The Pd-Sn colloidal solution was prepared as follows:

Solution A: 0.3 g PdCl₂ was dissolved in 2.15 g HCl solution and 5.0 mL deionised water at 70 °C with stirring (300 rpm)

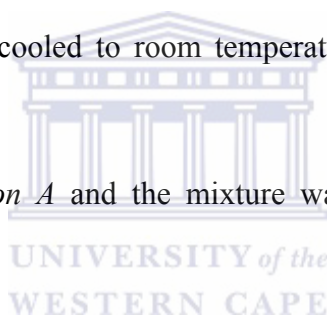
Solution B: 25 g SnCl₂·2H₂O was dissolved in 145 g HCl solution (preheated to 50 °C). The mixture was cooled to room temperature after which 30 mL deionised H₂O was added.

Solution B was added to *solution A* and the mixture was heated to 90-100°C for 15-20 minutes.

Solution C: 8.75 g KCl was dissolved in 250 mL deionised H₂O. 80 mL HCl was then added to the KCl solution.

Solution C was then added to *Solution (A+B)* and made up to 500 mL with deionised water.

The activated powder was then immersed in a 10 wt% solution of Na₂EDTA for 10 min as to strip away the tin component, rinsed with deionised water and then allowed to dry at 80 °C overnight.



3.2.2.3 Electroless deposition of palladium on the activated AB₅ metal surface.

The deposition of Pd layer was carried out by immersion of the activated powders in by immersion in 50 ml of the freshly-prepared electroless plating bath. The bath was prepared by first dissolving 2 g of PdCl₂ in 4.0 mL HCl (32 %) and 20 mL of deionised water, and then heated at 50 °C for 30 min with constant stirring at 300 rpm. After complete dissolution of PdCl₂, 160 mL of NH₄OH (28 %) and 27 g of NH₄Cl were added respectively. The plating bath was then allowed to stir over night without heating. The mixture was then transferred to 1L volumetric flask and made up to the mark with deionised water. The electroless plating bath, containing the activated and functionalised AB₅-type alloy, was subjected to constant agitation (300 rpm) for 30 minutes at 50°C. In addition, 50 mL of sodium hypophosphite (reducing agent) was rapidly added to initiate the reaction. The reducing agent was added separately to avoid decomposition during storage of the bath. Finally, the plated powders were washed with deionised water, filtered, and allowed to dry at 80°C.

3.3 MATERIALS AND SYSTEMS: CHARACTERISATION.

Fast kinetics and improved hydrogen sorption properties of AB₅-type alloys depends on the elemental composition, porosity and surface area, surface morphology and phase composition / crystal structure. Therefore, alteration of these factors may influence the performance of the alloy during hydrogenation either positively or negatively. Thus, an array of characterisation methods was conducted to determine the effect of the above-mentioned factors on the properties of AB₅-type alloys.

3.3.1 X-RAY DIFFRACTOMETRY (XRD).

XRD is a versatile, non-destructive technique that reveals detailed information about the phase composition and crystallographic structure of natural and manufactured materials. XRD is capable of the identification of single and multiple phases in unknown materials and the quantification thereof, detection of impurities, determination of the crystallographic structure of materials (i.e. space group determination; indexing; structure refinement; structure identification, orientation of crystallites), texture analysis, structure deformation, residual stress analysis, studies of lattice properties, and crystallite size determination.

X-rays have wavelengths on the order of a few angstroms, the same as typical interatomic distances in crystalline solids. This means that X-rays can be diffracted from minerals which, by definition, are crystalline and have regularly repeating atomic structures.

In X-ray diffraction technique, a beam of X-rays incident on a crystalline material undergoes scattering by the electrons associated with the atoms. The scattered X-rays, in turn, undergo interference due to the periodic arrangement of atoms in the crystal and its symmetry. The interference is constructive in certain directions only if the path length difference is equal to an integer number of wavelength (**Figure 3.1**).

The diffractions are defined from Bragg's Law ($n\lambda = 2d \sin \theta$), where the intensities of diffracted X-rays are measured and plotted against corresponding Bragg angles (2θ) to produce a diffractogram.

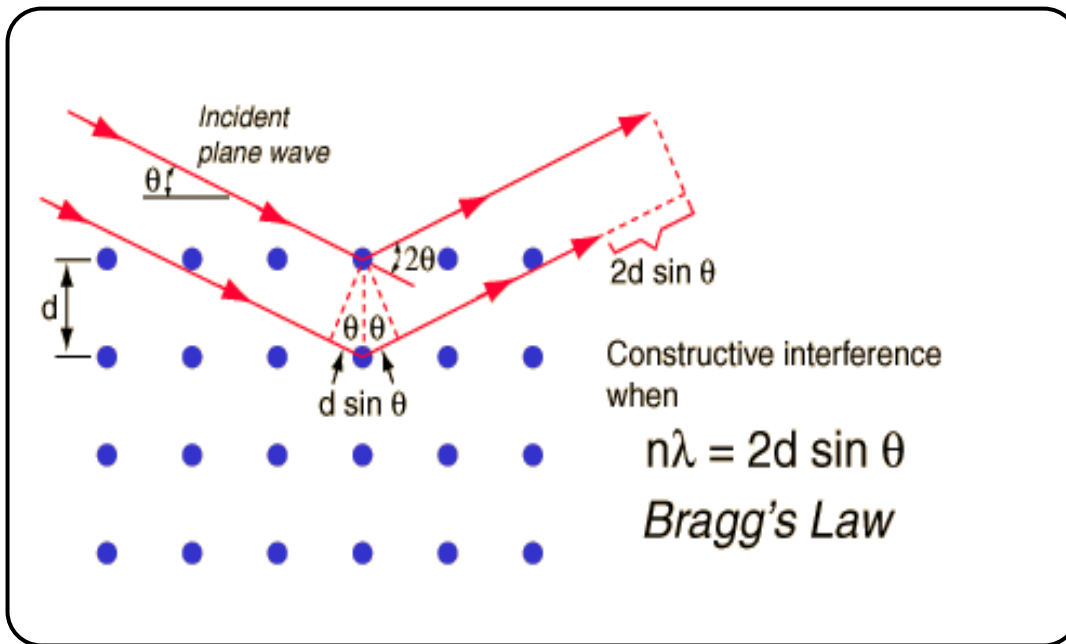


Figure 3.1: Constructive interference of X-rays [184].

The intensities of diffraction peaks are proportional to the densities or abundance of the corresponding crystal facets in the sample lattice. Diffractograms are unique for different materials and can therefore qualitatively be used in material identification [185,186].

The crystal structure of a material or the arrangement of atoms within a given type of crystal structure can be described in terms of its unit cell. The unit cell is a tiny box containing one or more atoms, a spatial arrangement of atoms. The unit cells stacked in three-dimensional space describe the bulk arrangement of atoms of the crystal.

When describing the structure of a solid material in the scientific literature, relevant data for the crystallographic unit cell are given. The unit cell is given by the length of the three axes, a , b and c (unit cell dimensions, unit cell parameters, cell edges; i.e. the lengths of the vectors \mathbf{t}_1 , \mathbf{t}_2 and \mathbf{t}_3) and the angles α , β and γ . Definition of the angles relative to the axes (\mathbf{t}_1 , \mathbf{t}_2 and \mathbf{t}_3 or equivalent a , b and c) is shown in **Figure 3.2**. In order to describe the atomic

arrangement, one has in addition to define the shape of the unit cell and also to state where the atoms are in the repeating unit cell. This is done by giving the position of the atoms as coordinates (x,y,z) . The atomic coordinates are given as fractions of the unit length of the vectors [187-189].

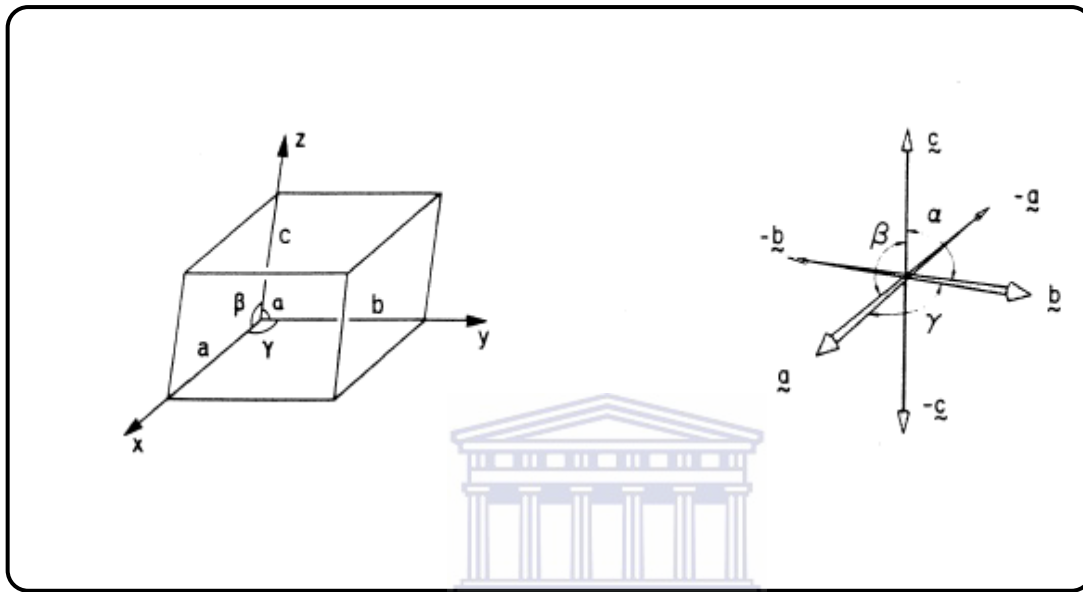


Figure 3.2: The definition of relations between angles and axes in unit cells. The unit cell is shown as the box on the left [188,189].

As a principal rule, any given atom can be transferred to one or more atoms, of the same type and with the same surroundings, within the unit cell by symmetry operations. In order to describe all the atoms in the unit cell it is enough to give the coordinates of a certain part of the atoms along with the necessary symmetry operations. Within a unit cell one often find several atoms of the same kind. If the surroundings of these atoms are identical, the atoms are related by symmetry operations. There are basically two general types of symmetry operations namely; translational symmetry and point symmetry operations. Translational symmetry describes the periodic repetition of a structural feature across a length or through

an area or volume. Point symmetry, on the other hand, describes the periodic repetition of a structural feature around a point. Reflection, rotation, and inversion are all point symmetries [187].

There are seven different crystal systems which also called space lattices. They differ by having different relations between unit cell axes and angles. The relations between the length of the unit cell axes and the angles between them are given in **Table 3.2** and simple unit cells (with one atom in each corner) are shown in **Figure 3.3**.

Table 3.2: Relations between the length of unit cell axes and the angles between them [187].

Relations (t1,t2,t3)		Crystal system
$a=b=c$	$\alpha = \beta = \gamma = 90^\circ$	Cubic
$a=b \neq c$	$\alpha = \beta = \gamma = 90^\circ$	Tetragonal
$a \neq b \neq c$	$\alpha = \beta = \gamma = 90^\circ$	Orthorhombic
$a \neq b \neq c$	$\alpha = \gamma = 90^\circ, \beta \neq 90^\circ$	Monoclinic
$a \neq b \neq c$	$\alpha \neq \beta \neq \gamma \neq 90^\circ$	Triclinic
$a=b=c$	$\alpha = \beta = \gamma \neq 90^\circ$	Trigonal (Rhombohedral)
$a=b \neq c$	$\alpha = \beta = 90^\circ,$ $\gamma = 120^\circ$	Hexagonal

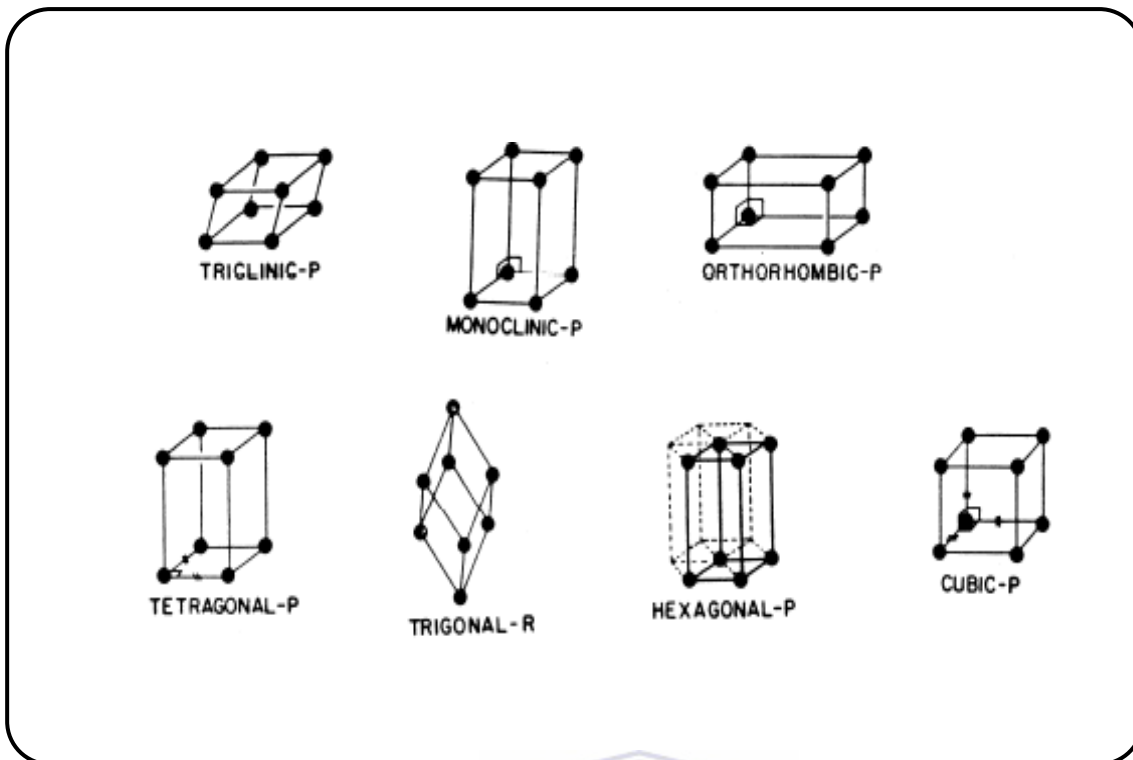


Figure 3.3: Schematic representation of the unit cells for the seven crystal systems (drawn with one atom in each corner of the unit cell). P (Primitive); I (Body Center); A, B and C (side Center); F (Face Center); R (Rhombohedral) [187].

Lattices can either be primitive (only one lattice point per unit cell) or non-primitive (more than one lattice point per unit cell). Combination of seven crystal systems with two different types of lattices results with 14 Bravais Lattices as shown in **Figure 3.4**.

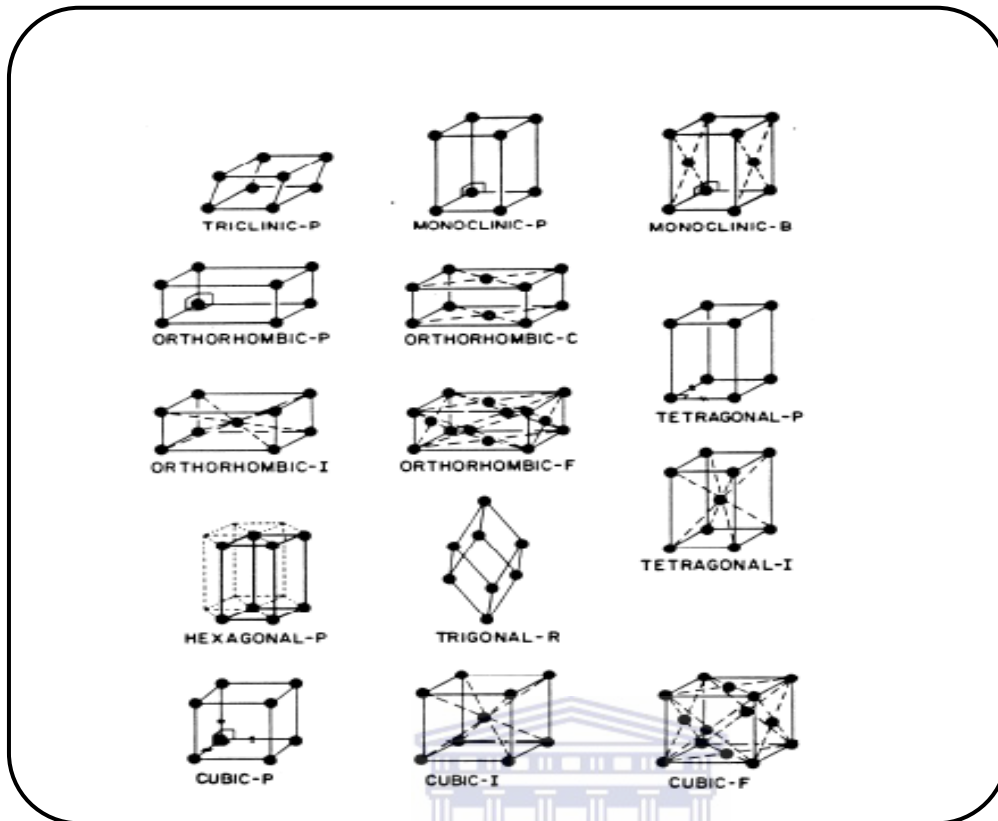


Figure 3.4: The 14 Bravais lattices. [187].

A crystal contains different lattice planes which are classified by using Miller indices, and these can be constructed from the unit cell fcc, **Figure 3.5**. A plane is assigned Miller indices from its reciprocal intersection with the three axes, a , b and c , of the unit cell given in multiplicity of the axis lengths and rounded up to integer values. For example, if the plane intersects in $(1, \infty, \infty)$ corresponding to **Figure 3.5.A**, the Miller index becomes $(1\ 0\ 0)$. The three Miller indices are denoted h , k , and l . The distance between parallel lattice planes, denoted as d , is a pivotal quantity in diffraction and it depends on the lattice periods $(a, b, c, \alpha, \beta, \gamma)$ and h, k, l .

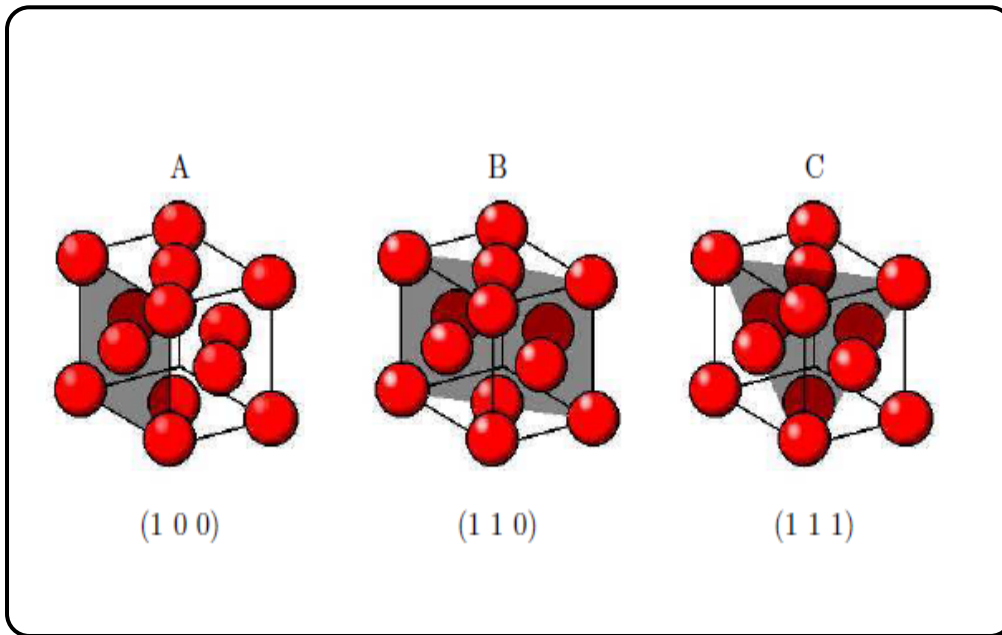


Figure 3.5: Low index lattice planes of a fcc solid [187].

These dependencies can be calculated from geometrical considerations. In general case ($a \neq b \neq c$; $\alpha \neq \beta \neq \gamma$) corresponding to triclinic structure of the material this dependence is rather complicated and can be formulated as follows [189]:

$$\frac{1}{d_{hkl}^2} = \frac{1}{s} \left[\left(\frac{h \sin \alpha}{a} \right)^2 + \left(\frac{k \sin \beta}{b} \right)^2 + \left(\frac{l \sin \gamma}{c} \right)^2 + 2 \frac{hk}{ab} (\cos \alpha \cos \beta - \cos \gamma) + 2 \frac{hl}{ac} (\cos \alpha \cos \gamma - \cos \beta) + 2bc (\cos \beta \cos \gamma - \cos \alpha) \right] \quad 3.1$$

where $s = 1 - \cos^2 \alpha - \cos^2 \beta - \cos^2 \gamma + 2 \cos \alpha \cos \beta \cos \gamma$

However, for higher crystal symmetries it is much simpler as given below:

Monoclinic ($a \neq b \neq c$; $\alpha = \gamma = 90^\circ$; $\beta \neq 90^\circ$):

$$\frac{1}{d_{hkl}^2} = \frac{h^2}{a^2 \sin^2 \beta} + \frac{k^2}{b^2} + \frac{l^2}{c^2 \sin^2 \beta} - \frac{2hl \cos \beta}{ac \sin^2 \beta} \quad 3.2$$

Hexagonal ($a=b \neq c$; $\alpha=\gamma=90^\circ$; $\beta=120^\circ$):

$$\frac{1}{d_{hkl}^2} = \frac{4}{3} \frac{h^2 + k^2 + hk}{a^2} + \frac{l^2}{c^2} \quad 3.3$$

Orthorhombic ($a \neq b \neq c$; $\alpha=\beta=\gamma=90^\circ$):

$$\frac{1}{d_{hkl}^2} = \frac{h^2}{a^2} + \frac{k^2}{b^2} + \frac{l^2}{c^2} \quad 3.4$$

Tetragonal ($a=b \neq c$; $\alpha=\beta=\gamma=90^\circ$):

$$\frac{1}{d_{hkl}^2} = \frac{h^2 + k^2}{a^2} + \frac{l^2}{c^2} \quad 3.5$$

Cubic ($a=b=c$; $\alpha=\beta=\gamma=90^\circ$):

$$\frac{1}{d_{hkl}^2} = \frac{h^2 + k^2 + l^2}{a^2} \quad 3.6$$



XRD can also be used for the determination of average particle size by use of the Scherrer equation, given as:

$$D = 0.9\lambda / \beta \cos \theta \quad 3.7$$

Where D = particle size, 0.9 = shape factor; λ = X-ray wavelength, β = peak-width at half peak-height (radians); θ = angle of reflection.

In this work, XRD was used for the determination of structural properties such as lattice parameters, strain, grain size as well as crystal structure and phase identification of the starting AB₅ metal alloy and its hydride. Experimental parameters are given as follows:

<u>Parameters</u>	<u>Settings</u>
X-ray diffractometer:	Bruker AXS D8 Advance
X-ray source:	Copper tube with Cu K _α ($\lambda = 1.5406 \text{ \AA}$)
X-ray detector:	Sodium iodide
Monochromator:	Graphite
Generator operation (mA):	40
Electron intensity (keV):	40
Scan range ($2\theta^\circ$):	15–90
Scan rate ($^\circ\text{C} / \text{min}$):	0.05

The XRD patterns were processed using Powder Cell software (version 2.4) for the simulation / refinement of powder patterns of starting (unmodified) and surface modified AB₅ type alloys on the basis of crystal structure data of the constituent phases (Rietveld analysis).

3.3.2 SCANNING ELECTRON MICROSCOPY (SEM) AND ENERGY DISPERSIVE SPECTROSCOPY (EDS).

In a typical SEM, electrons generated from a cathode filament are accelerated towards an anode which contains sample material. The electrons generated by the cathode filament are focused through one or two magnetic, condenser lenses to generate a highly focused electron beam with a very fine focal spot of 0.4 – 5 nm. Using pairs of deflector plates or scanning coils that form part of the microscope's objective lens, this beam is deflected horizontally or vertically across the sample so that it scans a rectangular area of the sample surface in a raster-like manner. The interaction of the highly accelerated electron beam with atoms in the surface of the sample material results in the emission and scattering of electrons which are picked up by a detector. Corresponding electric signals are generated in the detector, modulated and later amplified to produce a 3-dimensional reconstruction of the sample's surface which is captured and stored using an appropriate imaging technique [190]. From SEM image, particle size analysis of the sample material can be carried out. The average particle size (d) and standard deviation (σ) obtained from n_i number of particles ($n_i \geq 100$ particles, unless otherwise specified) and can be calculated using **Equations (3.8)** and **(3.9)** respectively:

$$d = \frac{\sum n_i d_i}{\sum n_i} \quad 3.8$$

$$\sigma = \left[\frac{\sum n_i (d_i - d)^2}{\sum n_i} \right]^{1/2} \quad 3.9$$

The AB₅ alloys were supported on double-sided conductive carbon tape and mounted on a sample stub. Samples were fitted into the vacuum chamber of the microscope (Hitachi X-650 EM and LEO S440). The experimental parameters are given as follows:

<u>Parameters</u>	<u>Settings</u>
Working distance (mm):	15
Filament current (μA):	75-80
Accelerating voltage (KeV):	25

Energy dispersive spectroscopy measurements were conducted using EDAX Genesis coupled with Hitachi X-650 SEM electron microscope for determination of elemental composition in the AB₅ type material. This technique provides a good indirect identification of the density of the deposited layer on the surface of the alloy. Samples were dispersed on double-sided conductive carbon tape, which in turn was adhered to aluminium sample stubs. The experimental parameters used are given as follows:

<u>Parameters</u>	<u>Settings</u>
Baseline:	1500 counts per second
Time:	100 live seconds
Working distance:	15 mm
Accelerating voltage:	-25 keV
Emission current:	-60 μA
Amperage time:	100 μs

As in the SEM much focused high energy electron beam is aimed at the sample material to be characterized. The interaction of the incident electron beam with atoms in the surface of the sample results in the excitation of an electron within the inner shells of atoms in the ground state. If the energy is sufficient, the electrons are ejected from the atom leaving behind electron holes. The filling of these electron holes by electrons in higher-energy, outer shells

results in the release of excess energy in the form of X-rays. The X-rays produced are characteristic of each element within the sample (since their energy distribution depends on the configuration of the electron shell to be a unique feature of every element). The X-rays can be detected, modulated and amplified to generate plots with spectral lines characteristic of each element within the sample. The atomic percentage (at %) and weight percentage (wt %) of elements can thus be obtained [191]. To obtain a rough estimate of concentration, the following relationship is used:

$$P_x = P_s W_x \quad \mathbf{3.10}$$

Where P_x is the relative line intensity measured in terms of number of counts for a fixed period, and W_x is the weight fraction of the desired element in the sample. The factor P_s is the relative intensity of the line under identical conditions. However, **Equation 3.10** carries with assumption that the emission from the species of interest is unaffected by the presence of other elements in the sample and this assumption may not be justified. As a result, concentration estimates may be in error by a factor of 2 or more [194].

EDS analyses in this study were conducted for determination of elemental composition of the starting material and total Pd loading on the modified AB₅-type alloy. As mentioned earlier, determination of Pd concentration lead to erroneous results. Therefore, alternative technique for determination of total amount Pd deposited on the metal surface is needed.

3.3.3 ATOMIC ABSORPTION SPECTROSCOPY.

Atomic Absorption Spectroscopy (AAS) is a technique that uses the absorption of light to measure the concentration of gas-phase atoms. A beam of light from the hollow cathode lamp is passed through the neutral atoms formed by the flame atomizer (**Figure 3.6**).

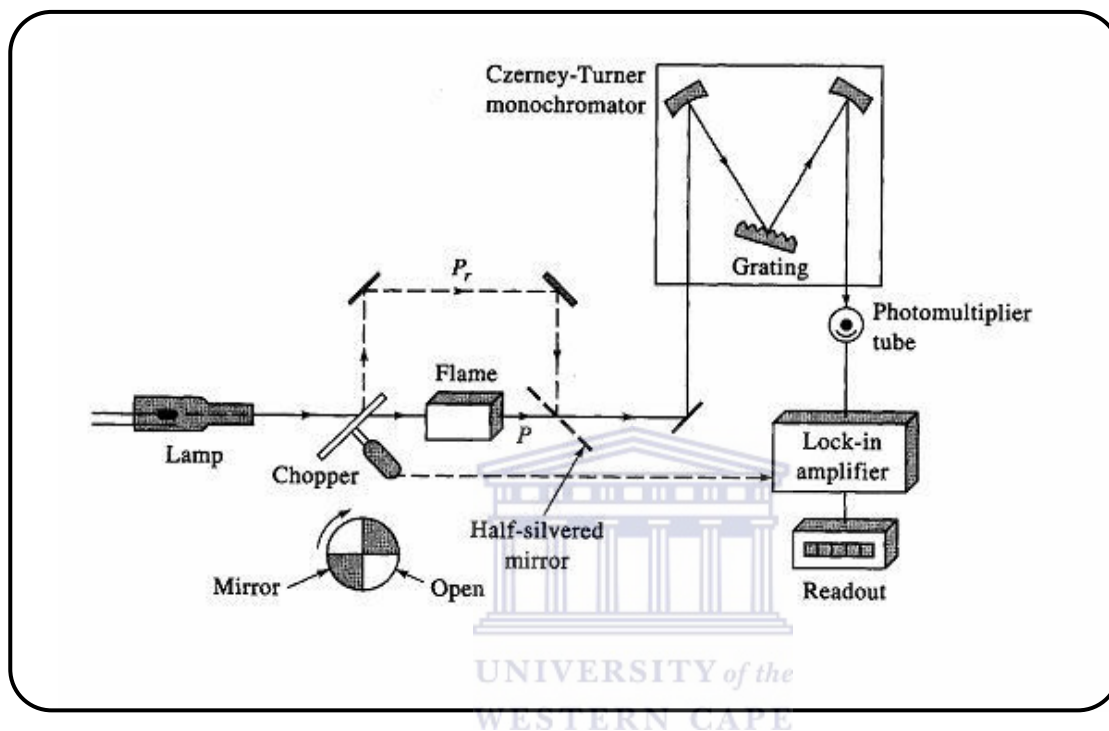


Figure 3.6: Schematic representation of double beam flame spectrophotometers [192].

The light produced by the hollow-cathode (HCL) lamp is emitted from excited atoms of the same element which is to be determined. Therefore the radiant energy corresponds directly to the wavelength which is absorbable by the atomized sample.

This method provides both sensitivity and selectivity since other elements in the sample will not generally absorb the chosen wavelength and thus, will not interfere with the measurement. Before the analyte is aspirated, a measured signal is generated by the photomultiplier tube (PMT) as light from the HCL lamp passes through the flame. When analyte

atoms are present in the flame, while the sample is aspirated, some of that light is absorbed by those atoms leading to a decrease in PMT signal which is proportional to the amount of analyte.

By careful construction of the calibration curve using standard solutions, the absorbance of the sample can be related to the concentration of the metal of interest in the sample solution according to Beers' Lambert Law [192].

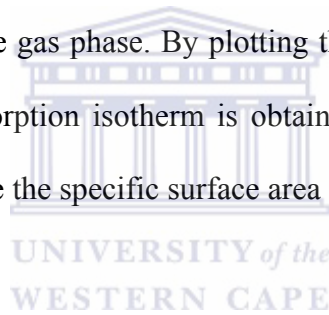
In this study, AAS was employed for determination of Pd metal deposited on AB₅ metal surface. A minimum of 5 standards were prepared in the range depending on the sensitivity of the instrument towards the analyte [193]. A blank solution (i.e. *aqua regia* and ultrapure water) was measured directly after the calibration standards to rule out contributions from the solvent and in that way ensure the stability of the analytical baseline.

The preparation of standards for analysis, 1.0 g of surface-modified materials was dissolved in 50 mL *aqua regia* solution (1 part HNO₃ per 3 parts HCl) while heating at 50°C for 30 minutes with constant stirring at 300 rpm. The solutions were allowed to cool to room temperature, then filtered and made up to the mark in 100 mL volumetric flask with ultrapure water. The experimental parameters using spectrometer (Philips PU9100) are given as follows:

<u>Parameters</u>	<u>Settings</u>
Wavelength (nm):	247.6
Air-C ₂ H ₂ flow rate (L/min):	0.9-1.2
Lamp current (mA):	15
Band pass (nm):	0.2

3.3.4 BRUNAUER-EMMETT-TELLER TECHNIQUE (BET).

The information of surface area and porosity is important the key in understanding the structure, formation and potential applications of different materials. The most widely used technique for estimating surface area is the so-called BET method [194-196]. The basic operation, solid samples are placed in an evacuated sample holder at constant temperature. The sample holder is filled with helium to flush contaminating gases from the sample surface and pores. The helium is then purged from the system. Evacuated samples are cooled to -196 °C in a liquid N₂ bath while the sample holder is filled with high-purity N₂ gas. Pressure within the sample holder is monitored over time and then rapidly reduced to reach an equilibrium state where the quantity of gas adsorbed onto the surface is equivalent to the quantity of gas removed from the gas phase. By plotting the quantity of N₂ adsorbed versus the equilibrium pressure an adsorption isotherm is obtained, which together with the BET equation can be used to determine the specific surface area of the materials of interest.



This adsorption isotherm can be defined as the plot of the dependence of the fractional coverage of surface-adsorbed molecules on pressure, at constant temperature [195]. The BET equation can be given as follows:

$$\frac{1}{v\left[\left(\frac{P}{P_0}\right)-1\right]} = \frac{c-1}{v_m c} \left(\frac{P}{P_0}\right) + \frac{1}{v_m c} \quad 3.11$$

Where v is the weight of N₂ adsorbed at a given relative pressure (P/P_0), v_m is the weight of gas producing monolayer coverage, and c is a constant related to the heat of adsorption.

Total surface area S_{total} and specific surface area S can be evaluated by the following equations:

$$S_{total} = \frac{v_m N_s}{V} \quad 3.12$$

$$S = \frac{S_{total}}{a} \quad 3.13$$

Where N is Avogadro's number; s is adsorption cross section; V is molar volume of adsorbent gas; a is molar mass of adsorbed species [196].

Sample preparation for BET analysis, 1.0 g of the sample material was dried in a vacuum oven at 80 °C overnight. The sample material was then transferred to a quartz sample tube and dried for 2 hours at 200 °C under constant nitrogen flow using a drying apparatus (Micromeritics Flow prep 060 Degasser).

3.3.5 VOLUMETRIC MEASUREMENTS OF HYDROGEN SORPTION PERFORMANCES

3.3.5.1 *Kinetic studies*

Volumetric measurements using a Sievert type apparatus were conducted for evaluation of kinetic behaviour of surface modified material. Roughly, 1.5 g of unmodified and surface modified samples was used for the measurement. Prior to measurements, the system and the reaction vessel were evacuated (10^{-5} mbar) for 2 hours.

The starting H_2 pressure of 34 bar aliquot was then introduced into the appropriate buffer cylinder, and a pressure baseline established, after which the reactor valve was opened to introduce H_2 to the sample material. After hydrogenation the reactor valve was closed and the unabsorbed hydrogen in the system was released by opening exhaust valve, followed by evacuation of the system. H_2 desorption was conducted by opening the reactor valve. Changes to the reference H_2 pressure were monitored by the data acquisition. The process of absorption and desorption was repeated for 3 cycles. Scan intervals of 10-30 seconds were

used. The volumetric system and reactor were maintained at 25 °C using a thermo stated oil bath. It should be noted that measurements of H₂ desorption capacity and kinetics are carried out by heating hydrogenated samples under vacuum.

H₂ absorption capacity was determined by calculating total amount of gaseous H₂ in the internal volumes of the gas-distributing system and reactor, starting from the monitored H₂ pressures, P_i , therein; as well as the temperatures, T_i , of these volumes using the following equation:

$$n = \sum \frac{P_i V_i}{Z(P_i, T_i) R T_i} \quad 3.14$$

Where n is the total number of moles of H₂ in the volumes V_i taken into account (maintained at the corresponding temperatures, T_i), $R=8.3143$ J/ (mole·K) is the gas constant, and Z is the compression factor of hydrogen gas at the specified pressure P_i and temperature T_i . Calculating starting (n_0) and actual (n_1) amounts of hydrogen gas in the system, the hydrogen absorption capacity (x) of the material will be expressed as:

$$x \left[\frac{\text{cm}^3}{\text{g}} \text{ STP} \right] = \frac{22400(n_0 - n_1)}{m} \quad 3.15$$

Where m is sample weight; 22400 cm³/mole is the molar volume of hydrogen at normal conditions ($T=0$ °C, $P=1$ bar).

The starting (n_0) and actual (n_1) number of moles of H₂ in the system were calculated as:

$$n_0 = \frac{P_0 V_j}{Z(P_0, T_0) R T_0} \quad 3.16$$

$$n_1 = P \left(\frac{V_s}{Z(P, T_s) R T_s} + \frac{V_C}{Z(P, T_R) R T_R} + \frac{V_j}{Z(P, T_0) R T_0} \right) \quad 3.17$$

Where P_0 is equal to the pressure in the system before opening reactor valve; P is the actual hydrogen pressure; V_j and V_C are the volumes of thermostated (at T_0) measurement system and connecting pipeline (at room temperature, T_R), respectively; V_S is the internal volume of reactor with the sample kept at temperature T_S . The amount of hydrogen desorbed by the material was calculated in a similar manner as hydrogen absorption capacity.

Kinetic curves were then constructed by plotting hydrogen absorption and desorption capacity (x) against time (t). An experimental kinetic data was fitted with JMA rate equation (see **Equation 2.2**) in order to see the effect of Pd on the kinetics of the AB₅ type alloys [197,198].

3.3.5.2 *Thermal cycling*

Thermal cycling was done for determining how fast hydrogen is absorbed and released during cooling and heating at approximately constant hydrogen pressure. After activation, the alloys were saturated with H₂ pressure at 30 bar followed by thermal cycling from 80 °C to 0 °C. The process was repeated at 18 bar, 12 bar, 5 bar and 3 bar.

The measurements for kinetics and thermal cycling were done using volumetric installation at Institute for Energy Technology (Norway) fitted with differential and absolute pressure transducers allowing for measurement of incremental changes in the starting pressure of the buffer cylinder (**Figure 3.7**).

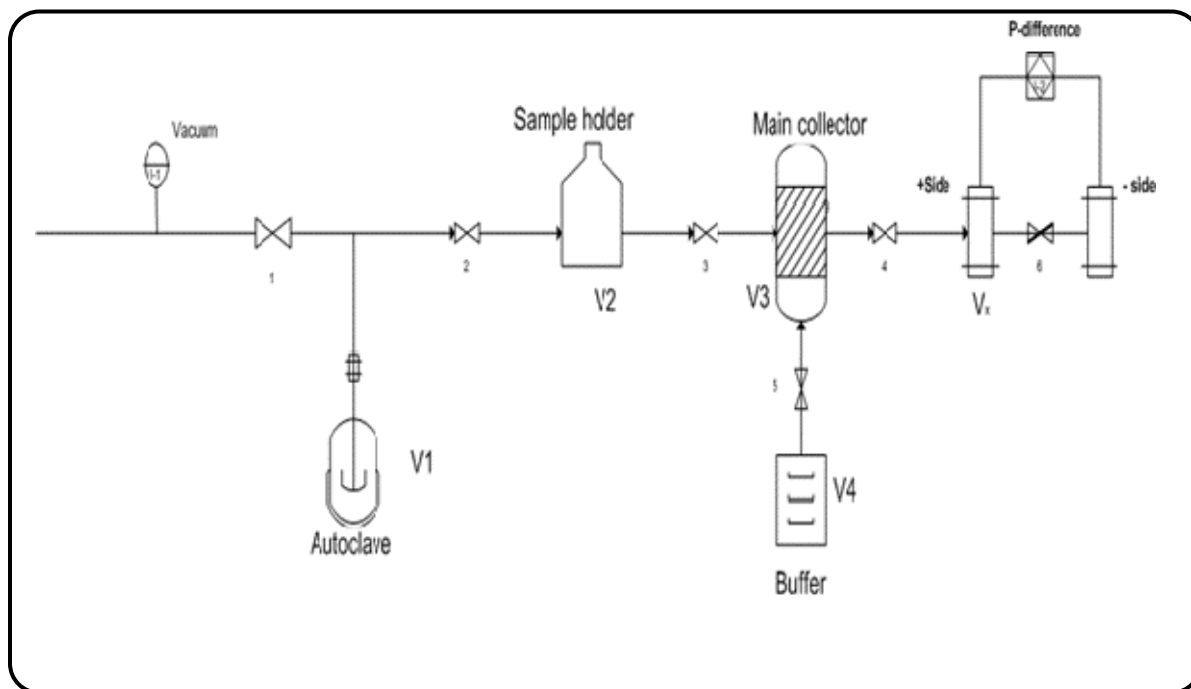


Figure 3.7: Schematics of the experimental setup (IFE) for studies of hydrogen absorption by the unmodified and surface modified AB₅-type alloys. V1: Autoclave = 32.50 cm³, V2: Sample holder = 25.81cm³, V3: Gas collector = 22.70cm³, V4: Buffer cylinder = 297.34 cm³, V_x: Positive side of the differential sensor = 39.26 cm³, V_y: Negative side of the differential sensor 70.07cm³

3.3.5.3 *Measuring of Pressure-Composition-Temperature equilibrium characteristics.*

The behaviour of MH systems is best represented by pressure –composition-temperature diagrams (PCT) to be a set of pressure – composition isotherms (PCI). The PCT diagram provides a clear understanding of the hydrogenation / dehydrogenation properties and phase transformations occurring in the hydrogen sorption material, hydride stability, and equilibrium relationships between the H₂ pressure and concentration. The isotherms are very sensitive to variations in composition and homogeneity of MH materials and were therefore

an excellent characteristic in assessing the quality of fabricated materials. The PCT relationship describes the dependence of the H₂ equilibrium pressure on the quantity of H₂ absorbed in the metal hydride-forming alloy and temperature [199].

The construction of PCT diagram for the unmodified AB₅-type alloy facilitated the determination of the H₂ sorption capacity, thermodynamic properties such as entropy (ΔS) and enthalpy (ΔH), and the absorption behaviour of the starting material [200]. The ΔH gives a good indication of the thermal stability of the MH alloys of interest and is directly related to the H₂ dissociation process [201].

The PCT studies were conducted using automated Sievert apparatus (PCT Pro-2000, Hy-Energy Scientific Instruments) (**Figure 3.8**). Approximately, 2 g of AB₅ type alloy was loaded onto the reactor vessel and activated by heating to 200 °C in a furnace under vacuum for evacuated for an hour. The activated sample was then subjected to several charge/discharge cycles at specified conditions. The measurements of the PCT characteristics of the starting material were initiated from the third cycle followed by subsequent measurements of absorption and desorption isotherms through the specified temperatures using standard volumetric procedures.

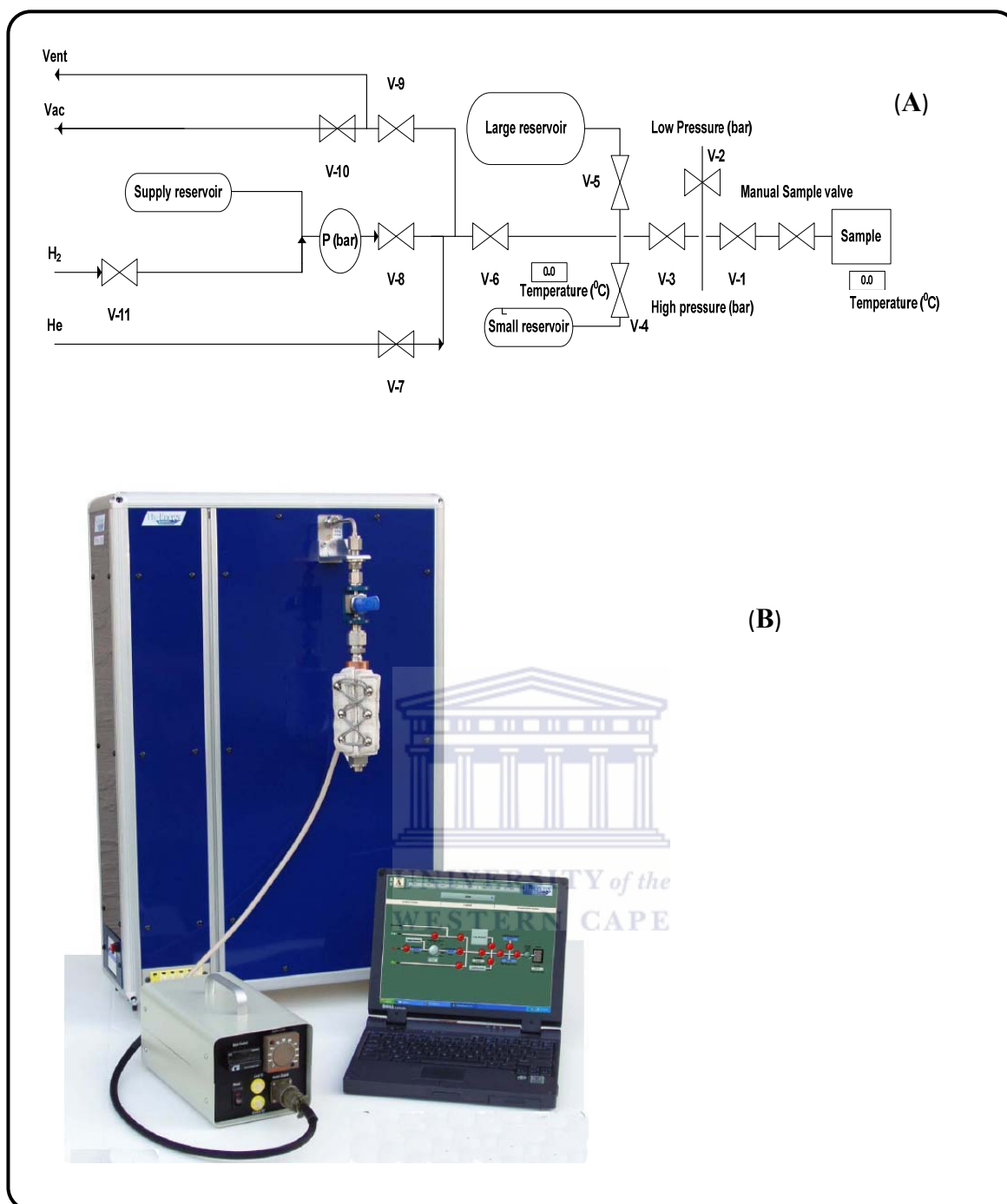


Figure 3.8: Schematics of experimental setup for PCT studies (A) and PCT picture (B).

3.3.6 MODELLING OF PHASE EQUILIBRIA IN THE SYSTEM OF AB₅ HYDRIDE-FORMING ALLOY WITH GASEOUS HYDROGEN.

3.3.6.1 *Approach.*

Modelling of phase equilibria (PCT diagrams) in the systems of hydrogen gas with hydride forming alloys is important both for the systemic evaluation of the available experimental data and for the optimisation of specific applications of metal hydrides.

To quantify the thermodynamic features of metal – hydrogen interaction, it is necessary to have a model of PCT diagram observed for real metal hydride material in the system with hydrogen gas [201]. The model should analytically represent the relationships between equilibrium hydrogen pressure (P), hydrogen concentration in the solid (C) and temperature (T). It is important from practical point of view, because the PCT model is a starting point for the modelling of kinetics of hydrogen uptake / release [202], and, further, heat-and-mass transfer performances in MH beds [203], to yield quantitative information for the development of various MH applications.

In the majority of application-oriented studies the formal-empirical approach for the modelling of PCT diagrams, where the experimental PCT data are fitted by arbitrarily selected equations, is used [203,204]. This approach is rather convenient for engineering solutions, but it is unsatisfactory from the phenomenological point of view, and it cannot be applied for the extrapolation of PCT relations outside the limits of the available experimental data.

Another approach is in the application of thermodynamic and statistic regularities to hydrogen systems with hydride-forming materials resulting in building up the PCT models. Similar models describing monomolecular adsorption, when two phases are co-exist in the adsorbate layer resulting in plateau behaviour of pressure – composition isotherms below critical temperature, were developed as early as in the mid of 1930th [205,206]. At the same

time Lacher [207] has improved this approach to describe PCT diagram of H – Pd system. The Lacher model was further modified by Rees and Kierstead [208,209], where more complicated systems exhibiting several plateau pressures on pressure – composition isotherms could be modelled.

Within PCT models realising thermodynamical or statistic approach, hydrogen in a metal is considered as a lattice gas, and concentration dependence of its partial molar entropy, $\bar{S}(\theta)$ is described by a configuration term (**Equation 3.18**).

$$\bar{S}(\theta) = \bar{S}_0 - R \ln \left(\frac{\theta}{1-\theta} \right) \quad 3.18$$

In that way, concentration dependence of partial molar enthalpy of the lattice gas, $\bar{H}(\theta)$, is determined by the H-H interaction energy (**Equation 3.19**) [201,210].

$$\bar{H}(\theta) = \bar{H}_0 + E_{HH}(\theta) \quad 3.19$$

Where $\theta = C / C_{\max}$ is a fraction of filling of the metal matrix with hydrogen (C and C_{\max} are the actual and maximum hydrogen concentrations, respectively), \bar{S}_0 and \bar{H}_0 are correspondingly, entropy and enthalpy of the infinitely diluted solution; $E_{HH}(\theta)$ is the energy of indirect H-H interaction.

Substituting of **Equation 3.18** and **Equation 3.19** into equation for the chemical potential of hydrogen atoms in the energetically-equivalent interstitials of the metal matrix, and further equating with the chemical potential of hydrogen in a gas phase yields:

$$X(\theta) = \ln P - \ln P_0 = 2 \ln \left(\frac{\theta}{1-\theta} \right) + \frac{E_{HH}(\theta)}{RT} \quad 3.20$$

Where P_0 is a plateau pressure calculated by Van't Hoff equation (**Equation 2.7**)

Equation 3.20 is a general equation of the PCT diagram whose specific form depends on the kind of the concentration dependence $E_{HH}(\theta)$. In the simplest case (an ideal solid solution),

$E_{HH}(\theta) \equiv 0$, and the **Equation 3.20** looks like adsorption Langmuir's equation. In this case the shape of pressure – composition isotherm in the $\ln P - \theta$ coordinates does not depend on temperature, and its shift along the $\ln P$ axis, when the temperature is changed, is calculated by **Equation 2.7**.

The Lacher-like models assume an attractive H–H interaction whose energy is proportional to hydrogen concentration:

$$E_{HH}(\theta) = -h \cdot \theta, \quad h > 0 \quad 3.21$$

that, being substituted into **Equation 3.20** yields:

$$\ln P = \ln P_0 + 2 \ln \left(\frac{\theta}{1-\theta} \right) - 8 \left(\frac{T_c}{T} \right) \theta \quad 3.22$$

Where $T_c = h/4R$ is the critical temperature, P is the equilibrium hydrogen pressure and P_0 is the concentration independent contribution to its value.

The characteristic feature of the Lacher model is an antisymmetry of the pressure – composition isotherms as to the point having abscissa $\theta=1/2$. Majority of the real systems show asymmetric behaviour of the PC isotherms, and their critical points correspond to $\theta_0 < 1/2$. This feature can be described in the framework of the general model (**Equation 3.20**) assuming that, apart from the attraction, the H–H repulsion contributes into E_{HH} , and this contribution increases with the filling fraction, θ . The corresponding corrections of the Lacher model introduced additional, non-linearly dependent on concentration terms into right-hand part of (**Equation 3.21**), so as their contribution becomes significant at $C \rightarrow C_{\max}$ [211-213]. The simplest case of the realisation of this approach is in the consideration of hydrogen in metal matrix as a Van der Waals lattice gas [213]. The concentration dependence of the energy of H – H attraction in this case is also described by **Equation 3.21**, but at $\theta \rightarrow 1$,

$E_{HH}(\theta) \rightarrow +\infty$ (hard core potential). Starting from these assumptions, the following sorption equation was derived [213]:

$$\ln P = \ln P_0 + 2 \ln \left(\frac{\theta}{1-\theta} \right) - \frac{27}{2} \left(\frac{T_c}{T} \right) \theta + 2 \left(\frac{\theta}{1-\theta} \right) \quad 3.23$$

where $T_c = 4h/27R$.

It has to be noted that in the model of the Van der Waals lattice gas the value of θ_0 corresponding to the plateau midpoint depends on temperature covering a range from $1/3$ ($T = T_c$) to $1/2$ ($T = 0$). Besides, the relation between the values of the entropy and enthalpy terms in the **Equation 2.7** (let denote them as ΔS_0 and ΔH_0 , respectively, taking into account that they are used for the calculation of the concentration-independent term, P_0) and apparent standard entropy and enthalpy (ΔS^0 and ΔH^0) calculated from van't Hoff dependencies of logarithm of plateau pressure versus reciprocal temperature are expressed as:

$$\Delta H^0 = \Delta H_0 - \frac{27}{2} RT_c \theta_{ov} \quad 3.24$$

$$\Delta S^0 = \Delta S_0 - 2R \left(\ln \frac{\theta_{ov}}{1-\theta_{ov}} + \frac{\theta_{ov}}{1-\theta_{ov}} \right) \quad 3.25$$

The Lacher model has been extended to the consideration of multi-plateau isotherms which are obtained by a superposition of several, depending on the experimentally observed number of plateaux, single-segment isotherms [208]:

$$C = C_{\max} \sum_{i=1}^m g_i \theta_i(P) \quad 3.26$$

Where m is the number of plateaux, g_i is the fraction of the i -th plateau segment.

When fluctuations in the chemical composition will be infinitesimal, a discreet partition on fractions, g_i can be substituted by a continuous distribution function, $\varphi(u)$. **Equation 3.26** can

be modified to introduce a convolution of the $\theta(P)$ and $\varphi(u)$ functions. Assuming $X = \ln [P(\theta)] - \ln [P(\theta_0)]$ as a fluctuating parameter, where θ_0 corresponds to the midpoint of the plateau, and a Gaussian distribution, the isotherm equation can be written as

$$\theta = C/C_{\max} = \frac{1}{\sigma\sqrt{2\pi}} \int_{-\infty}^{+\infty} \theta(X) \exp \left[-\frac{(X-u)^2}{2\sigma^2} \right] du \quad 3.27$$

where $\theta(X)$ is calculated by the solution (as respect to filling fraction, θ) of the **Equation 3.20** presented as **Equation 3.22** (Lacher model) or **Equation 3.23** (Van der Waals lattice gas model).

Finally assuming that the fluctuations of $\ln P_0$ are determined by the fluctuation in ΔS_0 and ΔH_0 , also distributed by Gaussian Law, the standard deviation, σ , is expressed via their corresponding standard deviations, σ_S and σ_H taking into account van't Hoff equation (see **Equation 2.7**) as:

$$\sigma^2 = \frac{\sigma_S^2}{R^2} + \frac{\sigma_H^2}{R^2 T^2} - \frac{2\rho_{SH} \sigma_S \sigma_H}{R^2 T} \quad 3.28$$

Where ρ_{SH} is a Pearson correlation between ΔS_0 and ΔH_0 .

Equation 3.28 gives the temperature dependence of the deviation of the real pressure-composition isotherms from ideal behaviour, including plateau slope. According to Shilov and Efremenko [214], the value of plateau slope $\partial \ln P_0 / \partial C$, is linearly dependent from the reciprocal temperature passing zero at some temperature T_0 . It follows that σ (which is proportional to the plateau slope in the midpoint) has a minimum at $T_0 = \sigma_H / \sigma_S$. Complete correlation, $\rho_{SH} = 1$, converts the model to the ideal case, $\sigma(T_0) = 0$.

The described model proposed by Lototsky *et al.* [213,215] was employed for the fitting of our experimental PCT data along with Van der Waals lattice gas model as a core. The

deviations of PCT diagrams from ideal behaviour were calculated using **Equations 3.27** and **3.28**, and the presence of several plateau segments was modelled by **Equation 3.26**.

3.3.6.2 *Algorithm.*

The calculations on the modelling PCT diagrams were carried out using software HY-PCT, version 3.1, © M. V. Lototsky, 2004. This section briefly presents the algorithm of the calculations applied in this software (programmed in Microsoft Visual Basic 6.0). The details were taken from the original publications [213,215], as well as from private communications with the author of the model.

The main element of the calculation algorithm allowing to calculate fitting parameters from experimental PCT data and further to plot the calculated PCT dependencies in the required pressure-temperature ranges is the calculation of a sought-for parameter (concentration, C ; or pressure, P) starting from the values of the variables (temperature, T ; and pressure, P , or concentration, C), and a finite set of the free arguments, $\{A_1, A_2, \dots, A_n\}$ to be the model coefficients:

$$C = C [T, P, (A_1, A_2, \dots, A_n)], \text{ or} \quad 3.29$$

$$P = P [T, C, (A_1, A_2, \dots, A_n)] \quad 3.30$$

The model coefficients $\{A_1, A_2, \dots, A_n\}$ allowing to describe the PCT diagram having m plateau segments on pressure-composition isotherm include:

1. Coefficient characterising the PCT diagram as a whole:
 - 1.1. Asymptotic hydrogen concentration, C_{\max}^* ;
2. Parameters of each i -th plateau segment ($i=1, 2, \dots, m$):

* since all the model concentrations are expressed in dimensionless filling fractions, θ , the hydrogen concentrations, C , can be presented in any units consistent with ones corresponding to the measured experimental concentrations, e.g., H/M, H/AB₅, cm³/g, etc.

- 2.1. Segment fraction, $g_i \left(\sum_{i=1}^m g_i = 1 \right)$ [dimensionless];
- 2.2. Critical temperature for the i -th segment, $(T_C)_i$ [K];
- 2.3. Concentration-independent contribution to entropy change upon hydrogenation for the i -th segment, ΔS_i [J/mol H₂/K];
- 2.4. Concentration-independent contribution to enthalpy change upon hydrogenation for the i -th segment, ΔH_i [J/mol H₂];
- 2.5. Standard deviation of the entropy for the i -th segment, $(\sigma_s)_i$ [J/mol H₂/K];
- 2.6. Standard deviation of the enthalpy for the i -th segment, $(\sigma_h)_i$ [J/mol H₂];
- 2.7. Pearson correlation coefficient for the i -th segment, $(\rho_{SH})_i$ [dimensionless].

In so doing, the model coefficients $\{A_1, A_2, \dots, A_n\}$ include $(7m+1)$ parameters where m is a number of plateau segments for metal – hydrogen system under consideration. These coefficients are used as free arguments when calculating concentration (**Equation 3.29**) or pressure (**Equation 3.30**) starting from known values of temperature and pressure or concentration. They are also fitting parameters of the model to be calculated from a set of experimental data $\{P_e, C_e, T_e\}$.

The calculation of the sought-for parameter C according to **Equation 3.29** is carried out according to algorithm schematically presented in **Figure 3.9**. The procedure includes two steps. Step 1 includes procedure for the calculation of the filling fraction, θ_i , for each plateau segment, i , starting from the values of temperature (T) and pressure (P), as well as arrays containing parameters of the plateau segments: $(T_C)_i$, ΔS_i , ΔH_i , $(\sigma_s)_i$, $(\sigma_h)_i$ and $(\rho_{SH})_i$. The more detailed description of this step will be presented below.

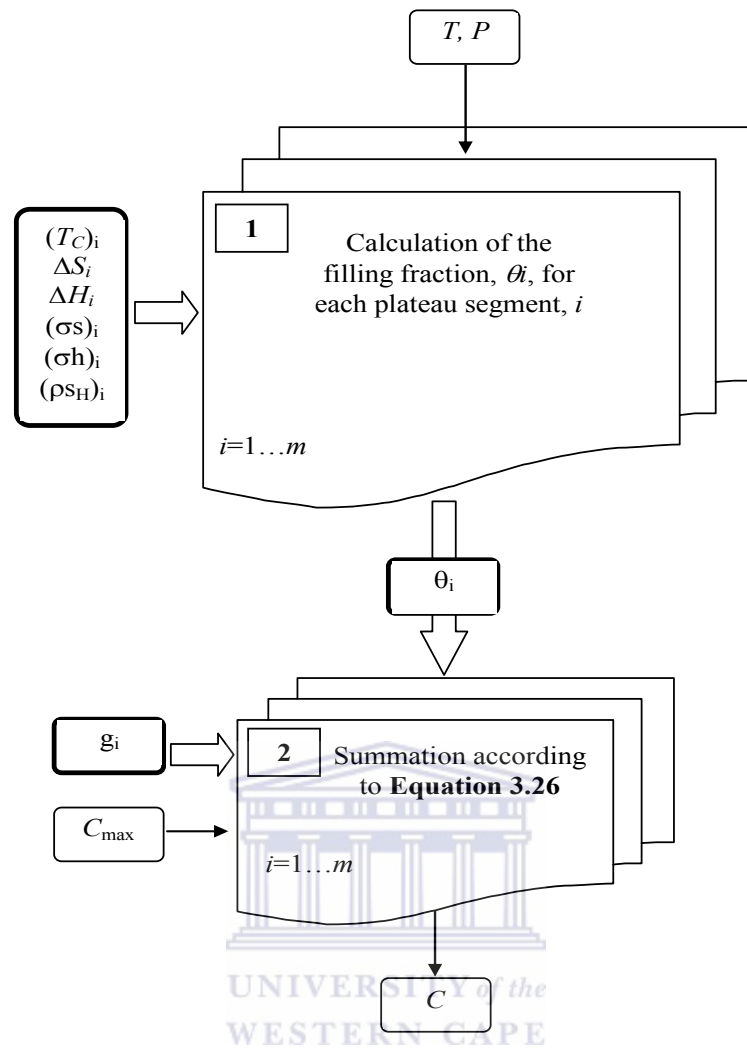


Figure 3.9: Schematic representation of the algorithm of calculation of the concentration according to **Equation 3.29**. The scalar starting data and calculation results are outlined by thin-line rounded boxes, and their flows are shown by line arrows. The data arrays are outlined by thick line rounded boxes, and their flows are shown by block arrows. Cyclic calculations are shown as multi-boxes.

The step 2 uses the output data from the step 1 (array of θ_i values), together with the value of C_{max} and array of g_i values for the plateau segments, as the input data. It realises the calculation of hydrogen concentration, C , using **Equation 3.26**.

The procedure of calculation hydrogen pressure starting from the known temperature and concentration (**Equation 3.30**) is realised as inverse solution of the **Equation 3.29** using

Newton method. The calculations of the concentration during the iteration process are carried out using the algorithm described above.

The algorithm of the calculation of the filling fraction for a plateau segment (step 1) is schematically shown in **Figure 3.10**. The procedure includes core PCT calculation (1.1, will be described below), to yield the value of the filling fraction, $\theta(X)$, corresponding to the “ideal” pressure – composition isotherm without sloping plateau. Starting from the temperature and standard deviations of entropy and enthalpy, as well as the Pearson correlation coefficient, the value of standard deviation, σ , is calculated according to **Equation 3.28** (1.2).

Finally, using the outputs from steps 1.1 and 1.2, the convolution according to **Equation 3.27** is made (1.3) to yield the sought-for filling fraction, θ . The integral in **Equation 3.27** was calculated by Gauss-Christophel quadrature formula using Hermit polynomial of the 10-th power to yield the accuracy better than 0.01 [215]:

$$\int_{-\infty}^{+\infty} \theta(X) \exp\left[-\frac{(X-u)^2}{2\sigma^2}\right] du \approx \frac{\exp\left(-\frac{X^2}{2\sigma^2}\right)}{\sqrt{\pi}} \sum_{j=1}^{n=10} \theta(\sqrt{2}\sigma\xi_j) \exp\left(\frac{\sqrt{2}X\xi_j}{\sigma}\right) \eta_j \quad 3.31$$

where ξ_j and η_j are roots and weight coefficients of the Hermit polynomial.

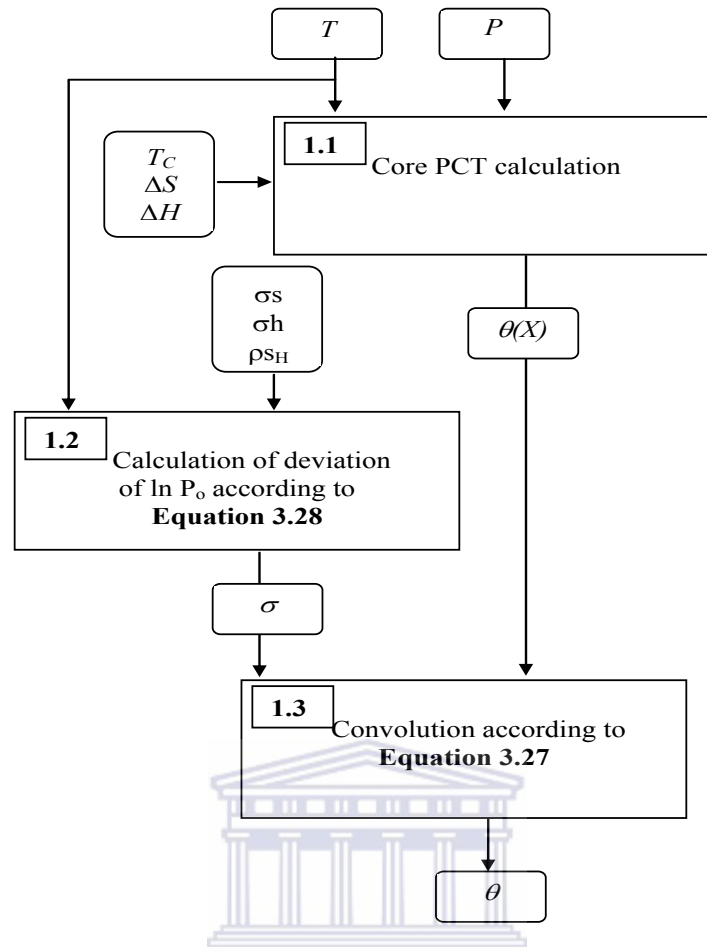


Figure 3.10: Schematic representation of the algorithm of calculation of the filling fraction, θ , for the i -th plateau segment. The indexes (i) for the elements of arrays containing parameters of the plateau segment are omitted.

For the core PCT calculation (1.1), **Equation 3.23** was represented as:

$X \equiv \ln P - \ln P_0 = H(\theta, Z)$, where:

$$\ln P_0 = -\frac{\Delta S_0}{R} + \frac{\Delta H_0}{RT};$$

$$H(\theta, Z) = 2 \ln \frac{\theta}{1-\theta} - \frac{27}{2} Z \theta + 2 \frac{\theta}{1-\theta}; \quad 3.32$$

$$Z = \frac{T_c}{T}$$

The calculation was arranged as a solution of the equation $X=H(\theta,Z)$ as respect to filling fraction, θ , by Newton iteration method. When $Z\leq 1$ ($T\geq T_C$; Figure 3.11a), this equation has a single root and can be resolved unambiguously. The case $Z>1$ (Figure 3.11b) is more complicated, because loop-like shape of the $H(\theta)$ function (dashed line in Figure 3.11) that corresponds to metastable state with the tendency of phase separation in the solid to form hydrogen-lean α -phase and hydrogen-rich β -phase.

According to Maxwell equal-area rule, the phase transition takes place at a constant pressure (corresponding to X_0 in Figure 3.11b) where $S_{ABC}=S_{CDE}$. In doing so, the root $\theta(X_\alpha)$ for $X<X_0$ is sought starting from the initial estimate of $\theta\approx\varepsilon$, and the root $\theta(X_\beta)$ for $X>X_0$ is sought starting from the initial estimate of $\theta\approx 1-\varepsilon$, where ε is an indefinitely small positive number. At $X=X_0$, $\theta(X_0)$ is assumed to be equal to θ_0 (plateau midpoint varied from 1/3 at $T=T_C$ to 1/2 at $T=0$ K).

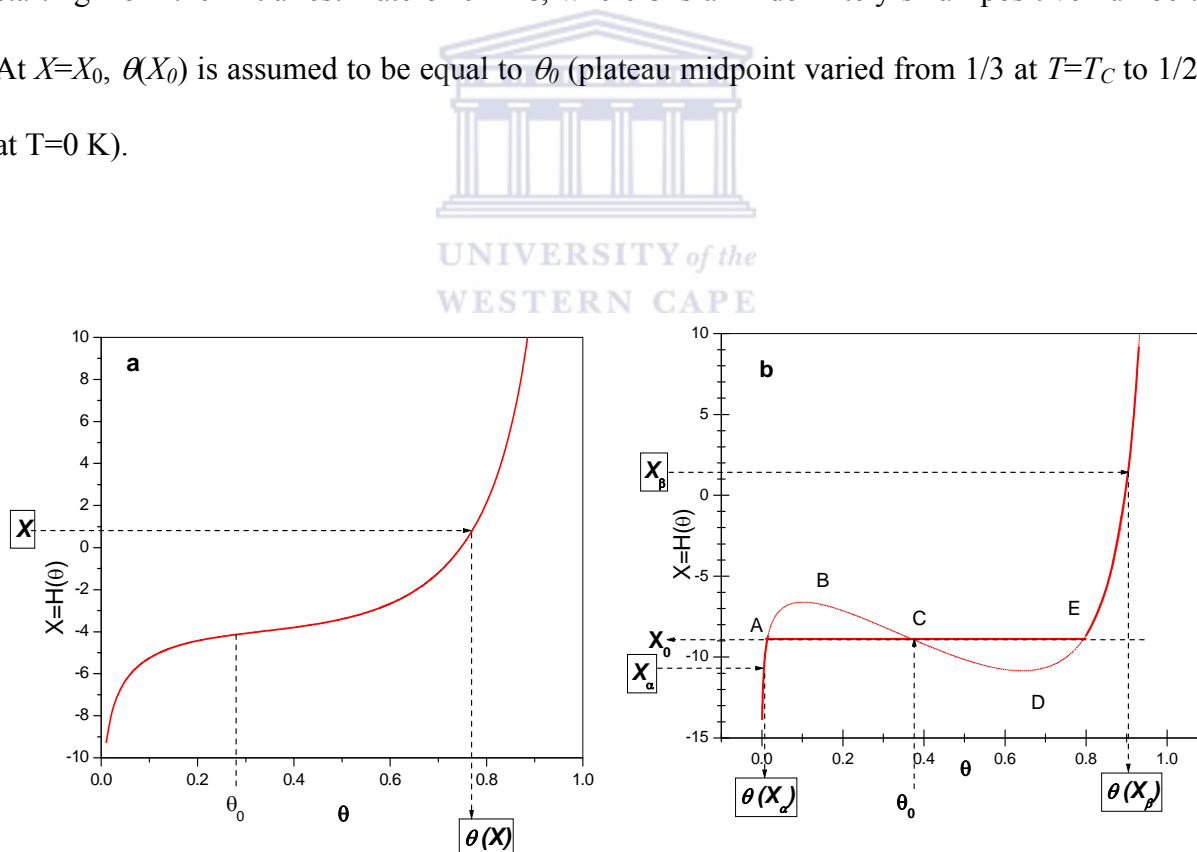


Figure 3.11: Schematic representation of the calculation $\theta(X)$ at $Z=T_C/T \leq 1$ (a) and $Z=T_C/T > 1$ (b)

The values of model coefficients were fitted to minimize the sum of squared distances from experimental points $\{P_e, C_e, T_e\}$ to the calculated PCT diagram built as a surface in the coordinates $C - \ln P - T$. The iterations were carried out using simplex algorithm followed by the application of the gradient-descent method [215].

3.3.7 TESTING OF METAL HYDRIDE UNITS.

3.3.7.1 *General layout of the experimental hydrogen storage unit for measuring temperature distribution in MH bed.*

The dynamic behaviour of the hydrogen absorption /desorption in the selected AB₅- material, together with temperature distribution in the MH bed, was studied in a 150 cm³ cylindrical reactor equipped with four thermocouples for the measurement of radial temperature distribution in the middle of MH bed (**Figure 3.12**).

The reactor was filled with 600 g of the La_{0.85} Ce_{0.15} Ni₅ H₂ storage alloy. The alloy showed reproducible H₂ absorption / desorption dynamics after completion of just one activation cycle: (1) initial evacuation, (2) 24-hours charging with H₂ at $P=50$ bar, (3) H₂ desorption at $P=1$ bar, and (4) final evacuation.

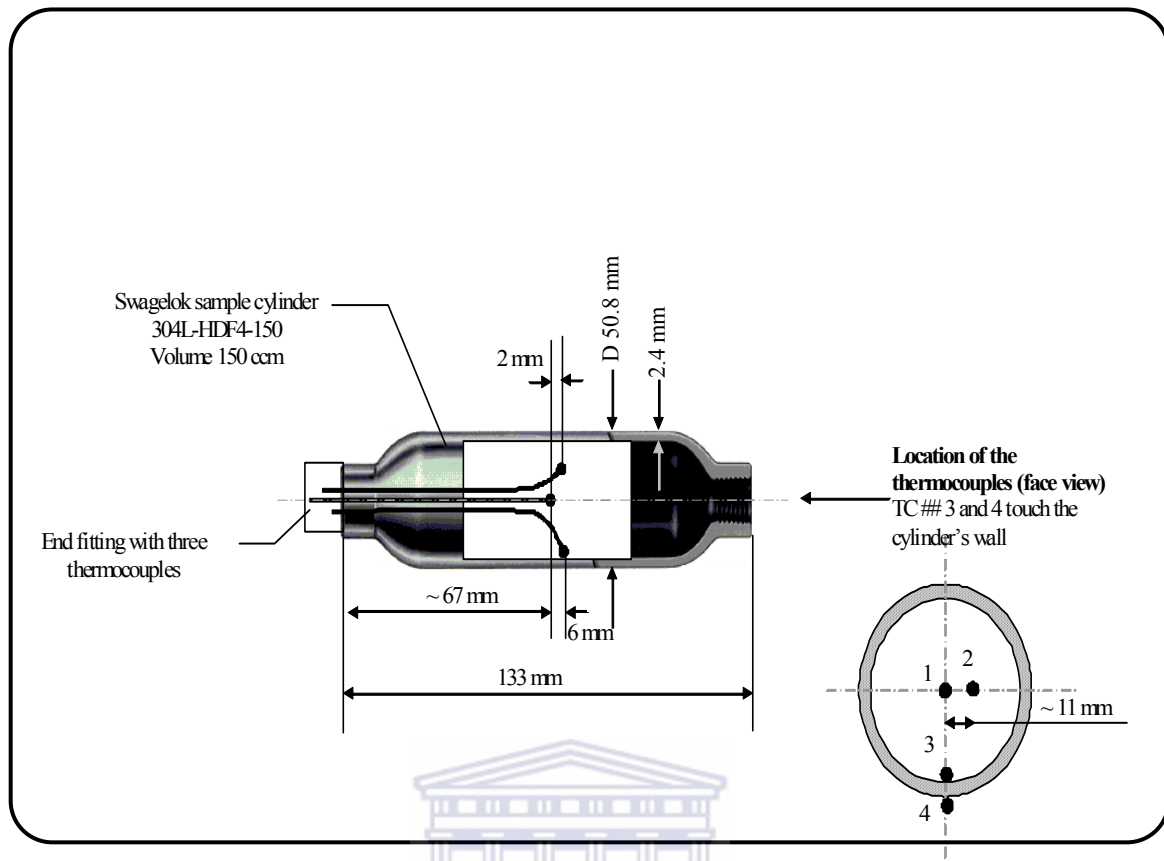


Figure 3.12: Schematic of the reactor for studying activation and heat and mass transfer performances of MH beds.

The evacuation was done using a rotary pump with a residual pressure of 5×10^{-2} bar. Both charge and discharge of the MH-reactor were carried out at constant pressures (1.5-5 bar for desorption and 10-50 bar for absorption); the unit was immersed in a thermostat ($T=20$ - 50°C). During the charge / discharge, hydrogen flow rate was logged, together with the temperatures in the centre of the MH-bed (T1), in between the centre and the wall of the reactor (T2), and on the inner (T3) and outer (T4) surfaces of the reactor wall.

3.3.7.2 Charge-discharge testing procedures.

The performance of the unit was studied using in house metal hydride testing station (**Figure 3.13**). Prior to experiment start-up the storage units were leak tested and volume calibrated using argon gas, and cycled several times (H_2 absorption / desorption) to reach reversible storage capacity and reproducible charge/ discharge rates.

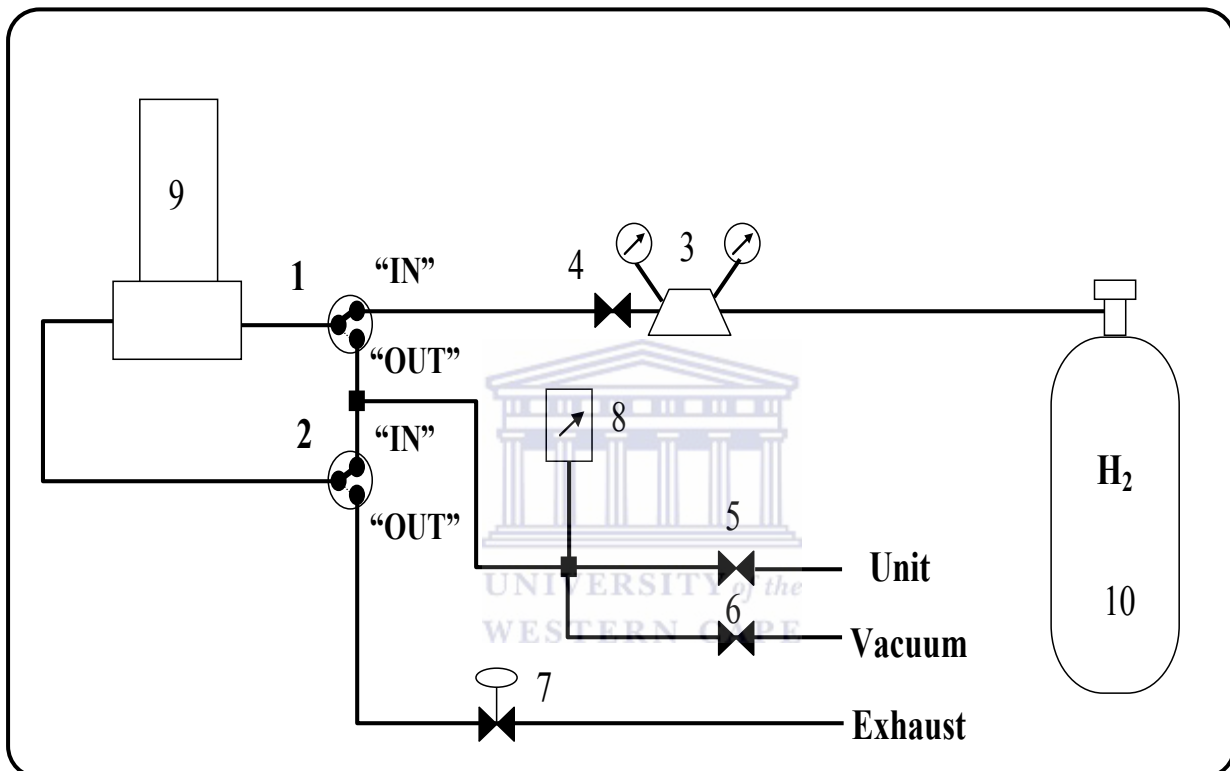


Figure 3.13: Schematic diagram of the set up for testing of hydrogen storage units. 1, 2 = 3 way ball valve (MFC input and output); 3= Reducer / charge pressure regulator; 4 =Shut-off stem valve; 5, 6 = Shut-off ball valves; 7 =Relief valve / discharge pressure regulator; 8 = Pressure sensor 0–100 bar; 9 = Mass flow controller 0–50 L H_2 / min; 10 = Hydrogen cylinder.

The absorption and desorption flow rates were controlled/monitored with a flow controller. The H_2 gas pressure was measured with a pressure gauge. The desired charging pressure could be set with a pressure regulator during absorption, while a relief valve was used to

control the discharge pressure. This made it possible to measure absorbing/desorbing H₂ flow rates and the corresponding gas pressure. Water bath was used as a heat source for heating/cooling of the unit. The hydrogen storage unit was tested in order to know the ability of the reactor to transfer heat in and out of the metal hydride bed.

3.4 CONCLUSION OF THE METHODOLOGY.

The AB₅ type alloys having the composition La_{1-x}Ce_xNi₅ (x=0-0.2) were prepared by arc melting.

The structural features and surface morphology of starting material AB₅ metal hydride-forming alloy was characterised using selected techniques. The selection of techniques was presented in terms of a review of the properties of interest and analytical considerations and the fundamental principles behind each technique. The techniques used in this work included XRD, SEM, EDS, AAS and BET. Therefore, starting material AB₅ metal hydride-forming alloy was surface modified with Pd using electroless deposition technique. The amount of Pd deposited on the material was characterised through qualitatively and quantitatively analyses using EDS and AAS, respectively. Volumetric measurements for hydrogen kinetic analysis and construction of the PCT diagrams were also investigated and their operation conditions were provided. The observed experimental PCT data was smoothed by fitting with phase equilibria model. The charge and discharge performances of experimental MH units were investigated using in house MH testing experimental setup.

CHAPTER 4: RESULTS AND DISCUSSION

4.1 SELECTION OF APPROPRIATE METAL HYDRIDE FORMING ALLOY.

The literature review conducted in this study showed for any material to be regarded as suitable metal hydride-forming alloy for metal hydride storage systems should exhibit faster absorption/desorption rate, resistance to surface poisoning and also operate at pressure and temperature range chosen for LT-PEMFC application ($P > 1\text{bar}$, $T < 80\text{ }^\circ\text{C}$). Among metal hydride forming alloys reviewed, AB_2 and AB_5 type alloys shown to be the promising materials for MH storage units due to their fast charge / discharge kinetics and tuneable PCT performances.

4.1.1 COMPARISON OF PERFORMANCES OF TYPICAL AB_2 -AND AB_5 -TYPE ALLOYS.

Earlier, SAIAMC developed an experimental prototype of metal hydride hydrogen compressor [210] using the AB_5 -type alloy ($\text{La}_{0.85}\text{Ce}_{0.15}\text{Ni}_5$) for the first and AB_2 -type alloy ($\text{Ti}_{0.77}\text{Zr}_{0.3}\text{Cr}_{0.85}\text{Fe}_{0.7}\text{Mn}_{0.25}\text{Ni}_{0.2}\text{Cu}_{0.03}$) for the second compression stage. Within this study we evaluated their applicability for LT PEMFC hydrogen storage application on the basis of detailed characterisation results of which are presented in this section. Both metal hydride-forming type alloys were evaluated in terms of phase structural characteristics, surface morphology and elemental composition, hydrogen sorption kinetics and PCT characteristics. Two batches of each alloy were studied to check the reproducibility of the material's performances in the course of their large-scale industrial production. The alloys used for hydrogen compressor [216] were acquired from the Institute for Energy Technology, originally supplied by LabTech Int., Ltd., Bulgaria (AB_5) and Japan Steel Works (AB_2). The

second batches of both AB₅ and AB₂ material were prepared for this study in collaboration with Guangzhou Research Institute of Non-Ferrous Metals, China, as described in **Section 3.2.1**. Results from characterisation (XRD, SEM, TEM, H sorption) of the MH-materials showed that both batches of the each material had almost identical properties. Hence, the MH-materials can be produced on a larger industrially scale that is suitable for high volume production of MH-units for portable and/or stand-alone LT PEMFC applications.

4.1.1.1 Phase-structural characteristics.

Phase identification of AB₂ and AB₅ was carried out using X-ray diffractometry (XRD). The results showed that AB₂ is a single phase (**Figure 4.1**). The lattice periods correspond satisfactory to results reported by Du *et al.* [217]: $a=4.924 \text{ \AA}$, $c= 8.0005 \text{ \AA}$ for the composition Zr_{0.5}Ti_{0.5} (Ni_{0.6}Mn_{0.3}V_{0.1}Cr_{0.05})₂. The lower values calculated in our case (see caption of **Figure 4.1**) are mainly originated from higher contents of titanium having the smaller atomic radius (1.40 Å) than that of zirconium (1.55 Å) [218]; the same tendency was observed in [217] when changing x in Zr_{1-x}Ti_x (Ni_{0.6}Mn_{0.3}V_{0.1}Cr_{0.05})₂ from 0 to 0.5.

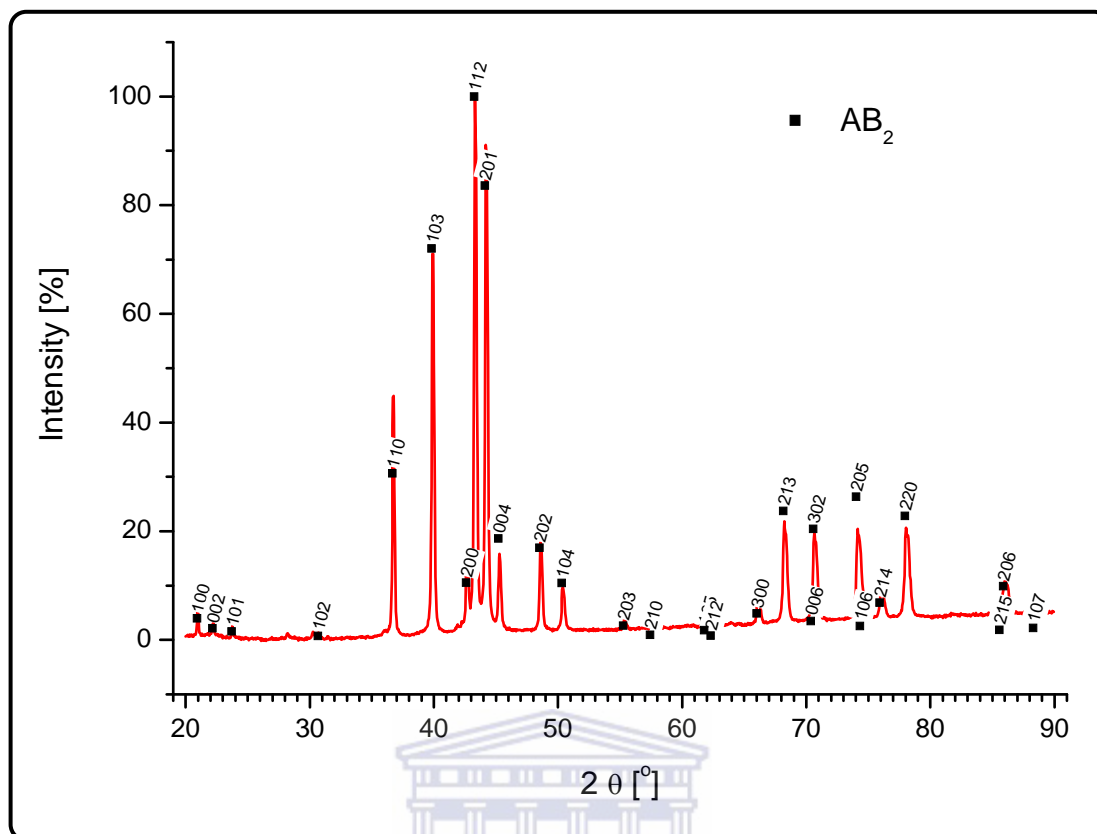


Figure 4.1: Indexed XRD pattern of the AB_2 -type alloy: AB_2 (C14, SG $P6_3/mmc$ (#194); $a=4.8989 \text{ \AA}$, $c=8.0202 \text{ \AA}$)

The XRD results for AB_5 revealed that free nickel is present in AB_5 alloy as a minority phase (**Figure 4.2**). The results are in agreement with ones reported by Lynch and Reilly [219] and Ogawa *et al.* [220]. Presence of nickel is typical for the industrially-produced AB_5 -type alloys, since to avoid the formation of RE-rich phases (e.g. A_2B_7) reducing reversible hydrogen storage capacity of the alloy, the starting charge contains some excess of Ni as compared to the stoichiometric RNi_5 composition [221]. From the other hand, the presence of free Ni on the AB_5 metal surface is expected to play an important role in the acceleration of hydriding kinetics due to its catalytic activity towards hydrogen dissociation / recombination processes.

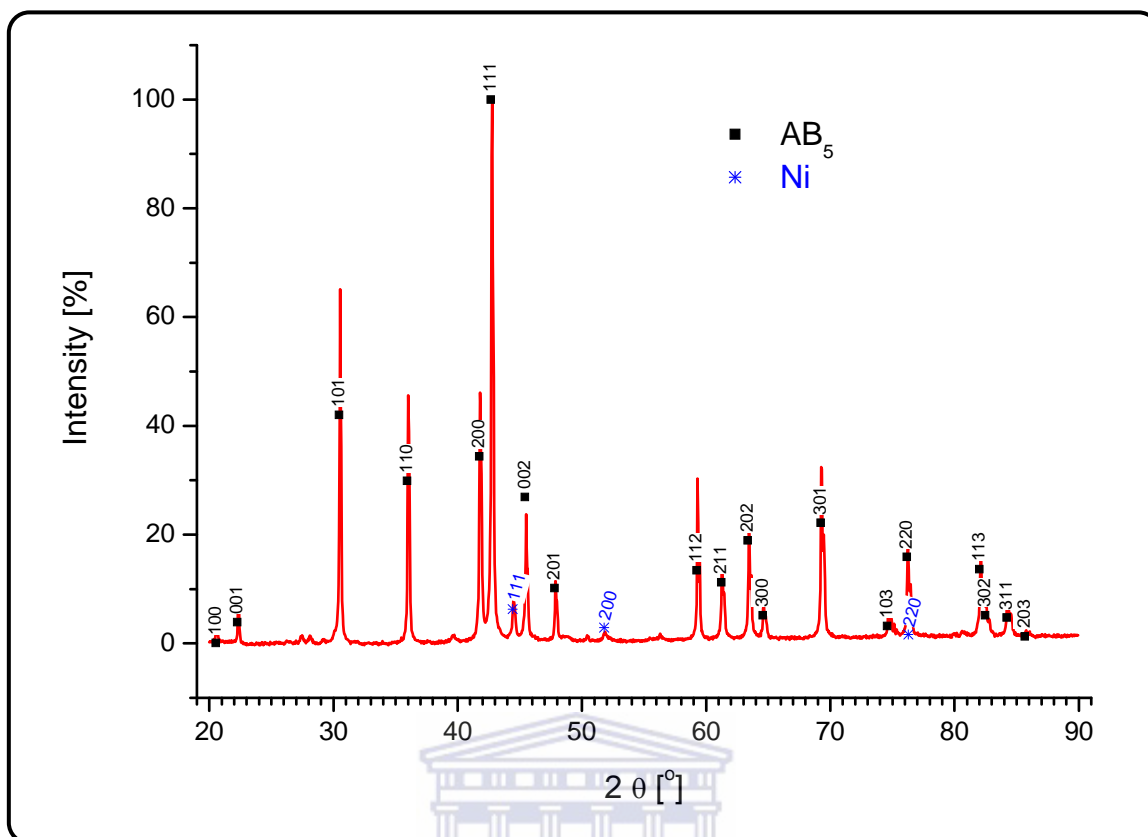


Figure 4.2: Indexed XRD pattern of the AB₂-type alloy: AB₅ (94.08 vol.%; SG *P6/mmm* (#191); $a = 4.9959 \text{ \AA}$, $c = 3.9905 \text{ \AA}$) Ni (5.92 vol.%; SG *Fm $\bar{3}m$* (#225); $a = 3.5283 \text{ \AA}$)

4.1.1.2 *Surface morphology and elemental composition.*

SEM images of AB₂ type alloy are shown in **Figure 4.3 (a)** and **(b)**. The AB₂ alloy powder consisted of particles varying in size (10-80 μm), which generally has irregular shape and relatively smooth surface. It was observed that the alloy particles have particle size \sim 10-80 μm while the majority of the particle exhibited particle size of \sim 20-30 μm .

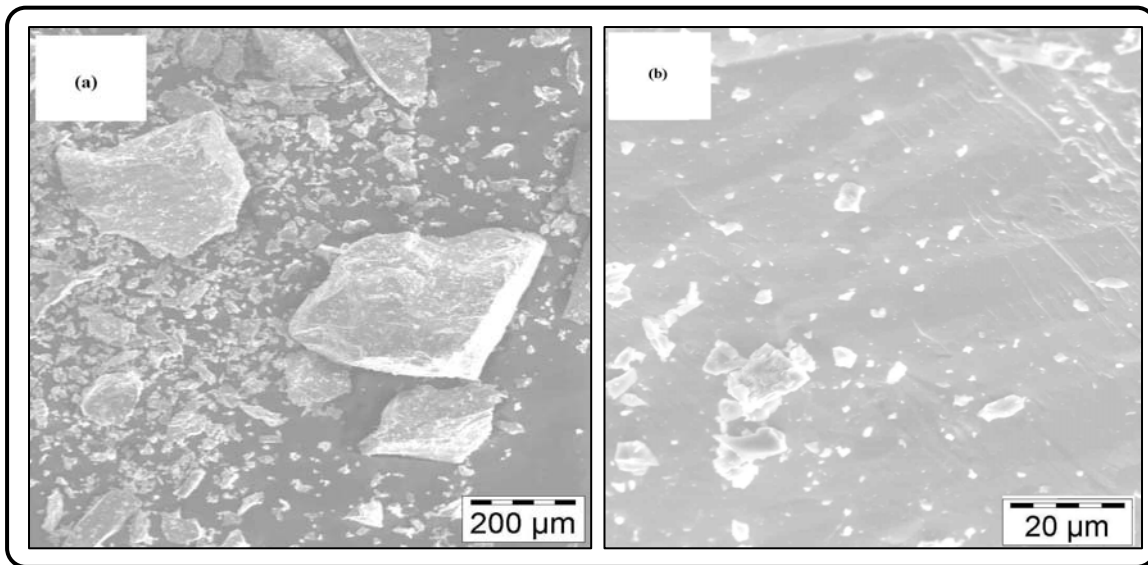


Figure 4.3 SEM images of AB₂ alloys (a) x 100 and (b) x 1100 magnification

Images of the AB₅ hydride-forming alloy are shown in **Figure 4.4 (a)** and **(b)**. The results showed that AB₅ type alloy had similar surface morphology to that of the AB₂ alloy with non porous structure and relatively smooth surface.

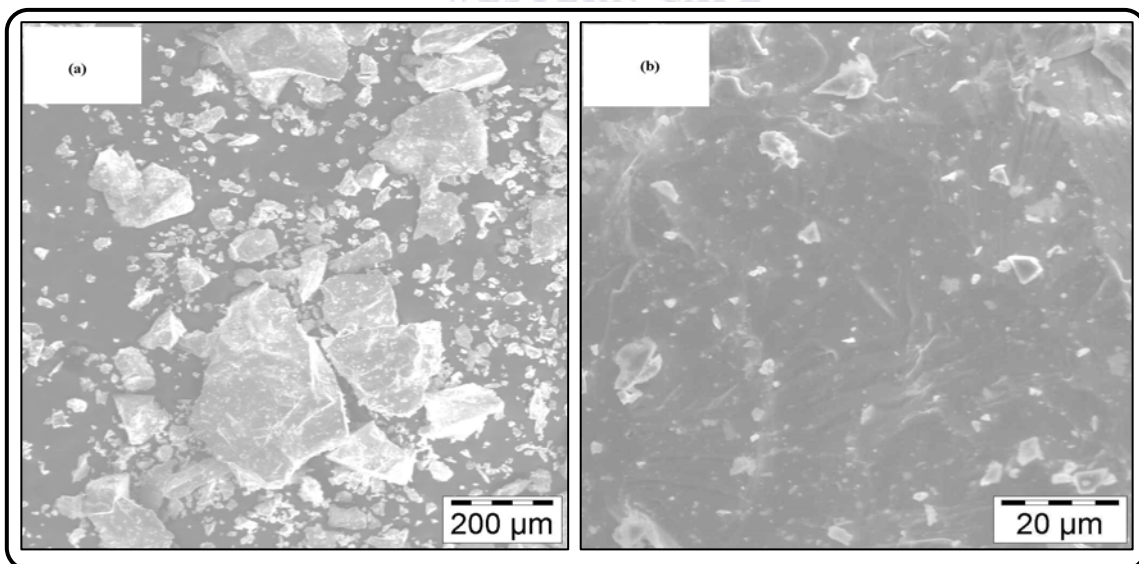


Figure 4.4: SEM images of AB₅ alloy (a) x100 (b) x1100 magnification.

The alloy powder consisted of slightly higher particle size (20-110 μm) compared to that of AB_2 type alloy. It was observed that the majority of the AB_5 alloy particles have particle size $\sim 40\text{-}60\ \mu\text{m}$. The particle size observed was much higher than that obtained by Williams [222] for (La, Ce, Nd, Pr) (Ni, Co, Mn, Al)₅ alloy. This is attributed to different compositions and milling conditions.

The elemental composition of the alloy powders were evaluated using EDS analysis. The EDS results (**Table 4.1 and Table 4.2**) showed a satisfactory correspondence with a target alloy composition (last columns). The EDS results for AB_5 alloy (**Table 4.2**) show some overestimation in Ce-content, most probably, because of enrichment of the alloy's surface with (hydr) oxides of cerium which are known to have higher affinity to oxidation than lanthanum.

Table 4.1: Elemental composition data of AB_2 type alloy

Element	EDS data				Target composition
	Line	Net counts	At%	Wt%	Wt%
Ti	TiK	83.86	21.04	16.88	21.07
Zr	ZrK	4.26	17.93	27.39	15.65
Cr	CrK	89.26	26.04	22.68	25.27
Fe	FeK	57.80	20.59	19.26	22.35
Mn	MnK	23.34	7.37	6.78	7.85
Ni	NiK	13.12	5.83	5.73	6.71
Cu	CuK	2.46	1.28	1.2	1.09
Total		-	100.08	99.92	99.99

Analysis of the dependencies of lattice periods in $\text{La}_{1-x}\text{Ce}_x\text{Ni}_5$ alloys on Ce concentration, x , (see **Section 4.2.1** below) allows us to conclude that the elemental composition of the AB_5 alloy is closer to the target formula $\text{La}_{0.85}\text{Ni}_{0.15}\text{Ni}_5$ rather than one resulted from the EDS data (**Table 4.2**). Taking into account rather low precision of the EDS analysis (see discussion in **Section 3.3.2** above), we consider this discrepancy as insignificant.

Table 4.2: Elemental composition data of AB_5 hydride-forming alloys

Element	EDS data			Target composition	
	Line	Net counts	At%	Wt%	
La	LaL	43.27	12.86	24.58	27.30
Ce	CeL	15.12	4.51	8.69	4.86
Ni	NiK	158.78	82.63	66.73	67.85
Total		-	100	100	100.01

UNIVERSITY of the
WESTERN CAPE

4.1.1.3 *Pressure-Composition Temperature characteristics.*

Figure 4.5 represents the absorption PCT data of AB_2 and AB_5 type alloys ($T=300$ K) constructed by the processing experimental PCT data obtained during the development of the prototype MH compressor [216] using the model [213]. As it can be seen, at $P < 50$ bar both alloys exhibited identical maximum hydrogen capacity in the range of 120 -140 ccm/g .

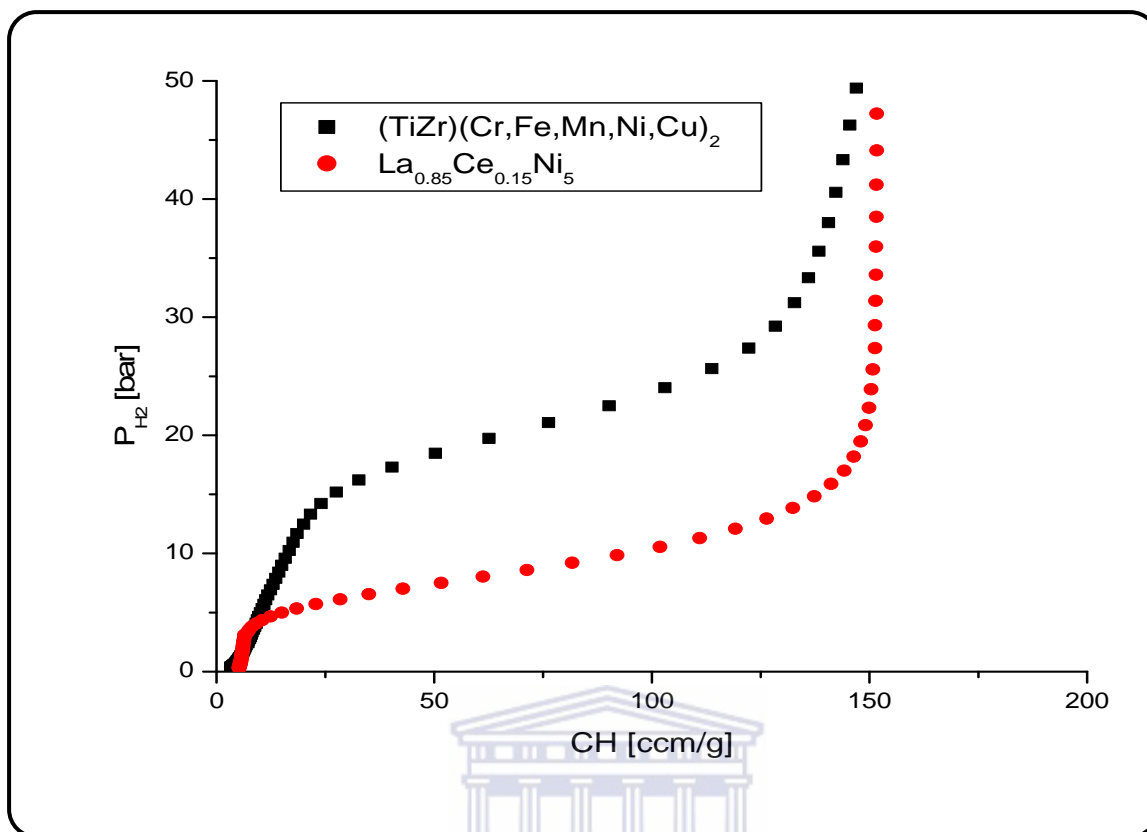


Figure 4.5: Calculated hydrogen absorption isotherms ($T=300$ K) for AB_2 and AB_5 .

As shown in the diagram, the AB_2 alloy exhibited high plateau pressure, above $P \sim 20$ bar in comparison to plateau pressure $P = 5-8$ bar for the AB_5 alloy. The high plateau pressure reduces the width of the plateau which represents the miscibility gap of α and β phases. As a result, total hydrogen capacity is achievable at pressure above $P = 35$ bar for AB_2 type, whereas for AB_5 alloy the capacity can be obtained at lower pressure ($P = 15$ bar). This shows that the AB_5 type alloy can absorb comparatively larger amount of hydrogen at ambient temperature and lower pressure, and thus can be employed as MH material for LT-PEMFC application.

4.1.1.4 Hydrogen absorption kinetics.

Studies of hydrogenation performance of the alloys were conducted using Sievert-type installation. **Figure 4.6** represents absorption kinetics of AB_2 compound before and after activation. It was observed that parent alloy absorbed hydrogen slowly ($H/AB_2 = 0.03$ in 8 hours) even after activation. Slow kinetics is attributed to the formation of ZrO_2 and TiO_2 oxide films on the metal surface behaving as a barrier that inhibits hydrogen dissociation and penetration into the bulk material [223-225]. Eliminating of this barrier (by dissolution of the oxides in the bulk alloy) can be achieved only by the application of several (up to 10) activation cycles including vacuum heating of the alloy followed by hydrogen absorption at room temperature and high (~ 100 bar) hydrogen pressure.

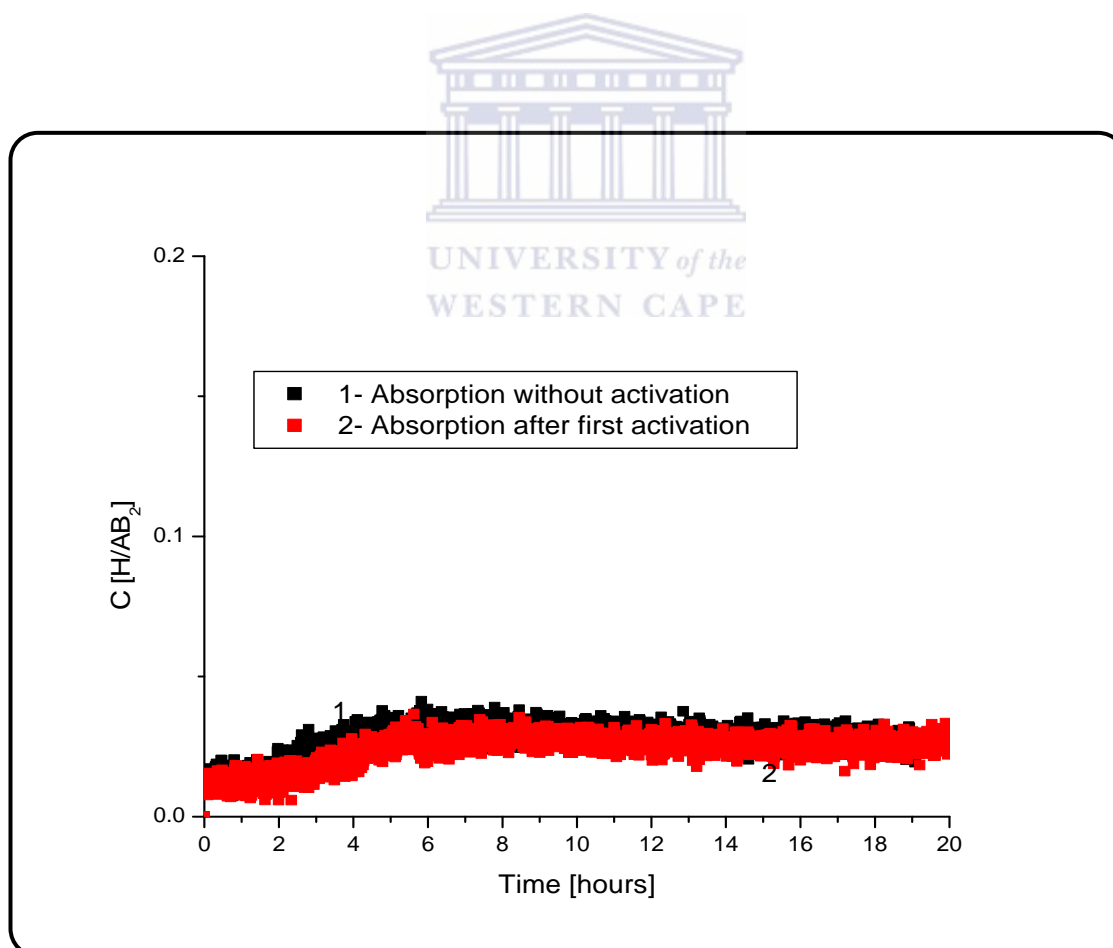


Figure 4.6: Dynamics of hydrogen absorption ($T = 20$ °C, $P_{H_2} = 50$ bar) for AB_2 type alloy.

Hydrogenation performance of air exposed AB₅ type alloy was found to have better hydrogenation performance after activation reaching hydrogen-to-metal ratio H/AB₅=2 (Figure 4.7) as compared to H/AB₅ = 0.75 obtained by Pratt *et al.* [226].

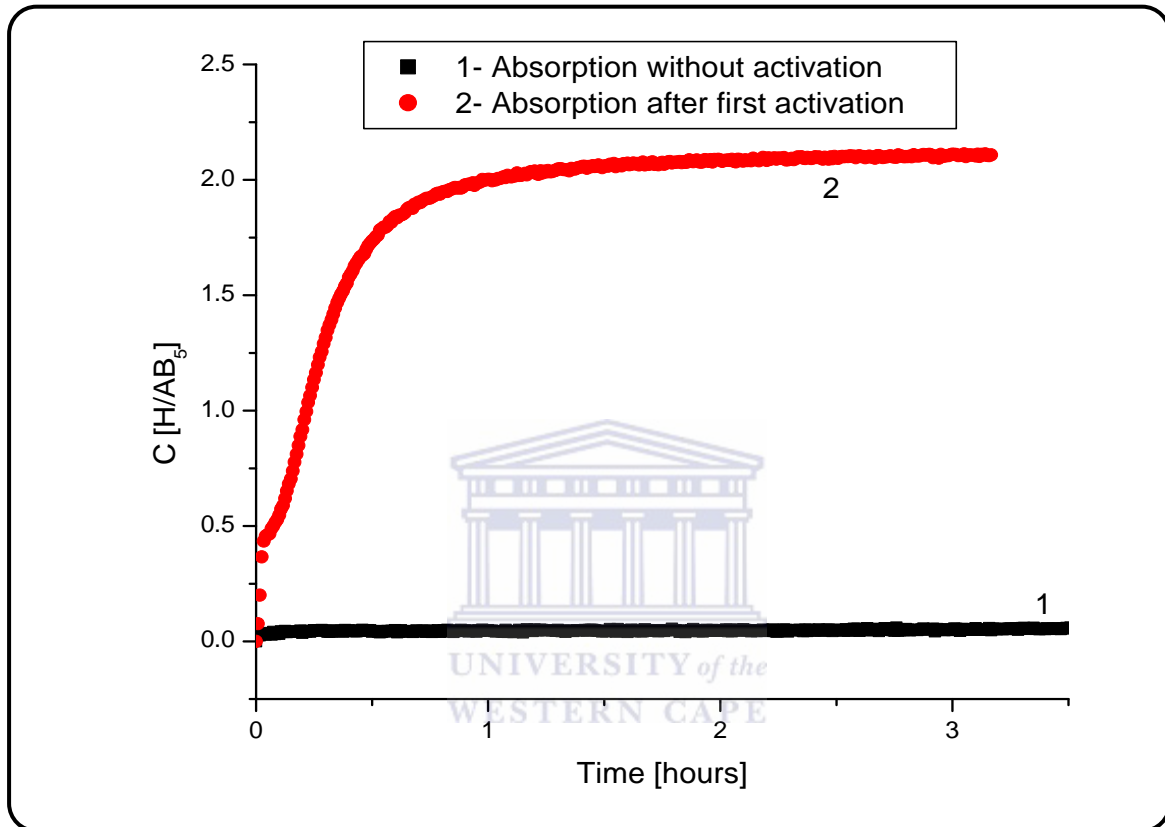


Figure 4.7: Dynamics of hydrogen absorption ($T=20\text{ }^{\circ}\text{C}$, $P_{\text{H}_2}=50\text{bar}$) of AB₅-type alloy.

AB₅ type alloy absorbed hydrogen at faster than AB₂ type alloy after activation. This shows that AB₅ type alloys are easily activated in comparison with AB₂ type alloy. The ease of activation is attributed to the metallic Ni detected from XRD. The complete activation (H/AB₅~6) is achieved in 2-3 activation cycles including vacuum heating of the alloy followed by hydrogen absorption at room temperature and $P_{\text{H}_2}\sim 50\text{ bar}$.

4.1.2 JUSTIFICATION OF SELECTION OF THE AB₅-TYPE ALLOY FOR THE APPLICATION.

Intermetallic compounds: AB₂ and AB₅ type alloys were evaluated in terms of phase structural characteristics, morphologies and elemental composition, thermodynamic characteristics and hydrogenation sorption properties for selection of the suitable material for optimisation of MH storage unit. AB₅ type alloy was identified as a suitable material for the application because of its easiness of activation due to the catalytic activity of metallic Ni observed as a minority phase by XRD which facilitated H₂ dissociation process. On the analysis of thermodynamic characteristics, AB₅ shows better behaviour at reasonable pressure – temperature conditions.

4.2 PREPARATION AND ADVANCED CHARACTERISATION OF AB₅ TYPE MATERIAL FOR THE APPLICATION

4.2.1 INTERRELATION BETWEEN COMPOSITION, STRUCTURE AND THERMODYNAMIC CHARACTERISTICS OF HYDROGENATION FOR La_{1-x}Ce_xNi₅ INTERMETALLICS

The effect of variation of Ce content on the structure of AB₅ type alloy was evaluated. **Figure 4.8** represents the XRD pattern of La_{1-x}Ce_xNi₅ alloy. It can be observed that, except for small amounts of impurity phase including metallic Ni, all the alloys consisted of LaNi₅ phase with a CaCu₅-type hexagonal structure. The presence of Ni in some samples (x=0.15, 0.2; **Figure 4.8 (c) and (d)**) may be due to inhomogeneity of the parent alloy.

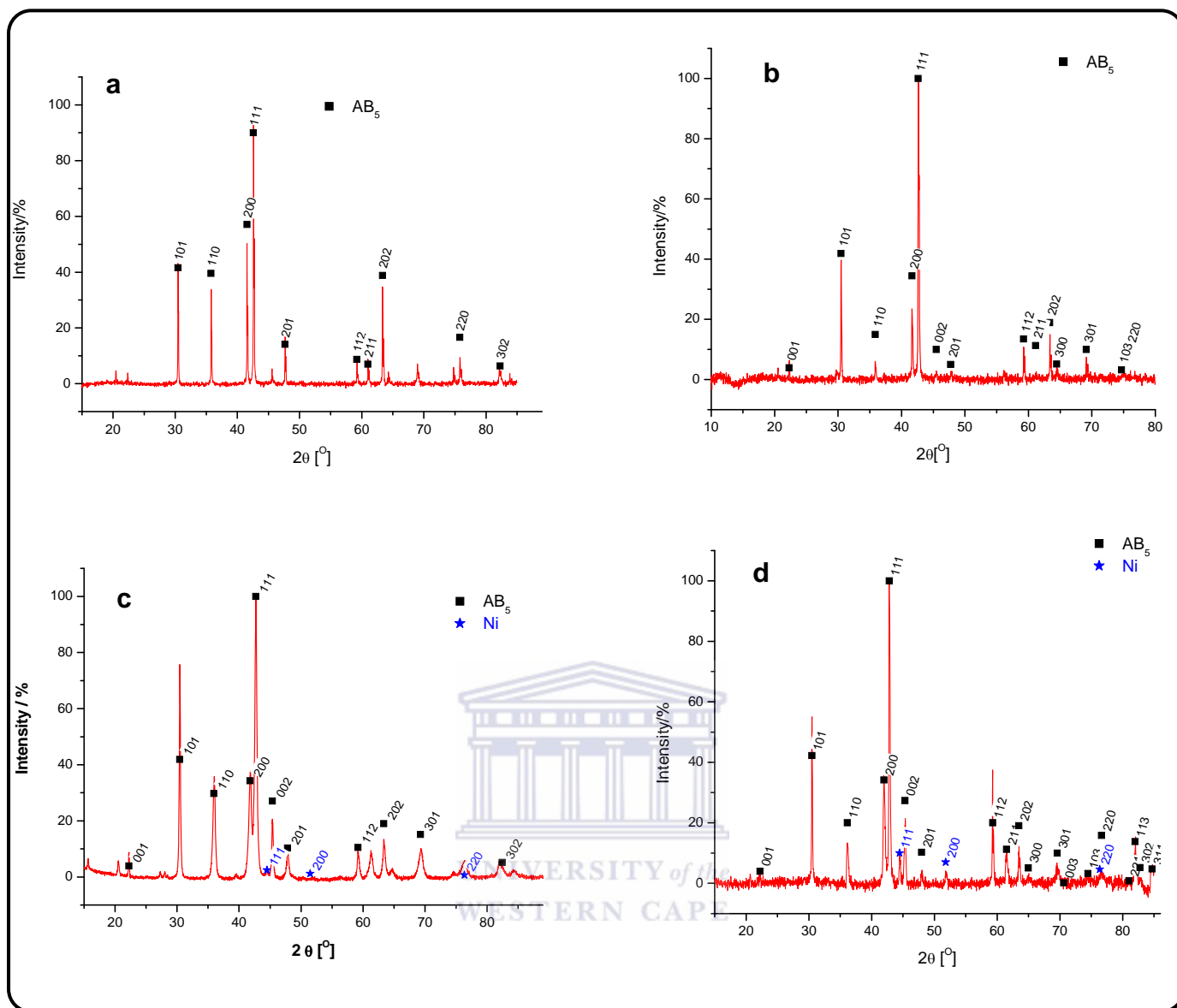
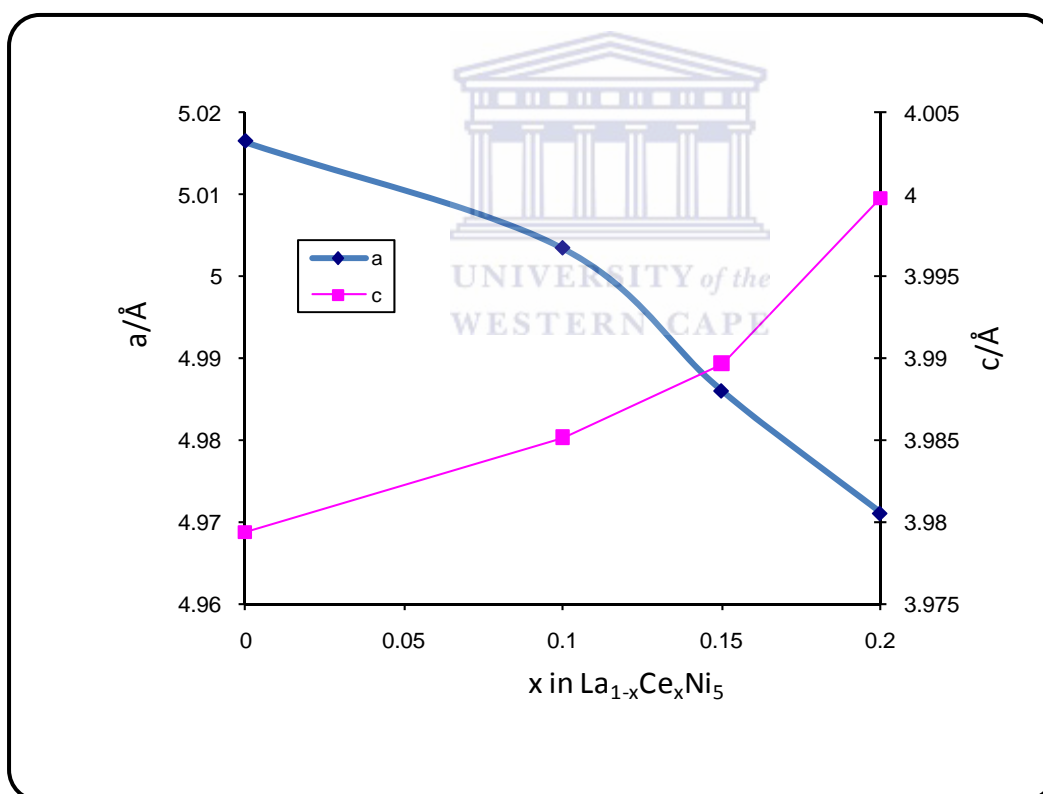


Figure 4.8: XRD pattern of $\text{La}_{1-x}\text{Ce}_x\text{Ni}_5$ when (a) $x=0$, (b) $x=0.1$, (c) $x=0.15$ and (d) $x=0.2$.

The calculated values of cell parameters from XRD results are listed in **Table 4.3**. It can be observed that increase of Ce content in the A site of the alloy results in decrease of parameter a and the cell volume remarkably, while the parameter c and c/a ratio increases slightly (**Figure 4.9** and **4.10**). This is in agreement with the result reported by Yuan *et al.* [227].

Table 4.3: Lattice parameters of $\text{La}_{1-x}\text{Ce}_x\text{Ni}_5$ alloy.

Parameters	x in $\text{La}_{1-x}\text{Ce}_x\text{Ni}_5$			
	0.0	0.1	0.15	0.2
$a/\text{\AA}$	5.0165	5.0035	4.9861	4.9712
$c/\text{\AA}$	3.9794	3.9852	3.9897	3.9998
c/a	0.793262	0.796482	0.800164	0.804594
$V/\text{\AA}^3$	86.727	86.404	85.9	85.604

**Figure 4.9:** Calculated lattice parameters with x value in $\text{La}_{1-x}\text{Ce}_x\text{Ni}_5$ alloys

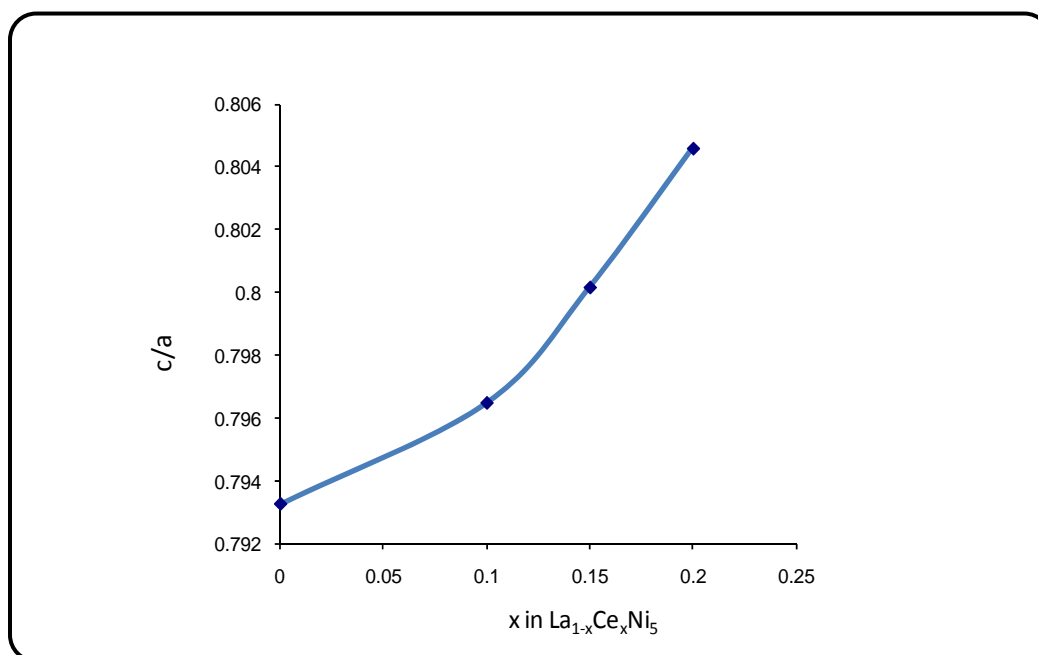


Figure 4.10: Dependence of c/a ratio on x value in $\text{La}_{1-x}\text{Ce}_x\text{Ni}_5$ alloys.

By plotting the cell volume against the x value of $\text{La}_{1-x}\text{Ce}_x\text{Ni}_5$ alloy, the cell volume of the alloy is found to decrease linearly with x value from 0 to 0.2 (**Figure 4.11**).

The shrinkage of unit cell with high Ce content and decrease in parameter a can be ascribed to its particular electron structure $4f^15d^16s^2$, and this leads to Ce element often having two different contributions (i.e. coexistence of Ce^{3+} , Ce^{4+}). As reported by [228-230], about 30% of Ce element is at four-valence state thus resulting in smaller average atomic radius of Ce (1.73Å) than that of La (1.87Å). Moreover, the anisotropic changes in lattice parameters can be attributed to lack of symmetry in 4f orbit of Ce atoms. However, the lattice parameter c was less affected by the cerium radius change since it depends essentially on radius of Ni.

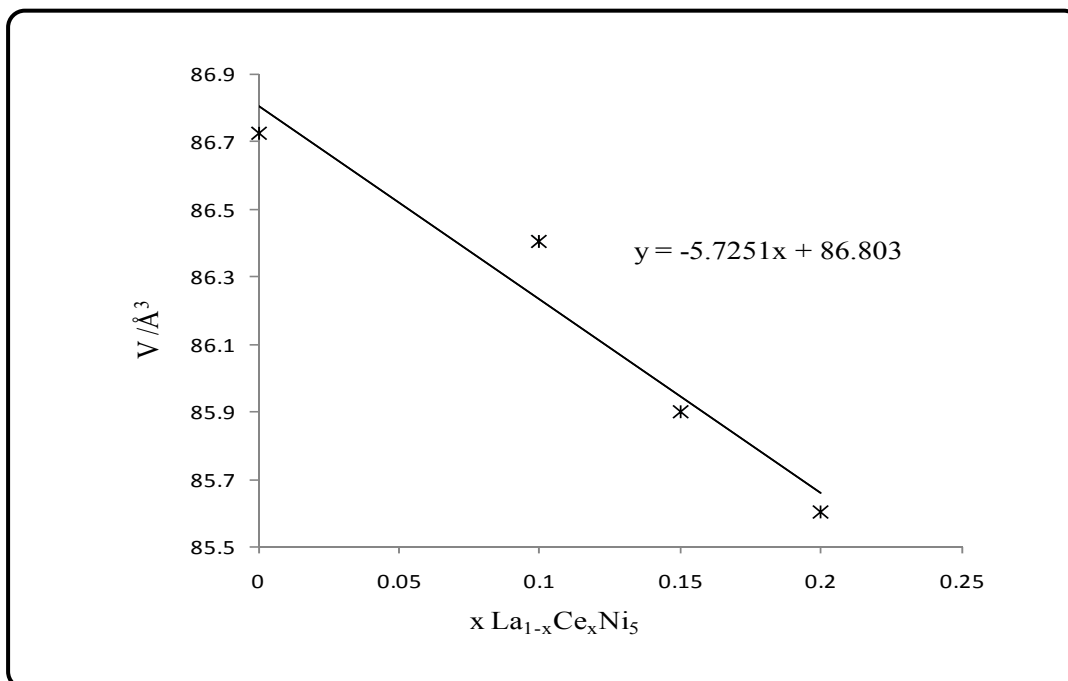


Figure 4.11: Relation of cell volume with x value in $\text{La}_{1-x}\text{Ce}_x\text{Ni}_5$ alloy

These results prove that the replacement of Ce for La in the alloy is successful, and this forms the fundament of the comparative evaluation of the thermodynamic characteristics of the partially substituted alloys.

Changes in the thermodynamic characteristics of the studied AB_5 -type alloys could be estimated from known thermodynamic data for other AB_5 -based hydride-forming alloys, where La is substituted with Ce [231]. Since similar data for hydride formation entropies (ΔS) are unavailable, a typical value of $\Delta S = -110 \text{ J}/(\text{mole H}_2 \text{ K})$ was assumed as a fixed value.

Figure 4.12 represents change of in hydride formation enthalpy (ΔH) and the equilibrium pressure (P_{eq}) in variation of Ce content in the alloy. It has been found that the increase in Ce content results in the increase of the equilibrium pressure.

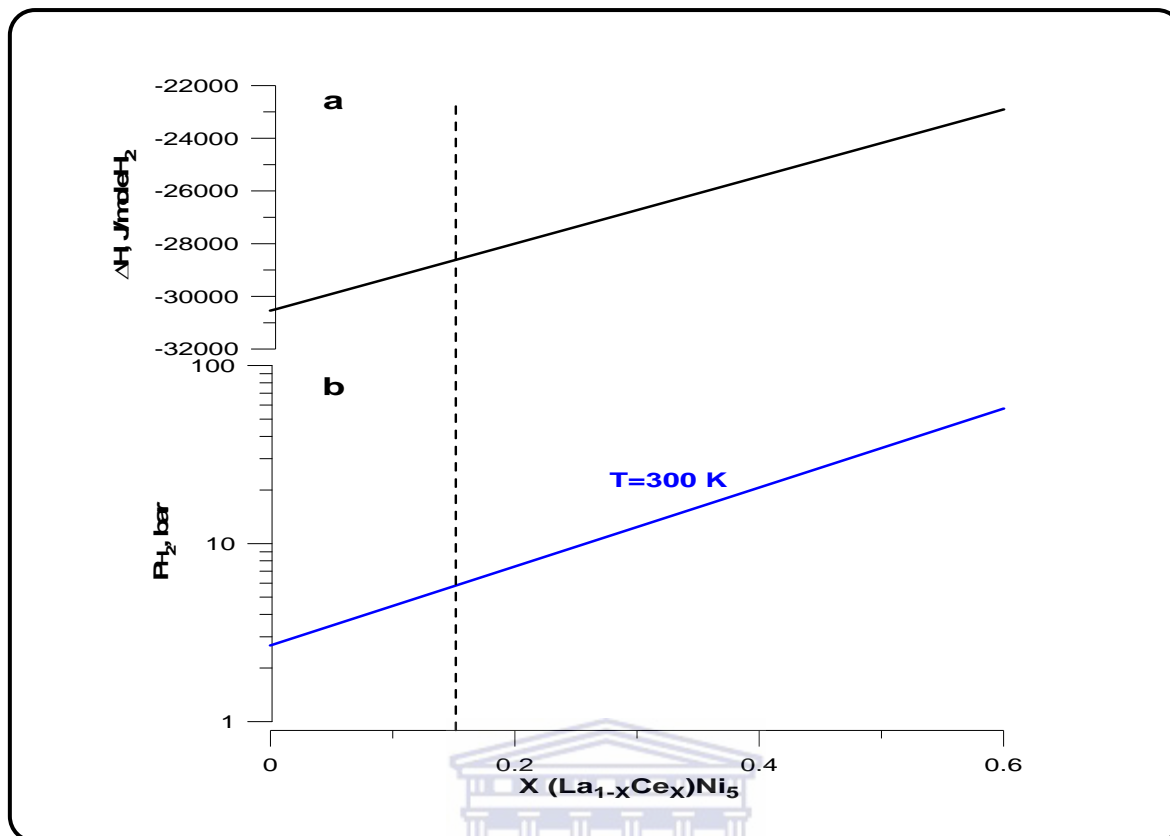


Figure 4.12: Estimated enthalpies of hydride formation for cerium-substituted intermetallide LaNi_5 (a) and corresponding values of equilibrium hydrogen pressure at room temperature (b) calculated assuming the entropy of the hydride formation equal to $-110 \text{ J}/(\text{mole H}_2\cdot\text{K})$

Enthalpy of hydride formation (ΔH), which is regarded as the important thermodynamic property gives an indication of the thermal stability of the alloy material. It was found that ΔH decrease with the increase in Ce concentration leading to a decrease in thermal stability of the corresponding hydride.

The dependence of ΔH with cell volume from literature was compared to the experimental values obtained from $\text{La}_{0.85}\text{Ce}_{0.15}\text{Ni}_5$ alloy (**Table 4.4**). It is seen that the increase in cerium

concentration results in the lowering unit cell volume and decrease of the hydride thermal stability. This correlation is similar to one observed by Yoshikawa *et al.* [232] where it was shown that the increase of size of interstitials available to host H-atoms in the metal matrix (actually, taking place when the unit cell volume increases) results in the increase of the hydride stability.

Table 4.4: Enthalpy and unit cell volume of x in $\text{La}_{1-x}\text{Ce}_x\text{Ni}_5$ alloy.

x Ce	$\Delta H/\text{kJmol}^{-1}\text{H}_2$	$V/\text{\AA}^3$
0	30	86.727
0.1	26	86.404
0.15	24.6	85.9
0.2	25.3	85.604

Based on the thermodynamic properties and enthalpies given in **Table 4.4**, it was observed that the $\text{La}_{0.85}\text{Ce}_{0.15}\text{Ni}_5$ alloy requires lower amount of energy than the parent LaNi_5 intermetallide, to initiate the expulsion of absorbed hydrogen. It was also deduced that the composition $\text{La}_{0.85}\text{Ce}_{0.15}\text{Ni}_5$ can give an equilibrium pressure at room temperature of about 5bar, which satisfies the pressure requirements of the given application.

4.2.2 PHASE COMPOSITION AND LATTICE PERIODS OF THE CONSTITUENT PHASES FOR $\text{La}_{0.85}\text{Ce}_{0.15}\text{Ni}_5$ ALLOY AND ITS HYDRIDE.

Figure 4.13 shows the XRD-pattern (Cu-K α) of the product of hydrogenation of the $\text{La}_{0.85}\text{Ce}_{0.15}\text{Ni}_5$ alloy. The hydrogenation was carried out in a Sieverts setup at a H_2 pressure of 50 bar and room temperature, followed by stabilization of hydride phase by the exposition of the hydrogenated material on air at the liquid nitrogen temperature. The product after hydrogenation was found to be a two-phase containing AB_5H_x hydride (70 vol. %), and α -solid solution $\text{AB}_5\text{H}_{\sim 0}$ (30 vol. %) (**Figure 4.13**).

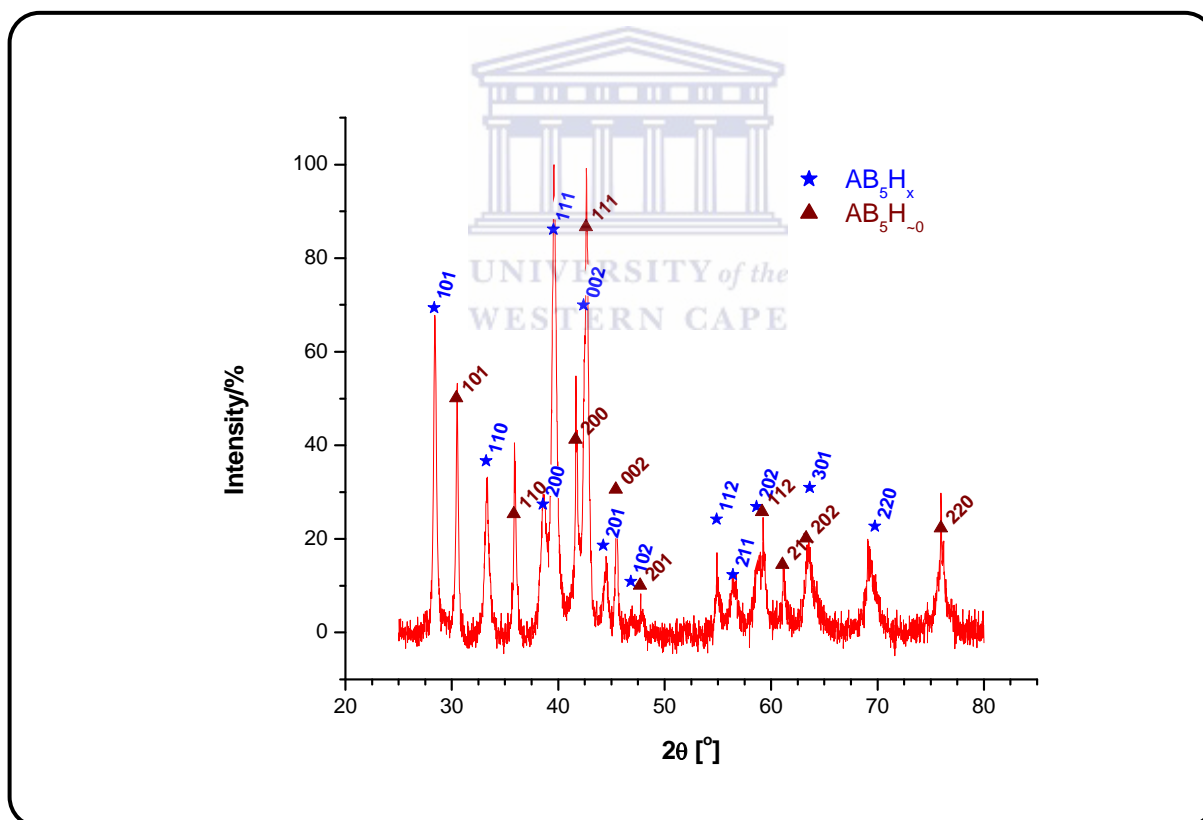


Figure 4.13: XRD pattern of AB_5H_x

The appearance of the α -phase is most probably caused by decomposition of the unstable β -hydride during carrying of the sample to the diffractometer and XRD measurement. As seen in **Figure 4.13**, the diffraction peaks shifted to smaller angles, implying an increase in the lattice parameters upon hydrogenation of AB_5 alloys as presented in **Table 4.5**. The increase in the cell volume is caused by the occupation of the interstitial sites of the alloy by hydrogen; the volume expansion upon hydrogenation was calculated to be of 24.2 % that fits well to the typical range (20–25%) reported by Dantzer [233].

Table 4.5: The unit cell constants and cell volumes of AB_5 alloy and hydride

Sample	a(Å)	c(Å)	V (Å ³)	Density (g/cm ³)
AB_5 alloy	5.0070	3.933	86.592	8.293
AB_5 hydride	5.391	4.236	107.133	6.703
Volume expansion calculated from the cell volumes of alloy and its hydride ($\Delta V/V_0$) = 24.2%				

The volume expansion upon hydrogenation is a very important parameter affecting to safe operation of MH containers. For the H storage materials whose hydrogenation, as a rule, is accompanied by significant volume increase ($\Delta V/V_0=24.2\%$ in our case), packing density of the material is the critical safety issue, because of generation of stresses in an alloy bed and deformation or destruction of the container, since the material expands when it absorbs hydrogen. As it was experimentally observed in [234] using AB_5 alloys, when the packing fraction of the hydride is higher than 61 vol. %, the significant stresses of the container's wall are observed. The stresses did not only increase with each hydrogen absorption / desorption cycle, but also continued to increase even after plastic deformation of the vessel, reaching 2-3 kbar after 100-150 cycles. The mechanism for stress accumulation was estimated as a two-step process in which agglomeration between the hydride particles occurs when the packing

fraction of hydride is higher than 61 vol. % in the initial cycles (Step 1), and then fine powder generated by pulverization during the cycles falls in gaps at the bottom of the vessel and causes the hydride packing fraction at the bottom of the vessel to gradually increase (Step 2). This mechanism seems to be universal for all solid-state hydrogen storage materials changing their volume and pulverizing in the course of hydrogenation / dehydrogenation. That is why we assume 60% as the allowed packing fraction for the hydrogenated material, i.e. **the packing density must not exceed $6.703 \times 0.6 = 4.02 \text{ g/cm}^3$** .

4.2.3 MORPHOLOGIES AND SPECIFIC SURFACE AREAS FOR STUDIES OF $\text{La}_{1-x}\text{Ce}_x\text{Ni}_5$ ALLOY AND ITS HYDRIDE.

Figure 4.14 represents SEM of AB_5 before and after exposure to 4 charge/discharge cycles. From **Figure 4.14** (a) it can be seen that AB_5 type alloy exhibited large particles whereas after exposure to several absorption and desorption cycles, disintegration of AB_5 alloy into small fine particles were observed as seen in **Figure 4.14** (b).

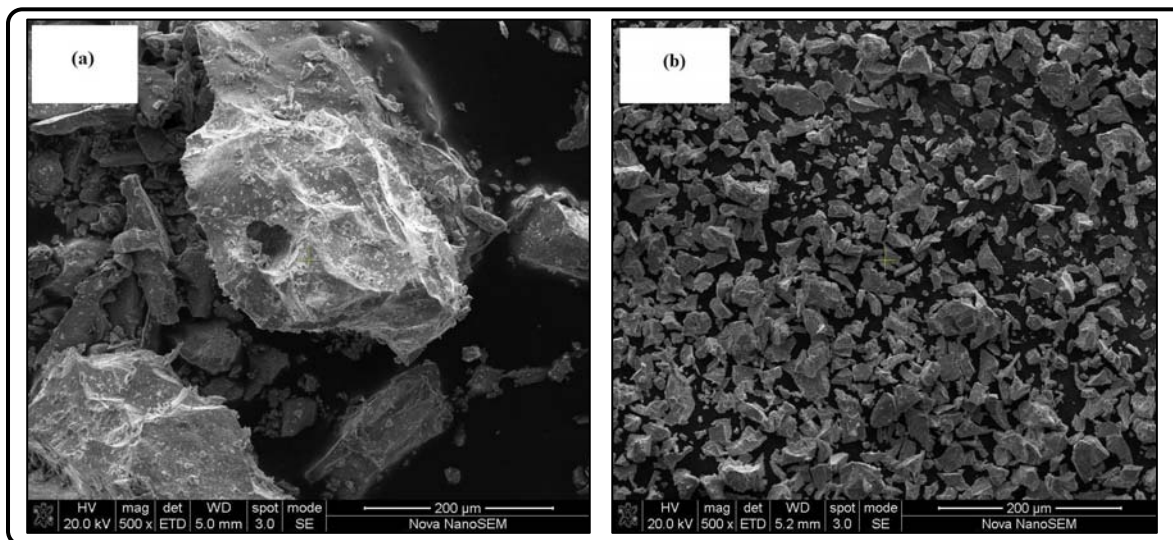


Figure 4.14: SEM images of AB_5 alloy (a) before hydrogenation and (b) after hydrogenation.

Particle size distribution of unhydrogenated AB₅ type alloy was investigated using Carl Zeiss Axiovision software. It was observed that the metal alloy consisted particle size in the range of 20-140 μm with majority having particle size of ~40-60 μm (**Figure 4.15**). The BET surface area of the alloy powder was found to be 0.1520 m²/g.

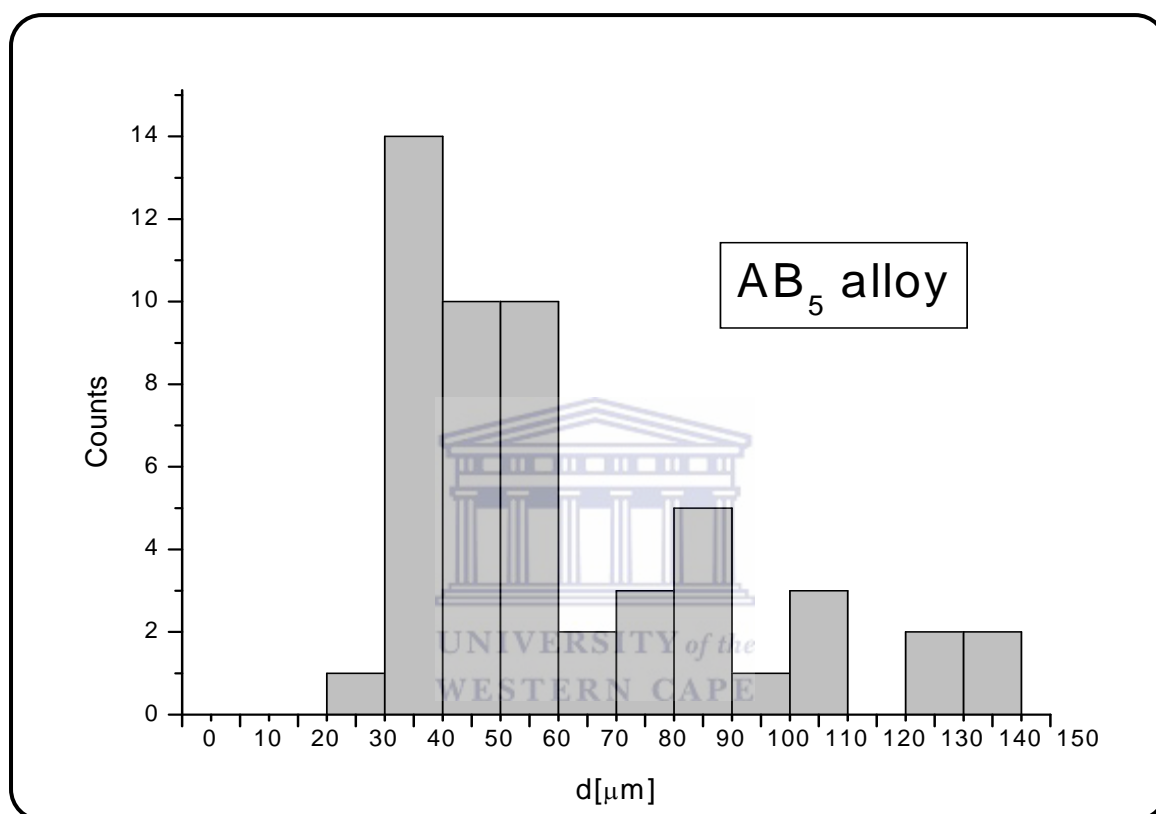


Figure 4.15: Particle size distribution of AB₅ type alloy before hydrogenation.

After hydrogenation the metal alloy pulverised into small particles exhibiting particle size of 10-50 μm with majority having particle size in the range of 20-30 μm as seen in **Figure 4.16**. The disintegrated AB₅ alloy exhibited higher BET surface area of 0.3800 m²/g, or 2.5 times larger than for the unhydrogenated AB₅ type alloy.

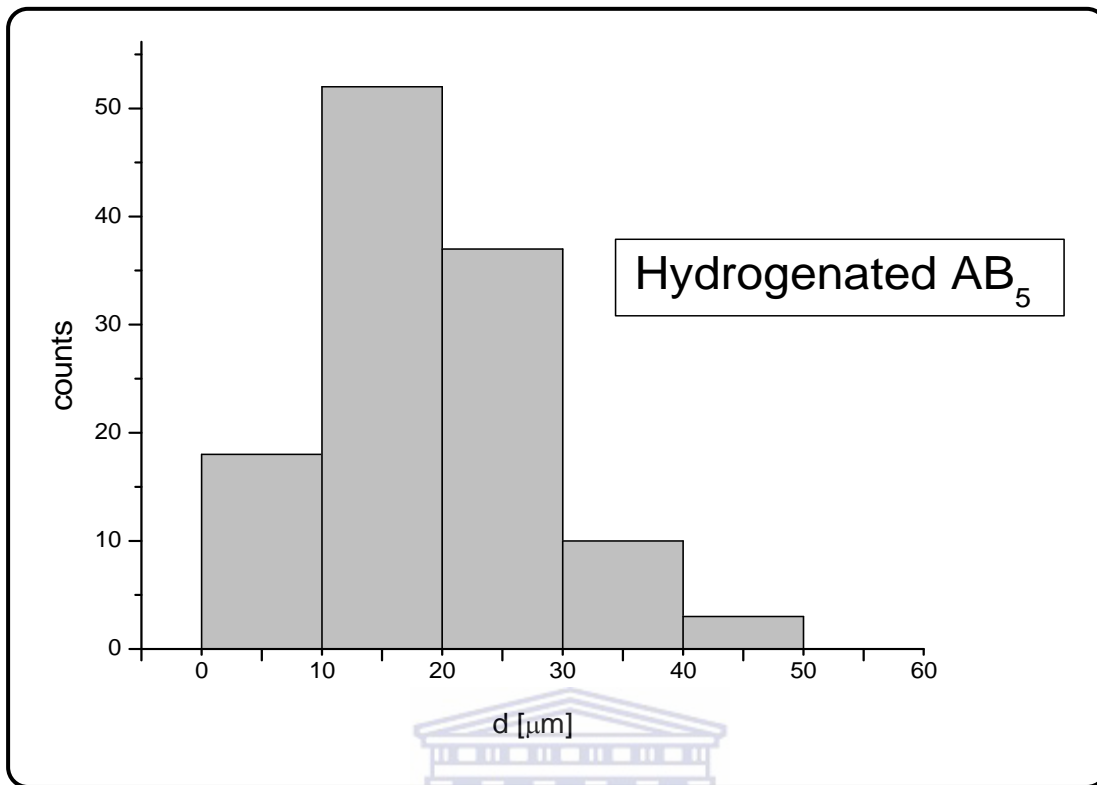


Figure 4.16: Particle size distribution of AB_5 alloy after exposure to charge/discharge cycles.

The disintegration of AB_5 type alloy is attributed to combination of significant volume increases during hydriding and corresponding decreases during dehydriding and the brittle nature of the hydride. This must be carefully considered during container design and construction because fine powder if not confined can migrate and interfere with the operation of moving parts such as valves. As a result, these decrepitated particles may entrained in the gas stream causing imperfect gas permeability and this will lead to gas impedance and poor heat and mass transfer.

4.2.4 HYDROGEN SORPTION CHARACTERISTICS OF $\text{La}_{0.85}\text{Ce}_{0.15}\text{Ni}_5$ ALLOY

4.2.4.1 *Activation and hydrogen absorption kinetics.*

AB_5 type alloys are easy to activate in comparison to other intermetallic compounds but the problem lies with longer incubation time needed to reach maximum hydrogen capacity or full activation. Therefore influence of palladium on the activation and hydrogen sorption properties was studied. Pd deposition was carried out using electroless plating technique. The influence of the water-soluble organic aminosilane (γ -APTES) was evaluated by pretreating/functionalising AB_5 sample prior deposition while the other (non-functionalised) sample was surface modified with Pd using conventional plating technique.

The morphological studies were carried out using HR-SEM due to smaller particles size of Pd, usually in the nano-range scale. Unmodified AB_5 type alloy was used as a reference material. **Figure 4.17** represents SEM images of unmodified **(a)**, Pd coated **(b)**, and γ -APTES pre-treated and Pd coated **(c)** $\text{La}_{0.85}\text{Ce}_{0.15}\text{Ni}_5$ alloy. **Figure 4.17 (a)** shows that unmodified AB_5 consists of clean smooth surface whereas Pd particles were observed on the AB_5 metal surface plated with Pd (**Figure 4.17 (b,c)**). The presence of Pd particles is expected to improve kinetics of AB_5 type alloy during hydrogenation. **Figure 4.17 (c)** presents the surface morphology of the functionalised AB_5 alloy with γ -APTES followed by electro-less deposition of Pd. In agreement to Williams *et al.* [116], Pd particles are uniformly distributed on the metal surface in comparison with randomly-distributed discontinuous coating of the non- functionalised AB_5 metal alloy **Figure 4.17(b)**.

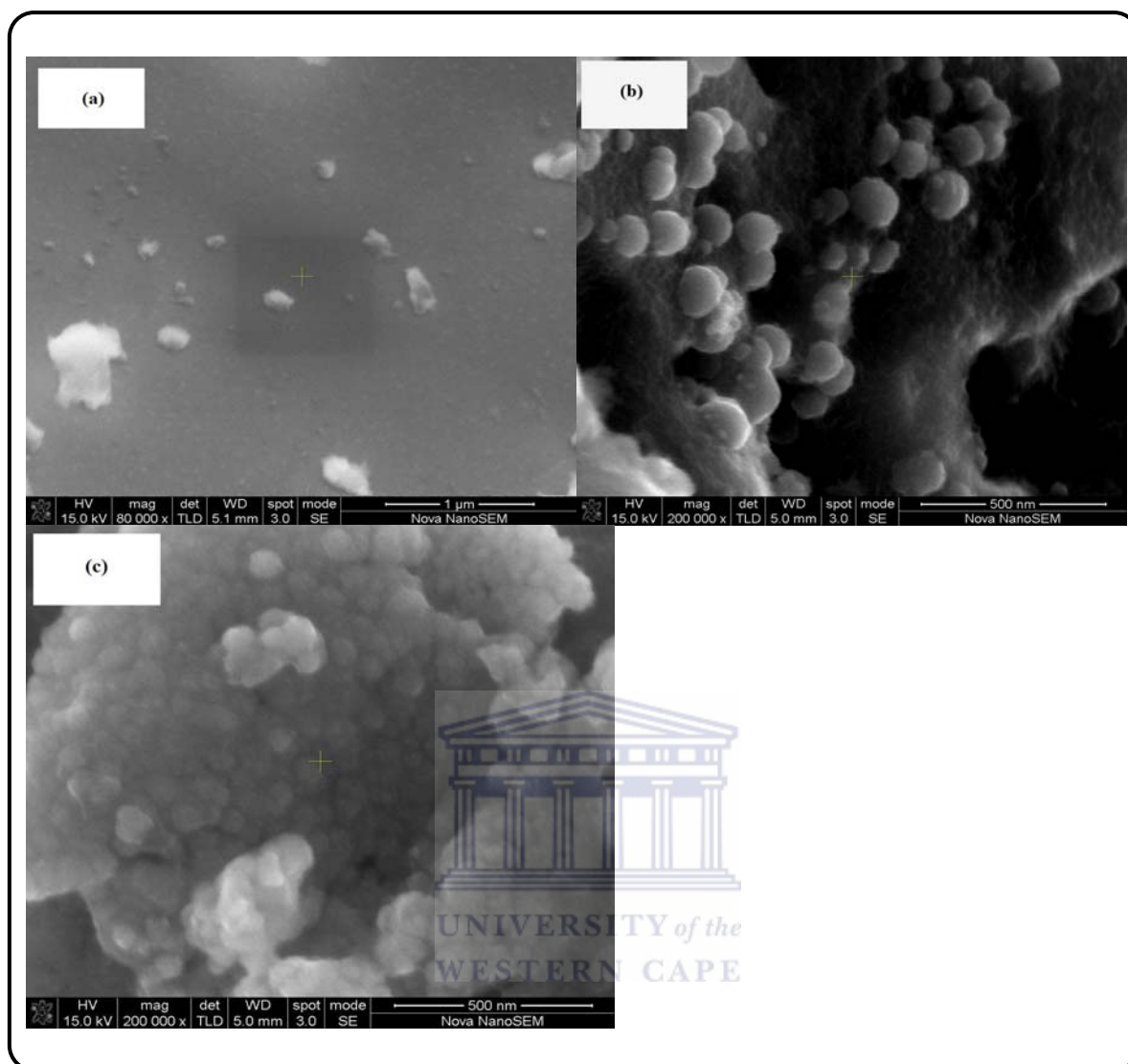


Figure 4.17: SEM images of (a) unmodified AB₅, (b) AB₅-Pd (c) AB₅ (γ-APTES) Pd.

The surface Pd loading of functionalised and non functionalised surface modified AB₅ was estimated using EDS. It was observed that the functionalised AB₅ showed Pd peak at very low intensity compared to non- functionalised as seen in **Figure 4.18 (a)** and **(b)**. This was evidence of high Pd surface loading of about 13.60 wt. % on the non- functionalised AB₅ metal surface whereas for functionalised AB₅ alloy only 2.32 wt. % was obtained (**Table 4.6**).

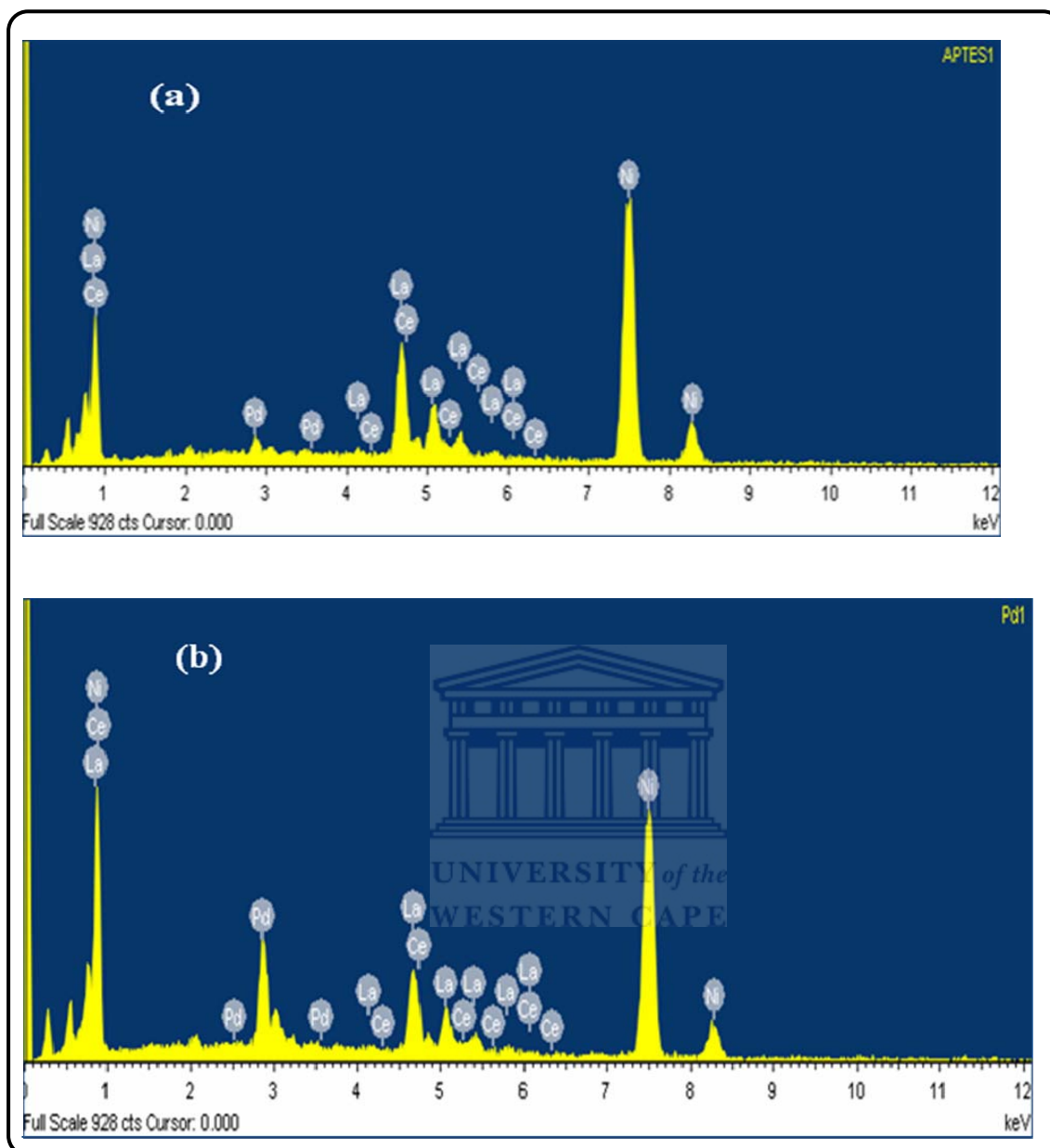


Figure 4.18: EDX spectrum of (a) AB_5 (γ -APTES) Pd and (b) AB_5 -Pd.

Table 4.6: Quantitative elemental composition data for AB₅-Pd and AB₅-(γ -APTES) Pd

Elemental line	AB ₅ (γ -APTES) Pd		AB ₅ -Pd	
	Wt. %	At. %	Wt. %	At. %
Ni K	65.91	81.77	61.26	77.18
Pd L	2.32	1.59	13.60	9.45
La L	26.99	14.15	21.69	11.55
Ce L	4.78	2.49	3.45	1.82

The total Pd loading determined using AAS was found to be 0.45 and 0.66 wt. % for functionalised and non-functionalised AB₅ respectively. Contrary to the finding of Williams *et al.* [116], non-functionalised AB₅ alloy exhibited increased Pd loading than pre-treated AB₅ type alloy. It may be assumed that the higher amount of cerium in the substrate material used in [116] facilitated the Pd deposition due to the formation of Pd-O-Ce chemical bonding. This chemical bonding is generated in the interface of the palladium particles and the metal oxide during the reaction and resulting to a strong contact that causes stabilization of the active cationic Pd [235]. It was also supposed that in our case γ -APTES pre-treatment resulted in the formation of although denser (Fig.4.17 (c)) but thinner coating than for the non-functionalised Pd-plated sample.

Based on the high Pd loading, non-functionalised AB₅ type alloy (without γ -APTES) was chosen for kinetic measurements. The absorption experiments with the same amount of metal hydride powder and charging pressure were preformed to investigate the effect of Pd on the activation and kinetics of the AB₅ type alloy.

Figure 4.19 represents the absorption kinetics of the unmodified and surface-modified AB₅ type alloy without activation. The results show that the unmodified sample for the first cycle exhibited longer incubation period for absorption to occur. This is attributed to the oxide film that forms on the metal surface preventing hydrogen dissociation and penetration into the interstitial sites and thus leading to slow absorption rate. The kinetics of the alloy were similar to the results obtained by Pratt *et al.* [226] where the freshly prepared AB₅-type alloys exhibited slow hydrogen sorption kinetics.

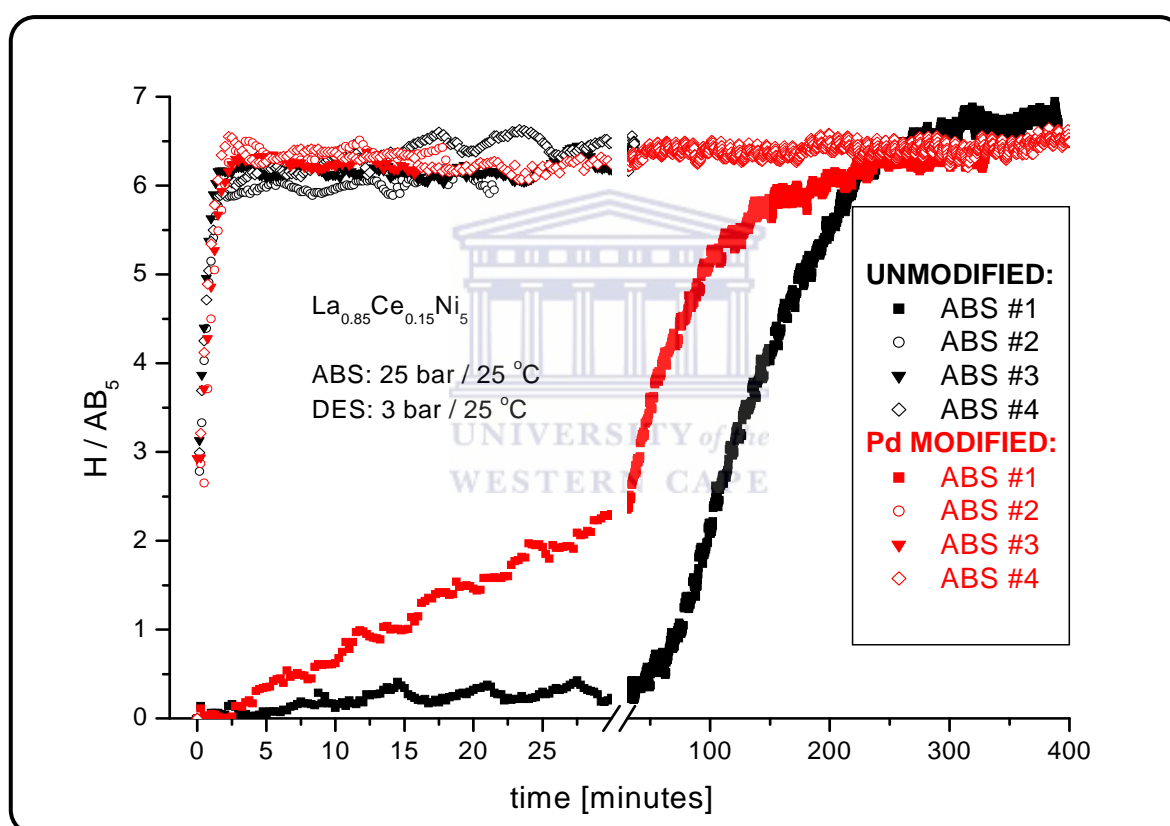


Figure 4.19: Dynamics of hydrogen absorption by the unmodified and surface modified AB₅ type alloy.

However, the incubation period of less than 10 minutes before the absorption of H₂ was observed for surface-modified AB₅ type alloy. This shows that Pd coated AB₅ alloy possesses

good absorption kinetic in comparison of over an hour incubation time for unmodified AB₅-type alloy. It is suggested that Pd mainly acts as a catalyst of hydrogen absorption, consequently, markedly improving initial activation.

For the subsequent charge cycles, both materials exhibited identical behaviour with short reaction time in comparison with first charge cycle due to the complete removal of oxide film leading to a clean fresh metal surface as observed by Shan *et al.* [115].

Kinetic curves were fitted into an experimental data and the parameters were calculated (Table 4.7) according to the following Avrami- Erfoveev Equation:

$$(H / AB_5) = (H / AB_5)_{MAX} \cdot \left\{ 1 - \text{Exp} \left[- \left(\frac{t}{t_0} \right)^n \right] \right\} \quad 4.1$$

Table 4.7: Kinetic parameters obtained by fitting experimental data using Equation 4.1.

Cycle #	UNMODIFIED			MODIFIED (NaH ₂ PO ₂ bath, 0.5 g/L Pd, 30 min 50 °C; ~0.6 wt.% Pd)		
	(H/AB ₅) _{MAX}	t ₀ [minutes]	n	(H/AB ₅) _{MAX}	t ₀ [minutes]	n
1	6.715(6)	153.8(2)	2.237(8)	6.299(5)	62.8(1)	1.072(4)
2	6.021(8)	0.40(1)	0.75(2)	6.180(7)	0.32(1)	0.78(3)
3	6.180(7)	0.32(1)	0.78(3)	6.27(5)	0.54(6)	0.8(1)
4	6.41(1)	0.37(2)	0.51(2)	6.421(2)	0.44(1)	0.83(3)

The index of power, *n*, for the first charge for unmodified and Pd surface-modified AB₅ alloys were found to be 2.237 and 1.072, respectively. This shows that the hydrogen absorption reaction for unmodified material is controlled by nucleation and growth

mechanism since the n value (2.237) fall within the range chosen for this mechanisms as rate limiting steps (**Figure 4.20**).

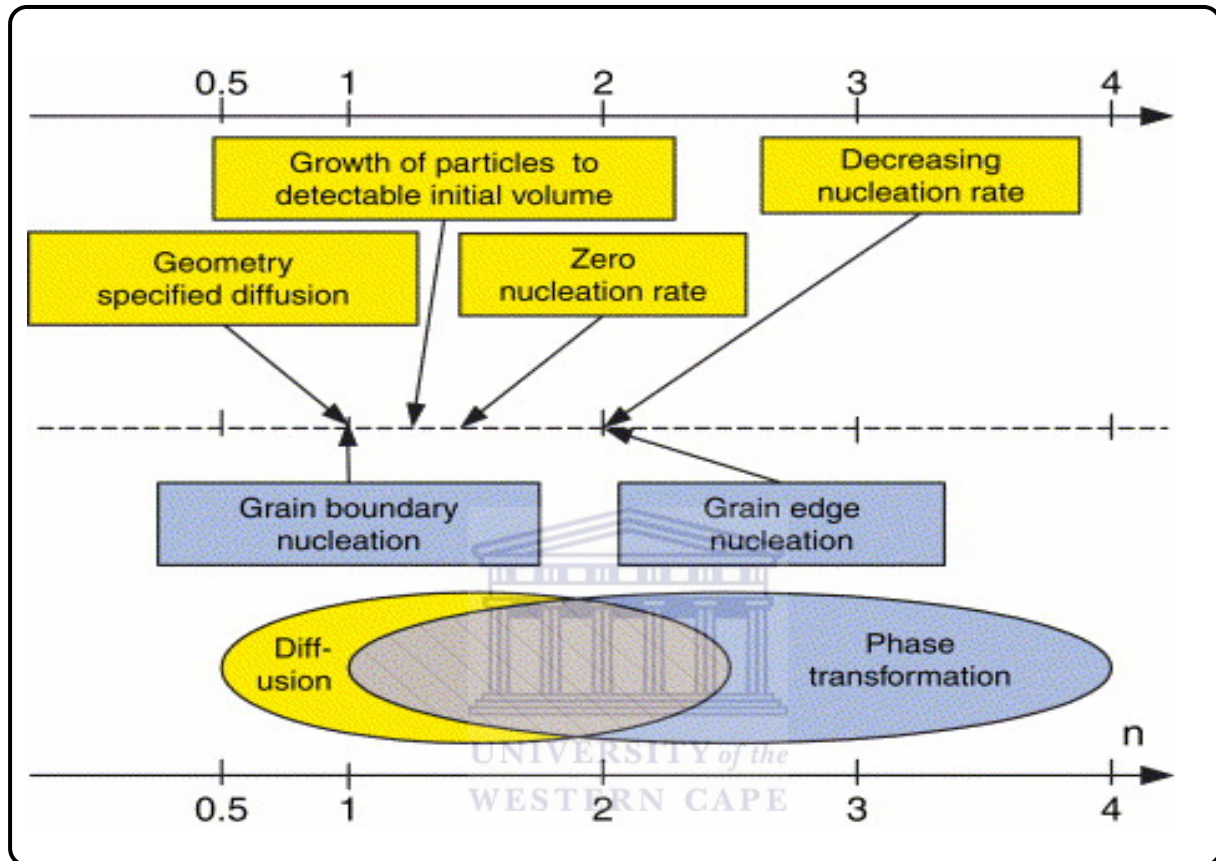


Figure 4.20: Index of power, n in **Equation 4.1**, depending on the rate-limiting step. Boxes with different background colours, blue and yellow are used to differentiate between the two mechanisms (diffusion or phase transformation) [91].

Furthermore, kinetic curve for unmodified alloy gives sigmoid shape which can be a result of protective surface oxide layers [52-54]. Therefore, it was suggested that surface processes, nucleation and growth, are rate limiting steps for the unmodified alloy. On the other hand, H_2 absorption rate for the Pd surface modified alloy was suggested to be diffusion, nucleation and growth controlled rather than surface process. From the second to the fourth charge for

both materials, the n values were found to be less than 1 meaning the absorption rate was purely controlled by the diffusion mechanism.

4.2.4.2 Thermal cycling in hydrogen.

The parent and surface modified AB₅ type alloys after exposing to 3-4 cycles for complete activation were saturated with hydrogen gas at specified pressure; the behaviour of the material during thermal cycling was studied. **Figure 4.21** and **4.22** represent the performance of the unmodified and surface-modified AB₅ type alloy during cooling and heating. The cooling rate was found to be faster at pressures in range 5-18 bar reaching maximum of 6 K/min and began to decrease as the reaction continues. During heating, maximum rate of 10 K/min was obtained.

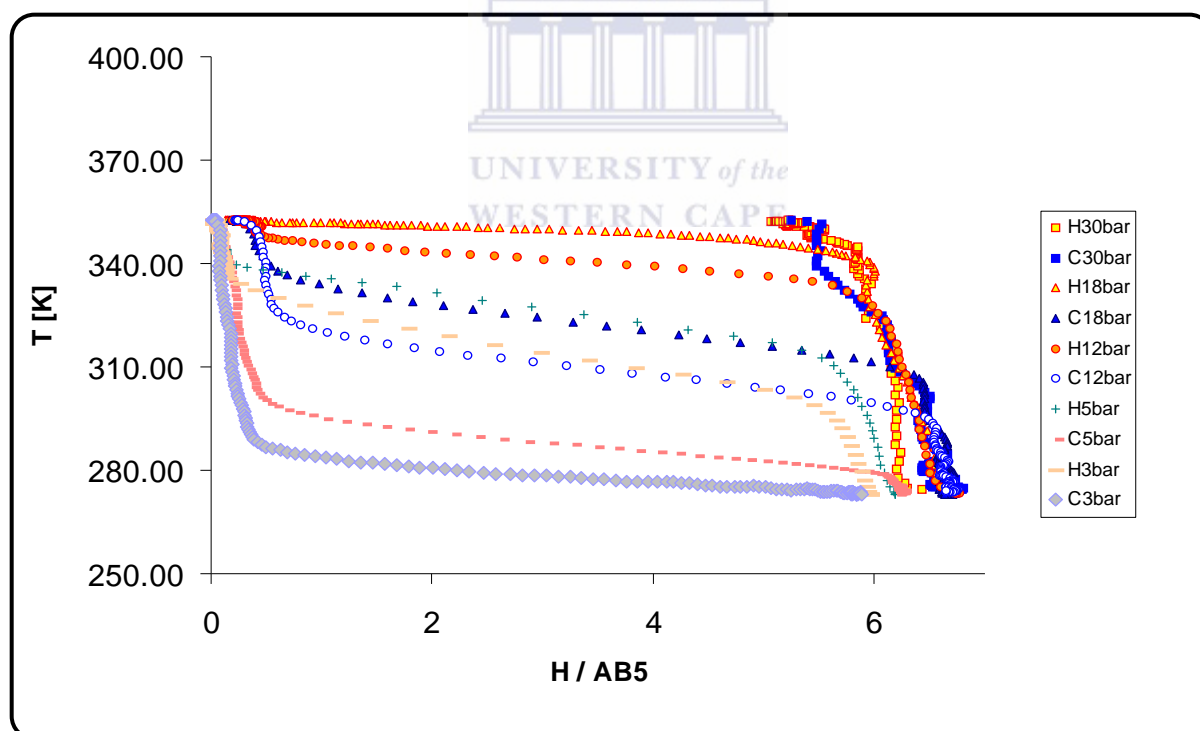


Figure 4.21: Thermal behaviour of unmodified AB₅ hydrogen storage alloy during cooling (C) and heating (H) at various pressures.

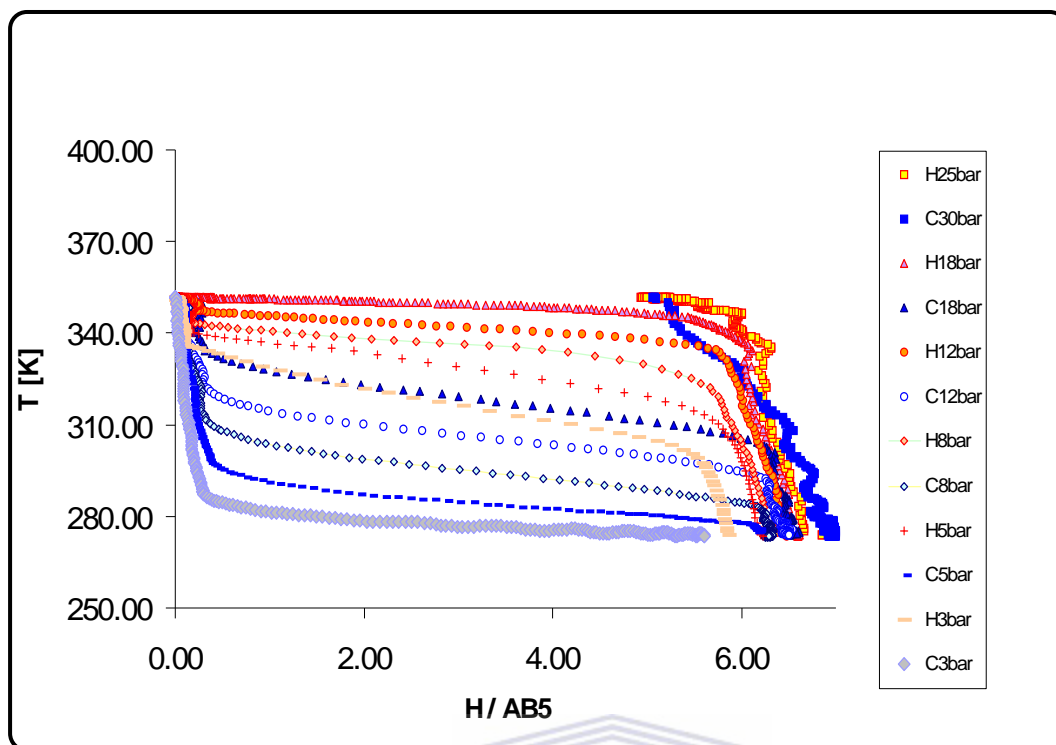


Figure 4.22: Thermal behaviour of Pd-surface modified AB₅ alloy during cooling (C) (and heating (H) at various pressures.

Modified AB₅ type alloy exhibited identical behaviour during thermal cycling as that observed for the unmodified AB₅ type alloy. The identical behaviour is due to the fact that Pd is only involved in the surface processes for enhancement of kinetics and reduction of incubation period. Thus, no influence was observed on the intrinsic properties of the alloy during thermal cycling.

4.4.2.3 *Measurement and modelling of pressure-composition isotherms.*

The pressure composition isotherms of the selected AB₅ type alloy were evaluated at different temperatures (10, 20, 40, 70, 75°C) and are presented in **Figure 4.23**. The distortion of the shapes of the isotherms was caused by experimental errors, first of all, instabilities of temperatures of the reactor and volumetric system.

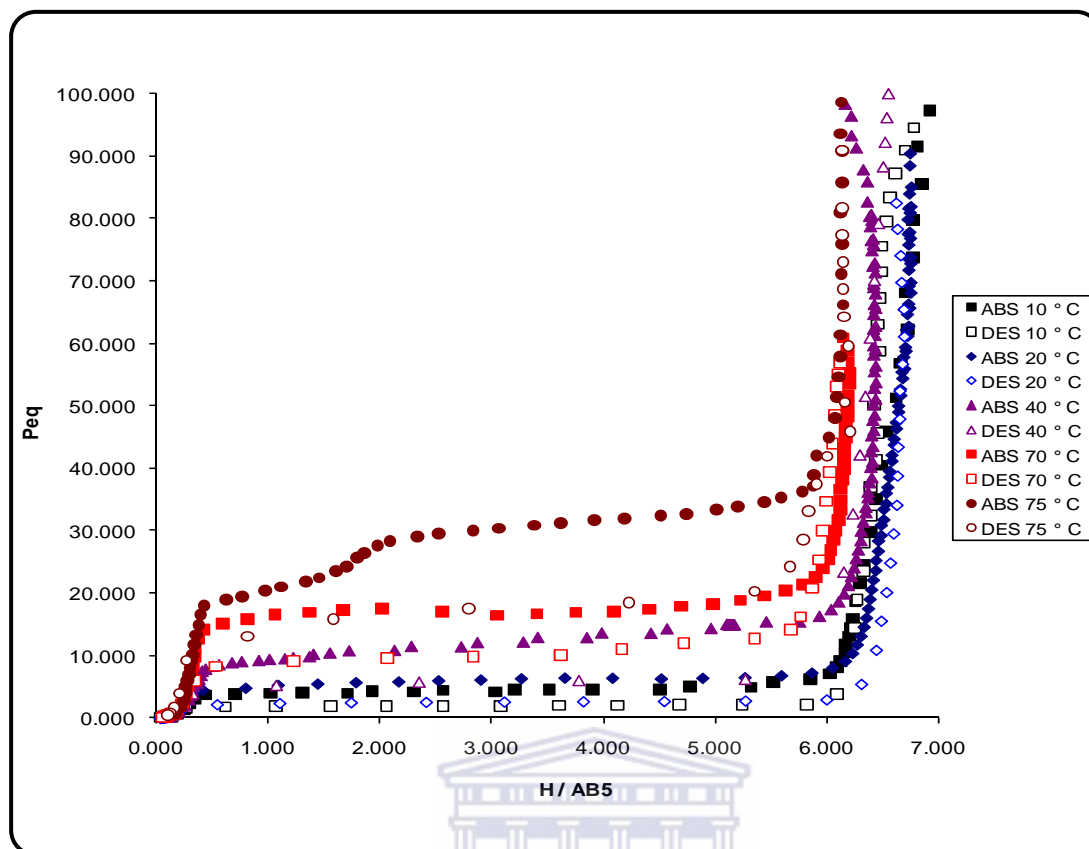


Figure 4.23: Hydrogen absorption / desorption isotherms for the $\text{La}_{1-x}\text{Ce}_x\text{Ni}_5$ alloy.

It is observed that the hysteresis increases with the increase in temperature as a result of lattice expansions upon hydrogenation and small differences in the free energy between hydrogenation and dehydrogenation. Slight sloping of the equilibrium plateau regions in the isotherms was also observed ($T = 75\text{ °C}$) and may have been a result of inhomogeneity in the AB_5 -type alloy. Similar to the results reported by Ivey and Northwood [236], the length of the plateau region was observed to decrease with increasing temperature.

The experimental data, including the measured dynamic isobars (**Figures 4.22**) and static isotherms (**Figure 4.23**) were fitted all together using the model of phase equilibria in metal-hydrogen systems developed by Lototsky *et al.* [213]. The PCT model assumed hydrogen occupies the metal matrix as a Van der Waals lattice gas, where parameters of α - β phase

transformation below critical temperature have a random nature. The model showed a good fit and presented in **Figure 4.24 (a)** and **(b)**.

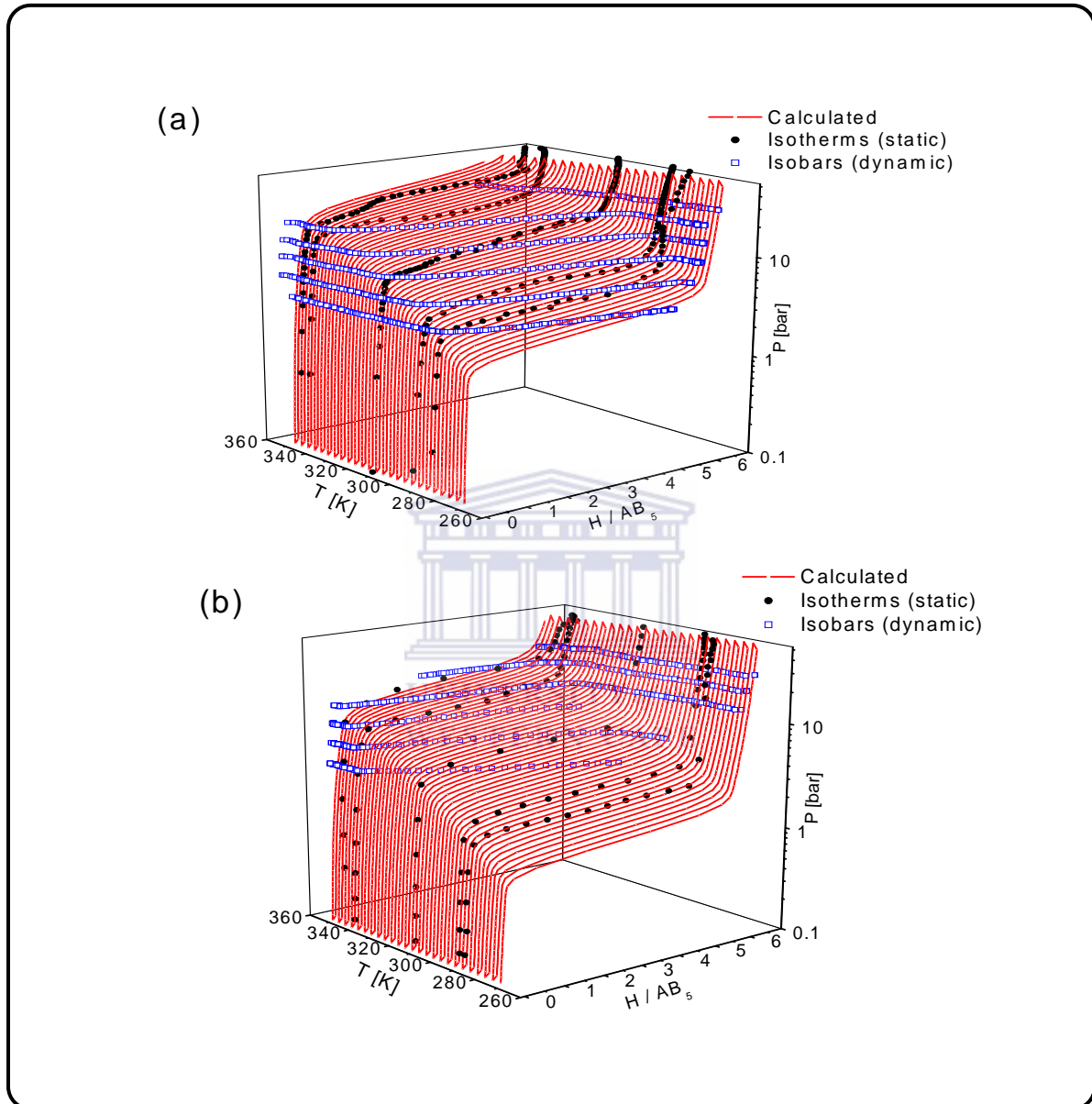


Figure 4.24: 3D plots of absorption (A) and desorption (B) equilibria for H – La_{0.85}Ce_{0.15}Ni₅ system: experimental data (points) and calculated PCT diagrams (lines)

The calculated fitting parameters of the PCT isotherms are listed in **Table 4.8** below. The value $C_{\max}=8.20$ is characteristic of the model asymptotic behaviour in β -region when the

hydrogen pressure increases infinitely. It is related to number of sites available in the metallic matrix for accommodating hydrogen atoms (filling fraction, $\theta \rightarrow 1$), rather than to really observed hydrogen concentrations at reasonable hydrogen pressures. Approaching filling fraction to 1, in accordance with **Equation 3.23**, results in a sharp increase of hydrogen equilibrium pressure due to repulsive H–H interactions at high hydrogen concentrations.

The observed asymptotic behaviour of $\ln(P)$ at small H concentrations corresponded to a nonzero H content in the material, $C=C_{\min}$. This phenomenon for the TiCr_2 –H system was accounted as resulting from H trapping by the sample [231]. We have modelled this feature of the isotherms by introducing an extra, imaginary low-pressure plateau segment (“zero” segment) with a low critical temperature $T_c \sim 0\text{K}$, as it was suggested in [213].

Table 4.8: Fitting parameter from Lototsky model.

Parameters	Absorption	Desorption
Asymptotic hydrogen concentration, C_{\max} [H/AB ₅]	8.20	8.20
“Zero” segment fraction	0.03	0.05
Main segment fraction	0.970	0.950
Critical temperature for the main segment, T_c [K]	445.5	445.4
Concentration-independent contribution to entropy change (main segment), ΔS [J/mol/K]	-91.18	-89.04
Concentration-independent contribution to enthalpy change (main segment), ΔH [kJ/mol]	-3.886	-5.222

Standard deviation of the entropy (main segment), σ_s [J/mol/K]	3.05	2.63
Standard deviation of the enthalpy (main segment), σ_h [kJ/mol]	0.347	0.312
Pearson correlation coefficient (main segment), ρ_{SH}	1.00	1.00

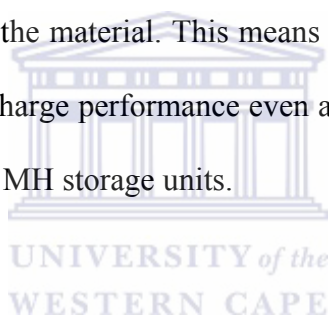
The apparent PCT properties of the AB₅ alloy calculated from the results of fitting of the experimental PCT data (using **Equation 3.24** and **3.25**) in the range $P = 0.1$ -10 bar and $T = 0$ -60 ° C are presented in **Table 4.9**.

Table 4.9: Summary of the calculated PCT properties for the AB₅ hydride-forming alloy

Parameters	Absorption			Desorption		
	T=0°C	T=30°C	T=60°C	T=0°C	T=30°C	T=60°C
Plateau midpoint (C ₀),H/AB ₅	3.288	3.172	3.045	3.210	3.086	2.962
ΔS^0 ,J/moleH ₂ K(C=C ₀)	-94.74	-93.41	-92.14	-92.60	-91.28	-90
ΔH^0 ,kJ/moleH ₂ (C=C ₀)	-23.547	-22.968	-22.405	-24.881	-24.302	-23.740
$d(\ln P)/d(H/AB_5)$	0.086	0.099	0.113	0.074	0.085	0.097
P (C=C ₀) bar	2.7913	8.3558	19.945	1.1996	3.8056	9.5267
θ_0	0.3932	0.3816	0.3704	0.3932	0.3816	0.3704

σ	0.214	0.229	0.241	0.179	0.193	0.204
C (P=1bar),H/AB ₅	0.293	0.277	0.262	1.148	0.241	0.181
C (P=5 bar),H/AB ₅	6.372	0.452	0.372	6.463	5.496	0.391
C (P=10 bar),H/AB ₅	6.552	4.835	0.466	6.597	6.140	3.454

It was observed that Ce substitution influences the thermodynamic behaviour of the AB₅ type alloy since it exhibited lower ΔH in comparison to that of parent LaNi₅ type alloy (-30 ± 0.04 kJ.mol⁻¹) [88,89]. This is attributed to low metal to hydrogen binding energy of Ce making it easier to expel absorbed H₂ from the material. This means that the alloy has reduced thermal stability which leads to good discharge performance even at low temperature and thus can be better suitable for optimisation of MH storage units.



4.3 INTEGRATION OF THE SELECTED AB₅-TYPE MATERIAL INTO HYDROGEN STORAGE UNIT FOR LT-PEMFC APPLICATIONS.

4.3.1 EXPERIMENTAL STUDY OF UPSCALE EFFECTS.

Successive operation of PEMFC systems depends on fast charge / discharge of the metal hydride hydrogen storage unit. Therefore, for any MH unit to be considered as suitable storage unit, fast absorption and desorption are required and these depend on fast removal or supply of heat.

4.3.1.1 Experimental study of charge/discharge performances and temperature distributions within 150 cm³ size MH reactor.

Temperature distributions during charge and discharge of MH-reactor based on a standard 150 cm³ size Swagelok stainless steel cylinder filled with 600 g of La_{0.85}Ce_{0.15}Ni₅ alloy were studied using in house testing station (see **Section 3.3.7**). K-type thermocouples were placed in the middle of the cylinder, for measuring of the temperatures in the centre of the MH-bed (T1), in between the centre and the wall of the reactor (T2), and on the inner (T3) and outer (T4) surfaces of the reactor wall (**Figure 4.25**).

After evacuation at room temperature, MH unit was charged with hydrogen at P = 50 bar, T = 30 °C. The first hydrogen absorption started only after 15 hrs after hydrogen input (**Figure 4.26 (a)**) being accompanied by a gradual heating of the MH bed and increase of the observed hydrogen flow rate from zero to ~0.5 L/min. After reaching the maximum (17–18 hrs), the absorption rate quickly fell to zero, being accompanied by cooling the MH bed to the

initial temperature maintained by the thermostat. The hydrogen absorption capacity achieved in 24 hours was about 50 L H₂ STP, or 83 L H₂ per 1 kg of the alloy.

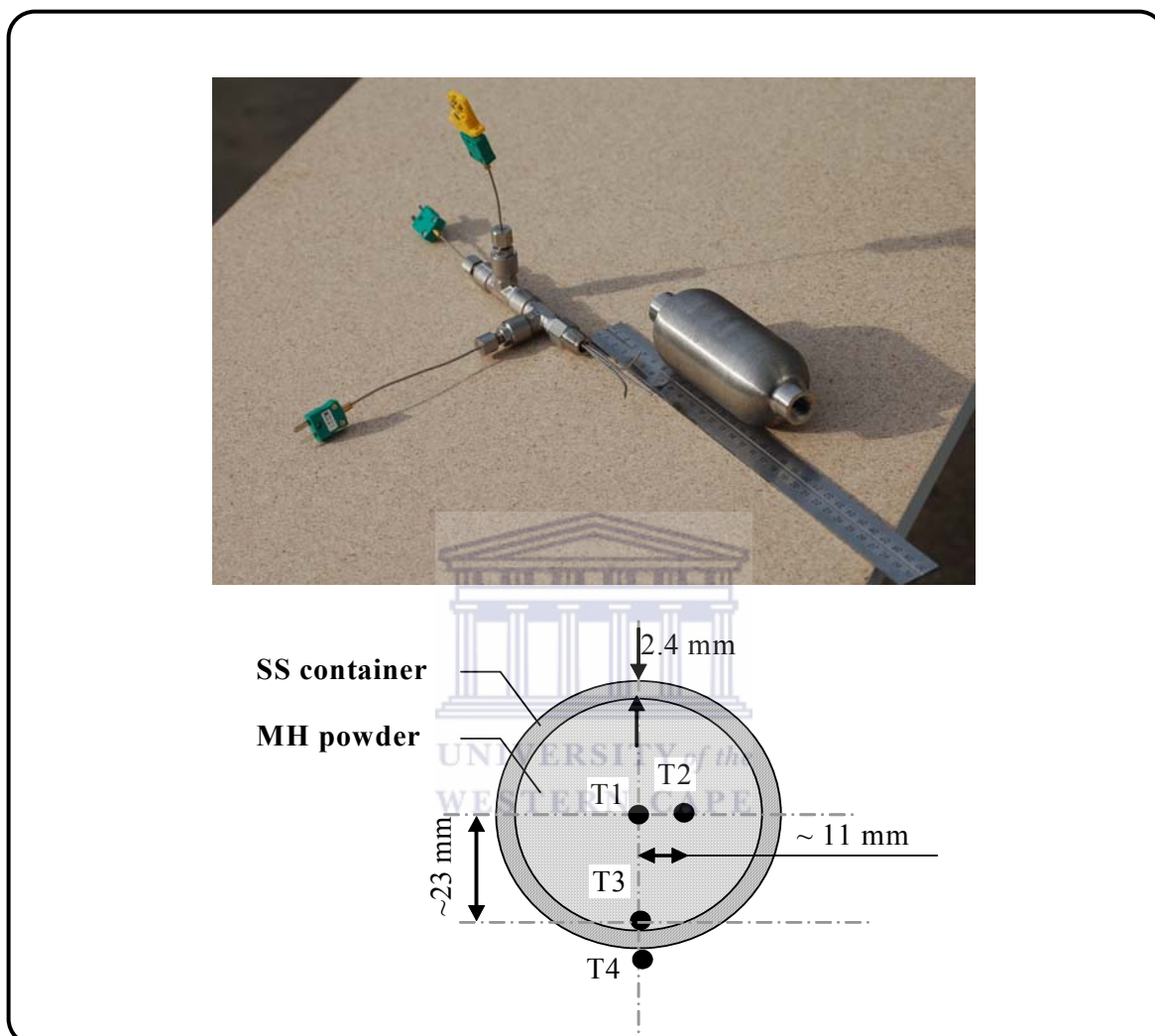
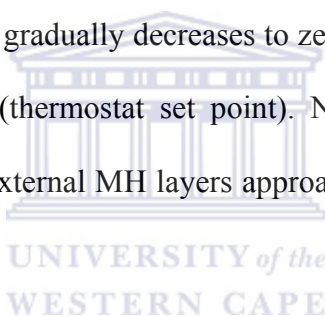


Figure 4.25: General view of the MH reactor before installation of the internal thermocouples (Top); and its schematic cross-section indicating location of the thermocouple joints (Bottom).

In contrast, the second charge of the discharged MH reactor started immediately after introducing H₂ gas (**Figure 4.26 (b)**). The initial hydrogen flow rate was as high as 10–30 L/min, and the temperature of the MH bed, due to exothermic hydrogen absorption, increased

in ~2 minutes up to 90–100 °C; as expected, the inner zone of the MH bed having poor effective thermal conductivity, was heated to higher temperatures than periphery layers, so as $T_1 > T_2 > T_3$. In turn, the heating of the MH bed resulted in the fast slowing down the charge flow rate, because of decrease of hydrogen absorption driving force, i.e. the difference of the actual charging pressure (50 bar) and the equilibrium hydrogen pressure corresponding to the actual MH temperature (about 50 bar at $T=100$ °C and hydrogen concentration corresponding to $H/AB_5 \sim 3$, as it can be calculated from the PCT diagram; **Section 4.2.4.3**). The rate of subsequent hydrogen absorption becomes, therefore, limited by cooling the MH bed. On the other hand, the hydrogen absorption rate obeys the kinetic equation (**Equation 2.2**), so the rate decreases as hydrogen concentration in the MH attains the maximum (equilibrium) value. As a result, the charge rate gradually decreases to zero, and the temperature of the MH bed returns to the initial value (thermostat set point). Note that due to the low thermal conductivity of the MH bed the external MH layers approach the thermal equilibration faster than the inner ones.

During the second charge, the MH material in the reactor was fully activated attaining maximum capacity (140–150 L/kg) in less than 40 minutes.



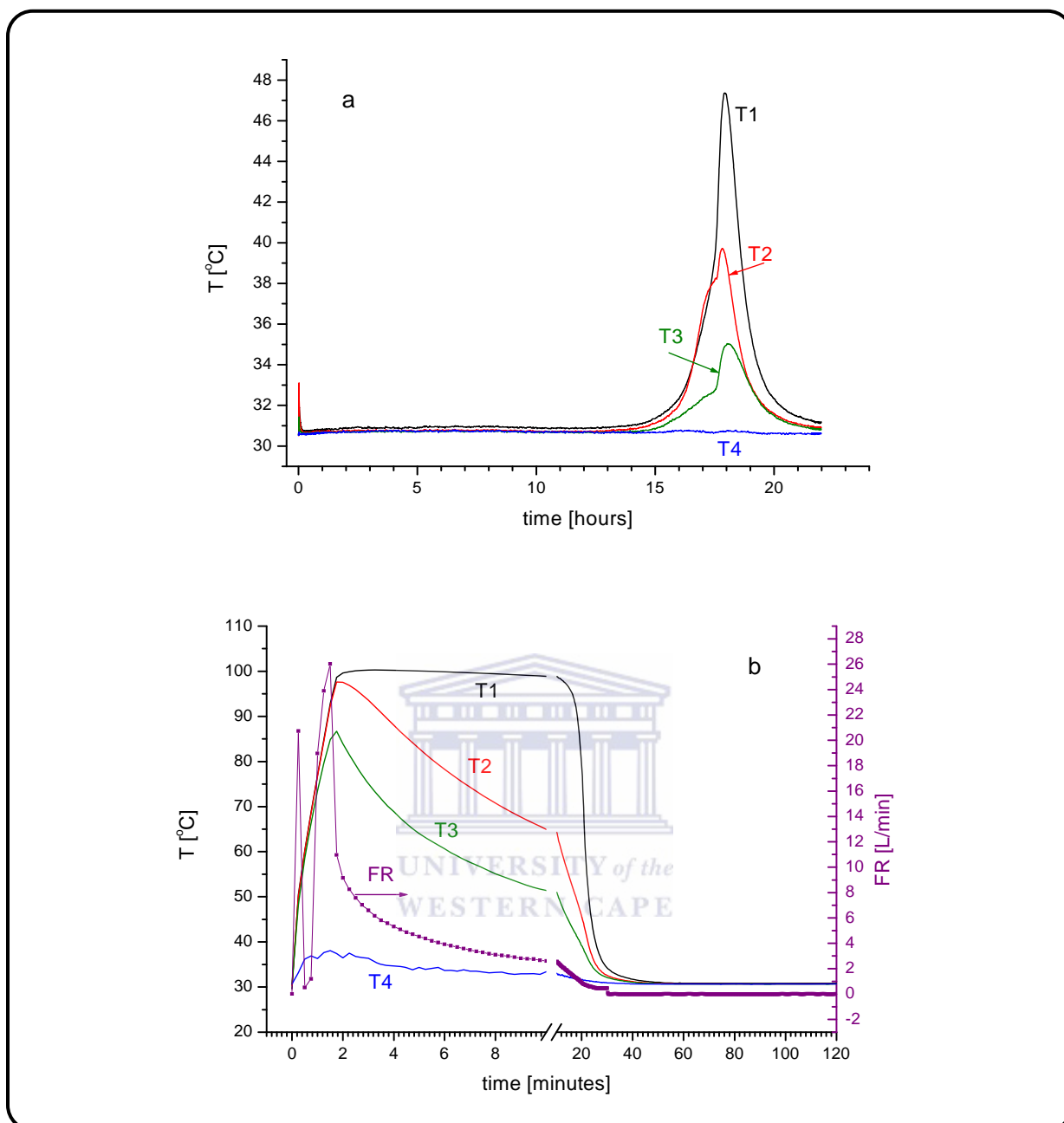


Figure 4.26: Performances of the MH reactor during first (a) and second (b) charge (P=50 bar, T=30°C).

The influence of pressure variation on the charge performance of MH was investigated at P = 10-50 bar while keeping temperature constant (T = 30 °C) are illustrated in **Figure 4.27 (a-d)**.

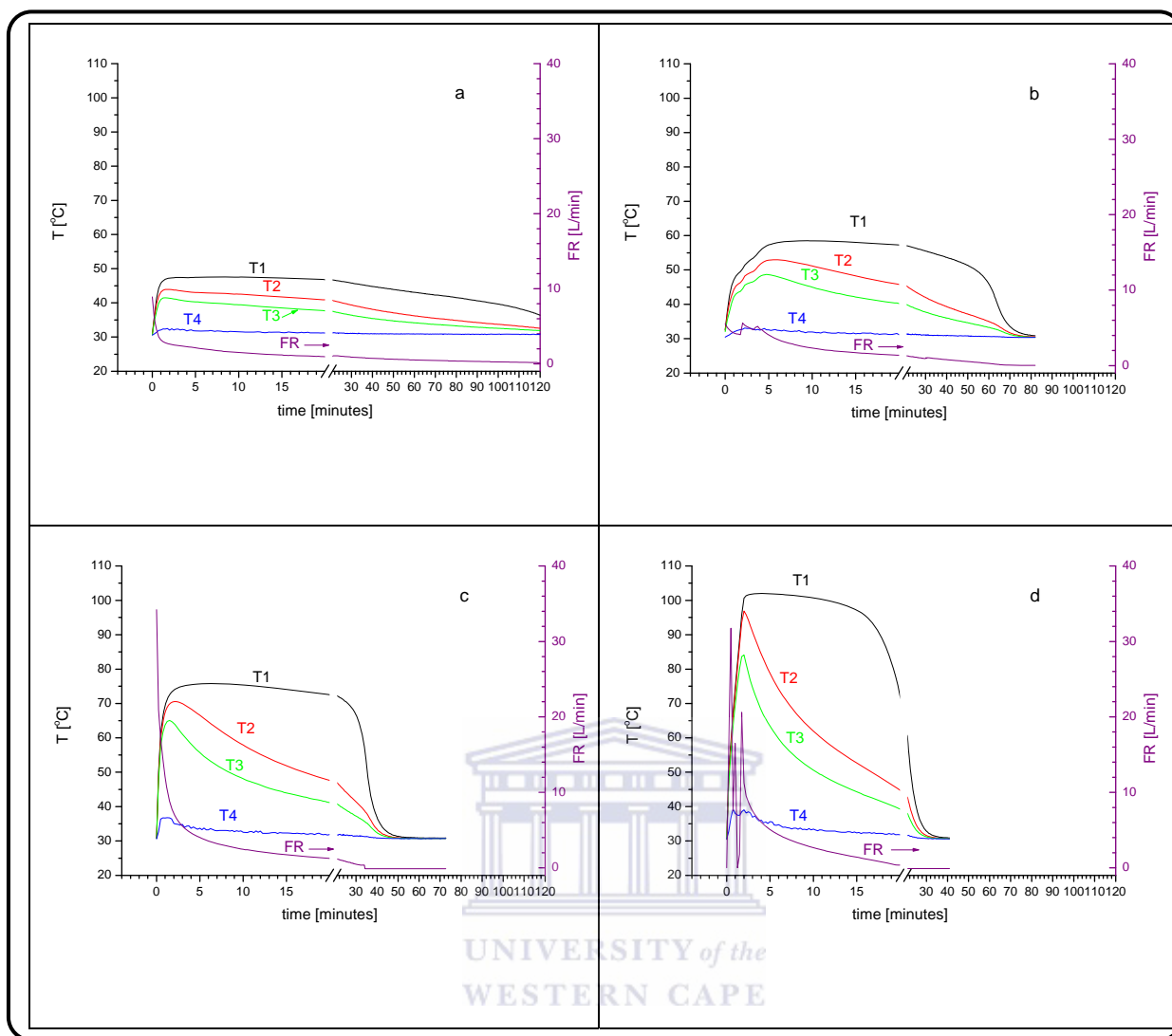


Figure 4.27: Influence of pressure on charge performance of MH unit at P = 10 (a), 15 bar (b), 25 bar (c) and 50 bar (d).

The increase of hydrogen charge pressure results in a significant increase of initial charge flow rate. At higher charge pressures instabilities of flow control system originated from the overrated hydrogen flow were observed (**Figure 4.27 (d)**). At the same time, the faster initial hydrogen absorption in the MH bed, due to its exothermic nature, results in the significant increase of its temperature and the corresponding fall of the H_2 absorption rate, since the equilibrium hydrogen pressure increases approaching to the operating pressure value and thus

reducing the absorption driving force. From the other hand, the higher MH temperatures achieved at the higher hydrogen pressures result in the increase of the temperature difference between the MH bed and surrounding to be a driving force for cooling the MH reactor. In so doing, the cooling becomes faster, and the hydrogen absorption whose rate is limited by the rate of heat removal from the MH bed completes earlier.

Due to low effective thermal conductivity of the MH bed, the temperature distribution within it is non-uniform and the layers closer to the wall of the reactor where heat exchange with the surrounding takes place are heated up slower and cooled down faster than the inner ones.

A correlation was observed when plotting the reciprocal time necessary to absorb a specified amount of hydrogen, 40 and 80 L H₂ (corresponding to H/AB₅=2,57 and 5.15, respectively), against the charging pressure (**Figure 4.28**). At P<25 bar the reciprocal times (values related to the apparent hydrogenation rate constant) depend on the pressure linearly approaching zero at the pressure 6–8 bar that is close to the equilibrium H₂ absorption pressure calculated from the PCT diagram (**Section 4.1.1.3**).

When the charge pressure increases further, deviations from the linear behaviour appear, indicating that the heat transfer performances influence on the charge dynamics in a greater extent practically becoming a single rate-limiting factor.

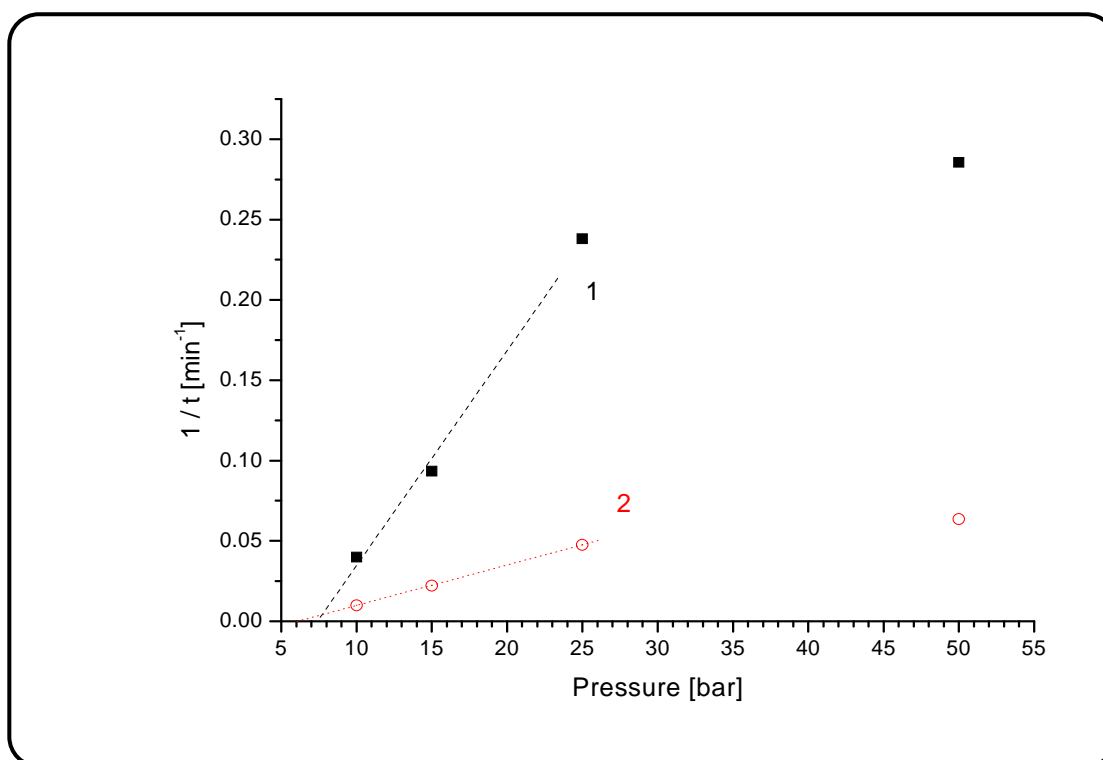
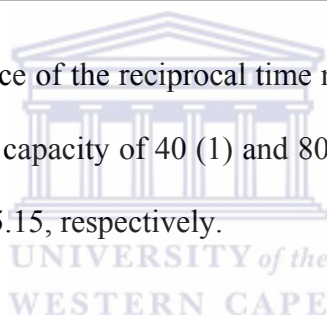


Figure 4.28: Pressure dependence of the reciprocal time necessary for charging MH reactor at $T_0=30\text{ }^\circ\text{C}$ to the capacity of 40 (1) and 80 (2) L H_2 corresponding to H/AB_5 value of 2.57 and 5.15, respectively.



The examples of the charge performance of the MH unit studied at $P=20\text{ bar}$ while varying the temperature ($T = 25\text{ }^\circ\text{C}$, $35\text{ }^\circ\text{C}$) are illustrated in **Figure 4.29 (a)** and **(b)** respectively. As it can be seen, the operation at same charge pressure results in similar temperature behaviours of the MH bed: the maximum temperature (axial region, T_1) increases to $\sim 65\text{ }^\circ\text{C}$ that corresponds well to the equilibrium temperature at the plateau midpoint and equilibrium H_2 pressure of 20 bar (see **Section 4.1.1.3**, **Figure 4.24**).

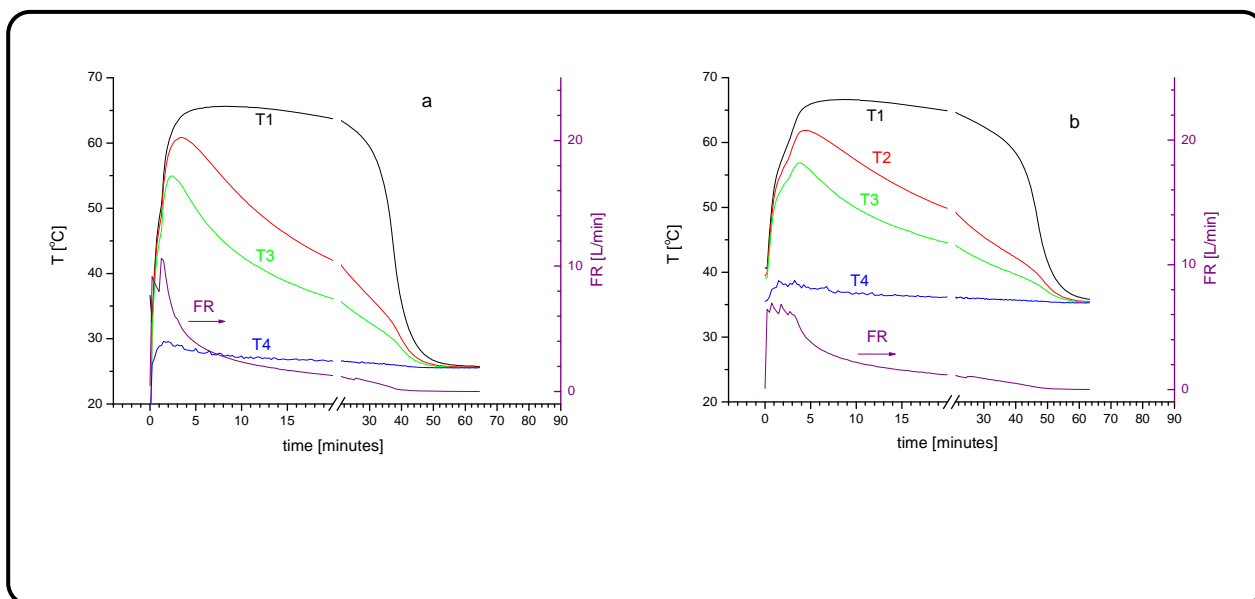


Figure 4.29: Influence of temperature variation at $T = 25\text{ °C}$ (a), $T = 35\text{ °C}$ (b) on the charge performance of the MH reactor.

At the same time, the increase of the surrounding temperature from 25 to 35 °C corresponds to the increase of the equilibrium hydrogen pressure from 6.5 to 9 bar, so the maximum driving force for the absorption at $P=20$ bar will be lower in the latter case. As a result, at the higher temperature lower rate of the hydrogen absorption takes place, and reaction requires longer time to complete. However, the influence of temperature in the studied range on the absorption dynamics is not so strong as the influence of the charging pressure; the extrapolation of linear dependencies of $1/t$ on the temperature (**Figure 4.30**) to zero shows that the capacity of 40 and 80 L H_2 can be achieved at the temperatures lower than 70 and 50 °C, respectively.

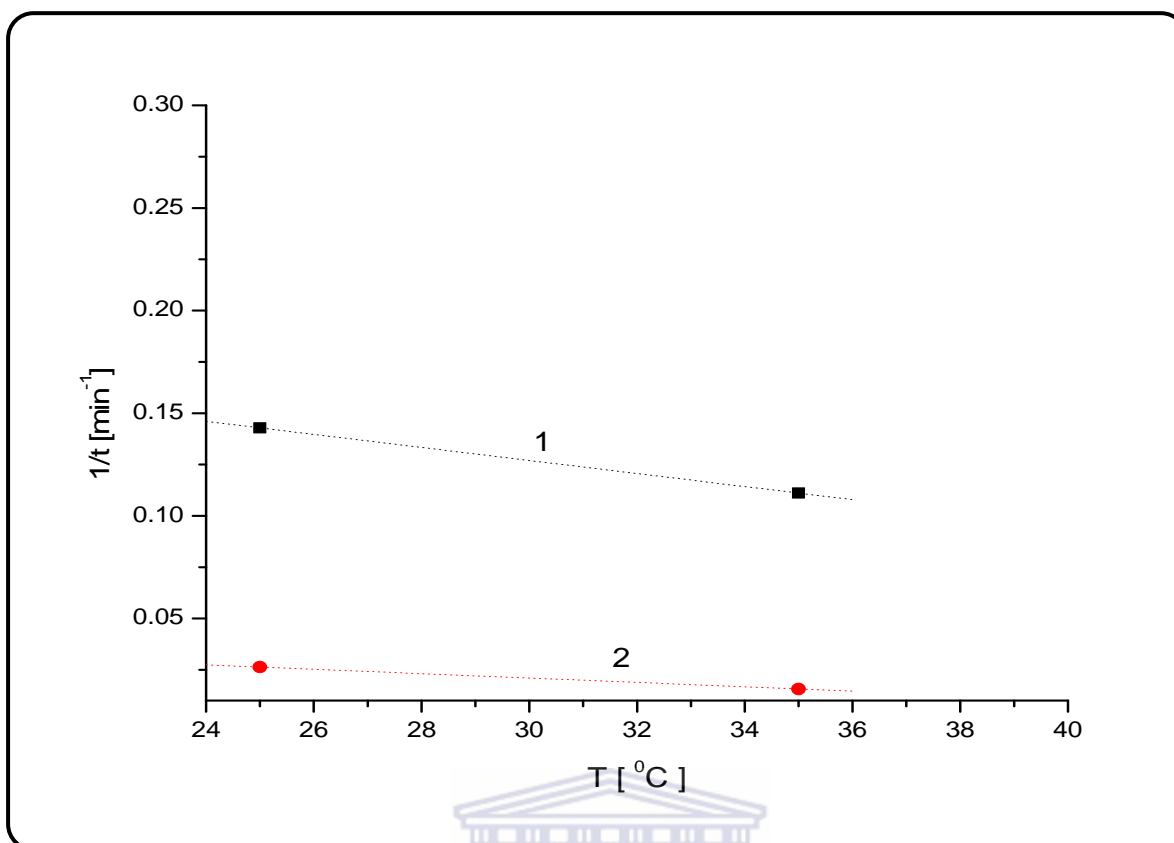


Figure 4.30: Temperature dependence of the reciprocal time necessary for charging MH reactor at $P=20$ bar to the capacity of 40 (1) and 80 (2) L H_2 corresponding to H/AB_5 value of 2.57 and 5.15 respectively.

The discharge performances of MH were studied at $P = 1.5\text{--}3$ bar and $T = 30\text{--}40$ °C (**Figure 4.31**). The thermal performance of the MH-reactor during endothermic desorption significantly affects the hydrogen discharge flow rate. Initially, (first 2-3 minutes) the flow rate rapidly slows down from 5–10 L H_2 (STP)/min to 0.5–1 L/min, due to fast cooling of the MH bed (temperature drop 10–15 degrees).

The desorption is slower than the absorption due to a smaller difference between the operating pressure (1.5–3 bar) and the equilibrium pressure (3.5–5 bar as can be derived from the desorption PCT; see Section 4.1.1.3, **Figure 4.24**). Over time the temperature approaches

its initial value (thermostat setting), and the hydrogen discharge flow rates slow down. The hydrogen desorption is fairly slow, the full discharge takes ~5 hours.

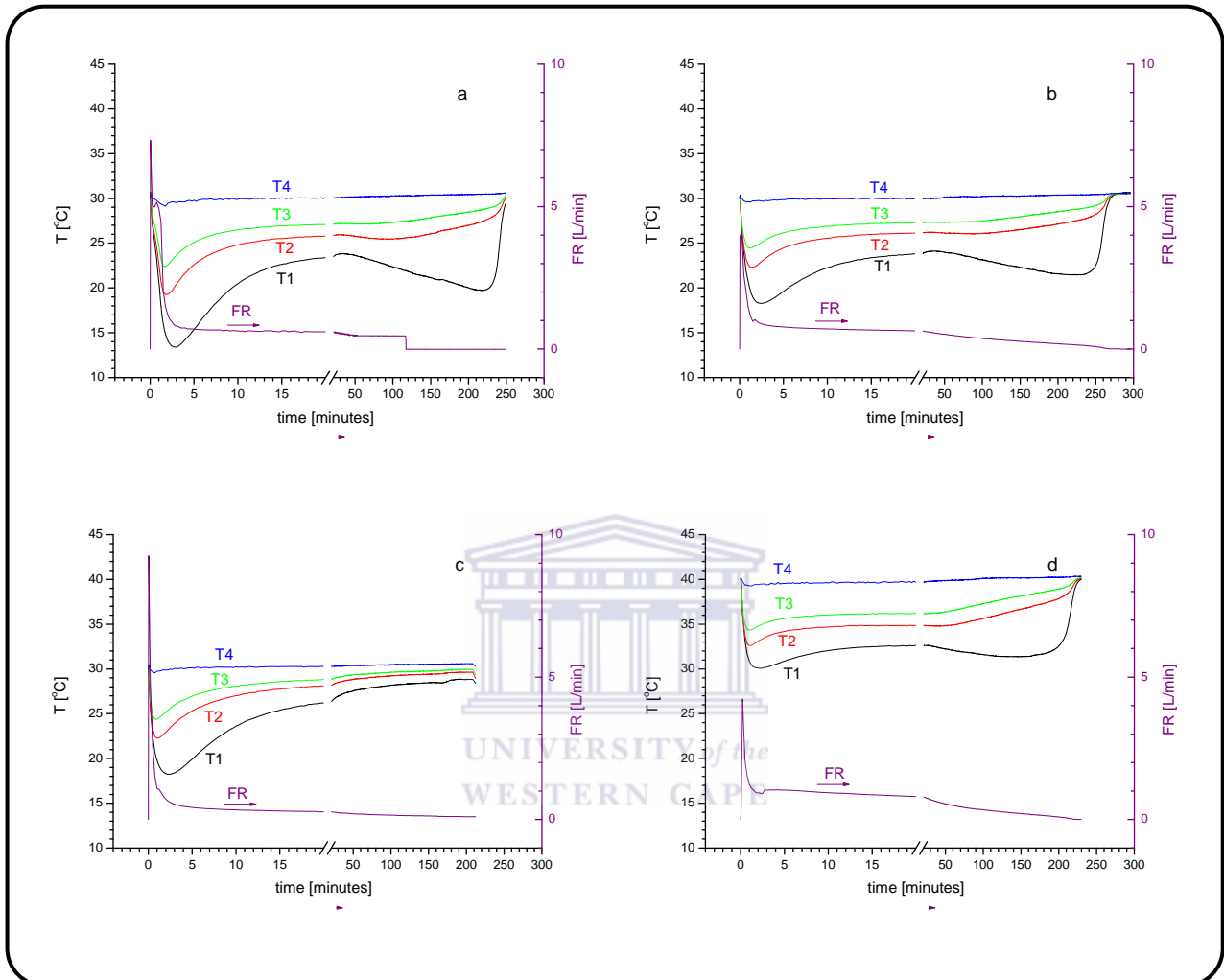


Figure 4.31: Discharge performance of MH unit at P = 1.5 bar, T = 30 °C (a); P = 2 bar, T = 30 °C (b); P = 3 bar, T = 30 °C (c); and P = 3 bar, T = 40 °C (d).

It can be concluded that heating/cooling of the MH-reactor during desorption (endothermic) and absorption (exothermic), which is limited by poor thermal conductivity in the MH-powder, significantly affects the hydrogen desorption/absorption flow rates independently of temperature and pressure variations. It was observed that the hydrogen flow rates slow down over time as the temperature approaches its initial value (thermostat setting). The desorption processes were slower than the absorption ones due to a smaller difference between the operating pressure and the equilibrium pressure (driving force for both absorption and desorption), slower reaction rates, and a more complicated thermal behaviour in the MH bed before completion of the discharge (**Figure 4.31** (a), (b) and (d)). This is likely due to exothermic re-absorption of hydrogen in the cold central region, resulting in the temporary temperature increase. Similar effects have been observed in other studies [233], where it was concluded that temperature gradients induce composition gradients within the hydride bed, making the local temperatures, composition or reactions rates very different from the average values.

In summary, hydrogen charge / discharge dynamic performances of even moderately up scaled MH beds (cylindrical geometry, volume 150 cm³, amount of MH 0.6 kg) are greatly dependent on their heat transfer characteristics, including effective thermal conductivity of the powdered MH material and the intensity of heat supply to (discharge) and removal from (charge) the reactor. The charge-discharge dynamics are also greatly dependent on pressure / temperature conditions, and for the studied MH material a reasonable charge rate can be achieved at $T < 30$ °C and $P_{H_2} > 10$ bar; and the discharge can be carried out at $P \leq 3$ bar and $T \geq 30$ °C.

4.3.1.2 *Charge-discharge performances of the prototype air heated / cooled 2.5L-size MH hydrogen storage unit.*

The prototype air heated-cooled MH hydrogen storage unit was developed by HySA Systems Competence Centre in collaboration with Resource Driven Technology Concept Centre (RETEZCA) at Tshwane University of Technology, within the special DST project A HI FAMBENI, focused on the development of experimental prototype of hydrogen-fuelled tricycle powered by air-cooled high-temperature PEM FC stack [238].

Layout and general view of the assembled unit are shown in **Figure 4.32** and **Figure 4.33** respectively.

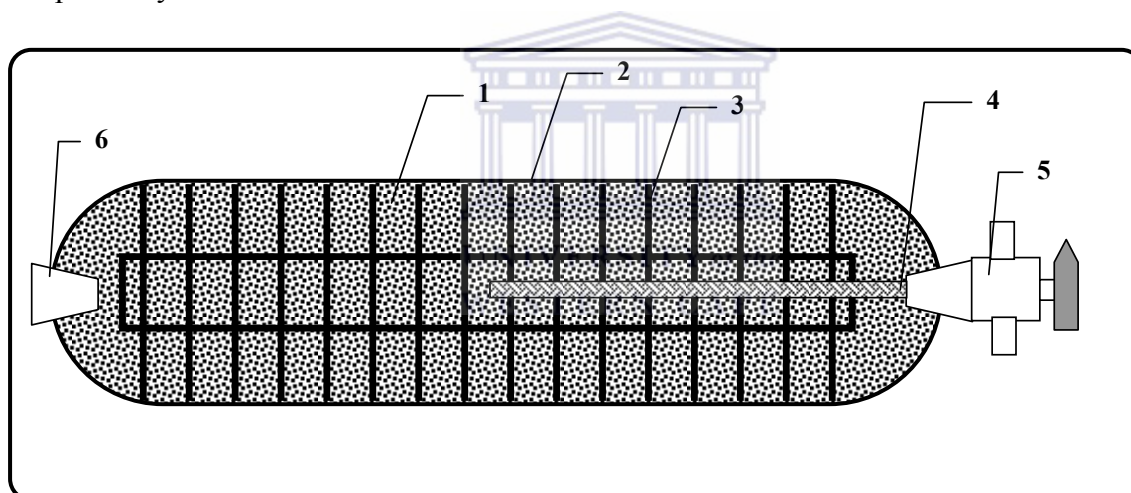


Figure 4.32: Layout of the air heated / cooled MH hydrogen storage unit: 1 – MH ($\text{La}_{0.85}\text{Ce}_{0.15}\text{Ni}_5$) powder; 2 – container (upgraded standard Swagelok 1 GAL size sample cylinder); 3 – heat exchanger; 4 – end fitting with a tubular filter element; 5 – 3-way valve; 6 – back plug.



Figure 4.33: General view of the assembled hydrogen storage unit

The unit (**Figure 4.32**) contains the powder of the $\text{La}_{0.85}\text{Ce}_{0.15}\text{Ni}_5$ material (1) loaded in the container (2) made on the basis of a standard Swagelok 1 GAL-size 304L stainless steel sample cylinder (102 mm internal diameter, 5.2 mm wall thickness). To approach a uniform temperature distribution within MH bed, the container was equipped with an internal heat exchanger (3) made as a set of 30 fins (aluminium disks), 3 mm in thickness, transversally placed in the container with the pitch of 30 mm. The fins were installed inside the cylinder after cutting-off its back-end cap, providing a firm thermal contact with the inner side of the cylinder's wall. The fins also had grooves to provide distribution of the MH powder loaded in the container.

After installation of the heat exchanger, the end cap was welded back, and gas distribution accessories including end fitting with $0.5\ \mu$ pore size tubular filter element (4) and 3-way ball

valve (5) were installed. The assembled container had internal volume of 2.56 L and was filled with 8.77 kg of the MH powder that corresponds to packing density of 3.43 g/cm^3 , or 51.1% of the material density in the hydrogenated state. The calculated hydrogen storage capacity of the unit (assuming the capacity of MH material of $120 \text{ cm}^3/\text{g STP}$) was about 1000 L H_2 STP.

Activation of the MH powder in the unit was carried out by its exposing to hydrogen gas at $P=50 \text{ bar}$, after 3-hour evacuation to $5 \cdot 10^{-2} \text{ mbar}$ (all operations were carried out at room temperature $T_0 \sim 15 \text{ }^\circ\text{C}$). Hydrogen absorption began after 4.5 hours-long induction period; the hydrogen storage capacity reached in 24 hours was 650-700 L H_2 STP that is lower than the estimated value.



Typical charge and discharge performances of the unit are presented in **Figure 4.34** and **Figure 4.35** respectively, showing time dependencies of the hydrogen input / output flow rate (FR), total amount of the absorbed / desorbed hydrogen, and the temperature (T) of the container's wall measured in the middle of the container.

As it can be seen from **Figure 4.34**, at the beginning the charge flow rate was quite high: in first five minutes it reaches 30-35 L/min. However, the exothermic hydrogen absorption resulted in the significant heating the MH bed (up to 35-40 $^\circ\text{C}$ in 10–15 minutes). As a sequence, the equilibrium hydrogen pressure increased up to $\sim 10 \text{ bar}$ (according to absorption PCT diagram, see **Figure 4.24**), thus reducing driving force for hydrogen absorption that was difference between operation pressure and equilibrium one. This resulted in a slowing hydrogen absorption down, and further absorption / charge of the unit took place at rather slow rate, 0.4-1 L/ min (following cooling the unit down), and the charge continued for a very long time not completing in 20 hrs (**Figure 4.34**).

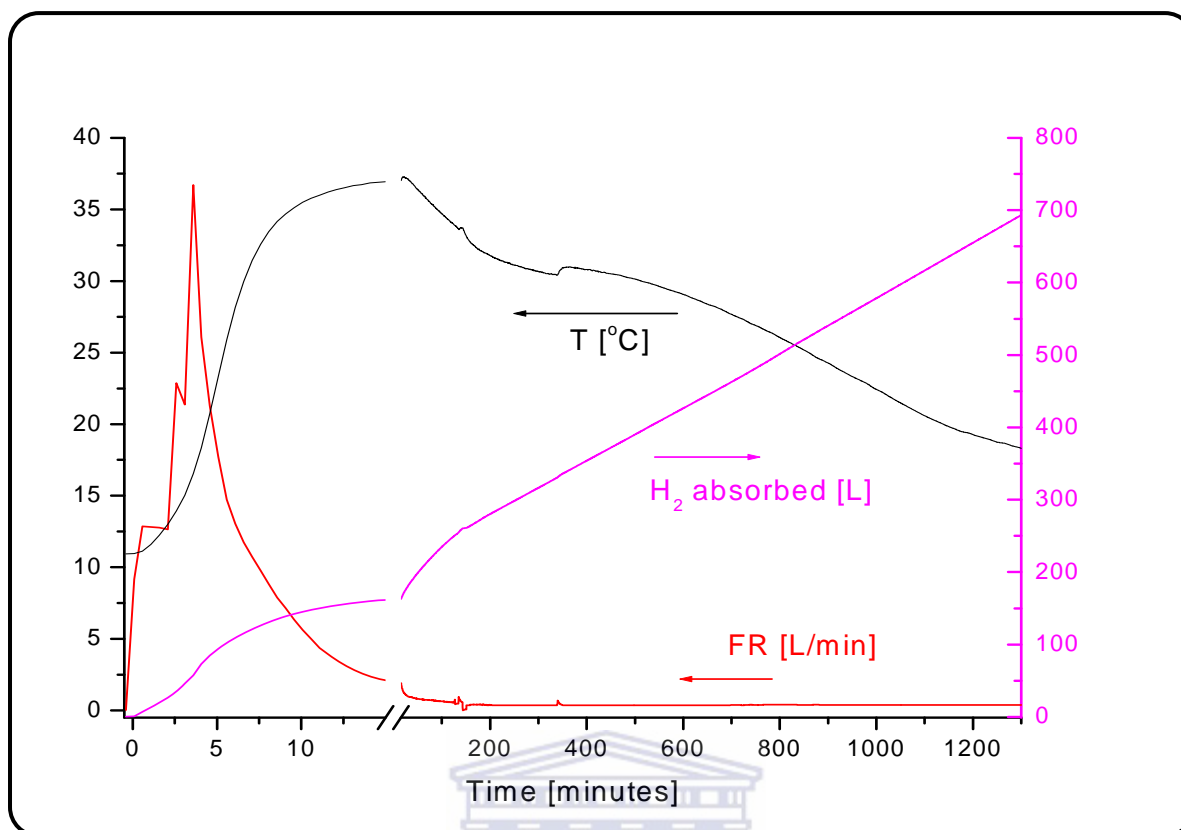


Figure 4.34: Charge performances of the prototype H₂ storage unit at charge pressure of 10 bar and ambient temperature of 12 °C.

Similar behaviour was observed in the course of the unit discharge (**Figure 4.35**). Initially fast hydrogen release (up to 35 L/min) took place. However, due to endothermic hydrogen desorption, it was accompanied by a significant cooling of the unit (from room temperature to almost 0°C). This, in turn, resulted in the lowering the equilibrium hydrogen pressure above MH down to ~1 bar (according to desorption PCT diagram, see **Figure 4.24**), and correspondingly, in the decrease of difference between the equilibrium and operation pressure to be driving force of desorption. As a final result, the discharge rate dropped down to 0.6-1 L/min and remained nearly constant for more than 10 hours, following gradual heating the unit up due to heat exchange with the environment.

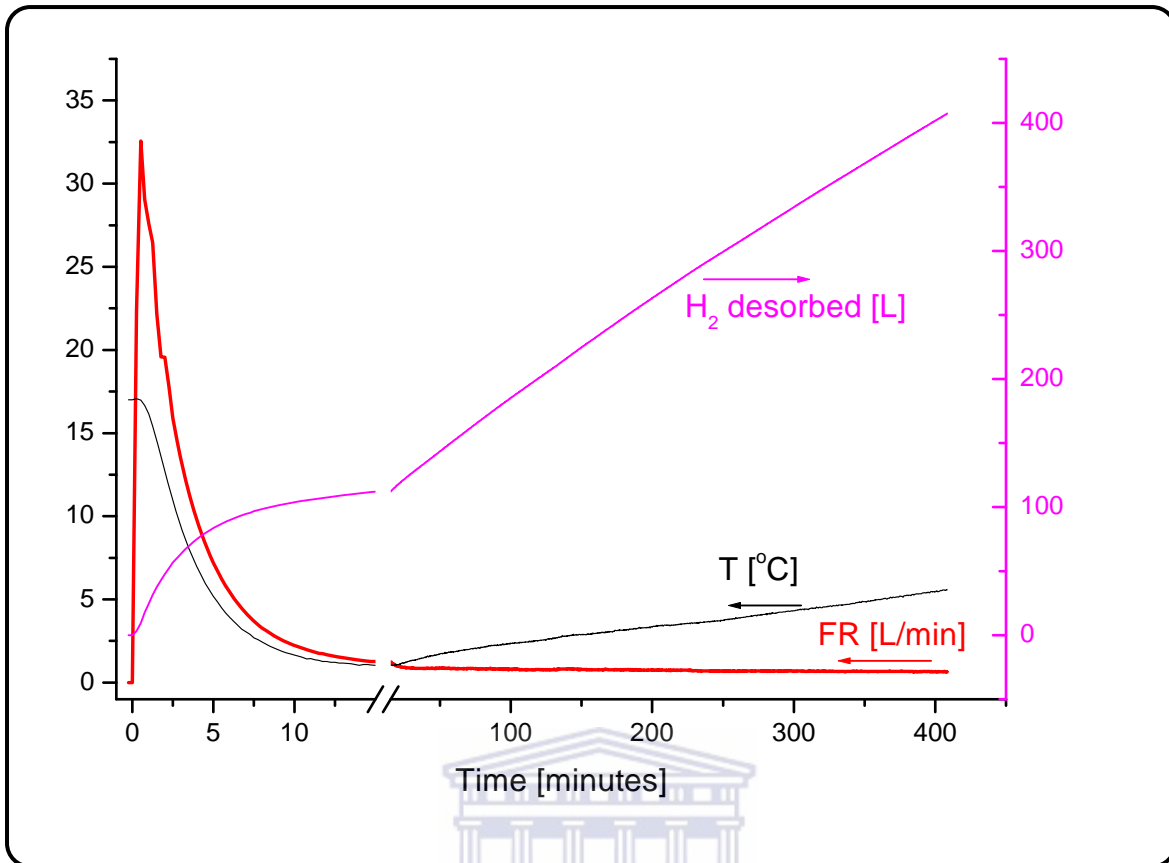


Figure 4.35: Discharge performances of the prototype H₂ storage unit at discharge pressure of 1 bar and ambient temperature of 17 °C.

The observed problems of the charge / discharge dynamics have their origin in a poor heat exchange between hydrogen storage tank and the environment and can be addressed by the intensification of heat removal from the MH during charging the tank (and / or by the increase of the charge pressure), and forced heating the tank during hydrogen discharge (that has been done in the final layout of the tricycle where exhaust heat from the FC stack was used for heating up the MH container). The improvement of the dynamic performances of the unit was achieved on a later stage, by the incorporation of water heated / cooled heat exchanger into MH bed to intensify its thermal management.

4.3.2 DESIGN AND CHARGE/DISCHARGE PERFORMANCES OF PROTOTYPE 1 GALLON SIZE WATER HEATED/COOLED HYDROGEN STORAGE UNIT.

A prototype water-cooled MH hydrogen storage unit for a LT PEMFC application has been developed (**Figure 4.36**) on the basis of the characterizations and heat and mass transfer analyses described above [239]. The MH-unit (**Figure 4.36**) was assembled from standard components (Swagelok), except for the self-made heat exchanger (2) consisting of ½-inch OD copper tubing with copper fins (thickness 0.5 mm, pitch 10 mm).

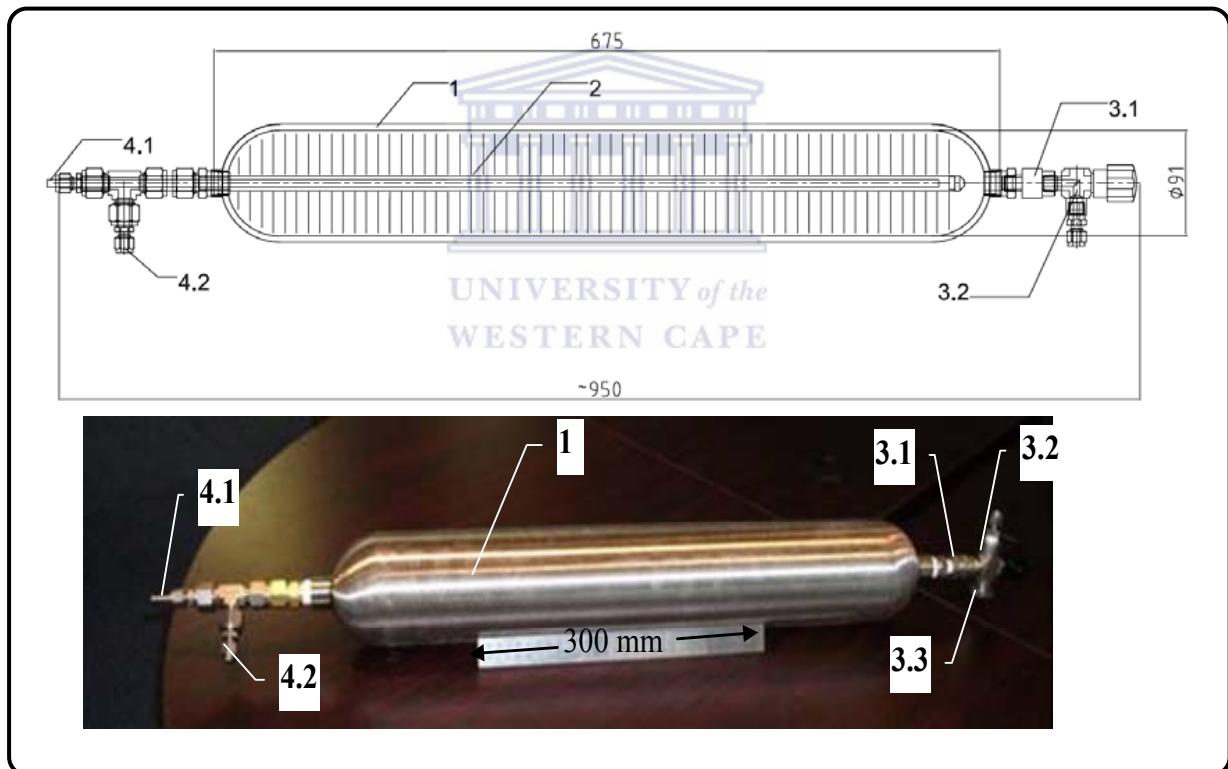


Figure 4.36: Schematic drawing (top) and photo (bottom) of the MH hydrogen storage unit, where 1 = stainless steel container; 2 = heat exchanger; 3 = H₂ manifold: 3.1 = filter, 3.2 = valve, 3.3 = overpressure protection (rupture disc); 4 = water manifold: 4.1 = inlet, 4.2 = outlet.

The fins had collapsible layout that allowed for their installation directly into MH container, without removing its end caps. In the assembled position inside the container the fins had a star-like shape (**Figure 4.37**).

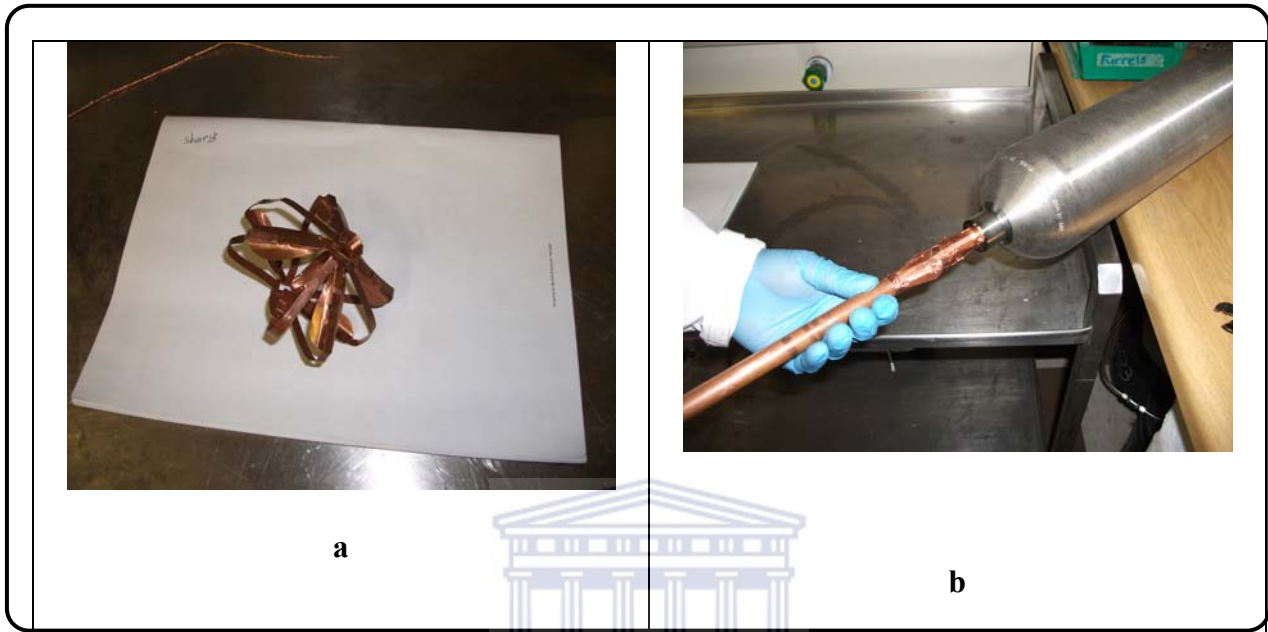


Figure 4.37: Collapsible copper fin element (a) and procedure of its insertion into MH container (b)

The supply of the heating/cooling water is provided via an internal ¼-inch OD stainless steel tube connected to input pipeline (**Figure 4.37; 4.1**) of the water manifold (4). Hydrogen charging of the MH-unit and hydrogen supply to the input pressure regulator of PEMFC-stack is provided via a hydrogen manifold (3) consisting of an in-line gas filter (3.1), shut-off valve (3.2), and a rupture disc with a burst pressure of 133 bar (3.3). The main part of the MH-unit is a one gallon (3.7 L) Swagelok sample cylinder filled with 13 kg of $\text{La}_{0.85}\text{Ce}_{0.15}\text{Ni}_5$ H storage alloy. This gives a bulk density of the material of ca. 3.5 g/cm^3 , or ca. 52% density

of the material in the hydrogenated state, which is below the upper limit (61%) for safe packing of AB₅-type hydrides in MH containers [234].

Activation of the MH unit was carried out at P = 50 bar, T = 20 °C and total hydrogen capacity of 490 L H₂ STP was achieved during the first activation cycle. The second absorption at same conditions resulted in the achievement of the calculated capacity of the unit (~ 2 m³ H₂).

The performance of the developed MH-unit, with a total weight of 22 kg, during charge (P= 15 bar, T= 10 °C) and discharge (P= 1 bar, T= 40 °C) were studied and are presented in **Figure 4.38** and **4.39**, respectively. Time dependencies of the following parameters are presented in the Figures: room temperature (T1), cooling / heating water temperature at the input (T2) and output (T4) of the unit, temperature of the MH bed (T3; additional thermocouple was temporarily placed inside the unit, in between the axial core pipe of the internal heat exchanger and the wall of the container), the temperature of container's wall (T5), and input / output hydrogen flow rate (FR). The joints of thermocouples measuring temperatures of the MH bed and container's wall were located approximately in the middle of the unit.

As it can be seen from **Figure 4.38**, at the beginning the charge flow rate was quite high: in first five minutes it reaches 35-40 L/min. However, the exothermic hydrogen absorption resulted in the significant heating the MH bed (up to 35-40 °C in 10–15 minutes) and this followed by a slow decrease to a constant flow rate of 10-5 L/min.

The charge completed in less than 6 hrs reaching absorption hydrogen storage capacity of 2000 L H₂ (STP).

It can be observed that the MH unit demonstrated faster reaction times than the air-cooled unit described in the previous section, and this is due to effective cooling/heat removal induced by the incorporated water-cooled heat exchanger.

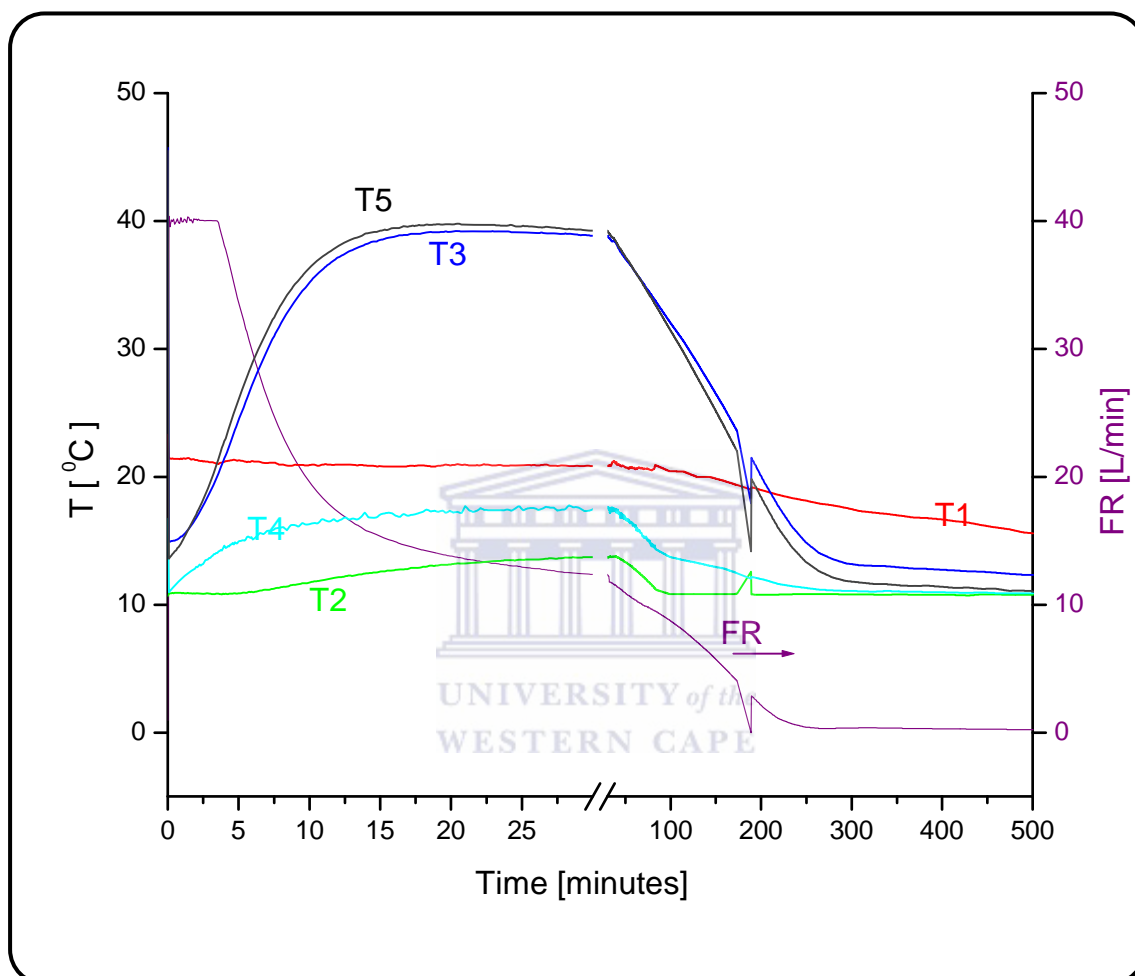


Figure 4.38: Charge performances of the developed prototype MH hydrogen storage unit.

The disturbances at $t \sim 170$ min are caused by the power surge. Similar performances were observed in the course of the unit discharge (**Figure 4.39**). Initially fast hydrogen release (up to 45 L/min) took place followed by cooling of the unit to 20-25 °C. As a reaction proceeds, the discharge rate slowly dropped down to from rate of 5-10 L/min and remained nearly constant. The discharge process was complete in less than 6 hrs and attaining hydrogen

desorption capacity of 1900 L H₂ (STP). The good discharge performance is attributed to low thermal stability of the material (see **Section 4.4.2.3**, **Table 4.9**) even at low temperature and fast heat removal induced by high thermal conductivity of incorporated heat exchangers.

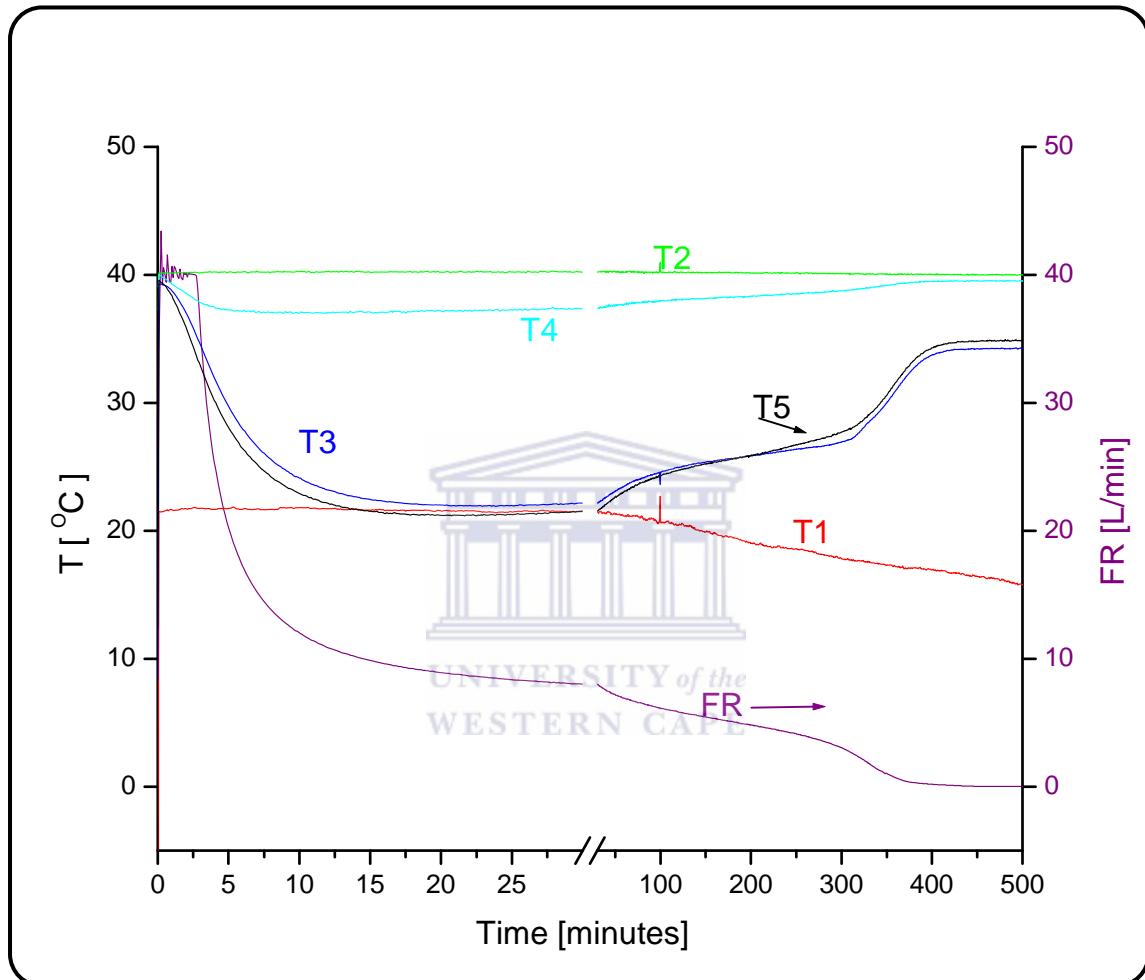


Figure 4.39: Discharge performance of the developed prototype MH hydrogen storage unit.

In summary, hydrogen charge / discharge dynamic performances of water cooled prototype MH hydrogen storage unit (cylindrical geometry, volume 1 gallon, amount of MH 13 kg) are greatly dependent on the heat transfer characteristics of the MH bed. The incorporation of the water-cooled internal heat exchangers reduces the up-scaling effects emanating from poor

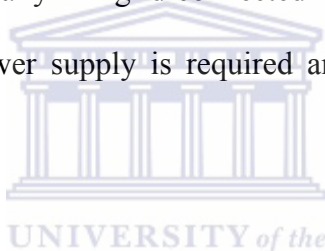
thermal conductivity of MH powder bed. The achieved hydrogen storage capacity shows that the MH unit can provide more than 2 hrs of full-load operation of a 1 kW LT PEMFC-stack.



CHAPTER 5: CONCLUSIONS AND RECOMMENDATIONS

5.1 CONCLUSIONS.

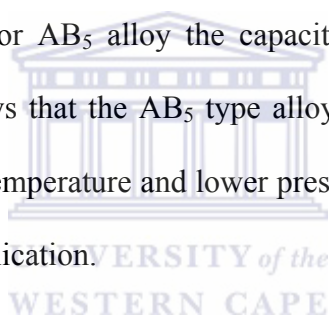
Hydrogen FC systems represent an economically and technically feasible option for reliable power supply and reduce world's dependence on imported oil reserve, as well as green house gas emissions. These systems give off water as the harmless by-product; thus they hold a great promise in meeting in a unique way the Kyoto obligation. Due to their ability to start rapidly at very high power density, fuel cells, particularly low temperature proton exchange membrane fuel cells (LT-PEMFCs), appear as strong contenders to replace conventional batteries and generators, especially in grid-connected applications (telecommunication) where good quality, reliable power supply is required and where interruptions could last several hours.



One promising method that can address the existing issues of hydrogen storage which limit the wide application of hydrogen FC systems is storing hydrogen as a solid inside the materials forming metal hydrides. In comparison to conventional storage methods, solid state methods exhibit features of low-pressure operation, compactness, safety, tailorable delivery pressure, excellent absorption /desorption kinetics, modular design for easy scalability. The alloys within the class of intermetallic compounds, viz. AB_2 and AB_5 type alloys were identified as the appropriate hydrogen storage materials due to their fast charge / discharge kinetics and tuneable PCT performances. These materials have been widely used in numerous applications. In this study their applicability for LT PEMFC hydrogen storage application on the basis of detailed characterisation results was evaluated in selecting the most suitable materials

The materials were evaluated in terms of their phase structural characteristics, surface morphology and elemental composition, hydrogen sorption kinetics and PCT characteristics using XRD, SEM/EDS and volumetric (Sievert) techniques. Hydrogenation performance of air exposed AB₅ type alloy was found to be better than ones for AB₂-type material at same conditions. The AB₅-type materials were found to be easily activated due to the presence of metallic Ni (detected by XRD) which facilitated hydrogen dissociation processes.

From the thermodynamic characterisation, it was found that AB₂ alloy exhibited high plateau pressure, above P~20 bar at room temperature, in comparison P = 5–8 bar for the AB₅ alloy. As a result, total hydrogen capacity of 120 -140 ccm/g was achievable at pressure above P = 35 bar for AB₂ type, whereas for AB₅ alloy the capacity was obtained at relatively low pressure (P = 15 bar). This shows that the AB₅ type alloy can absorb comparatively larger amount of hydrogen at ambient temperature and lower pressure, and thus can be employed as MH material for LT-PEMFC application.



It was revealed that increase of Ce content in the La_{1-x}Ce_x Ni₅ (x=0-0.2) alloy affects the thermodynamic behaviour of the partially substituted AB₅ type alloys. It was shown that increase of Ce content resulted in decreases in |ΔH| (with La_{0.85}Ce_{0.15}Ni₅ alloy having ΔH = – 24.6 kJmol⁻¹H₂) resulting to a reduced thermal stability as compared to the parent LaNi₅ compound (ΔH = –30 kJmol⁻¹H₂). It was also deduced that the composition La_{0.85}Ce_{0.15}Ni₅ can give an equilibrium pressure at room temperature of about 5 bar, which satisfies the pressure / temperature requirements of the given application.

XRD studies of the La_{0.85}Ce_{0.15} Ni₅ alloy and its hydride were carried out. The volume expansion upon hydrogenation (ΔV/V₀) was found to be 24.2 %, which is volume that should

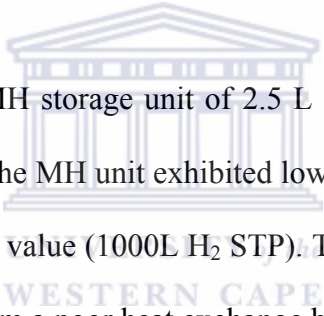
be reserved for expansion to prevent strain stress on the storage container. After charge and discharge cycles the material pulverised into fine particles (20-30 μm) with higher BET surface area of 0.3800 m^2/g , or 2.5 times larger than for AB₅ type alloy before hydrogenation. These small particles may entrained in the gas stream causing imperfect gas permeability and this will lead to gas impedance and poor heat and mass transfer. Therefore, during design and development of hydrogen storage unit this phenomenon should be carefully considered.

Influence of palladium deposition using electroless deposition technique on the activation and hydrogen sorption properties of AB₅ type alloy was carried out and was compared to pre-treated AB₅ type alloy with γ -APTES functionalisation prior electroless deposition. The unfunctionalised AB₅ type alloy (without γ -APTES) exhibited high Pd loading of 13.60 wt. % and 0.66 wt. % as determined by EDS and AAS analysis respectively. The kinetics of the Pd-modified alloy was greatly increased for the first cycle in comparison to unmodified alloy whereas for the second, third and fourth cycles, the kinetics were the same. This was evident to the removal of the oxide films after the first cycle leading to a clean fresh metal surface enabling fast H₂ dissociation processes.

Phase equilibria of the La_{0.85} Ce_{0.15} Ni₅ alloy with gaseous hydrogen were experimentally studied using volumetric (Sievert) techniques including thermal cycling at constant H₂ pressure and measurements of pressure-composition isotherms. The obtained data was processed using the model of phase equilibria in metal-hydrogen systems. It was observed that the hysteresis increases with the increase in temperature as a result of lattice expansions upon hydrogenation and small differences in the free energy between hydrogenation and dehydrogenation. Slight sloping of the equilibrium plateau regions in the isotherms was also observed (T= 75 °C) and may have been a result of inhomogeneity in the AB₅-type alloy.

The length of the plateau region was observed to decrease with increasing temperature. This showed that the alloy have better performance at lower temperatures as confirmed by low ΔH leading to a decreased thermal stability thus can be better suitable for optimisation of MH storage units.

Studies of experimental MH-reactor containing 600 g of $\text{La}_{0.85}\text{Ce}_{0.15}\text{Ni}_5$ alloy using in house testing unit revealed that heating/cooling of the MH-reactor during desorption and absorption which is limited by poor thermal conductivity in the MH-powder, significantly affects the hydrogen desorption/absorption flow rates. Thus the MH exhibited poor charge / discharge dynamic performances.



An air cooled/heated prototype MH storage unit of 2.5 L size which comprising 8.77 kg of $\text{La}_{0.85}\text{Ce}_{0.15}\text{Ni}_5$ alloy was tested. The MH unit exhibited lower hydrogen storage capacity (600 -700L H_2 STP) than the estimated value (1000L H_2 STP). The MH unit showed poor charge / discharge dynamics originated from a poor heat exchange between hydrogen storage tank and the environment. Therefore, intensification of heat supply to / removal from the MH unit was shown to be necessary.

A water cooled/heated prototype MH storage unit based on a standard 1 gallon Swagelok sample cylinder with incorporated internal exchanger was developed and tested. The unit comprises 13 kg of $\text{La}_{0.85}\text{Ce}_{0.15}\text{Ni}_5$ alloy. The unit exhibited faster reaction rates which are attributed to insertion of internal heat exchangers capable of considerably increasing temperature response during heating/cooling mainly due to their high thermal conductivity. High hydrogen storage capacity (1900-2000 L H_2) showed that the MH unit can provide more than 2 hrs of full-load operation of a 1 kW LT PEMFC-stack.

To conclude, in the course of addressing hypothesis and sub-objectives, AB₅ type alloy was selected as a suitable MH material for LT-PEMFC application. Partial substitution of parent alloy demonstrated a promising approach in tuning the thermodynamic properties of the alloy that satisfy the requirements of the given application. Electroless deposition of Pd catalytic layers on metal alloy for enhanced activation and hydrogen absorption performance still remains the effective surface modification method. Modelling of phase equilibria (PCT diagrams) in the systems of hydrogen gas with hydride forming alloys is important both for the systemic evaluation of the available experimental data and for the optimisation of specific applications of metal hydride. The use of the metal alloys on a larger scale of MH reactor/unit undergoes a negative influence on the attractive properties (fast absorption/desorption) of the AB₅ type alloy due to poor heat and mass transfer originated from disintegration of metal powders into fine particles of low effective thermal conductivity. Incorporation of internal heat exchangers into MH unit appears to be an effective method of enhancing heat and mass transfer and thus enables the MH unit to meet supply demand of more than 2 hrs of full-load operation of a 1 kW LT PEMFC-stack.

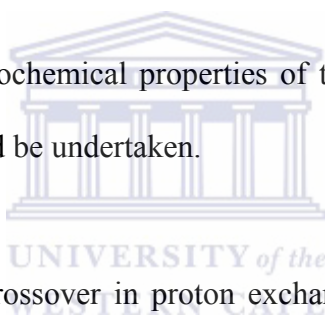
The knowledge emanating from this project is expected to pave the way in industrialization of new class of metal hydrogen absorbing materials for LT-PEMFC systems. These systems can therefore be used in various stationary applications and thus reduce the dependence of energy supply from fossil fuels.

Research results obtained within this study were presented at the Second Annual RETECZA Conference, 11 - 13 August 2010, Kwa-Maritane Bush Lodge [238], and 18th World Hydrogen Energy Conference, May 16 - 21, 2010, Essen, Germany [239].

5.2 RECOMMENDATIONS AND FUTURE WORK.

Based on the analyses and conclusions of the study, a number of recommendations regarding future research directions of investigation were made:

1. Impurities in hydrogen such as carbon monoxide and sulfur compounds have the effect of poisoning the alloy surface. Surface poisoning of the parent LaNi_5 hydride with CO results in more than four hydrogen atoms per LaNi_5 formula remained in the CO-treated hydride. The Ce substituted alloys can be used in improving dehydrogenation kinetics due to higher equilibrium pressure of the $\text{La}_{1-x}\text{Ce}_x\text{Ni}_5$ alloys.
2. Investigation of the electrochemical properties of the surface-modified materials for battery applications should be undertaken.
3. The issues of methanol crossover in proton exchange membrane observed in direct methanol fuel cell can be addressed by employing partially Ce substituted alloys as support materials on Pd/Pt catalyst since CeO_2 (normally observed on the LaCeNi_5 alloy due to strong affinity to oxygen) is effective in methanol decomposition and also interaction of CeO_2 with Pd/Pt results in stabilization of the Pd/Pt species and thus resulting in activation of Pd/Pt catalysts.
4. Efforts of combining internal heat exchangers and development of MH compacts on the basis of metal alloy and heat inert additives as heat and mass transfer enhancement techniques should be made.



CHAPTER 6: BIBLIOGRAPHY

- [1] Boyle G., *Renewable Energy: Power for a Sustainable Future*. Oxford University Press: Oxford. 1996.
- [2] Leonhard W., *Distributed Generation and its Effects on the Future Supply Grid. In EPE Proceedings - Discussion*. Graz, Austria. 2001.
- [3] European commission, *Hydrogen Energy and Fuel Cells: A vision of our future*; Luxembourg, 2003.
- [4] European Commission; *The Kyoto protocol*. Available [ONLINE] <http://ec.europa.eu/environment/climat/Kyoto.htm>.
- [5] Kyoto Protocol to the United Nations Framework Convention on Climate Change, 1998. Available [ONLINE] <http://unfccc.int/resource/docs/convkp/kpeng.pdf>.
- [6] Energy Efficiency and Renewable Energy; Fuel Cell Technologies Program: Fuel Cells. Available [ONLINE] http://www1.eere.energy.gov/hydrogenandfuelcells/fuel_cells.
- [7] National Renewable Energy Laboratory: Innovation for Our Future. Available [ONLINE] <http://www.nrel.gov/programs/hydrogen.html>.
- [8] Emergency backup power systems. Available [ONLINE] <http://www.toolbase.org/TechnologyInventory/ElectricalElectronics/emergencypower-backup-systems>.
- [9] Department of Energy H₂ program. Fuel cells for Backup Power. Available [ONLINE] http://www1.eere.energy.gov/hydrogenandfuelcells/education/pdfs/early_markets_backup_power.pdf.
- [10] Perry, M. L.; Kotso, S.: A Back-up Power Solution with No Batteries, *INTELEC 2004 Proceedings*.(2004) 210-217.

- [11] Dogterom, J.: Hydrogen and Fuel Cell Business Development in Canada. Case Study: Fuel Cell Telecom Installations, HySA Systems Business Seminar, 2 November 2009, Cape Town.
- [12] Teledyne Brown Engineering report, Fuel cell power systems for remote application, DOE/GO/10217-T1.1998.
- [13] IFC report, Phase I feasibility study of an integrated hydrogen PEMFC system, DOE/GO/10214-T1. March 1998.
- [14] Thomas G.: *Overview of Storage Development DOE Hydrogen Program*; Sandia National Laboratory, 2000. Available [ONLINE].
http://www1.eere.energy.gov/hydrogenand_fuel_cells/pdfs/storage.pdf
- [15] College of the Desert, Hydrogen Properties: Hydrogen Fuel Cell Engines and Related Technologies, 2001.
- [16] Weast R. C.: *Handbook of chemistry and physics*, 57th ed. CRC Press, Boca Raton, 1976.
- [17] Eklund, G.; Von Krusenstierna, O.: *International Journal of Hydrogen Energy* **8(6)** (1983) 463-470.
- [18] Barthélémy, H.: *International Journal of Hydrogen Energy*. (2010) 1-9.
- [19] Larminie J., Lowry J., Hydrogen Supply. *Electric vehicle Technology explained*. John Wiley & son Ltd. England. (2003)120-122
- [20] Sandi G., Hydrogen storage and its limitation. *The electrochemical Society Interface* **13(3)** (2004) 40-44.
- [21] Sherif S.A., Zeytinoglu N., Veziroglu T.N.: *International Journal of Hydrogen Energy*. **22 (7)** (1997) 683-688.
- [22] U.S department of energy. Fuel cell technologies program, hydrogen storage. Available [ONLINE]

- http://www.eere.energy.gov/hydrogenandfuelcells/storage/hydrogen_storage.html.
- [23] Energy, Environment and sustainable Development: *Hydrogen Storage in Hydrides for Safe Energy Systems*; ENK6-CT-2002-00600, 2002.power. Available [ONLINE] <http://www.nrel.gov/docs/fy07osti/41572.pdf>.
- [24] Energy Conversion devices: Portable Canisters. Available [ONLINE] <http://www.energyconversiondevices.com/portable.php>
- [25] Chao, B.S.; Young, R.C.; Myasnikov, V.; Li, Y.; Huang, B.; Gingl, F.; Ferro, P.D.; Sobolev, V.; Ovshinsky, S. R: *Recent Advances in Solid Hydrogen Storage Systems*. Available[ONLINE].http://www.mrs.org/s_mrs/sec_subscribe.asp?CID=2643&DID=179552&action=detail
- [26] MacKey, K.: *Vodorodnye soedineniya metallov* (Metal Hydrogen Compounds), Moscow: Mir, 1968.
- [27] Kolachev, B.A.; Shalin, R. E.; Il'yin A. A.: *Splavynakopitelib vodoroda* (Hydrogen-Accumulating Alloys), Moscow: Metallurgiya, 1995.
- [28] Sandrock, G.: *Journal of Alloys and Compounds*. **293-295** (1999) 877-888.
- [29] Antonov, V. E.; Baier, M.; Dorner, B.: *Journal of Physics*. **14** (2002) 6427.
- [30] Tarasov, B. P.; Lototsky, M. V.; Yarty's V. A.: *Russian Journal of General Chemistry*, **77 (4)** (2007)694 -711.
- [31] Mottram, R. S.; Yartys, V.; Guegan, P. W.; Harris, I.R.: *International of Journal of Hydrogen Energy*.**24** (1999) 257.
- [32] Eigen, N.; Kunowsky, M.; Klassen, T.; Bormann, R.: *Journal of Alloys and Compounds*. **430** (2007) 350-355.
- [33] Wang, J.; Ebner, A. D. Ritter, J. A.: *Journal of Physical Chemistry C*.**111** (2007) 14917-14924.

- [34] Kim, J.W.; Shim, J. H.; Kim, S. C.; Remhof, A.; Borgschulte, A.; Friedrichs, O.; Gremaud, R.; Pendolino, F.; Zuttel, A.; Cho, Y.W.; Oh, K.H.: *Journal of Power Sources* (2009),doi:10.1016/j.jpowsour.2009.02.083.
- [35] Zhou, L.: *Progress and Problems in Hydrogen Storage Methods*, Renewable & Sustainable Energy Reviews. **9** (2005).
- [36] Schüth, F.; Bogdanovic, B.; Felderhoff, M.: *The Royal Society of Chemistry*, September 2004.
- [37] Bogdanovic, B.; Scwickardi, M.: *Journal of Alloys and Compounds*. **253-254** (1997) 1–9.
- [38] Bogdanovic, B.; Brand, R. A.; Marjanovic, A.; Schwickardi, M.; Tölle, J.: *Journal of Alloys and Compounds*. **302** (2000) 36–58.
- [39] Akiba, E. and Okada, M., *MRS Bulletin*. 2002, September. 699.
- [40] Lototsky, M. V.; Savenko, A. F.; ShChur, D. V.; Pishuk, V.K.; Yartys, V.A.; Mukhachev, A. P.: *Trudy IX Mezhd. konf. Vodorodnoe materialovedenie ikhimiya uglerodnykh nanomaterialov* (Proc. IX International; conference). Kiev: Naukova Dumka, (2005) 823.
- [41] Lennard-Jones J. E.: *Trans. Faraday Society*. **2** (1932) 333.
- [42] Mueller, W. M.; Blackledge, J. P.; Libowitz, G. G.: *Metal Hydrides; Thermodynamics of MH Systems*. Academic Press Inc. (London) LTD. London. (1968)50-56.
- [43] Schlapbach, L.: *Hydrogen in Intermetallic Compounds II; Topics in Applied Physics*, Springer-Verlag. **67** (1992).
- [44] Bloch, J.: *Journal of Alloys and Compounds*. **312** (2002) 135-153.
- [45] Wang, C. S.; Wang, X.-. H.; Lei, Q.; Chen, P.; Wang, Q. D.: *International Journal of Hydrogen Energy*. **21** (1996) 471- 478.

- [46] Martin, M.; Gommel, G.; Borkhardt, C.; Fromm, E.: *Journal of Alloys and Compounds*. **238** (1996) 193-201.
- [47] David E.: An overview of advanced materials for hydrogen storage. *Journal of Material Processing Technology*. **162-163** (2005) 169-177
- [48] Mao, J.; Guo, Z.; Yu, X.; Liu, H.; Wu, Z.; Ni, J.: *International Journal of Hydrogen Energy*. **35** (2010) 4569-4575.
- [49] Avrami, M.: Kinetics of phase changes. I: General theory. *Journal of Chemical Physics*. **7** (1939) 1103-1112.
- [50] Jackson, K. A.: Kinetic processes: Crystal growth, diffusion and phase transformations in materials. Wiley-VCH, Weinheim. 2004.
- [51] Arrhenius Equation. Available [ONLINE]
http://en.wikipedia.org/wiki/Arrhenius_equation.
- [52] Gerasimov, K. B.; Goldberg, E. L.; Ivanov, E.Y.: *Journal of Less-Common Metals*. **131** (1987) 99-107.
- [53] Léon, A.; Knystautas, E. J.; Huot, J.; Schulz, R.: *Journal of Alloys and Compounds*. **345** (2002) 158-166.
- [54] Léon, A.; Knystautas, E.J.; Huot, J.; Schulz, R.: *Thin Solid Films*. (2005).
- [55] Sastry, M. V. C.; Viswanathan, B.; Srinivasa Murthy, S.: *Metal Hydrides*. Narosa Publishing House, New Delhi. 1998.
- [56] Schlapbach, L.; Züttel, A.: *Nature* .**414** (2001) 353-358.
- [57] Züttel, A.: Material for hydrogen storage. *Materials Today*. **9** (2003) 24-33.
- [58] Wilson, P. R.; Bowman Jr., R. C.; Mora, J. L.; Reiter, J. W.: *Journal of Alloys and Compounds*. **446-447** (2007) 676-680.
- [59] Libowitz, G. G.; Hayes, H. F.; Gibb, T. R. P.: *Journal of Physical Chemistry*. **62** (1958) 76.

- [60] Reilly, J.J.; Wiswall, R.H.: *Inorganic Chemistry*. **13** (1974) 218-222.
- [61] Yamanaka, K.; Saito, H.; Someno, M.: *Journal of Chemistry Society. Japan*. **8** (1975) 1267.
- [62] Nambu, T.; Ezaki, H.; Yukawa, H.; Morinaga, M.: *Journal of Alloys and Compounds*. **293-295** (1999) 213-216.
- [63] Banerjee, S.; Mukhopadhyay, P.: *Phase transformations: Examples from titanium and zirconium alloys 1st Ed.* Pergamon Material Series, Amsterdam, Netherlands. (2007) 756-758
- [64] Villars, P.; Calvert, L.D.: *Pearson's handbook of crystallographic data for intermetallic phases*, 2nd Ed. Materials Park, OH: ASM; 1991.
- [65] Friauf, J.B.: *Journal of American Chemistry Society*. **49** (1927) 3107.
- [66] Schulze, G. E.R.: *Z Elektrochem*. **45** (1939) 849.
- [67] Edwards, R. A.: *Metal Trans*. **3** (1972) 1365.
- [68] Nature of Laves Phases: Available [ONLINE] http://laves.mpie.de/laves_phases.html
- [69] Ohta, Y.; Pettifor, D. G.: *Journal of Physics: Condens. Matter*. **2**(1990) 8189-8194.
- [70] Stein, F.; Palm, M.; Sauthoff, G.: *Intermetallics*. **12** (2004) 713-720.
- [71] Van Midden, H.J.P.; Prodan, A.; Zupanic, E.; Zltko, R.; Makrids, S.S.; Stubos, A.K.: *Journal of Physical Chemistry*. **114** (2010) 4221-4227
- [72] Hong, S.; Fu, C. L.: *Physics Reviews B*. **66** (2002) 94109.
- [73] Switendick, A.C.Z.: *Physical Chemistry*. **117** (1979) 89.
- [74] Douglas, I.; Derek, N.: *Journal of Less-Common Metals*. **115** (1986) 23-33.
- [75] Willems, J. J.G.; Buschow, K. H. J.: *Journal of Less-Common Metals*. **129** (1987) 13-30.
- [76] Zijlstra, H.; Westendorp, F. F.: Influence of Hydrogen on the Magnetic Properties of SmCo₅. *Solid state Comm*. **7** (1969) 857-859.

- [77] van Vucht, J.H.N.; Kuijpers, F. A.; Bruining, H. C .M.: Reversible Room-Temperature Absorption of Large Quantities of Hydrogen by Intermetallic Compounds. *Philips Res.Repts.*, **25** (1970) 133-140.
- [78] Sandrock, G. D.: *Hydrogen Metal Systems; Production and Utilization of Hydrogen and Future Aspects*. Kluwer Academic Publishers, London, 1994.
- [79] Sandrock, G.: 'State-of-the-art review of hydrogen storage in reversible metal hydrides for military fuel cell applications', U.S. Department of Commerce, National Technical Information Service, USA, 1997.
- [80] Notten, P. H.L.; J.L.C. Daams, J.L.C.; Einerhand, R.E.F.: *Journal of Alloys and Compounds*, **210** (1994) 221-232.
- [81] Notten, P. H.L.; J.L.C. Daams, J.L.C.; Einerhand, R.E. F.: *Journal of Alloys and Compounds*, **210** (1994) 233-241.
- [82] Percheron-Guégan, A.; Lartigue, C.; Achard, J.-C.; Germi, P.; Tasset, F.: *Journal of the Less-Common Metals*, **74** (1980) 1-12.
- [83] Lartigue, C.; Percheron-Guégan, A.; Achard, J.-C. ; Tasset, F.: *Journal of Less-Common Metals*, **75** (1980) 23-29.
- [84] Latroche, M.; Rodriguez-Carvajal, J.; Percheron-Guégan A.; Bourée-Vigneron,F.: *Journal of Alloys and Compounds*, **218** (1995) 64-72.
- [85] Joubert, J.-M.; Latroche, M.; Cerný, R.; Bowman Jr., R. C.; Percheron-Guégan, A.; Yvon, K.: *Journal of Alloys and Compounds*, **293-295** (1999) 124-129.
- [86] Kolachev, B.A.; Shahn, R.E.: *A A Il'in Alloys for Hydrogen Storage Reference Book, "Metallurgy"*, Moscow. (1995) 87-138.
- [87] Yvon, K.; Fischer, P.: 'Hydrogen in intermetallic compounds', L. Schlapbach Ed., Topics in Applied Physics, Springer, Berlin, **63**, 1988,
- [88] Barrett, C.S.; Massalski, T. B.: *Structure of Metals*, 3rd Ed.; Pergamon, Oxford, 1980.

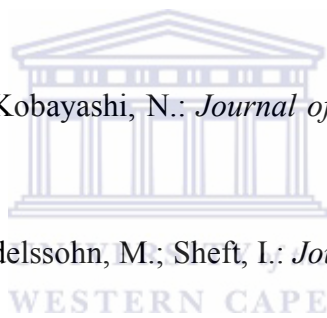
- [89] Filatova, E. A.; Yakovleva, N. A.; Semenenko, K. N.: *Russian Chemical Bulletin*. **48** (October 1999) 10.
- [90] Førde, T.: Experimental Studies and Theoretical Comparison of four different Metal Hydride Storage Units. PhD Thesis. Institute for Energy Technology, Kjeller Norway, 2007.
- [91] Førde, T.; Maehlen, J. P.; Yartys, V. A.; Lototsky, M. V.; Uchida, H.: *International Journal of Hydrogen Energy*. **32** (2007) 1041-1049.
- [92] Mungole, M. N.; Balasubramaniam, R.: *International Journal of Hydrogen Energy*. **20** (1995) 51-57.
- [93] Sandrock, G. D.; Goodwell, P. D.: *Journal of Less-Common Metals*. **73** (1980) 161.
- [94] Han, J. L.; Lee, J. Y.: *Journal of Less-Common Metals*. **152** (1989) 329-338.
- [95] Yuan, X.; Liu, H-S.; Ma.Z-F.; Xu, N.: *Journal of Alloys and Compounds*. **359** (2003) 300-306.
- [96] Paul Boncour, V.; Joubert, J. M.; Latroche, M.; Percheron-Guegan, A.: *Journal of Magnetic Materials*. **246** (2002) 330-332.
- [97] Schweppe, F.; Martin, M.; Fromm, E.: *Journal of Alloys and Compounds*. **253-254** (1997) 511-514.
- [98] Liu, F.-J.; Suda, S.: *Journal of Alloys and Compounds*. **231** (1995) 742-750.
- [99] Liu, F.-J.; Suda, S.: *Journal of Alloys and Compounds*. **232** (1996) 204-211.
- [100] Wang, X.-L.; Suda, S.: *Journal of Alloys and Compounds*. **231** (1995) 380-386.
- [101] Wiley, D. B.; Harris, I. R.; Pratt, A.S.: *Journal of Alloys and Compounds*. **293-295** (1999) 613-620.
- [102] Yang, H.; Yaun, H.; Ji, J.; Sun, H.; Zhou, Z.; Zhang, Y.: *Journal of Alloys and Compounds*. **330-332** (2002) 640-644.
- [103] Sun, Y-M.; Suda, S.: *Journal of Alloys and Compounds*. **330-332** (2002) 627-631.

- [104] Uchida, H.: *International J. of Hydrogen energy*. **24** (1999) 861-869.
- [105] Chen, W.: *Journal of Power sources*. **92(1-2)** (2001) 102-107.
- [106] Iwakura, C.; Matsuoka, M.; Asai, K.; Kohno, T.: *Journal of Power Sources*. **38** (1992) 335.
- [107] Matsuoka, M.; Asai, K.; Fukumoto, Y.; Iwakura, C.: *Electrochem. Acta*. **38** (1993) 65.
- [108] Chio, W.; Yamataka, K.; Zhang, S. G.; Inoue, H.; Iwakura, C.: *Journal of Electrochemistry Society*. **146** (1999) 46.
- [109] Iwakura, C.; Chio, W. K.; Zhang, S. G.; Inoue, H.: *Electrochem. Acta*. **44** (1999) 1677.
- [110] Uchida, H. H.; Watanabe, Y.; Matsumura, Y.; Uchida, H.: *Journal of Alloys and Compounds*. **231** (1995) 679-683.
- [111] Ikoma, M.; Komori, K.; Kaida, S.; Iwakura, C.: *Journal of alloys and Compounds*. **284** (1999) 92-98.
- [112] Imoto, T.; Kato, K.; Higashiyama, N.; Kimoto, M.; Itoh, Y.; Nishio, K.: *Journal of Alloys and Compounds*. **282** (1999) 274-278.
- [113] Zhang, P.; Wang, X.; Tu, J.; Chen, G.: *Journal of rare earths*. **27** (2009) 510.
- [114] Kaiya, H.; Ookawa, T.: *Journal of Alloys and Compounds*. **231** (1995) 598-603.
- [115] Shan, X.; Payer, J. H.; Wainright, J. S.: *Journal of Alloys and Compounds*. **426** (2006) 400-407.
- [116] Williams W.; Nechaev A.N.; Lototsky M.V.; Yartys V.A.; Solberg J.K.; Denys R.V.: *Material Chemistry and Physics*. **115** (2009) 136-141.
- [117] Ren, J.; Williams, M.; Lototsky, M.; Davids, W.; Ulleberg, Ø: *International Journal of Hydrogen Energy*. **35(16)** (2010) 8626-8630.
- [118] Wu, H.; Anan, A. A.: U.S. Patent. **5,451,474**(1995).

- [119] Harris, I. R.; Willey, D. B.; Pederzollic, D.; Pratt, A. S.; Swift, J.; Walton, A.: *Journal of Alloys and Compounds*. **330-332**(2002)806-809.
- [120] Roa, F.; Way, F. D.; McCormick, R. L.; Paglieri, S. N.: *Chemical Engineering Journal*. **93** (2003) 11-22.
- [121] Ambrosio, R. C.; Ticianelli, E.A.: *Surface and Coatings Technology*. **197** (2005) 215-222.
- [122] Bratanich, T. I.; Bulanov, V. N.; Skorokhod, V. V.: *Powder Metallurgy and Metal Ceramics*. **41(5-6)** (2002)309-316.
- [123] Zaluski, L.; Zaluska, A.; Tessier, P.; Strom-Olsen, J. O.; Schulz, R.: *Journal of alloys and Compounds*. **217** (1995) 295-300.
- [124] Shan, X.; Payer, J. H.; Wainright, J. S.: *Journal of Alloys and Compounds*. **430** (2007) 262-268.
- [125] Doll, G.L.; Mensah, B. A. Mohseni, H.; Scharf, T. W.: *Journal of Thermal Spray Technology*. **19(1-2)** (2010) 510.
- [126] Xomeritakis, G.; Lin, Y.S.: *Journal of Membrane Science*. **120** (1996) 261-272.
- [127] Alvisi, M.; Galtieri, G.; Giorgi, L.; Giorgi, R.; Serra, E.; Signore, M.A.: *Surface and Coatings Technology*. **200(5-6)** (2005) 1325-1329.
- [128] McCool, B. A.; Lin, Y.S.: *Journal of Materials Science*. **36** (2001) 3221-3227.
- [129] Yeung, K.L.; Christiansen, S.C.; Varma, A.: *Journal of Membrane Science*. **159**(1999)107-122.
- [130] Xu, X.; Song, C.: *Applied Catalysis A: General*. **300** (2006) 130-138.
- [131] Joseph, B.; Schiavo, B.: *Journal of Alloys and Compounds*. 2009.
- [132] Li, G.; Liu, X.; Guo, Q.; Tang, J.; Yan, B.: *Materials Science Forum*. **534-536** (2007) 785-788.

- [133] Itoh, N.; Tomura, N.; Tsuji, T.; Hongo, M.: *Microporous and Mesoporous Materials*. **39** (2000) 103-111.
- [134] Keuler, J. N.; Lorenzen, L.; Sanderson, R. D.; Linkov, V.: *Plating and Surface Finishing*. **August** (1997) 34-40.
- [135] Dressick, W.J.; Dulcey, C. S.; Georger, J. H.; Calabrese, G. S.; Calvert, J.M.: *Journal of the Electrochemical Society*. **141(1)**(1994)210-220.
- [136] Rao, C. R.K.; Trivedi, D.C.: *Coordination Chemistry Reviews* .**249** (2005) 613-631.
- [137] Geng, M.: *Journal of Alloys and Compounds*. **215** (1994) 151-153.
- [138] Xu, L., Liao, J., Haung L., Ou, D., Guo, Z., Zhang, H., Ge, C., Gu, N., Liu J.: *Thin solid Films*. **434** (1-2) (2003) 121-125.
- [139] Goodell, P. D.: *Journal of the Less-Common Metals*. **74** (1980) 175-184.
- [140] Murray, J.; Miller, H.; Bird, P.; Goudy, A. J.: *Journal of Alloys and Compounds*. **231** (1995) 841-845.
- [141] Singh, B. K.; Singh, A. K.; Imam, A. M.; Srivastava, O. N.: *International Journal of Hydrogen Energy*. **26** (2001) 817-821.
- [142] Suzuki, Y.; Haraki, T.; Uchida, H.: *Journal of Alloys and Compounds*. **330-332** (2002) 488-491.
- [143] Kim, K. J.; Montoya, B.; Razani, A.; Lee, K. H.: *International Journal of Hydrogen Energy*. **26** (2001) 609-613.
- [144] MacDonald, B. D.; Rowe, A. M.: *International Journal of Hydrogen Energy*. **31** (2006) 1721-1731.
- [145] Klein, H. P.; Groll, M.: *International Journal of Hydrogen Energy*. **29** (2004) 1503-1511.
- [146] Qin, F.; Chen, J. P.; Lu, M.Q.; Chen, Z.J.; Zhou, Y. M.; Yang, K.: *Renewable Energy*. **32** (2007) 2034-2052.

- [147] Melnichuk, M.; Silin, N.; Peretti, H. A.: *International Journal of Hydrogen Energy*. **34** (2009) 3417-3424.
- [148] Nagel, M.; Komazaki, Y.; Suda, S.: *Journal of the Less-Common Metals*. **120** (1986) 35-43.
- [149] Suda, S.; Komazaki, Y.: *Journal of the Less-Common Metals*. **172-174** (1991) 1130-1137.
- [150] Isselhorst, A.; Groll, M.: *Journal of Alloys and Compounds*. **231** (1995) 888-894.
- [151] Laurencelle, F.; Dehouche, Z.; Morin, F.; Goyette, J.: *Journal of Alloys and Compounds*. **475** (2009) 810-816.
- [152] Sheft, I.; Gruen, D. M.; Lamich, G. J.: *Journal of the Less-Common Metals*. **74** (1980) 401-409.
- [153] Suda, S.; Komazaki, Y.; Kobayashi, N.: *Journal of Less-Common Metals*. **89** (1983) 317.
- [154] Ron, M.; Gruen, D.; Mendelssohn, M.; Sheft, I.: *Journal of the Less-Common Metals*. **74** (1980) 445-448.
- [155] Bershadsky, E.; Josephy, Y.; Ron, M.: *Journal of the Less-Common Metals*. **153** (1989) 65-78.
- [156] Kim, K. J.; Feldman, K. T.; Lloyd, G.; Razani, A.; Shanahan, K. L.: *International Journal of Hydrogen Energy*. **23** (1998) 355-362.
- [157] Kim, K. J.; Lloyd, G.; Razani, A.; Feldman, K. T.: *Powder Technology*. **99** (1998) 40-45.
- [158] Kim, K. J.; Lloyd, G. M.; Feldman, K. T.; Razani, A.: *Applied Thermal Engineering*. **18** (1998) 1325-1336.
- [159] Sanchez, A.R.; Klein, H. P.; Groll, M.: *International Journal of Hydrogen Energy*. **28** (2003) 515-527.



- [160] Chen, Y.; Sequeira Cesar, A. C.; Chen, C.; Wang, X.; Wang Q.: *International of Hydrogen Energy*. **28** (2003) 329-333.
- [161] Mellouli, S.; Askri, F.; Dhaou, H.; Jemni, A.; Ben Nasrallah, S.: *International Journal of Hydrogen Energy*. **32** (2007) 3501-3507.
- [162] Mellouli, S.; Askri, F.; Dhaou, H.; Jemni, A.; Ben Nasrallah, S.: *International Journal of Hydrogen Energy*. **35** (2010) 1693-1705.
- [163] Muthukumar, P.; Prakash M. M.; Srinivasa, M. S.: *International Journal of Hydrogen Energy*. **27** (2002) 1083-1092.
- [164] Laing, B.; Zhang, Z. X.; Wang, Y. Q.: *Journal of Xi'an Jiaotong University*. **38** (2004) 89-92.
- [165] Bedbak, S. S.; Ram G. M.: *International Journal of Hydrogen Energy*. **30** (2005) 1127-1137.
- [166] Mosher, D. A.; Arsenault, S.; Tang, X.; Anton, D. L.: *Journal of Alloys and Compounds*. **446-447** (2007) 707-712.
- [167] Laurencelle, F.; Dehouche, Z.; Goyette, J.; Bose, T. K.: *International Journal of Hydrogen Energy*. **31** (2006) 762-768.
- [168] Murthukumar, P.; Prakash M.M.; Srinivasa M.S.: *International Journal of Hydrogen Energy*. **30** (2005) 879-892.
- [169] Park, J. G.; Jang, K. J.; Lee, P. S.; Lee, J. Y.: *International Journal of Hydrogen Energy*. **26** (2001) 701-706.
- [170] Klein, H. P.; Groll, M.: *Applied Thermal Engineering*. **22** (2002) 631-639.
- [171] Ram, G. M.; Srinivasa, M. S.: *International Journal of Refrigeration*. **22** (1999) 137-149.
- [172] Nakagawa, T.; Inomata, A.; Aoki, H.; Muira, T.: *International Journal of Hydrogen Energy*. **25** (2000) 339-350.

- [173] Willers, E.; Groll, M.: *International Journal of Hydrogen Energy*. **24** (1999) 269-276.
- [174] Kim, K. J.; Feldman, K. T.; Lloyd, G.; Razani, A.: *Applied Thermal Engineering*. **17** (1997) 551-560.
- [175] Bjurstrom, H.; Komazaki, Y.; Suda, S.: *Journal of the Less-Common Metals*. **13** (1987) 225-234.
- [176] Lee, S. G.; Lee, H. H.; Lee, K. Y.; Lee, J. Y.: *Journal of Alloys and Compounds*. **235** (1996) 84-92.
- [177] Park, J. G.; Han, S. C.; Jang, H. Y.; Lee, S. M.; Lee, P. S.; Lee, J. Y.: *International Journal of Hydrogen Energy*. **27** (2002) 941-944.
- [178] Veerraj, C. H.; Ram, G. M.: *International Journal of Hydrogen Energy*. **34** (2009) 4340-4350.
- [179] Supper, W.; Groll, M.; Mayer, U.: *Journal of Less-Common Metals*. **104** (1984) 279-286.
- [180] Anevi, G.; Jansson, L.; Lewis, D.: *Journal of Less-Common Metals*. **104** (1984) 341-348.
- [181] Jemni, A.; Ben Nasrallah, S.: *International Journal of Hydrogen Energy*. **20**(1) (1995) 43-52.
- [182] Jemni, A.; Ben Nasrallah, S.: *International Journal of Hydrogen Energy*. **20**(11) (1995) 881-891.
- [183] Yang, F.S.; Wang, G.X.; Zhang, Z.X.; Meng, X.Y.; Rudolph, V.: *International Journal of Hydrogen Energy*. **35** (2010) 3832-3840.
- [184] XRD Basics, Available [ONLINE]
<http://hyperphysics.phy-astr.gsu.edu/hbase/quantum/bragg.html>
- [185] Lipson, H.; Steeple, H.: *Interpretation of X-ray Powder Diffraction Patterns*, Macmillan and Company Ltd, London. **4, 5** (1970) 93-94, 113-114.

- [186] Cullity, B. D.: *Elements of X-ray diffraction*. 2nd Edition, Ontario, Addison-Wesley Publishing Company Inc. **7** (1978) 188-226.
- [187] Crystal structure. Available [ONLINE] http://en.wikipedia.org/wiki/Crystal_structure
- [188] Hawkins, J. A.; Rittenhouse, J. L.: *Journal of Chemical Education* .**85** (**1**) (January 2008).
- [189] Lattice geometry, lattice vectors and reciprocal vectors. Available [ONLINE] <http://ocw.mit.edu/courses/earth-atmospheric-and-planetary-sciences/12-108-structure-of-earth-materials-fall-2004/lecture-notes/lec7.pdf>
- [190] Scanning Electron Microscopy, Available [ONLINE] http://en.wikipedia.org/wiki/Scanning_electron_microscope.
- [191] Energy Dispersive X-Ray Spectroscopy, Available [ONLINE] http://en.wikipedia.org/wiki/Energy-dispersive_X-ray_spectroscopy.
- [192] Skoog, D. A.; Holler, F. J.; Crouch, S. R.: *Principles of instrumental Analysis 6th Edition*. David Harris, Thomson Brooks/Cole, USA. (2007) 230-317.
- [193] Lajunen, L. H. J.: *Spectrochemical Analysis by Atomic Absorption and Emission*, Bath, Royal Society of Chemistry. **2** (1992) 45-48.
- [194] Brunauer, S.; Emmett, P. H.; Teller, E.: *Journal of American Society*. **60** (1938) 309-319.
- [195] Atkins, P. W.: *Physical Chemistry*, Oxford University Press, London. **28** (1979) 942.
- [196] Brunauer-Emmett-Teller Theory, Available [ONLINE] http://en.wikipedia.org/wiki/BET_theory.
- [197] Rudman, P. S.: *Journal of Applied Physics*. **50** (1979) 7195-7199.
- [198] Karty, A.; Grunzweig-Genossar, J.; Rudman, P. S.: **50** (1979) 7200-7209.
- [199] Bliznakov, S.; Lefterova, E.; Bozukov, L.; Popov, A.; Andreev, P.: *Techniques for Characterization of Hydrogen Absorption/Desorption in Metal Hydride Alloy*,

- Proceedings of the International Workshop” Advanced Techniques for Energy Sources Investigation and Testing” Sofia, Bulgaria.4-9 September 2004.
- [200] Cheethan, A. K.; Day, P.: *Solid State Chemistry Techniques*. New York, Oxford University Press .**2**; **10** (1987) 56, 68-71; 372.
- [201] Fukai, Y.: *The Metal Hydrogen System*. New York, Springer-Verlag, 1993.
- [202] Larsen, J. W.; Livesay, B. R.: *Journal of Less-Common Metals*. **73** (1980) 79 – 88.
- [203] Pons, M.; Dantzer, P.: Determination of thermal conductivity and wall heat transfer coefficient in hydrogen storage materials.– Hydrogen Energy Progress. IX. Proc. 9-th World Hydrogen Energy Conf., Paris, France, 22-25 June 1992.– Ed. by T.N.Veziroğlu, C.Derive and J.Pottier., MCI, Paris, vol.2, p.961-970
- [204] Ben Nasrallah, S.; Jemni, A.: *International Journal of Hydrogen Energy*. **22**(1) (1997) 67–76.
- [205] Fowler, R. H.: Adsorption isotherms. Critical conditions.– Proc. Cambridge Philos. Soc., **32** (1936) 144–151.
- [206] Peierls, R. : Statistical theory of adsorption with interactions between the adsorbed atoms.– Ibid., 471–476.
- [207] Lacher, J. R.: Proc. Roy. Society. London, Ser. **A161 (A907-20)** (1937)525-545.
- [208] Kierstead, H. A.: *Journal of Less-Common Metals*.**71** (1980) 303.
- [209] Kierstead, H. A.: *Journal of Less-Common Metals*. **75** (1980) 267-271.
- [210] Flanagan, T. B.; Oates, W. A.; Thermodynamics of intermetallic compound–hydrogen systems. – Hydrogen in Intermetallic Compounds. I. – Ed. by L.Schlapbach, Springer-Verlag. (1988) 49–85.
- [211] Harashima, A.; Tanaka, T.; Sakaoku, T.: *Journal of Physical Society Japanese*. **3** (1948) 208-213.

- [212] Marinin, V. S.; Umerenkova, K. R.; Shmalko, Yu. F.; Lobko, M. P.; Lototskyy, M. V.: Interacting lattice gas model for hydrogen subsystem of metal hydrides.– *Functional Materials*. **9 (3)** (2002) 395–401
- [213] Lototskyy, M.V.; Yartys, V.A.; Marinin, V.S.; Lototskyy, N.M.: *Journal of Alloys and Compounds* .**356–357** (2003) 27–31.
- [214] Shilov, A.L.; Efremenko, N.E.: *Journal of Physical Chemistry*. **60 (12)** (1986) 3024–3028.
- [215] Lototskyy, M. V.: *Kharkov Univ. Bull., Chemical Sciences*. **477 (5/28)** (2000) 45–53.
- [216] Lototskyy, M.; Halldors, H.; Klochko, Ye.; Ren, J.; Linkov, V.: Hydrogen Materials Science and Chemistry of Carbon Nanomaterials, ICHMS'2009 XI International Conference, Yalta-Crimea-UKRAINE, August 25-31, 2009.
- [217] Du, Y. L.; Yang, X. G.; Zhang, Q. A.; Lei, Y. Q.; Zhang, M.S.: *International Journal of Hydrogen Energy*.**26** (2001) 333-337.
- [218] Slater, J. C.: *Journal of Chemical Physics*. **39** (1964) 3199–204.
- [219] Lynch, J.; Reilly, J. J.: *Journal of Less-Common Metals*. **87** (1982) 225.
- [220] Ogawa, T.; Ohnishi, K.; Misawa, T.: *Journal of Less-common metals*.**138** (1988)143.
- [221] Baichtok, Yu. K.; Mordkovich, V. Z.; Dudakova, N. V.; Avetisov, A. K.; Kasimtsev, A.V.; Mordovin, V. P.: *Journal for Alternative Energy and Ecology, ISJAE*. **2(10)** (2004) 50–54.
- [222] Williams, M.: Palladium Surface-modified rare earth metal-based AB₅-type metal hydride-forming materials. Thesis, University of the Western Cape.2008.
- [223] Uchida, H. H.; Wulz, H.-G.; Fromm, E.: *Journal of Less-Common Metals*. **172,174** (1991)1076.
- [224] Ström-Olsen, J. O; Zhao, Y.; Ryan, D.H.; Huai, Y.; Cochrane, R.W.: *Journal of Less-Common Metals*.**172, 174** (1991) 922.

- [225] Züttel, A.; Meli, F.; Schlapbach, L.: *Journal of Alloys and Compounds*. **200** (1993) 157.
- [226] Pratt, A. S.; Willey, D.B.; Harris, I. R.: *Platinum Metals Review*, **43(2)** (1999) 50-58
- [227] Yuan, X. X.; Liu, H.S.; Ma, Z.F.; Xu, N.X.: *Journal of Alloys and Compounds*. **359** (2003) 300.
- [228] Joubert, J. M.; Latroche, M.; Percheron-Gu'egan, A.: *Journal of Alloys and Compounds*. **275–277** (1998) 118.
- [229] Paul-Boncour, V.; Joubert, J. M.; Latroche, M.; Percheron-Gu'egan, A.: *Journal of Alloys and Compounds*. **330–332** (2002) 246–249.
- [230] Zeng, Q. X.; Joubert, J.M.; Latroche, M.; Jun, D.; Percheron-Gu'egan, A.: *Journal of Alloys and Compounds*. **360** (2003) 290–293.
- [231] Kolachev, B.A.; Shalin, R. E.; Il'in, A. A.: Hydrogen Storage alloys.- Moscow: Metallurgy. (1995) 384.
- [232] Yoshikawa, A.; Matsumoto, T.; Yagisawa, K.: *Journal of Less-Common Metals*. **88**(1982) 73-79.
- [233] Dantzer, P.: *Materials Science and Engineering A*. **329-331** (2002) 313-320.
- [234] Nasako, K.; Ito, Y.; Hiro, N.; Osumi, M.: *Journal of Alloys and Compounds*. **264** (1998) 271–276.
- [235] Matsumura, Y.; Shen, W.-J.; Ichihashi, Y.; Ando, H.: *Catalysis Letters*. **68** (2000) 181-183.
- [236] Ivey, D. G.; Northwood, D. O.: *Journal of Materials Science*, **18** (1983) 321-347.
- [237] Beeri, O.; Cohen, D.; Gavra, Z.; Johnson, J. R.; Mintz, M. H.: *Journal of Alloys Compounds*. **267** (1998) 113.

- [238] Bujlo, P.; Ulleberg, Ø.; Mabunda, R. ; Lototskyy, M.; Ren, J. ; Ntsendwana, B.: Fuel Cell System for Light Duty Vehicle - A Hi Fambeni Tricycle, SECOND ANNUAL RETECZA CONFERENCE, 11 - 13 August 2010 Kwa-Maritane Bush Lodge.
- [239] Ulleberg, Ø.; Lototskyy, M.; Ntsendwana, B.; Ren, J.; Klochko, Ye.: Metal hydride hydrogen storage units for low-temperature PEMFC power systems; oral presentation at 18th World Hydrogen Energy Conference, May 16 - 21, 2010, Essen, Germany.

